

AD-A268 103



DOCUMENTATION PAGE

Form Approved

OMB No. 0704-0188

This system is designed to provide a single source for information, including the time for reviewing instructions, searching existing data sources, gathering and maintaining the collection of information, and sending comments regarding this burden estimate or any other aspect of this system, its burden, or Washington Headquarters Services, Directorate for Information Operations and Reports, 1215 Jefferson Road, Suite 1204, Washington, DC 20540-6001.

1. REPORT DATE May 93		3. REPORT TYPE AND DATES COVERED THESIS/DISSERTATION	
4. TITLE AND SUBTITLE An Analysis of Simulated and Actual DMSP SSM/T-2 Brightness Temperatures		5. FUNDING NUMBERS 	
6. AUTHOR(S) Frank A. Leute IV			
7. PERFORMING ORGANIZATION NAME(S) AND ADDRESS(ES) AFIT Student Attending: Colorado State Univ		8. PERFORMING ORGANIZATION REPORT NUMBER AFIT/CI/CIA- 93-016	
9. SPONSORING, MONITORING AGENCY NAME(S) AND ADDRESS(ES) DEPARTMENT OF THE AIR FORCE AFIT/CI 2950 P STREET WRIGHT-PATTERSON AFB OH 45433-7765		10. SPONSORING / MONITORING AGENCY REPORT NUMBER	
11. SUPPLEMENTARY NOTES			
12a. DISTRIBUTION AVAILABILITY STATEMENT Approved for Public Release IAW 190-1 Distribution Unlimited MICHAEL M. BRICKER, SMSgt, USAF Chief Administration		12b. DISTRIBUTION CODE DTIC ELECTE AUG 17 1993 S A D	
13. ABSTRACT (Maximum 200 words)			
14. SUBJECT TERMS			
15. NUMBER OF PAGES 99		16. PRICE CODE	
17. SECURITY CLASSIFICATION OF REPORT	18. SECURITY CLASSIFICATION OF THIS PAGE	19. SECURITY CLASSIFICATION OF ABSTRACT	20. LIMITATION OF ABSTRACT

93 3 15 050

93-18981



**Best
Available
Copy**

93-216

THESIS

AN ANALYSIS OF SIMULATED AND ACTUAL DMSP SSM/T-2 BRIGHTNESS
TEMPERATURES

Accession For	
NTIS CRA&I	<input checked="checked" type="checkbox"/>
DTIC TAB	<input type="checkbox"/>
Unannounced	<input type="checkbox"/>
Justification	
By	
Distribution/	
Availability Codes	
Dist	Availability or Special
A-1	

Submitted by

FRANK A. LEUTE IV

Department of Atmospheric Science

DTIC QUALITY INSPECTED 3

In partial fulfillment of the requirements
for the degree of Master of Science
Colorado State University
Fort Collins, Colorado
Summer, 1993

COLORADO STATE UNIVERSITY

May 13, 1993

WE HEREBY RECOMMEND THAT THE THESIS PREPARED UNDER OUR SUPERVISION BY FRANK A. LEUTE IV ENTITLED AN ANALYSIS OF SIMULATED AND ACTUAL DMSP SSM/T-2 BRIGHTNESS TEMPERATURES BE ACCEPTED AS FULFILLING IN PART REQUIREMENTS FOR THE DEGREE OF MASTER OF SCIENCE.

Committee on Graduate Work

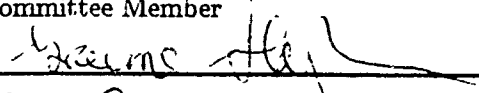


Committee Member



Committee Member

Committee Member



Adviser



Department Head

ABSTRACT OF THESIS

AN ANALYSIS OF SIMULATED AND ACTUAL DMSP SSM/T-2 BRIGHTNESS TEMPERATURES

Defense Meteorological Satellite Program (DMSP) Special Sensor Microwave/T-2 (SSM/T-2 or T-2) global brightness temperature maps are related to some of the known observed general circulation features of the atmosphere and surface characteristics of Earth. The brightness temperatures from two regions with different large scale circulations are compared and contrasted.

The concept of the invariance of the weighting functions with respect to water vapor overburden is tested. It is demonstrated that the levels where the 183 ± 1 and 3 GHz brightness temperatures match the thermodynamic temperature are levels of approximately equal overburden. Water vapor overburden (integrated water vapor above a given level) was retrieved and mapped on a constant pressure surface from T-2 brightness temperatures and atmospheric temperature-pressure data. A simple physical retrieval scheme based on the approximately equal overburden, irrespective of the moisture profile, for the 183 ± 1 GHz frequency was developed and demonstrated. This simple retrieval could be used to initialize more sophisticated retrievals.

Simulation studies of some factors which affect brightness temperatures at the SSM/T-2 frequencies were conducted and the results discussed. These factors included moisture profiles, backgrounds with different emissivities, and low level water clouds.

FRANK A. LEUTE IV
Department of Atmospheric Science
Colorado State University
Fort Collins, Colorado 80523
Summer, 1993

ACKNOWLEDGEMENTS

I would like to thank my advisor, Dr. Graeme Stephens, for his assistance, guidance, and most especially his patience over the last two years. I would like to extend my gratitude to Dr. Thomas Vonder Haar and Dr. V. Chandrasekar for their evaluation of this thesis.

I extend my sincere gratitude to Mr. Bruce Thomas of Aerospace Corporation, Omaha, for providing the SSM/T-2 data used in this thesis. I would like to thank Col. Carl Bjerkås, Mr. Vincent Falcone, and Capt. Don Rhudy for obtaining the release of the SSM/T-2 data from Aerospace. I extend a heartfelt thank you to Ian Wittmeyer for his invaluable programming and plotting assistance. I could not have finished this study without the assistance of Tim Schneider, Darren Jackson, Frank Evans, Tak Wong and Tom Greenwald. They provided me technical assistance with computer operations and data acquisition. I thank Sue Lini and Heather Jensen for their administrative assistance.

I conclude by thanking my wife, Tara, for her love, encouragement, support, and understanding.

Aspects of this work were supported by NOAA Grant NA90AA-D-AC822, NOAA Grant NA90 RAH 00077, and NASA grant NAG8-876.

CONTENTS

1 INTRODUCTION	1
1.1 BACKGROUND	1
1.2 MICROWAVE/MILLIMETER WAVE SATELLITE RETRIEVALS	4
1.3 USE OF THE 183 GHz ABSORPTION LINE	6
1.4 MOTIVATION, OBJECTIVES, AND THESIS OUTLINE	8
1.4.1 Motivation	8
1.4.2 Objectives	8
1.4.3 Thesis Outline	8
2 THE DMSP SSM/T-2 AND T-1 INSTRUMENTS AND DATA ANALYSIS	10
2.1 DMSP Block 5F Satellite Characteristics	10
2.1.1 SSM/T-2 Channel Characteristics	11
2.1.2 T-2 Output Parameters	13
2.1.3 SSM/T-1 Channel Characteristics	13
2.1.4 SSM/T-2 and T-1 Scan Patterns	14
2.2 SSM/T-2 DATA	15
2.3 T-2 BRIGHTNESS TEMPERATURE MAPS	15
2.3.1 Channel 1 Brightness Temperature Maps	17
2.3.2 Channel 2 Brightness Temperature Maps	18
2.3.3 Channel 3 Brightness Temperature Maps	18
2.3.4 Channel 4 Brightness Temperature Maps	18
2.3.5 Channel 5 Brightness Temperature Maps	19
2.4 CHANNEL COHERENCE	20
3 MICROWAVE RADIATIVE TRANSFER AND WEIGHTING FUNCTIONS	38
3.1 THE RADIATIVE TRANSFER EQUATION FOR MICROWAVE REMOTE SENSING	39
3.1.1 Brightness Temperatures	39
3.2 WEIGHTING FUNCTIONS	42
3.2.1 Relative Humidity-based Weighting Functions	42
3.2.2 Transmission-based Weighting Functions	43
3.3 ATMOSPHERIC PROFILES, PROPAGATION MODEL, AND CLOUD MODELS	44
3.3.1 Atmospheric Profiles	46
3.3.2 The Propagation Model	46
3.3.3 Cloud Models	47

4 SENSITIVITY EFFECTS FOR THE DMSP SSM/T-2	48
4.1 DEPENDENCE ON MOISTURE PROFILES	48
4.2 DEPENDENCE ON BACKGROUND	54
4.2.1 Ocean Background	54
4.2.2 Land Background	59
4.3 DEPENDENCE ON CLOUDS	60
4.3.1 Dependence on Layer Thickness	66
4.3.2 Dependence on Layer Location	66
4.3.3 Dependence on Cloud Liquid Water Content	66
4.4 SCAN ANGLE EFFECTS	73
4.5 INTERPRETATION OF RESULTS	73
5 WATER VAPOR BURDEN	76
5.1 WATER VAPOR BURDEN AND THE SSM/T-2 FREQUENCIES	76
5.2 CHANNEL 2 WATER VAPOR BURDEN MAP	79
6 CONCLUSIONS AND SUMMARY	90
6.1 SUMMARY	90
6.2 CONCLUSIONS	91
6.3 DISCUSSION OF FUTURE WORK	93

LIST OF FIGURES

1.1	Hypotheses on water vapor feedback mechanisms (Stephens, personal communication). The left portion of the diagram is the feedback as presently perceived, with increasing temperature leading to increased water vapor largely in the boundary layer. The right portion of the diagram is the additional modification to the feedback by increasing the upper tropospheric moisture through convection.	3
2.1	Footprint patterns for the SSM/T-2 and SSM/T-1 (D. Rhudy, personnel communication).	16
2.2	Channel 1 brightness temperature map for 10-14 March 1993.	21
2.3	Channel 1 brightness temperature map for 16-18 March 1993.	22
2.4	Channel 2 brightness temperature map for 10-14 March 1993.	23
2.5	Channel 2 brightness temperature map for 16-18 March 1993.	24
2.6	Channel 3 brightness temperature map for 10-14 March 1993.	25
2.7	Channel 3 brightness temperature map for 16-18 March 1993.	26
2.8	Channel 4 brightness temperature map for 10-14 March 1993.	27
2.9	Channel 4 brightness temperature map for 16-18 March 1993.	28
2.10	Channel 5 brightness temperature map for 10-14 March 1993.	29
2.11	Channel 5 brightness temperature map for 16-18 March 1993.	30
2.12	Channel 5 versus Channel 4 brightness temperatures for the two Pacific areas.	32
2.13	Channel 5 versus Channel 3 brightness temperatures for the two Pacific areas.	33
2.14	Same as Figure 2.12 except Channel 5 vs. Channel 1.	34
2.15	Channel 4 versus Channel 2 brightness temperatures for the two Pacific areas.	35
2.16	Same as Figure 2.12 except Channel 4 vs. Channel 1.	37
3.1	Brightness temperature spectra from 1-200 GHz for cases (1) tropical atmosphere with no water vapor and reflectivity (R) = 0.3; (2) tropical atmosphere ($CWV = 41.2\text{g/m}^2$) and $R = 0.3$; (3) tropical atmosphere with a cloud ($LWC = 0.5\text{g/m}^2$) from 1-2 km and $R = 0.3$ and case (4) same as case (2) except $R = 0.0$. The locations of the SSM/I and SSM/T-2 channels are indicated by "1" and "2", respectively.	40
3.2	Clear sky weighting functions for the SSM/T-1 channels 1-4 for a tropical atmosphere, reflectivity = 0.03, and a column water vapor (CWV) = 41.2 kg/m^2	45
4.1	Clear sky weighting functions for the SSM/T-2 channels for a tropical atmosphere over an ocean background with a reflectivity factor of 0.3 and a thermometric temperature of 300 K.	50
4.2	The same as Figure 4.1 except for a midlatitude summer atmosphere.	51
4.3	The same as Figure 4.1 except for a midlatitude winter atmosphere.	52

4.4	The same as Figure 4.2 except with $2 \times$ water vapor profile.	53
4.5	Clear sky transmission for the tropical atmosphere.	55
4.6	Clear sky transmission for the midlatitude atmosphere.	56
4.7	Clear sky transmission for the midlatitude winter atmosphere.	57
4.8	Weighting functions as in Figure 4.1 except for stratus cloud ($w = 0.15 \text{ gm}^{-3}$) from 0.5-2.0 km (cloud model 1).	61
4.9	The same as Figure 4.8 except for cumulus cloud ($w = 1.0 \text{ gm}^{-3}$) from 1.0-3.5 km (cloud model 2).	62
4.10	The same as Figure 4.8 except for altostratus cloud ($w = 0.40 \text{ gm}^{-3}$) from 2.5-3.0 km (cloud model 3).	63
4.11	The same as Figure 4.8 except for stratocumulus cloud ($w = 0.55 \text{ gm}^{-3}$) from 0.5-1.0 km (cloud model 4).	64
4.12	The same as Figure 4.8 except for nimbostratus cloud ($w = 0.61 \text{ gm}^{-3}$) from 0.5-2.5 km (cloud model 5).	65
4.13	Brightness temperatures for Cloud Model 1 and a tropical atmosphere with LWC from 0.01 to 0.50 gm^{-3}	69
4.14	Brightness temperatures as in Figure 4.13 except for Cloud Model 2.	70
4.15	Brightness temperatures as in Figure 4.13 except for Cloud Model 3.	71
4.16	Brightness temperatures as in Figure 4.15 except for $R = 0.0$	72
4.17	Brightness temperatures as a function of observation angle for a tropical at- mosphere.	74
4.18	The same as Figure 4.17 except for a midlatitude summer atmosphere and T_{sf_c} $= 285 \text{ K}$	74
5.1	Water Vapor Overburdens at $183.31 \pm 1 \text{ GHz}$ for 47 Atmospheric Cases.	81
5.2	Water Vapor Overburden as in Figure 5.1 except at 180.31 GHz	82
5.3	Water vapor burden for $183 \pm 1 \text{ GHz}$. Atmospheres are abbreviated as in text.	83
5.4	Same as in Figure 5.4 except for $183 \pm 3 \text{ GHz}$	83
5.5	The same as Figure 5.3 except for $183.31 \pm 7 \text{ GHz}$	84
5.6	The same as Figure 5.3 except for 150 GHz	84
5.7	Map of pressure, p^* , where $T_t = T_b$	86
5.8	Water vapor burden on a constant pressure (393 mb) surface.	89

LIST OF TABLES

2.1	SSM/T-2 Channel Characteristics (after Griffin <i>et al.</i> , 1993).	12
2.2	SSM/T-1 Channel Characteristics.	14
3.1	Cloud Type Characteristics (after Isaacs and Deblonde, 1987)	47
4.1	Brightness temperatures (K) for emissivities from 0.82 to 0.66 (reflectivities from 0.34 to 0.18) for a midlatitude winter atmosphere.	58
4.2	Comparison of brightness temperatures for land ($\epsilon = 1.0$) and ocean($\epsilon = 0.7$) surfaces.	67
4.3	Brightness temperatures for variable cloud thickness (Δz (km)) and LWC (gm^{-3}) for a fixed cloud base (1 km), emissivity (0.97), and a tropical atmosphere.	67
4.4	Brightness temperatures for variable cloud base and LWC for a fixed emissivity ($\epsilon = 1.0$) and atmosphere (tropical).	68
5.1	Water Vapor Overburdens (U) at 183.31 ± 1 GHz for $T_b = T_t$	78
5.2	Water Vapor Overburden (U) at 183.31 ± 3 GHz for $T_b = T_t$	80

Chapter 1

INTRODUCTION

1.1 BACKGROUND

Water vapor plays a vital role in establishing our present-day climate. It is the most significant contributor to the observed greenhouse effect of the planet (Stephens and Tjemkes, 1992). Water vapor links the processes of evaporation, cloud formation, and precipitation. Latent heat release plays a large role in the dynamical flow fields of the tropical atmosphere and knowledge of the distribution, transport, and divergence of water in all phases is critical to work pertaining to the difficult problem of cloud feedback and its role in climate change (Stephens, personal communication).

The source of water vapor is primarily at the earth's surface whereas its sink is in the process of precipitation. Combining these sources and sinks with the atmospheric circulation means the distribution of water vapor in the atmosphere is highly variable both in spatial and temporal scales (Prabhakara and Dalu, 1980). Thus, it is necessary to establish a dense network for observing water vapor and its distribution. Present day observations are largely based in the use of radiosonde data and these data lack in the necessary global coverage needed for understanding the role of water vapor in climate.

Water vapor also affects the exchange of radiation between the atmosphere and space directly by its influence in atmospheric emission and indirectly by its role in cloud formation processes (Bates and Stephens, 1991). GEWEX (the Global Energy and Water Cycle Experiment, part of the World Climate Research Program) has the basic theme of developing a quantitative understanding of how water shapes the energy budget of the climate system of earth. The connections and relationships between the global hydrological cycle and the energy budget are critical to the question (and potential problem) of climate

change (Stephens and Tjemkes, 1992). The typical climate change scenario ($2 \times \text{CO}_2$) predicts a global warming of approximately twice (or treble, depending on the model) the CO_2 -induced warming with water vapor feedback than without this feedback (Houghton *et al.*, 1990). The first part of the water vapor feedback is due to the direct greenhouse effects of doubled CO_2 which directly leads to increased sea surface temperature (SST). The increased SST increases evaporation in the boundary layer which increases humidity in the boundary layer. The increase of water vapor in the boundary layer through its greenhouse effect increases the SST. The second part of the feedback process was hypothesized by Lindzen (1990). Water vapor feedback is also thought to be modulated by the changes in the vertical distribution of water vapor. Lindzen argues that the increased warming near the ground results in increased and deeper cumulus convection. This increased cumulus convection, he claims, leads to drying of the upper troposphere (above 5 km) and elevation of the altitude at which convected heat is deposited. Since greenhouse absorption is most important above 5 km these cumulus effects are negative and hence, should diminish the effect of CO_2 warming. In contrast to this view, present day climate models actually produce a moistening of the upper troposphere associated with this convection. Both hypotheses are depicted in Figure 1.1 (Stephens, personal communication). Attempts to study quantitatively the distribution and transport of water vapor in the atmosphere have been made using the global radiosonde network (e.g. Peixoto and Oort, 1983). Unfortunately, these studies have met limited success since these radiosonde observations are confined mainly to land areas since this is where the radiosonde stations are primarily located. Important atmospheric phenomenon restricted to oceanic areas are thus largely ignored (e.g. many aspects of El Niño, including westerly wind bursts and the location of moisture convergence/divergence). Early work on transports based on infrared (IR) water vapor data have been reported by Wittmeyer (1990). However, Wittmeyer and Vonder Haar (1993) and others report serious adverse cloud impacts in baroclinic zones. Schwartz and Doswell (1991) contend that more observations are essential in both time and space to improve mesoscale weather forecasting and further, that remote sensing systems have yet to approach the radiosonde's capability to resolve the vertical thermodynamic structure of the atmosphere. While the later may or may not remain true in the age

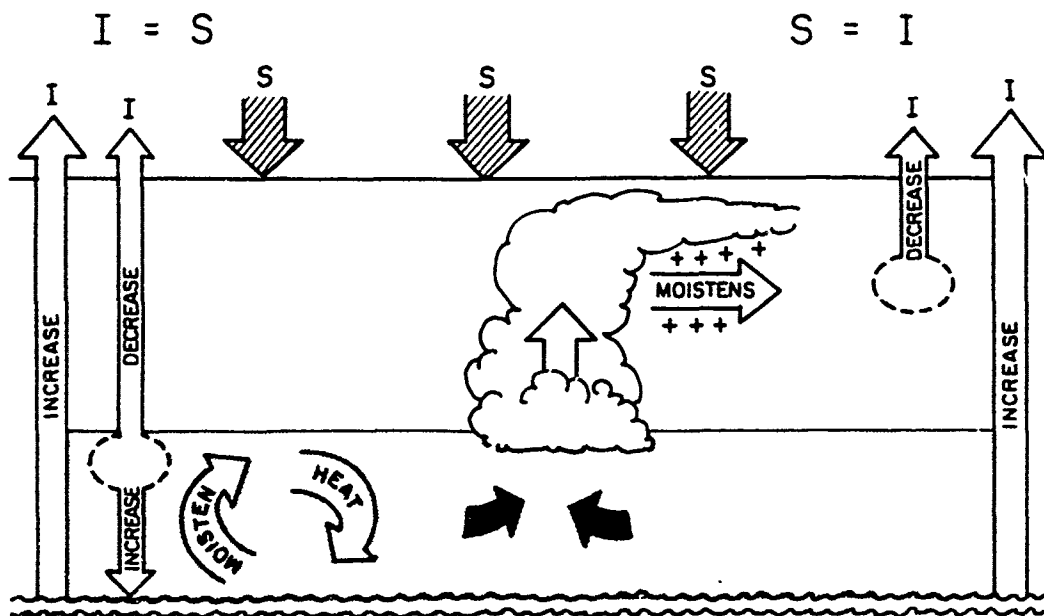


Figure 1.1: Hypotheses on water vapor feedback mechanisms (Stephens, personal communication). The left portion of the diagram is the feedback as presently perceived, with increasing temperature leading to increased water vapor largely in the boundary layer. The right portion of the diagram is the additional modification to the feedback by increasing the upper tropospheric moisture through convection.

of new microwave (millimeter wave) instruments, the former may be improved drastically by these new remote sensing systems. Certainly, the future lies, in many respects, in the advancement of the capabilities of remote sensing and the application of these capabilities to the measurement of atmospheric phenomena.

Satellites are used for many applications of remote sensing. The theory and practice of remote sensing spans many disciplines and is intimately related to inversion theory (see Twomey, 1977). The deployment of satellites expanded the opportunities for deriving the distribution of water vapor over the entire globe (as opposed to the limitations with land- and ship-based radiosondes). Moreover, many of the satellites launched in the 1970s and 1980s were restricted to measurements of the total precipitable water. The launch of the Special Sensor Microwave/Water Vapor Sounder (SSM/T-2 or T-2 which is described in more detail in the next chapter) heralds a new era in water vapor studies with its apparent capability of profiling atmospheric water vapor although not with the vertical resolution of current radiosondes.

Observing system simulation experiments (OSSEs) were carried out by Hoffman *et al.* (1990) to attempt to determine the impact of the Special Sensor Microwave/Temperature (SSM/T) sensors, in addition to other sensors. In these experiments the addition of the SSM/T-2 and SSM/T-1 data improves moisture analysis, especially in the tropics and the extratropics of the Southern Hemisphere. Root mean square (RMS) errors for relative humidity forecasts were decreased from 29% to 22% in the OSSEs with the SSM/T-2 data included. In the Southern Hemisphere, the SSM data improved the 500 hPa height forecasts by 12 hours.

1.2 MICROWAVE/MILLIMETER WAVE SATELLITE RETRIEVALS

The potential benefits of using passive microwave sensors to measure atmospheric parameters was first recognized in the 1940's. Nonetheless, it was only during the early 1960's when the first microwave radiometer was used on a spacecraft for the purpose of atmospheric remote sensing. The U.S. Mariner 2 Venus Probe in 1962 took the first satellite microwave emission observations of a planetary atmosphere. The two-channel

radiometer determined an upper limit on water vapor in Venus' atmosphere and retrieved a planetary surface temperature near 600°K (Barath *et al.*, 1964). The first U.S. satellite to make microwave observations of the earth's atmosphere was Nimbus 5 in 1972.

Microwave temperature retrieval on satellites operated by National Oceanic and Atmospheric Administration (NOAA) began with the Nimbus 5 (Nimbus E) Satellite Microwave Spectrometer and continued with the Nimbus 6 Scanning Microwave Spectrometer (SCAMS). The SCAMS used three channels (52.85 GHz, 53.85 GHz, and 55.45 GHz) in the oxygen absorption band between 50 and 60 GHz. The follow-on to the SCAMS is the Microwave Sounding Unit (MSU). It serves as a complement to the infrared temperature sounding unit called the High Resolution Infrared Sounder 2 (HIRS/2). The MSU has four channels (50.30 GHz, 53.74 GHz, 54.96 GHz, and 57.95 GHz) in the oxygen absorption band. The MSU is a 'Dicke' radiometer where the output of the receiver is proportional to the difference between the brightness temperature of the scene being viewed and the temperature of the internal radiation source. The primary purpose of the MSU is to make temperature soundings in the presence of clouds although MSU brightness temperature data are also currently being analyzed to understand certain aspects of the Earth's climate (Spencer *et al.*, 1990).

Water vapor retrieval from satellites occurs primarily in two regions of the electromagnetic spectrum, the infrared and microwave/millimeter wave regions. The HIRS/2 component of the polar orbiting TIROS-N operational vertical sounder (TOVS) (Smith *et al.*, 1979; Hillger and Vonder Haar, 1981) and the VISSR atmospheric sounder (VAS) on Geostationary Operational Environmental Satellites (GOES) (Smith, 1983) are examples of infrared instruments. These instruments use the absorption in the 6.7 μm infrared vibration band. They have had limited success in obtaining operationally useful water vapor profiles, in part because of the limitation of all infrared sensors that moisture sounding is impossible at levels below cloud top.

The appeal of microwave/millimeter wave sounding is that temperature retrievals suffer limited, if any, degradation due to the presence of clouds. For years the concept of using microwave remote sensing for water vapor retrieval was discussed. The first

efforts focused on the use of the weak H_2O rotational line at 22.235 GHz for sensing total precipitable water. The Nimbus 5 (Nimbus E) Satellite Microwave Spectrometer (NEMS) used channels at 22.235 and 31.4 GHz to measure atmospheric water vapor and liquid water over the oceans, even in the presence of many types of clouds. NEMS also measured the atmospheric temperature profile (as mentioned above) from 0-20 km (Staelin *et al.*, 1976).

Millimeter wavelengths also possess the advantage of low emissivity values for the ocean surface versus infrared wavelengths. The low emissivity values provide a relatively cold background that provides enough contrast to allow the retrieval of low level moisture fields (Hoffman *et al.*, 1990). The accuracy of these low level retrieved values decreases with high surface wind speeds due to the formation of foam on the ocean surface. This foam causes the emissivity of the ocean to increase, thus effectively reducing the contrast of this background surface. Additionally, millimeter wavelengths are able to sense through clouds so we can measure water vapor in the atmosphere below the clouds.

The Special Sensor Microwave/Imager (SSM/I) which has been carried on DMSP satellites since 1987 is also used to retrieve precipitable water. Jackson (1992) presents a review of several of the methods used for retrieval of precipitable water with the SSM/I. The SSM/I also makes use of the water vapor line at 22.235 GHz.

1.3 USE OF THE 183 GHz ABSORPTION LINE

The water vapor rotation absorption line feature at 183.31 GHz is about 20 times stronger than the rotation feature at 22.235 GHz (Waters, 1976). For this reason some researchers have discussed, in both abstract and definitive terms, its potential use to profile atmospheric water vapor since the 1970's.

Gaut *et al.* (1975) performed a study of a variety of microwave remote sensing systems to satisfy Air Force meteorological data requirements. The simulation and retrieval exercises investigated the following parameters: (a) total integrated water vapor, (b) the vertical distribution of water vapor, (c) temperature profile, and (d) the integrated and vertical distribution of cloud liquid water. While emphasizing channels below 60 GHz,

higher frequency channels (including those in the vicinity of 183 GHz) were also evaluated. The higher frequency channels were explored because: (a) it was desired to remove the effects of variable surface emissivity over land at the lower frequencies used to obtain water vapor information, (b) it was hypothesized that the higher frequency channels could provide information on cloud vertical structure, and (c) higher frequency channels were expected to be more sensitive to the integrated water vapor of clouds with relatively small liquid water content (Isaacs, 1987).

The pioneering work in the theory of using the 183 GHz rotation line for atmospheric remote sensing was written by Schaerer and Wilheit (1979). Several authors (Kakar, 1983; Kakar and Lambrechtsen, 1984; and Rosenkranz *et al.*, 1982) have since discussed various methods for the retrieval of clear sky atmospheric moisture profiles using channels around the 183 GHz line.

Subsequently, the theory has been extended to include clouds in the instrument field of view (FOV). Isaacs and Deblonde (1987) examined some of the effects of beam-filling liquid water clouds on millimeter wave moisture retrievals. They compared retrieved soundings with radiosondes from clear sky and cloudy conditions in simulation studies. Wilheit (1990) performed similar simulation studies expanding on the work he did previously with Schaerer. Both of these simulation studies were limited by the constraint of only one cloud layer.

Wang *et al.* (1983) showed experimentally that the 183 GHz line could be used for profiling atmospheric water vapor. They used an instrument, the Advanced Microwave Moisture Sounder (AMMS), from an airborne platform and this work was for clear sky cases. Lutz *et al.* (1991) used the algorithm developed by Wilheit for profiling atmospheric water vapor even in the presence of clouds. This work again used measurements from the AMMS. They showed the retrieved profiles were in general agreement with those from radiosonde data. Lutz *et al.* also noted that the algorithm did not perform very well in the vicinity of surface fronts. With the concept proven by these aircraft studies the next step was to put a moisture sounder on a satellite.

1.4 MOTIVATION, OBJECTIVES, AND THESIS OUTLINE

1.4.1 Motivation

The attraction for working with SSM/T-2 data is the opportunity to work data from the newest microwave instrument, also the first with frequencies near 183 GHz, on an Air Force meteorological satellite. The work on data from this instrument has barely begun and the ability to learn about some of the capabilities of the SSM/T-2 is a special opportunity. The ability to retrieve moisture soundings over the entire globe regularly is also appealing to the needs of GEWEX and other major global climate research programs. The T-2 will also help improve the output of numerical weather prediction models. Additionally, during the testing of the capabilities of an instrument a researcher may also learn of its limitations, whether they be inherent or due to the advancement of the science.

1.4.2 Objectives

This thesis attempts to achieve the following objectives:

1. Develop an understanding of many of the sensitivity factors which affect the microwave brightness temperatures, specifically for the SSM/T-2 frequencies.
2. Relate T-2 brightness temperature features to characteristics of the general circulation of the atmosphere and characteristics of the earth's surface.
3. Develop a simple physical retrieval of columnar water vapor which may be used to assist in the interpretation of the T-2 data and which may be used in initializations of more complex schemes. This retrieval scheme assumes the thermodynamic temperature and brightness temperature are equal at a level of approximately equal water vapor overburden (column water vapor above this level) irrespective of the temperature and moisture profiles.

1.4.3 Thesis Outline

Chapter 2 overviews the characteristics of the satellites which carry the SSM/T-2 and the characteristics of the instruments flown on these satellites. Chapter 2 also presents

brightness temperature maps for two T-2 data periods and an analysis of these data is presented. Chapter 2 concludes with scatter plots of brightness temperatures from two regions which demonstrate distinctly different temperature and moisture properties. Chapter 3 develops the radiative transfer equation as it applies to microwave remote sensing. It continues with a discussion of retrievals, first temperature (briefly) and then water vapor and introduces the concepts of weighting functions. Chapter 3 concludes with a description of various models (atmospheric propagation, atmospheric temperature/pressure, and cloud) used in the simulations discussed in this work. Chapter 4 analyzes the response of the DMSP SSM/T-2 channels to a variety of factors (what is called the forward problem) including: the profile of atmospheric moisture, the presence of clouds, the characteristics of clouds, and the background against which the atmosphere is viewed. The analysis of cloud effects here is limited only to low level water clouds. The possible effects of ice scattering at 183 GHz is not considered in this study although it may be important under some circumstances. Chapter 5 introduces the concept of water vapor burden and through the use of figures and tables, it is shown that the vapor burden is (nearly) constant at a given frequency near the 183 GHz absorption line and is only slightly dependent on the moisture and temperature profile. The water vapor burden is mapped onto a constant pressure surface thus providing the water vapor burden above this surface. Chapter 6 presents conclusions based on the work contained herein and a discussion about possible applications of the SSM/T-2 instrument and the possibilities of unified retrievals using other instruments from the DMSP microwave suite.

Chapter 2

THE DMSP SSM/T-2 AND T-1 INSTRUMENTS AND DATA ANALYSIS

2.1 DMSP Block 5D Satellite Characteristics

DMSP Block 5D Satellites operate in a sun synchronous, near-polar orbit with a nominal altitude of 800 km. The inclination angle of the orbit is 98.8° and an orbit period of 102.0 min. The orbit produces 14.1 orbit revolutions of the satellite per day. The combination of these parameters produces data void areas, diamond-shaped in appearance near the equator, in a 24 hour period. This missing coverage has obvious drawbacks when the data are to be applied to study the tropics (such as in the use of SSM/I to monitor tropical cyclone intensity and position). These data void regions shift with each orbit and complete coverage of the tropical regions is achieved after 72 hours. The orbit inclination also results in circular sectors of 230 km at both poles that are never sampled. The swath width for the SSM/I and SSM/T channels is 1400 km perpendicular to the satellite subtrack. The SSM/I is a conically scanning radiometer (with a constant scan angle of 45 degrees aft of the satellite) as compared to the SSM/T radiometers which are cross-track scanning sounders (which scan in a fashion similar to the OLS described below).

The primary instrument on the DMSP satellites is the Operational Linescan System (OLS) which is a four channel imager. The OLS visible channel for very high resolution has a resolution of 600 m. Since the bandwidth of this channel is very broad, the instrument receives more radiation from a given scene (e.g. as compared to the imagers on NOAA polar orbiter satellites) and hence has a greater sensitivity. The maximum swath width for the OLS is 2500 km. The OLS produces the visible and IR imagery used for many operational requirements by forecasters in the Department of Defense (DOD).

The F8 DMSP spacecraft, launched in 1987, was the first satellite with the Special Sensor Microwave/Imager (SSM/I). The SSM/I is a seven-channel passive microwave radiometer which operates at four frequencies. It receives both vertically and horizontally linearized radiation at 19.3, 37.0, and 85.5 GHz and vertical only at 22.2 GHz (Hollinger *et al.*, 1990). Data from this instrument are used for the determination of the following environmental parameters:

1. Ocean surface wind speeds.
2. Ice coverage, age and extent.
3. Cloud water content.
4. Integrated water vapor (precipitable water).
5. Precipitation over water.
6. Soil moisture.
7. Land surface temperature.
8. Snow water content.
9. Cloud amount.

The SSM/I is also flown on F11 together with the SSM/T-2 and SSM/T-1. These instruments being on the same satellite offer the possibility of a synergistic (also called a unified) approach to atmospheric retrieval where deficiencies of one instrument perhaps can be diminished or removed through the use of another instrument.

2.1.1 SSM/T-2 Channel Characteristics

The Defense Meteorological Satellite Program (DMSP) Special Sensor Microwave (also called Millimeter Wave) Water Vapor Sounder (SSM/T-2) currently flies on the F-11 satellite which was launched on November 28, 1991. The SSM/T-2 possesses 5 channels: three dual-pass bands located on the 183 GHz (1.64 mm) water vapor absorption line, one

on the line's wing (150 GHz), and a window channel (91.655 GHz). The local descending nodal crossing time of F-11 is approximately 0514. The T-2 is a total-power radiometer which measures the total power seen by the antenna over the signal processing integration time. The objective of the SSM/T-2 is to provide global measurements of the vertical profile of water vapor to support Air Force applications including the input of these profiles to numerical weather forecast models. The characteristics of the SSM/T-2 channels are shown in Table 2.1 (including the noise equivalent temperature uncertainty, NEDT).

Table 2.1: SSM/T-2 Channel Characteristics (after Griffin *et al.*, 1993).

Chan. No.	Center Frequency (GHz)	Nadir FOV (km)	Beam Acceptance (degrees)	Peak Altitude (hPa)	Pol.	NEDT (°K)	Response
1	183.31 ± 3	48	3.3	650	V	0.6	water vapor
2	183.31 ± 1	48	3.3	500	V	0.8	water vapor
3	183.31 ± 7	48	3.3	800	V	0.6	water vapor
4	91.655	88	6.0	Surface	V	0.6	surface
5	150.0	54	3.7	1000	V	0.6	surface

The T-2 was originally designed to be a four channel instrument (minus the channel near 92 GHz). The work of Isaacs and Deblonde (1985) showed that retrievals were not very accurate under some conditions (specifically, tropical atmospheres) without the 91.655 GHz channel.

The T-2 views both an internal hot-load target ($\sim 300^\circ\text{K}$) and cosmic background radiation for calibration measurements. The T-2 also underwent a calibration study led by the Geophysics Directorate of the Air Force's Phillips Laboratory. This calibration study included independent measurements and model calculation studies. These independent measurements were performed by the NASA Millimeter-wave Imaging Radiometer (MIR) carried on the NASA ER-2 aircraft (Racette *et al.*, 1992). The MIR and T-2 contain essentially the same channels with the exception of the window channel which for the MIR is located at 89 GHz. The NASA ER-2 equipped with the MIR undeflew selected DSMP satellite passes including ocean, coastal, and land background cases. RMS differences of $0.7\text{--}1.4^\circ\text{K}$ were measured between the T-2 and the MIR.

Radiative transfer model calculations were also conducted (at coincident times and locations with the model of Eyre and Woolf (1988)) using radiosonde data and estimates of the surface emittances. Although the comparisons of the model calculations with the T-2 data showed collocated RMS differences of 6.5°K, the calibration team concluded based on the data they had obtained that the SSM/T-2 suffers no significant bias in its calibration (Griffin *et al.*, 1993).

2.1.2 T-2 Output Parameters

The following parameters are derived from T-2 data using the operational retrieval retrieval scheme of A. Stogryn (Boucher *et al.*, 1993):

1. Relative humidity at 1000, 850, 700, 500, 400, and 300 mb levels.
2. Specific humidity at 1000, 850, 700, 500, 400 and 300 mb levels.
3. Water vapor mass (kg/m^2) between levels surface-1000, 1000-850, 850-700, 700-500, 500-300, and above 300 mb.

Although these parameters are produced operationally, the actual retrieval of data on water vapor from T-2 data is complex for reasons described in the next chapter and there remains considerable scope for research in understanding these complexities.

2.1.3 SSM/T-1 Channel Characteristics

The Special Sensor Microwave/Temperature Sounder (SSM/T-1) was developed and built by Aerojet ElectroSystems Company for the U.S. Air Force Space Systems Division Defense Meteorological Satellite Program (DMSP). The design methodology was a top-down systems development approach. The SSM/T-1, first launched in 1978, was designed to support Air Force and Department of Defense operational weather forecasting, specifically the data required by the Air Force Global Weather Central (AFGWC) numerical weather prediction (NWP) models. To incorporate the T-1 data, the T-1 is designed to emulate radiosonde temperature and pressure measurements, i.e. retrieve temperatures at the standard pressure levels, thicknesses between these levels, and the temperature and

pressure of the tropopause. Channel selection was such that the weighting functions are distributed as evenly as possible throughout the atmosphere (Falcone and Isaacs, 1987). Weighting functions for channels 1–4 of the T-1 were shown in Figure 3.1. The channel characteristics for the SSM/T-1 are shown in Table 2.2.

Table 2.2: SSM/T-1 Channel Characteristics.

Center Frequency (GHz)	Nadir FOV (km)	Beam Acceptance (degrees)	Peak Altitude (km)	NEDT (°K)	Response
50.5	204	14	0	0.6	surface
53.2	204	14	2	0.4	T at 2 km
54.35	204	14	6	0.4	T at 6 km
54.9	204	14	10	0.4	T at 10 km
58.4	204	14	30	0.5	T at 30 km
58.825	204	14	16	0.4	T at 16 km
59.4	204	14	22	0.4	T at 22 km

The SSM/T-1 is a passive 'Dicke' radiometer which scans in a cross-track fashion. The radiometer has a scan time of 32 seconds and a dwell time for each scene of 2.7 seconds; the instrument takes 0.3 seconds between each scene and the warm and cold calibrations occur during the remaining time. The SSM/T-1 operates in an oxygen absorption band using seven frequencies between 50 and 60 GHz and is similar to the MSU which was described above. The variation of the dry air absorption at each of these frequencies provides the basis for the retrieval of temperature profiles (Curtis and Shipley, 1987).

2.1.4 SSM/T-2 and T-1 Scan Patterns

The scan pattern for the SSM/T-2 is similar to the SSM/T-1. Since the SSM/T-2 operates at a longer wavelength than the SSM/T-1 and hence has a smaller footprint, or field of view, the SSM/T-2 samples four times as many scene stations (28 versus 7) per scan revolution, and must scan four times as fast to provide coincident samples. The result is that the SSM/T-2 produces 16 times as many total stations scenes. The footprint pattern is shown in Figure 2.1. The reason for coincident samples is that to produce water

vapor retrievals the T-2 operational algorithm also requires four of the seven measured T-1 frequency channels (Channels 1-4) to provide the requisite temperature sounding. The pattern in Figure 2.1 is changed by the presence of a glare obstructor or GLOB, on the satellite. The GLOB is designed to protect the OLS from solar insolation which could degrade the instrument but this also means that 1 scene of T-1 data and 4 scenes of T-2 data on the sun side of the satellite are degraded and therefore not used.

2.2 SSM/T-2 DATA

The SSM/T-2 data used for this thesis was kindly provided by Mr. Bruce Thomas of the DMSP Omaha Field Office of Aerospace Corporation. The data were obtained for approximately 78 revolutions of satellite F-11 in March 1993. The data package received from Aerospace Corporation consisted of T-2, T-1, and SSM/I data in a VMS back-up save set format. All data received from Aerospace were in sensor data record (SDR) format (also known as antenna pattern corrected temperatures).

The T-2 data set consists of 13 words in each record. Word 1 contains information on the scan scene (which provides the scan angle for the sensor) and the background against which the sensor is viewing (land, ocean, sea ice, or coast). The reason for the differentiation between backgrounds is to have a mechanism to help facilitate the determination of the surface emission for each viewing scene. A discussion of emissions for various backgrounds is included in Chapter 4. Word 2 contains the Julian hour (referenced to 00 UTC 31 December 1967), and words 3 and 4 are the Julian minute and second, respectively. Word 5 is the longitude (from 0.-360° East) and word 6 is the latitude ($\pm 90^\circ$) which together determine the earth location of the scan scene. Word 7 provides the terrain height (m) and word 8 is the 1000hPa height (m) from the operational forecasting model at AFGWC. Words 9-13 are the sensor data records (SDRs) for the five T-2 channels (Kelvin) (B. Thomas, personal communication).

2.3 T-2 BRIGHTNESS TEMPERATURE MAPS

The T-2 brightness temperatures fields for the available data from March 1993 were mapped and contoured. Since the 4 scan scenes on one side of the swath are unusable

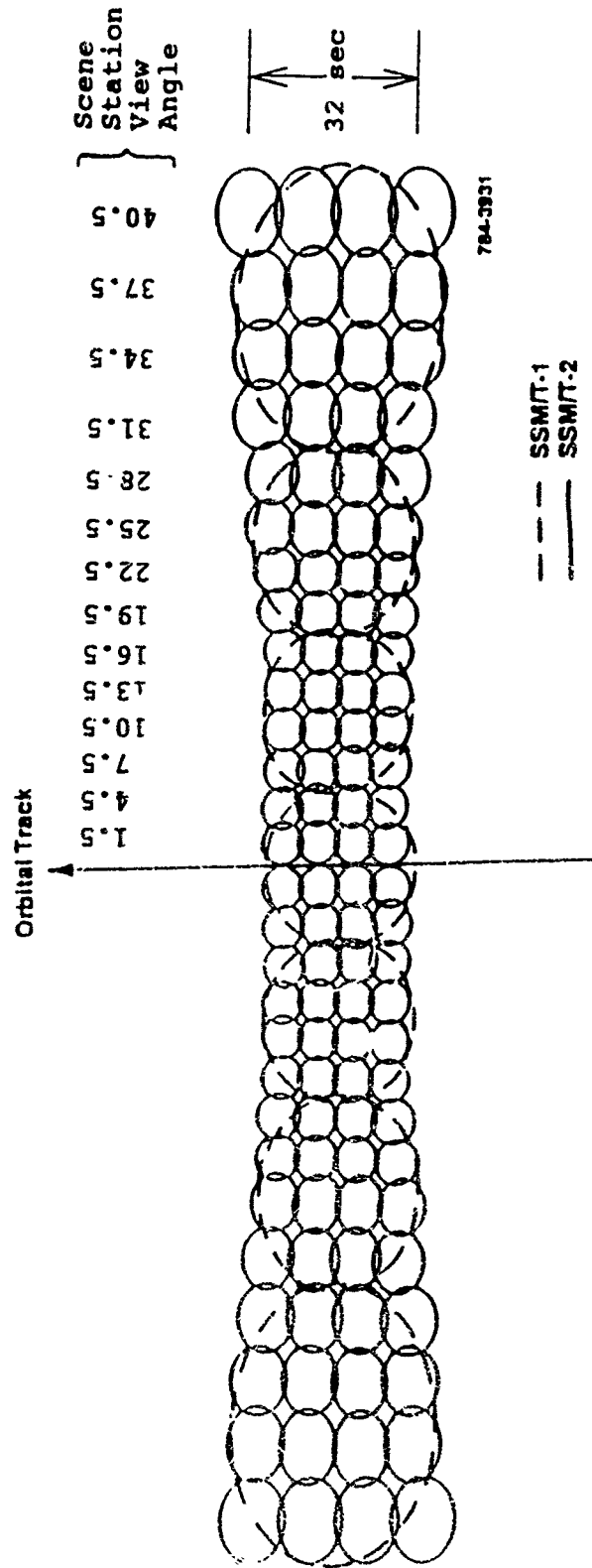


Figure 2.1: Footprint pattern for the SSM/T-2 and T-1. (D. Rhudy, personnel communication).

because of the shielding by the GLOB as mentioned above and because of the brightness temperature changes as a function of scan scene angle (discussed in further detail in Chapter 4), the outer 4 scenes on the other side of the scan were also removed. This results in a scan line that is considerably less than the 1400 km swath width mentioned above but it does mean a data set which is more representative requiring no corrections to the T-2 brightness temperatures for angle effects. The result of this is that there are areas during the two periods which are not sampled and these areas are represented by gray in the colored diagrams.

Data were binned into 1 degree latitude \times longitude bins and then averaged. Since resolution at nadir is about 50 km, bins twice the size of nadir resolution should be representative for the data.

2.3.1 Channel 1 Brightness Temperature Maps

Channel 1, at 183.31 ± 3 GHz, is used for the determination of mid-upper tropospheric water vapor and relative humidity information. As shown below (in Figures 4.1-4.3), the peak of the weighting function for this channel lies between 3-6 km for the three McClatchey atmospheres. Figures 2.2 and 2.3 are the Channel 1 brightness temperatures for the periods 10-14 March and 16-18 March 1993, respectively.

The areas in red which are located both north and south of the equator (e.g. roughly 20-25° from the equator) delineate the location of subsidence associated with the subtropical highs. This prominent feature is also prevalent in the distributions for other frequencies. The subtropical high in the North Atlantic extends from western Africa westward all the way to the Caribbean Sea.

Figure 2.3 suggests a more coherent and stronger ITCZ in the Pacific Ocean (the white and green color shading with several purple pixels). The South Pacific Convergence Zone (SPCZ) (from the central South Pacific extending northwest to east of New Guinea) is also more distinct in this figure. Both features appear cold (and thus moist) in contrast to the the warm (and thus dry) subsiding air poleward of these features.

2.3.2 Channel 2 Brightness Temperature Maps

The weighting functions of Channel 2 peak highest in the atmosphere (Figures 4.1–4.3 with peaks between 5–8 km) and measurements provided by Channel 2 thus applies to upper tropospheric moisture. Figure 2.4 and 2.5 are the Channel 2 brightness temperature maps for the two time periods described above. Maps for this channel have less spread of brightness temperatures than for Channel 1. Channel 2 shows several areas with high brightness temperatures over the oceans and these are: (1) in the central North Pacific near 10–15° latitude and near the date line, (2) in the eastern North Pacific south of Baja, California, (3) in the eastern North Atlantic off the west coast of Africa, (4) in the South Atlantic off the coast of Brazil and (5) near Madagascar in the Indian Ocean. These brightness temperatures indicate that the atmosphere is very dry in the upper levels and these regions are also over the subsidence regions indicated in Figures 2.2 and 2.3. The coldest brightness temperatures over the tropical oceans occur near Fiji in the western Pacific and in the central Indian Ocean. The cold brightness temperatures indicate deep convection in these areas and elevated amounts of upper tropospheric moisture.

2.3.3 Channel 3 Brightness Temperature Maps

Channel 3, located at 183.31 ± 7 GHz, senses levels of water vapor that occur deeper into the atmosphere according to the location of the weighting function maxima for this channel that are depicted in Chapter 4. Figure 2.6 and 2.7 are the brightness temperature maps for 10–14 March and 16–18 March, respectively. Once again, there exists coherence in the subsidence regions such that the broad areas of red color are the regions of subtropical high pressures underlying those dry regions noted in reference to the maps of Channels 1 and 2 brightness temperature. Similarly, the moist tropical regions where the deepest convection occurs appear relatively cold (indicated by white–green colors).

2.3.4 Channel 4 Brightness Temperature Maps

Channel 4, the window channel at 91.655 GHz, primarily senses the surface of the earth. Figures 2.8 and 2.9 are show the brightness temperatures from Channel 4 for the time periods described above. The red color across the land masses (especially Australia)

in the southern hemisphere point to clear skies (at least predominantly), a warm surface and a high emissivity for these land masses. This is not surprising when considering that the land has had the entire summer to become warm and dry. The lower emissivity of the adjacent ocean surfaces results in much lower brightness temperatures and it is easy to differentiate between land masses and ocean surfaces.

East of Japan there are four curved features with brightness temperatures warmer than the surrounding region. Daily maps of brightness temperatures (not shown) indicate this feature is a mesoscale storm system which has been viewed by the T-2 on successive satellite passes (over several days). The cloud features associated with this low-pressure system show up as warm brightness temperatures over the cold ocean background, resembling a comma cloud.

Regions of the tropical oceans show little structure. The yellow and brown colors extend farther south in the Southern Hemisphere as compared to the northern extent in the Northern Hemisphere due to warmer sea surface temperatures and low level moisture over these oceans, since the weighting functions corresponding to this channel peak at/near the surface. Since SSTs typically lag by about two months, SSTs in the southern oceans should be just beginning their fall from the yearly temperature maximum.

2.3.5 Channel 5 Brightness Temperature Maps

Channel 5, at 150 GHz, is located on the line wing of the absorption line at 183.31 GHz. As shown in Chapter 4, the weighting function for this channel peaks in the lower troposphere or at the earth's surface (depending on the moisture profile of the atmosphere). Figures 2.10 and 2.11 are the brightness temperature maps for the periods 10-14 and 16-18 March 1993. The maps hint at the ITCZ and associated convection (with the light yellow and white pixels) in the tropical oceans. Otherwise, there is not a great deal of structure to the temperature differences that hasn't already been said in the previous subsections.

Figure 2.11 does indicate a stronger SPCZ than does Figure 2.10. Australia has high brightness temperatures over the entire country likely indicating a high emissivity for the land and a dry atmosphere above it. Again, the land surfaces are easily found in the brightness temperature maps due to the emissivity contrasts with ocean surfaces.

The brightness temperature maps in Figure 2.2-2.11 provide an opportunity to examine some of the general circulation features of the atmosphere and to see the surface characteristics of ocean and land masses at the frequencies of the SSM/T-2.

2.4 CHANNEL COHERENCE

A helpful way of analyzing and understanding the properties of the T-2 channel brightness temperatures is to consider the relationships between channels. Here we consider two regions which are characterized by distinctly different large scale circulation features and thus different temperature and moisture properties.

The two areas selected are located over the Pacific Ocean. The first area corresponds approximately to the TOGA COARE (Coupled Ocean-Atmosphere Response Experiment) domain and is defined as the area 160-170° East longitude and 0-10° South latitude. This area is largely under the control of deep convection and ascent as part of the Hadley and Walker circulations and represents a region of relatively high moisture content at all levels. The brightness temperatures from this area are compared and contrasted with an area in the Eastern Pacific defined by the coordinates 110-120° West longitude and 10-20° North latitude. This East Pacific area is located in a region dominated by a subtropical high with its (assumed) associated strong subsidence and lower column water vapor. Time constraints did not permit a detailed analysis of the cloudiness over these regions during this study.

The brightness temperatures for these regions and for the 5 channels are plotted against each other in the form of scatter diagrams. Figure 2.12 shows Channel 5 versus Channel 4 for the two Pacific regions. The East Pacific (EP) region shows a very small scatter for the brightness temperature data. The Channel 4 temperatures are relatively low (as compared to the Channel 5) since this channel is designed to see the surface. As discussed in Chapter 4, the emissivity of the ocean surface is relatively low (~ 0.7) and it provides a cold background. Channel 5, on the line wing, provides both surface effects and the effects of low level water vapor. The brightness temperature indicates an emission temperature near 280 K. The West Pacific (WP) area shows a window brightness



226-0 234-0 242-0 250-0 258-0 266-0 274-0 282-0
 222-0 230-0 238-0 246-0 254-0 262-0 270-0 278-0 286-0

SSM/T-2 Channel 1
 1 Degree Bin Averages
 March 10-14, 1993

Figure 2.2: Channel 1 brightness temperature map for 10-14 March 1993.



226-0 234-0 242-0 250-0 258-0 266-0 274-0 282-0
 222-0 230-0 238-0 246-0 254-0 262-0 270-0 278-0 286-0

SSM/T-2 Channel 1
 1 Degree Bin Averages
 March 16-18, 1993

Figure 2.3: Channel 1 brightness temperature map for 16-18 March 1993.



220-0 228-0 236-0 244-0 252-0 260-0 268-0 276-0
 216-0 224-0 232-0 240-0 248-0 256-0 264-0 272-0 280-0

SSM/T-2 Channel 2
 1 Degree Bin Averages
 March 10-14, 1993

Figure 2.4: Channel 2 brightness temperature map for 10-14 March 1993.



220-0 228-0 236-0 244-0 252-0 260-0 268-0 276-0
 216-0 224-0 232-0 240-0 248-0 256-0 264-0 272-0 280-0

SSM/T-2 Channel 2
 1 Degree Bin Averages
 March 16-18, 1993

Figure 2.5: Channel 2 brightness temperature map for 16-18 March 1993.



204-0 216-0 228-0 240-0 252-0 264-0 276-0 288-0
 198-0 210-0 222-0 234-0 246-0 258-0 270-0 282-0 294-0

SSM/T-2 Channel 3
 1 Degree Bin Averages
 March 10-14, 1993

Figure 2.6: Channel 3 brightness temperature map for 10-14 March 1993.



SSM/T-2 Channel 3
1 Degree Bin Averages
March 16-18, 1993

Figure 2.7: Channel 3 brightness temperature map for 16-18 March 1993.



192-8 206-3 219-8 233-3 246-8 260-3 273-8 287-3

186-0 199-5 213-0 226-5 240-0 253-5 267-0 280-5 294-0

SSM/T-2 Channel 4

1 Degree Bin Averages

March 10-14, 1993

Figure 2.8: Channel 4 brightness temperature map for 10-14 March 1993.



192-8 206-3 219-8 233-3 246-8 260-3 273-8 287-3
 186-0 199-5 213-0 226-5 240-0 253-5 267-0 280-5 294-0

SSM/T-2 Channel 4
 1 Degree Bin Averages
 March 16-18, 1993

Figure 2.9: Channel 4 brightness temperature map for 16-18 March 1993.



190-0 206-0 222-0 238-0 254-0 270-0 286-0 302-0
 182-0 198-0 214-0 230-0 246-0 262-0 278-0 294-0 310-0

SSM/T-2 Channel 5
 1 Degree Bin Averages
 March 10-14, 1993

Figure 2.10: Channel 5 brightness temperature map for 10-14 March 1993.



190-0 206-0 222-0 238-0 254-0 270-0 286-0 302-0
 162-0 198-0 214-0 230-0 246-0 262-0 278-0 294-0 310-0

SSM/T-2 Channel 5
 1 Degree Bin Averages
 March 16-18, 1993

Figure 2.11: Channel 5 brightness temperature map for 16-18 March 1993.

temperature of 10-15 degrees higher than the East Pacific area. This likely occurs due to more emission by the water vapor (near the surface, emitting at a high temperature) in the wetter atmosphere in the West Pacific. The scatter of data from the West Pacific indicates that the area contains many inhomogeneities. Possible reasons for this scatter will be discussed later.

Figure 2.13 depicts the brightness temperatures of the 150 GHz channel and the 183 ± 7 GHz channel. Since these two channels are adjacent to each other, it is expected that the two channels would be well correlated. For the East Pacific area, the Channel 3 and 5 temperatures are nearly equal, with most of the Channel 3 temperatures within 10° of 280 K. For the WP region, Channel 3 becomes opaque more quickly and therefore, most of the temperatures are below 275 K. The vertical correlation of brightness temperature (and therefore water) shows up very well for the WP region. An almost linear relationship between these two channels is inferred by the data.

Figure 2.14 is the scatter plot of the brightness temperatures of Channels 1 and 5. The EP area again exhibits higher brightness temperatures for channels which peak above the surface, implying a dry upper atmosphere. Additionally, there is not much scatter of the data for this region, implying a profile which is nearly invariant. Channel 1 brightness temperatures for the WP region are about 20° colder than the EP region. This indicates that this channel is sensing water vapor at a colder temperature which means a higher altitude.

Perhaps the best depiction of the differences in the two areas is shown in Figure 2.15. This figure plots the window channel (Channel 4) against the channel closest to the absorption line (Channel 2). Figure 2.15 shows that the EP area has a high Channel 2 brightness temperature, implying the channel peaks well down in the atmosphere. The WP area has noticeably lower brightness temperatures for Channel 2, indicating a peak of the channel higher in the vertical (and consequently, at a lower thermometric temperature than for the EP). Channel 4 brightness temperatures are governed by the low emissivity of the cold ocean surface in the EP and the higher thermal temperature of the surface and lower atmosphere combined for the WP region.

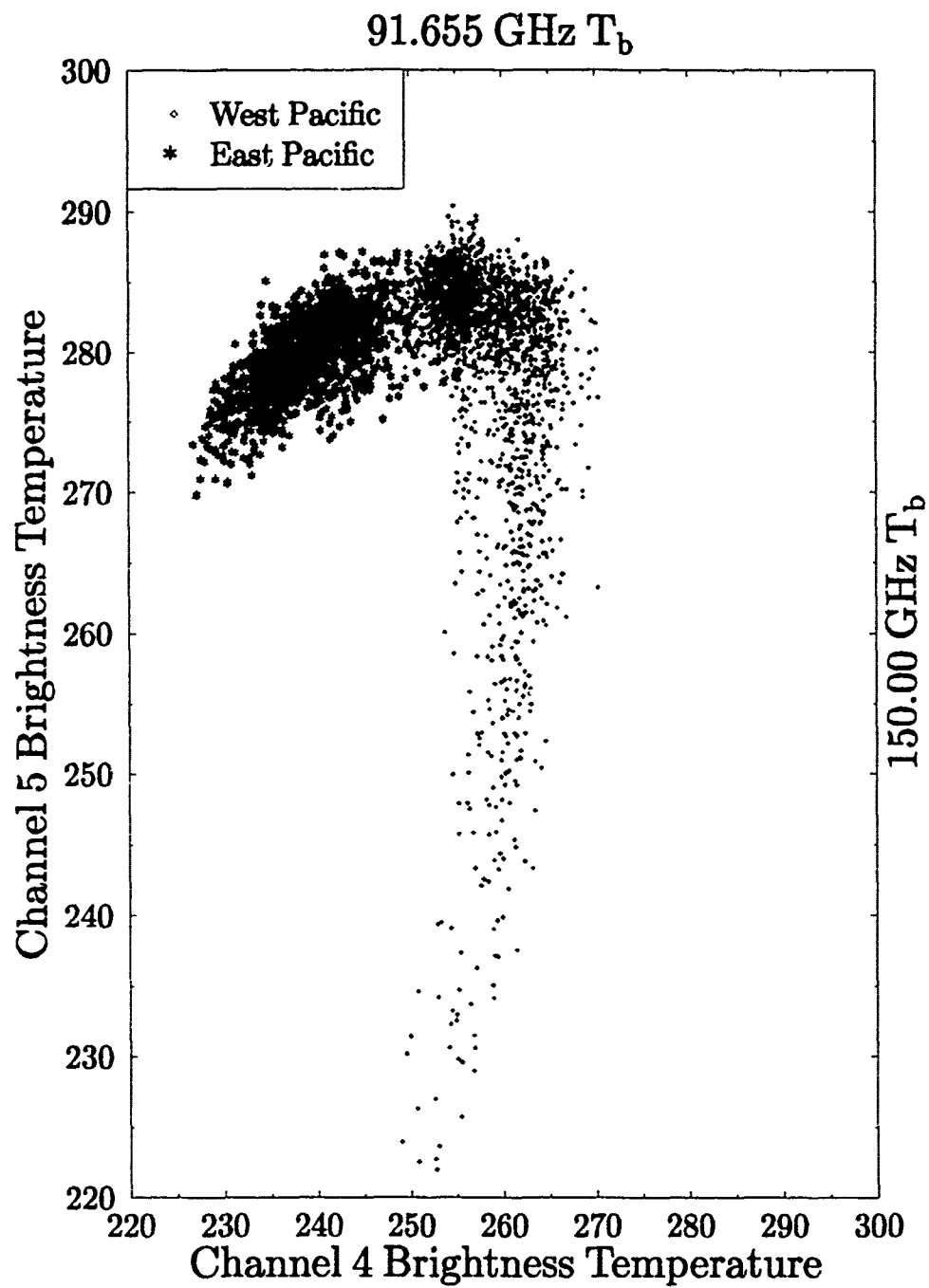


Figure 2.12: Channel 5 versus Channel 4 brightness temperatures for the two Pacific areas.

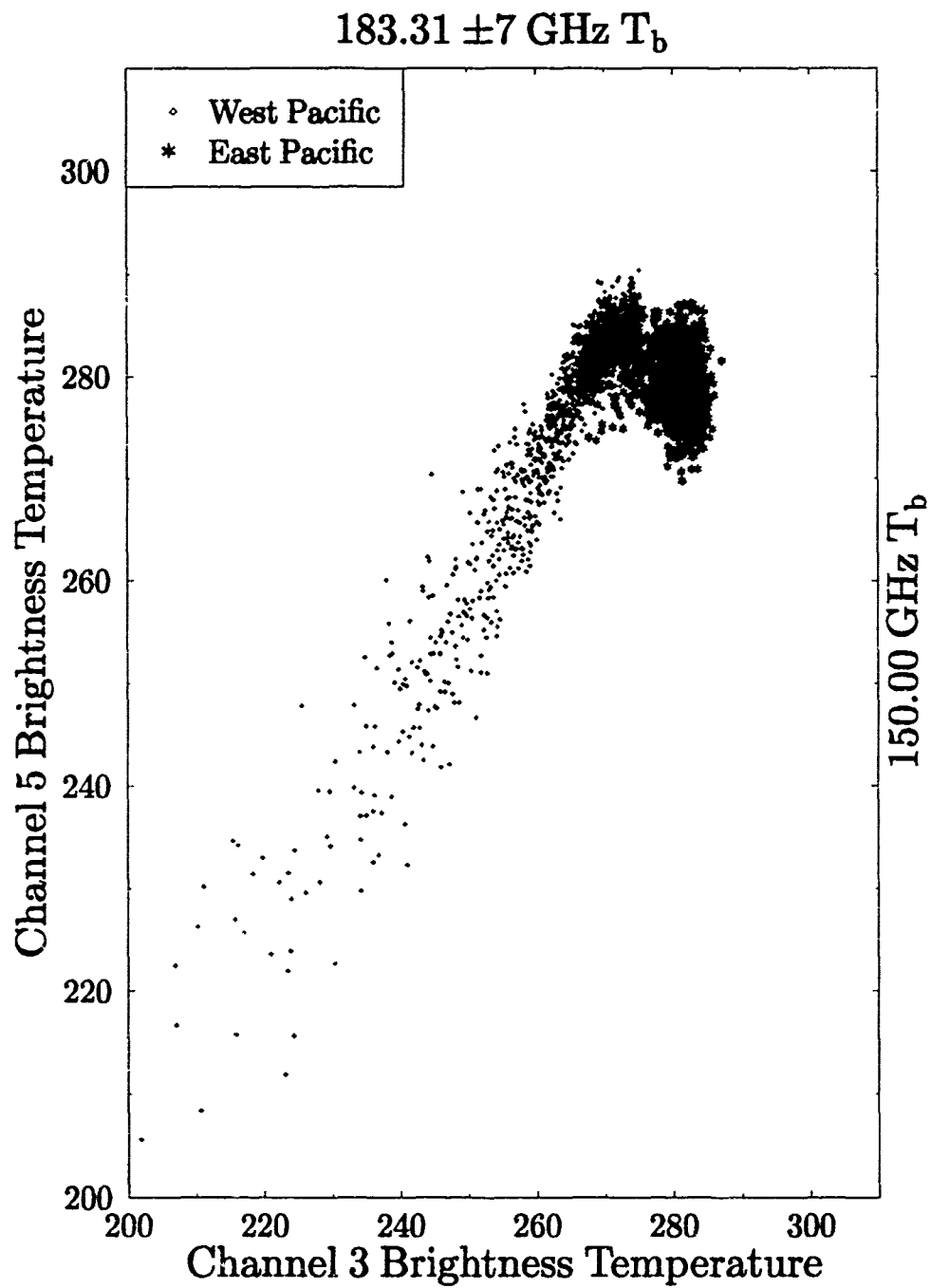


Figure 2.13: Channel 5 versus Channel 3 brightness temperatures for the two Pacific areas.

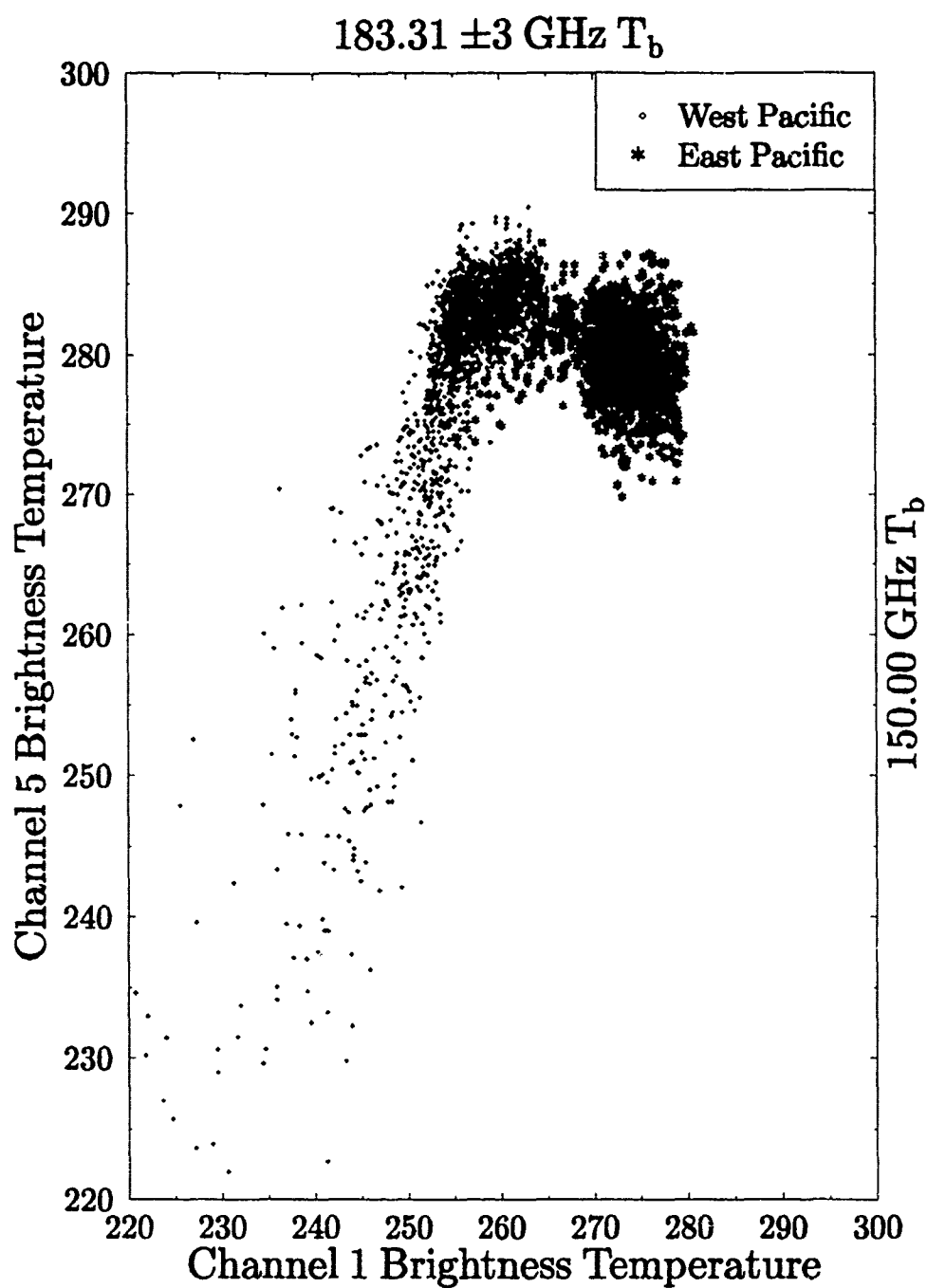


Figure 2.14: Same as Figure 2.12 except Channel 5 vs. Channel 1.

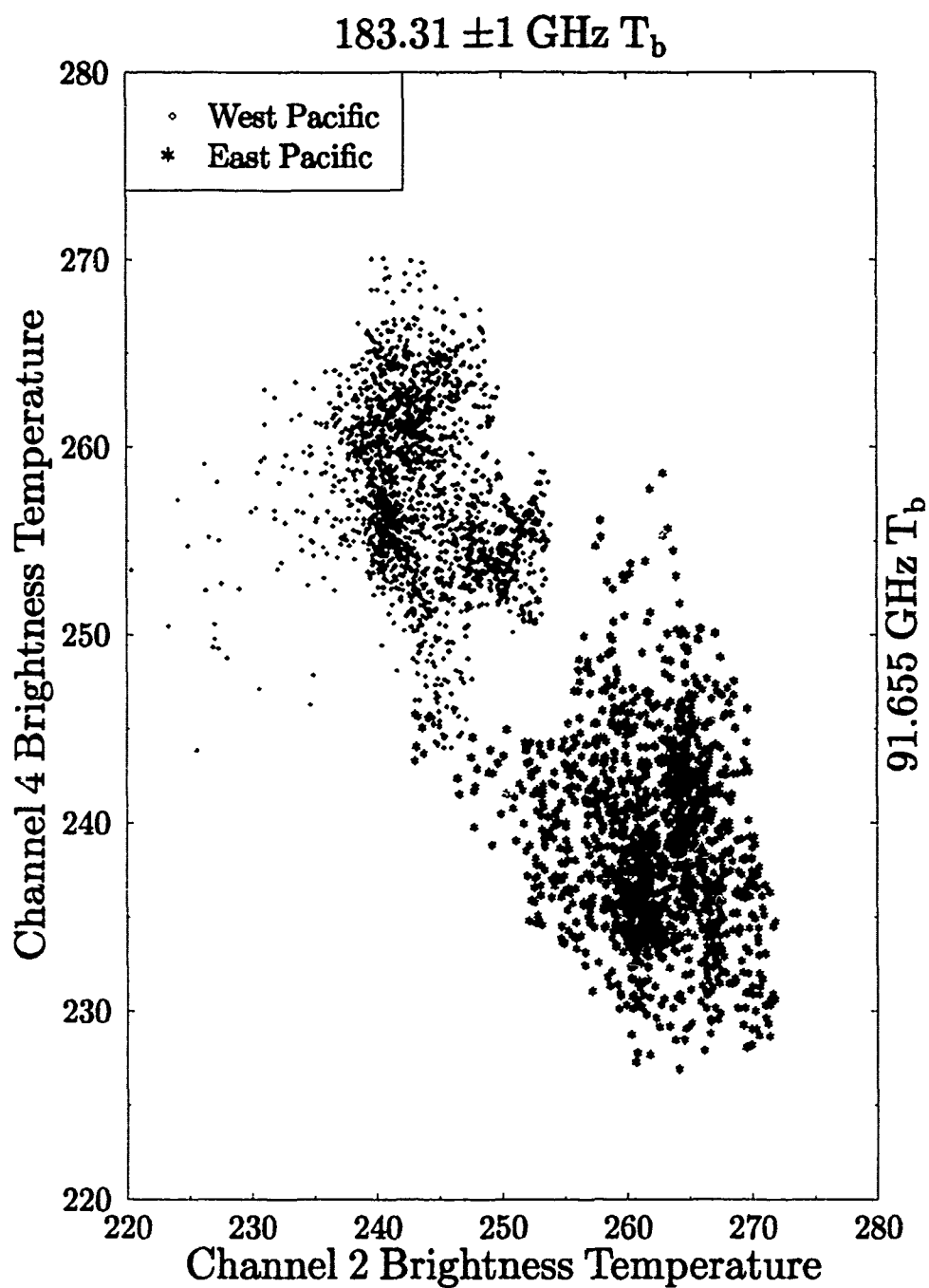


Figure 2.15: Channel 4 versus Channel 2 brightness temperatures for the two Pacific areas.

Figure 2.16 also shows a distinct difference in the brightness temperatures for the two Pacific areas. This figure depicts the brightness temperatures for Channel 4 versus Channel 1. The explanation of these features is basically the same as the previous paragraph as the Channel 1, mid-upper tropospheric peak for the weighting function, brightness temperature is high for the region with subsidence and is low for the region with an abundance of water vapor. Conversely, the Channel 4 brightness temperatures are high for the WP and relatively low for the EP. SST differences certainly play a part in these brightness temperature differences, with higher SSTs (which means higher brightness temperatures) for the WP. Additionally, water vapor near the surface and cloud effects also contribute to the higher brightness temperatures in the WP region.

The effect of ice and mixed phase and partial cloud cover clouds cannot be quantitatively nor qualitatively examined from these figures or from the brightness temperature maps. This is an area where future research is needed.

In this section it has been shown that:

1. Areas with distinctly different moisture profiles (such as regions of large scale subsidence versus moist ascent) can be uniquely identified through the use of brightness temperature plots.
2. Surface characteristics can be inferred from the brightness temperature plots.

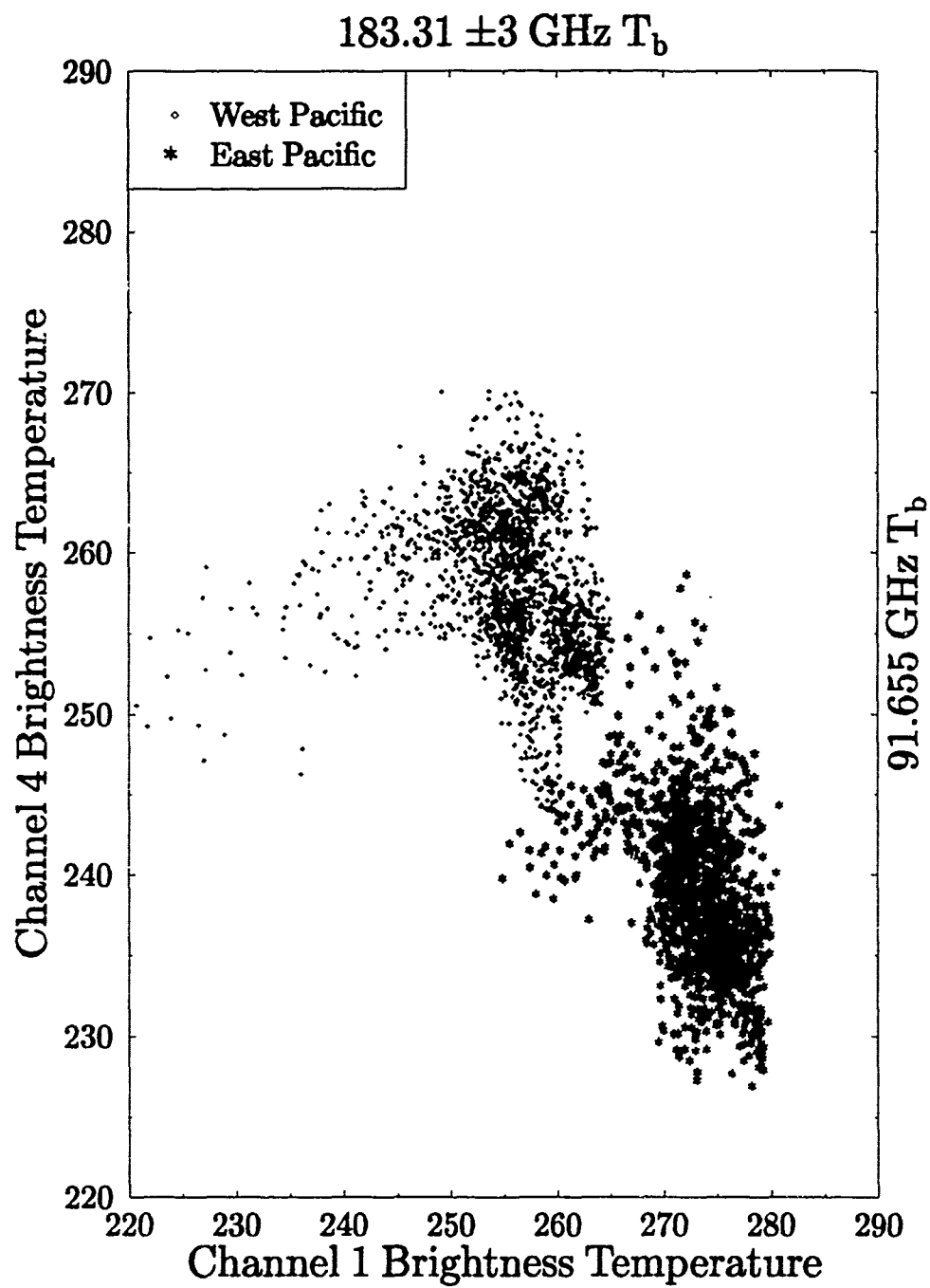


Figure 2.16: Same as Figure 2.12 except Channel 4 vs. Channel 1.

Chapter 3

MICROWAVE RADIATIVE TRANSFER AND WEIGHTING FUNCTIONS

Emission from the atmosphere and the Earth's surface provide the source of radiation received at satellite altitude by microwave instruments. Radiation detected by these instruments is changed by the processes of absorption, emission and scattering within the atmosphere. These processes depend on the properties of the Earth's surface, atmospheric constituents especially water vapor and the concentration of hydrometeors and information about these properties can be retrieved from measurements of this radiation (Stephens, 1993). As stated, detection of atmospheric water vapor, and specifically its vertical profile is the objective of the SSM/T-2 Millimeter Wave Moisture Sounder.

For the frequencies of interest, clear sky absorption arises primarily from water vapor and to a lesser extent oxygen absorption (Waters, 1976.) Ozone also absorbs in this region, but to a much lesser extent than water vapor and oxygen, and ozone absorption has a negligible effect on brightness temperatures. Cloud droplets also absorb in the microwave/millimeter wave region.

Figure 3.1 provides a physical perspective on microwave emission and shows some of the effects of water vapor, surface reflectance, and cloud liquid water on this emission. Case (2) shows the emission spectra found over a cold surface (e.g. ocean) versus case (4) which presents the spectra found over a warm surface (e.g. land). The difference in spectra between case 1 and case 2 shows how water vapor changes the brightness temperatures. These effects lead to temperature decreases over land (warm background) and increases over ocean (cold background). Similarly, the change in spectra between cases 2 and 3 show the effects of cloud droplet (Rayleigh) absorption. Finally, the spectra change from case

2 to case 4 is an example of how surface characteristics may change intensities measured by a satellite radiometer.

3.1 THE RADIATIVE TRANSFER EQUATION FOR MICROWAVE REMOTE SENSING

The radiative transfer equation describes how, in a mathematical sense, radiation is transferred from one layer to another. The generalized form of this equation which includes the effects of both absorption and emission of energy is written as:

$$dI = -k_\nu[I - B]ds, \quad (3.1)$$

where I is the intensity, k_ν is the volume absorption coefficient, and B is the emission represented by Planck's function. Equation (3.1) neglects scattering, which is common for many problems in microwave radiative transfer and it also assumes the condition of local thermodynamic equilibrium. The principles of emission-based sensing are used for many atmospheric applications including the remote sensing of sea surface temperature (SST), column water vapor, cloud liquid water content, precipitation rate, temperature profiles, and clouds.

3.1.1 Brightness Temperatures

At the wavelength of microwave/millimeter wave radiometers, the Rayleigh-Jeans distribution applies — that is, radiant energy and temperature are synonymous. This temperature is referred to as the brightness temperature, and, for satellite radiometers is a measure of the upwelling thermal microwave radiation from the medium (in this case the atmosphere) below. Using the Rayleigh-Jeans approximation, assuming specular reflection and for a nadir viewing radiometer, this brightness temperature, $T_b(\nu)$, can be expressed as:

$$T(\nu) = \int_0^\infty \exp(-\tau(h, \infty))\gamma(\nu, h)T(h)dh + \exp(-\tau(0, \infty)) \times \\ \left[(1 - R)T_{sf} + R \int_0^\infty \exp(-\tau(0, h))\gamma(\nu, h)T(h)dh \right] + R \exp(-2\tau(0, \infty))T_{cb}, \quad (3.2)$$

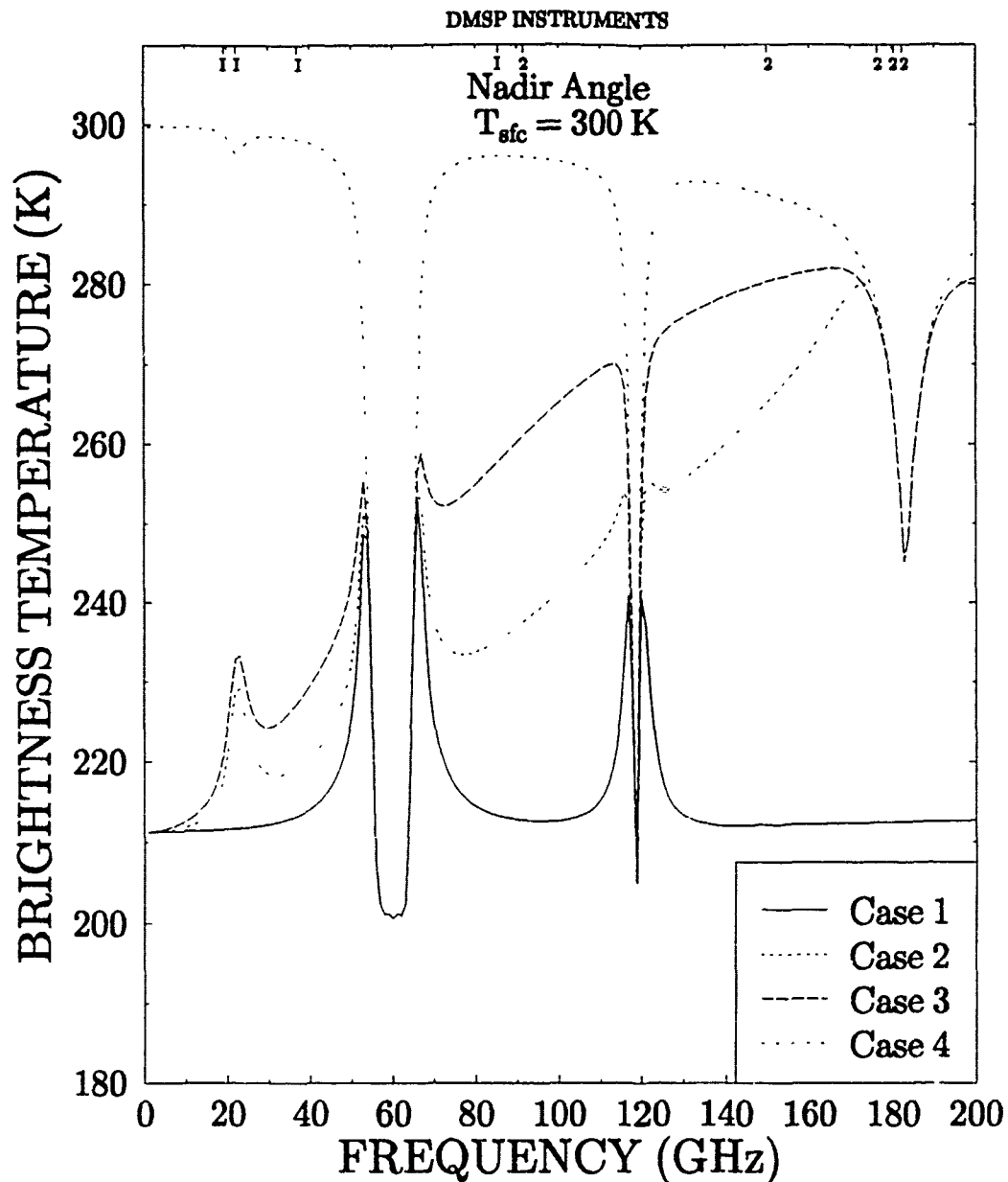


Figure 3.1: Brightness temperature spectra from 1–200 GHz for cases (1) tropical atmosphere with no water vapor and reflectivity (R) = 0.3; (2) tropical atmosphere ($\text{CWV} = 41.2\text{g/m}^2$) and $R = 0.3$; (3) tropical atmosphere with a cloud ($\text{LWC} = 0.5\text{g/m}^2$) from 1–2 km and $R = 0.3$ and case (4) same as case (2) except $R = 0.0$. The locations of the SSM/I and SSM/T-2 channels are indicated by “I” and “2”, respectively.

where $\tau(z, y) = \int_z^y \gamma(\nu, x) dx$ represents the optical depth between heights z and y , R is the reflectivity of the surface ($(1-R)$ is the emissivity (ϵ) of the surface), $\gamma(\nu, h)$ the volume absorption coefficient of the atmosphere at a height h for a frequency ν , $T(h)$ the temperature profile of the atmosphere, T_{fc} the thermometric temperature of the surface, and T_{cb} the cosmic background (2.7°K) temperature. Each term on the right hand side of (3.2) has a related physical description. The first term is the contribution to the brightness temperature due to upward emission by the atmosphere. The second term is the 'surface term' which is the radiation emitted by the Earth's surface which reaches the satellite. The third term is the downwelling radiation of the atmosphere which is reflected by the Earth's surface to the satellite. The last term is the cosmic background temperature which is reflected by the earth's surface to the satellite. The angular dependence of quantities has been omitted here and is taken to be understood.

There is some debate as to the necessity of the cosmic background term. Some researchers state that this term can be ignored whereas Kakar (1983) argues that for a channel on the wing of the absorption line (e.g. such as the 150 GHz channel of the SSM/T-2) that this term would add approximately 0.5°K to the measured brightness temperature. The term is retained in the radiative transfer model introduced below and used to produce the results of subsequent chapters.

In calculating brightness temperatures from (3.2), the state of the polarization of radiation has not been considered. The main sources of polarization arise from reflection by the surface and by scattering from irregular particles in the atmosphere. The latter effects are ignored and only the effects of polarization due to surface reflection are considered. By ignoring any cross polarization effects within the atmosphere, (3.2) becomes the radiative transfer equation for the vertical state of polarization assuming R represents the surface reflectivity for vertical polarization. In any event, the effects of surface reflectivity are minimal for Channels 1 and 2, and thus the effects of polarization are of little consequence for the study described in this thesis.

3.2 WEIGHTING FUNCTIONS

For atmospheric temperature profiling, (3.1) may be expressed in the form:

$$T_b(\infty) = \int_0^{\infty} K(\nu, h)T(h)dh + A, \quad (3.3)$$

where A represents terms independent of the temperature profile and $K(\nu, h)$, the temperature weighting function, is weakly dependent on the temperature profile. These weighting functions are a basis for selection of channels for temperature profiling instruments and, in some cases, a basis for the temperature profile retrieval itself.

Smith *et al.* (1979) show weighting functions for the TOVS instrument suite. The MSU operates in the same oxygen absorption band as the SSM/T-1 instrument. The depicted weighting functions (shown in Figure 3.2) give a demonstration of the vertical resolution of each of the channels. The weighting functions appear in the integral equations relating temperature to the measured radiances (as in (3.3)).

3.2.1 Relative Humidity-based Weighting Functions

This discussion of constituent retrievals follows from the work of Schaerer and Wilheit (1979). Constituent retrievals are unfortunately a nonlinear problem because the absorption coefficient appears both in the transmission factor ($\exp(-\int \gamma dx)$) and in the radiation factor $\gamma(h)T(H)$ of (3.2). Therefore, the effect of $\gamma(\nu, h)$ at one height is dependent on $\gamma(\nu, h)$ at all other heights and so the problem of constituent retrieval is also a non-local one.

Similarly, (3.1) can be expressed as (Schaerer and Wilheit (1979)):

$$T_b(\infty) = \int_0^{\infty} G(h)\gamma(h)dh + B, \quad (3.4)$$

where B represents terms independent of $\gamma(h)$; however, no insight comparable to the temperature profiling example evolves since $G(h)$ is strongly dependent on $\gamma(h)$. Nonetheless, (3.4) can still be linearized. A small change in the brightness temperature $\Delta T_b(\infty)$ due to a small change in the absorption as a function of height, i.e. $\Delta \gamma(h)$, can be expressed as:

$$\Delta T_b(\infty) = \int_0^{\infty} G[h, \gamma(h), T(h)]\Delta \gamma(h)dh. \quad (3.5)$$

After some manipulation we find an expression for $G(h, \gamma(h), T(h))$:

$$G(h, \gamma(h), T(h)) = \exp(-\tau(h, \infty)) [T(h) - T_{b\uparrow}(h)] + \\ R \exp(-\tau(0, \infty)) \exp(-\tau(0, h)) [T(h) - T_{b\downarrow}(h)], \quad (3.6)$$

where $T_{b\uparrow}$ and $T_{b\downarrow}$ are the upwelling and downwelling brightness temperatures at height h , respectively. The weighting function with respect to absolute water vapor, $\rho(h)$, is:

$$G_\rho(h) = G(h) \frac{\partial \gamma(h)}{\partial \rho(h)} \quad (3.7)$$

and with respect to relative humidity, $RH(h)$:

$$G_{RH}(h) = G(h) \frac{\partial \gamma(h)}{\partial \rho(h)} \frac{\partial \rho(h)}{\partial RH(h)} = G(h) \frac{\partial \gamma(h)}{\partial \rho(h)} \rho_{sat}(h) \quad (3.8)$$

where $\rho_{sat}(h)$ is the saturation vapor pressure of water at a height h . In this way, weighting functions based on the relative humidity profile $RH(h)$ are produced; these being related to brightness temperature changes by

$$\Delta T_{b\uparrow} = \int_0^\infty G_{RH}(h) \Delta RH(h) dh. \quad (3.9)$$

3.2.2 Transmission-based Weighting Functions

Transmission-based weighting functions assume a different yet comparable form and are similar to those used for temperature retrievals. Isaacs and Deblonde (1987) used these weighting functions for their study of cloud effects on 183 GHz retrievals. These weighting functions are also the same as those used for infrared measurement techniques where both vertical profiles of water vapor and total precipitable water are derived (Prabhakara and Dalu, 1980).

Define $T(\tau, \mu) = \exp(-\tau/\mu)$ as the transmittance of the atmosphere. Neglecting the dependence on the zenith angle (as above), the derivative of the transmittance becomes: $dT = \exp(-\tau) d\tau$ or $dT = \exp(-\tau) (-\gamma dh)$. Using the Rayleigh-Jeans limit, (3.2) becomes:

$$T_{b\uparrow}(\infty) = T(\tau_o) T_{sfz} (1 - R) + \int_1^0 T(\tau) dT(\tau) + T(\tau) R \int_1^0 T(\tau) dT(\tau) + T^2(\tau_o) R T_{ob} \quad (3.10)$$

where τ_o is the optical depth from the satellite to the surface. By grouping common factors together, Equation 3.10 can be simplified to:

$$T_{bf}(\infty) = [T_{sf}(1 - R) + RT(\tau_o)T_\infty]T(\tau_o) + [1 + T(\tau)R] \int_1^0 T(\tau)dT(\tau) \quad (3.11)$$

where there is now only one integral term.

Defining a weighting function $W(Z)$ for a vertical coordinate Z as $W(Z) = \frac{dT(Z)}{dZ} = T(Z)\gamma(Z)$ then the previous equation can be written:

$$T_{bf}(Z_\infty) = [T(Z_o)(1 - R) + RT(Z_o)T_\infty]T(Z_o) + [1 + T(Z)R] \int_{Z_o}^{Z_\infty} T(Z)W(Z)dZ. \quad (3.12)$$

Weighting functions derived in this manner are convenient since they closely resemble the weighting functions often used for temperature retrievals. Transmission is a quantity easily calculated in a propagation model, and these models permit the calculation of the derivative of transmission with height and hence, the weighting functions themselves.

As an example of transmission-based temperature weighting functions, Figure 3.2 shows weighting functions plotted for channels 1-4 of the SSM/T-1 temperature sounder for a tropical atmosphere with a thermometric temperature of 300 K. Figure 3.2 is comparable to Figure 2, Liou *et al.* (1979) and the MSU channels of Figure 1, Smith *et al.* (1979).

Weighting functions from the two different methods appear very similar when plotted. Plots of the transmission-based weighting functions for the SSM/T-2 are discussed later in Chapter 4.

3.3 ATMOSPHERIC PROFILES, PROPAGATION MODEL, AND CLOUD MODELS

To simulate microwave brightness temperature requires the use of models to represent various aspects of the atmosphere and the propagation of microwave energy through the atmosphere. We use simulations of the brightness temperatures to understand how they vary with changing atmospheric properties and to study these effects in isolation. The selection of the models described below was made for a variety of reasons including the use of a model(s) in similar studies done previously, the most current model available, the computational efficiency of the model, and its simplicity.

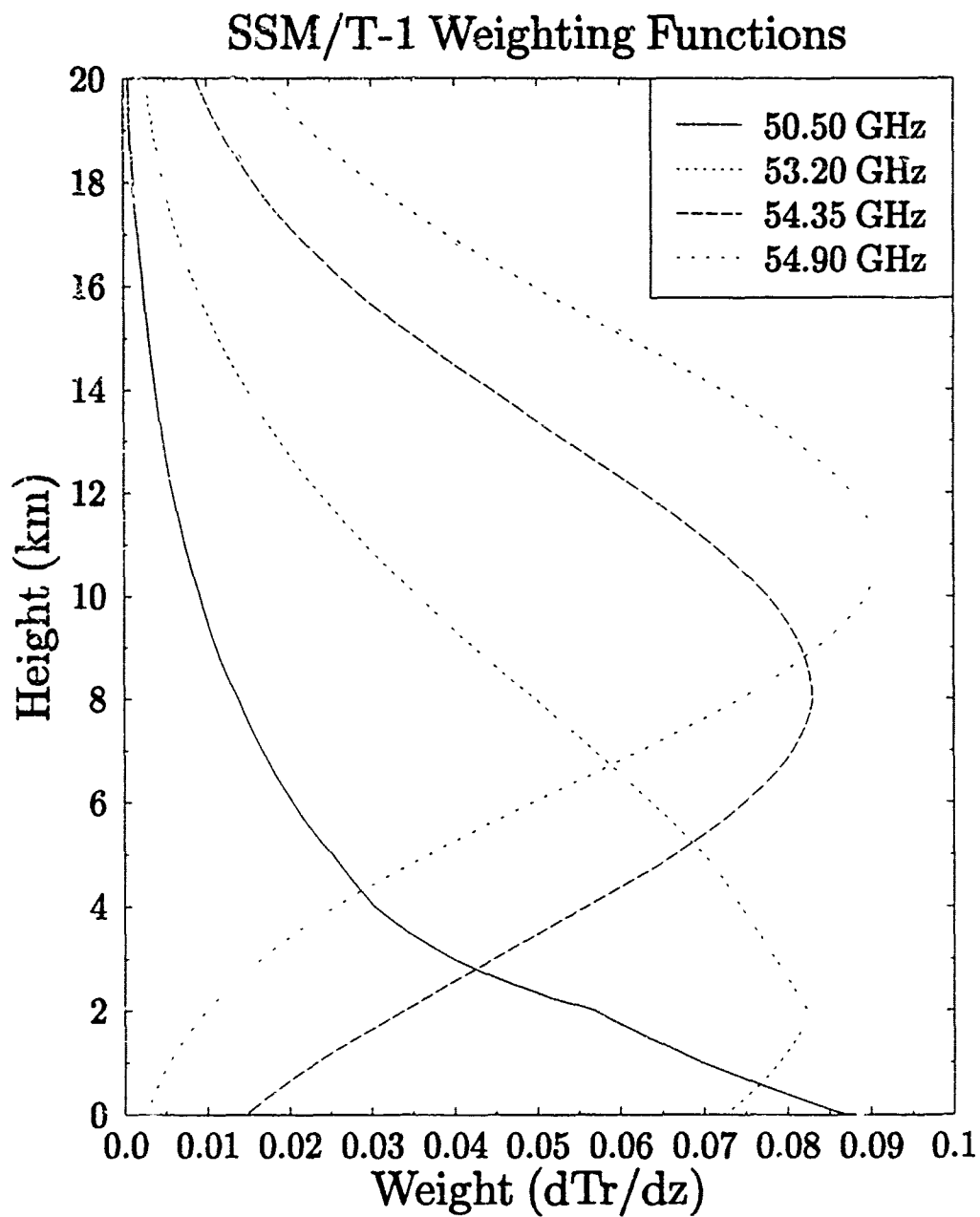


Figure 3.2: Clear sky weighting functions for the SSM/T-1 channels 1-4 for a tropical atmosphere, reflectivity = 0.03, and a column water vapor (CWV) = 41.2 kg/m².

3.3.1 Atmospheric Profiles

McClatchey *et al.* (1972) standard atmosphere profiles of mid-latitude winter, mid-latitude summer, and tropical atmospheres were used as the reference for height (km), pressure (mb or hPa), temperature ($^{\circ}\text{K}$ or K), density (gm^{-3}) and water vapor density (gm^{-3}). The radiative transfer code also included a feature which would allow the water vapor density to be increased or decreased by a common factor throughout the atmosphere. This is used to increase the number of different atmospheres for the simulations discussed in Chapter 5.

3.3.2 The Propagation Model

The Liebe millimeter wave propagation model (MPM92) (which is an updated version of MPM89 (Liebe, 1989) and Liebe, personal communication) allows the specification of an input atmospheric profile. The atmospheric profile provides the necessary meteorological parameters to allow the computation of the volume absorption coefficient, γ . Knowledge of the volume absorption coefficient then allows the computation of the optical depth, τ . From the optical depth the calculation of the transmittance is straightforward and the transmission-based weighting function follows as described above.

The MPM92 model accounts for dry air attenuation, oxygen and water vapor line absorption, water vapor continuum, and Rayleigh cloud droplet absorption. The Zeeman effect for oxygen for pressures less than 0.7 kPa and Doppler broadening for water vapor are also included. One distinct advantage of MPM92 is the small number of lines used in the model. The model uses 44 O_2 and 30 H_2O local line contributions versus the over 500 contributing spectral lines for frequencies below 1 THz. The small number of lines in MPM92 require considerably less computation time than do other codes (i.e. RAD-TRAN). Versions of MPM have been used by various researchers (e.g. Wang *et al.* (1992) and Fleming *et al.* (1991)) to study atmospheric propagation at millimeter/microwave wavelengths.

3.3.3 Cloud Models

To simulate cloud effects within the field of view (FOV) of the radiometer, a set of cloud models was chosen to be incorporated within the atmospheric attenuation profiles. The cloud models chosen (after Isaacs and Deblonde, 1987) are from the Air Force Geophysics Laboratory FASCODE model (Falcone *et al.*, 1979). Cloud parameters for the five cloud models are given in Table 3.1.

Table 3.1: Cloud Type Characteristics (after Isaacs and Deblonde, 1987)

Cloud Model	Type	Mode Radius, μm	Liquid Water Content, gm^{-3}	Vertical Extent, km
1	Stratus	2.7	0.15	0.5-2.0
2	Cumulus	6.0	1.00	1.0-3.5
3	Altostratus	4.5	0.40	2.5-3.0
4	Stratocumulus	6.25	0.55	0.5-1.0
5	Nimbostratus	3.0	0.61	0.5-2.5

Cloud attenuation was calculated using the Rayleigh absorption approximation of Mie's forward scattering function (Liebe, 1989). Cloud liquid water content (w , gm^{-3}) and frequency are the required variables. Cloud attenuation (calculated by Liebe's MPM92 model) was added to the clear sky absorption for each layer of the atmosphere for the entire cloud layer as specified by the cloud model. The MPM model assumes that the cloud fills the entire FOV and that there is only one cloud layer. These assumptions will tend to overestimate and underestimate the effects of clouds, respectively.

Chapter 4

SENSITIVITY EFFECTS FOR THE DMSP SSM/T-2

This chapter is devoted primarily to the discussion of forward radiative transfer simulations of the SSM/T-2 brightness temperatures and how these temperatures respond to a variety of different atmospheric parameters. The approach is to build an understanding of this radiative transfer problem before tackling the inverse problem — that of retrieving moisture information from brightness temperature measurements. There are a number of factors which influence brightness temperatures and hence, the retrieval of moisture profiles using 3 channels near 183 GHz and a window channel near 92 and a line wing channel at 150 GHz. These factors will be referred to as sensitivity factors and include: the thermometric temperature and its vertical profile, the surface reflectivity (emissivity), the humidity (moisture) profile, the characteristics of clouds (both water clouds and perhaps ice clouds), the surface elevation, the channel noise, and scan angle. The influence of some of these factors on T-2 simulated brightness temperatures is now examined.

4.1 DEPENDENCE ON MOISTURE PROFILES

For the simulation studies described below, three basic atmospheric profiles are used: a tropical (T) profile, a midlatitude (MLS) summer profile, and a midlatitude winter (MLW) profile (McClatchey *et al.*, 1972). The water vapor density data for each profile will also be multiplied by a constant factor at each level to provide a method of varying the column water vapor (CWV) amount. Since each moisture profile is characterized by a different column water vapor amount and since each atmosphere has a different temperature profile, the simulated channels of the T-2 will respond differently to each profile.

The clear sky weighting function profiles for an ocean background with an emissivity of 0.7 are shown in Figures 4.1–4.3 with altitude as the ordinate and the weighting function $\frac{dT}{dz}$ (or $\frac{dT_r}{dz}$ as designated in the figures) as the abscissa. These profiles are plotted for the nadir angle and for values the column water vapor CWV (kg m^{-2}) as given.

Comparing these figures it can easily be seen how the amount of moisture in the atmosphere affects the location of the peaks of the weighting functions. For example, for the tropical and midlatitude summer atmospheres the 182.31 GHz channel peaks between 7 and 8 km whereas for the midlatitude winter atmosphere the channel peaks between 5 and 6 km. Similar effects are seen for the other channels where the more moisture in the atmosphere the higher in the atmosphere the channel peaks. Even the 'window' channel (91.655 GHz) sees the effects of moisture in the atmosphere and this serves as a reminder that the 'window' is not entirely transparent.

It can also be seen from Figures 4.1–4.3 the broadness of the weighting functions as depicted for these cases. This broadness is an obvious limitation of the system in that the resolution for retrievals is limited by the lack of sharpness of these weighting functions. The resolution of the T-2 was expected to be on the order of 2–3 km based on the weighting functions of this type (e.g. Schaerer and Wilheit, 1979).

Additionally, from Figures 4.1–4.3 it is relatively easy to develop some intuition as to the purpose of each channel, at least for clear-sky conditions. The two channels closest to the 183 GHz line relate to the measurement upper tropospheric moisture; the line wing channel (150 GHz) to low level moisture; and the window channel senses low level moisture and surface characteristics, including the emissivity and perhaps the thermometric ('skin') temperature. The remaining channel is relevant to midtropospheric moisture determinations.

As a final examination of how moisture changes the weighting functions of the SSM/T-2, the midlatitude summer profile will again be used. In this case, the specific humidity is increased by a factor of two throughout the entire atmosphere (20 km). Figure 4.4, compared to Figure 4.2, shows how the increased moisture at all levels moisture changes the weighting functions significantly.

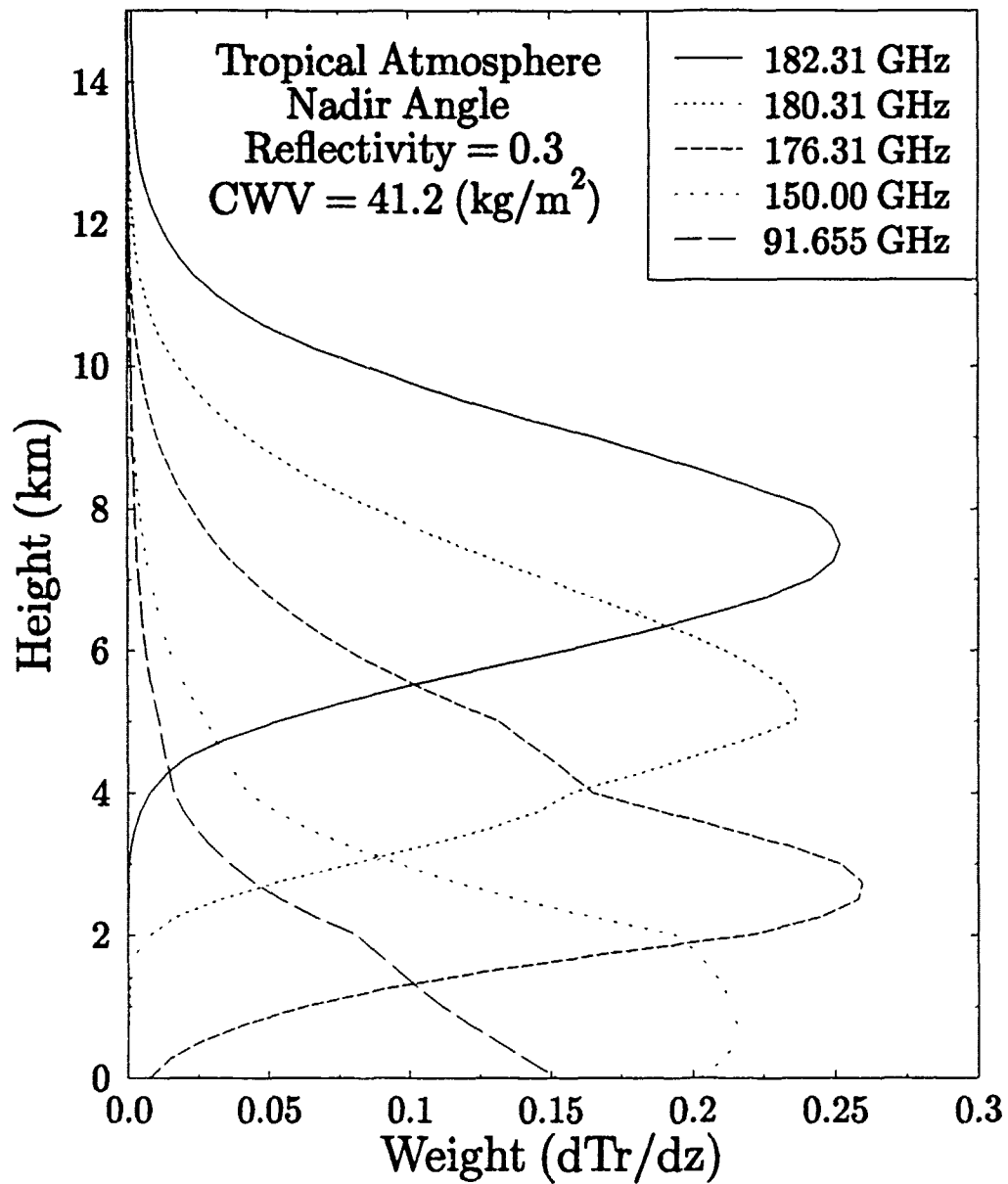


Figure 4.1: Clear sky weighting functions for the SSM/T-2 channels for a tropical atmosphere over an ocean background with a reflectivity factor of 0.3 and a thermometric temperature of 300 K.

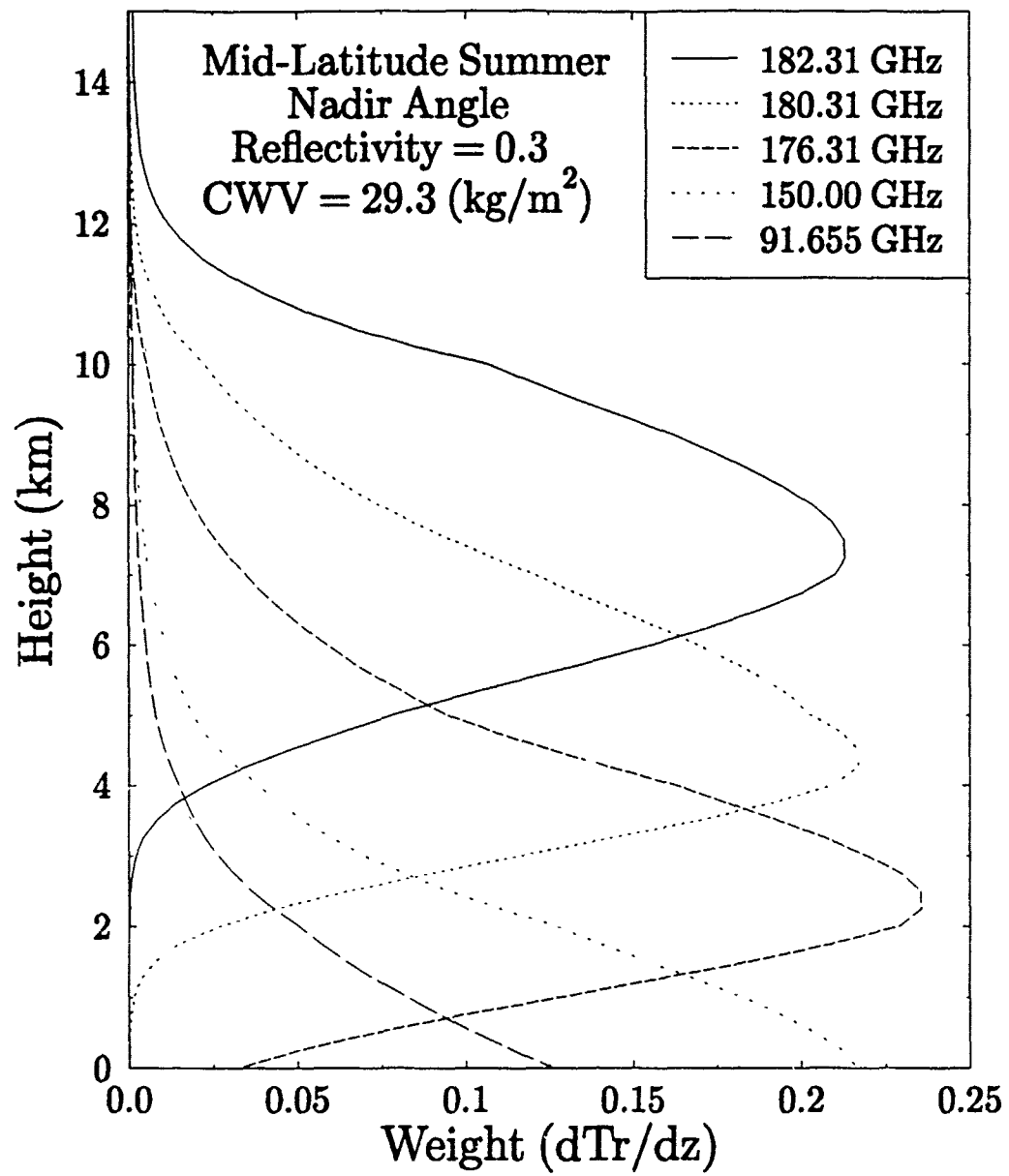


Figure 4.2: The same as Figure 4.1 except for a midlatitude summer atmosphere.

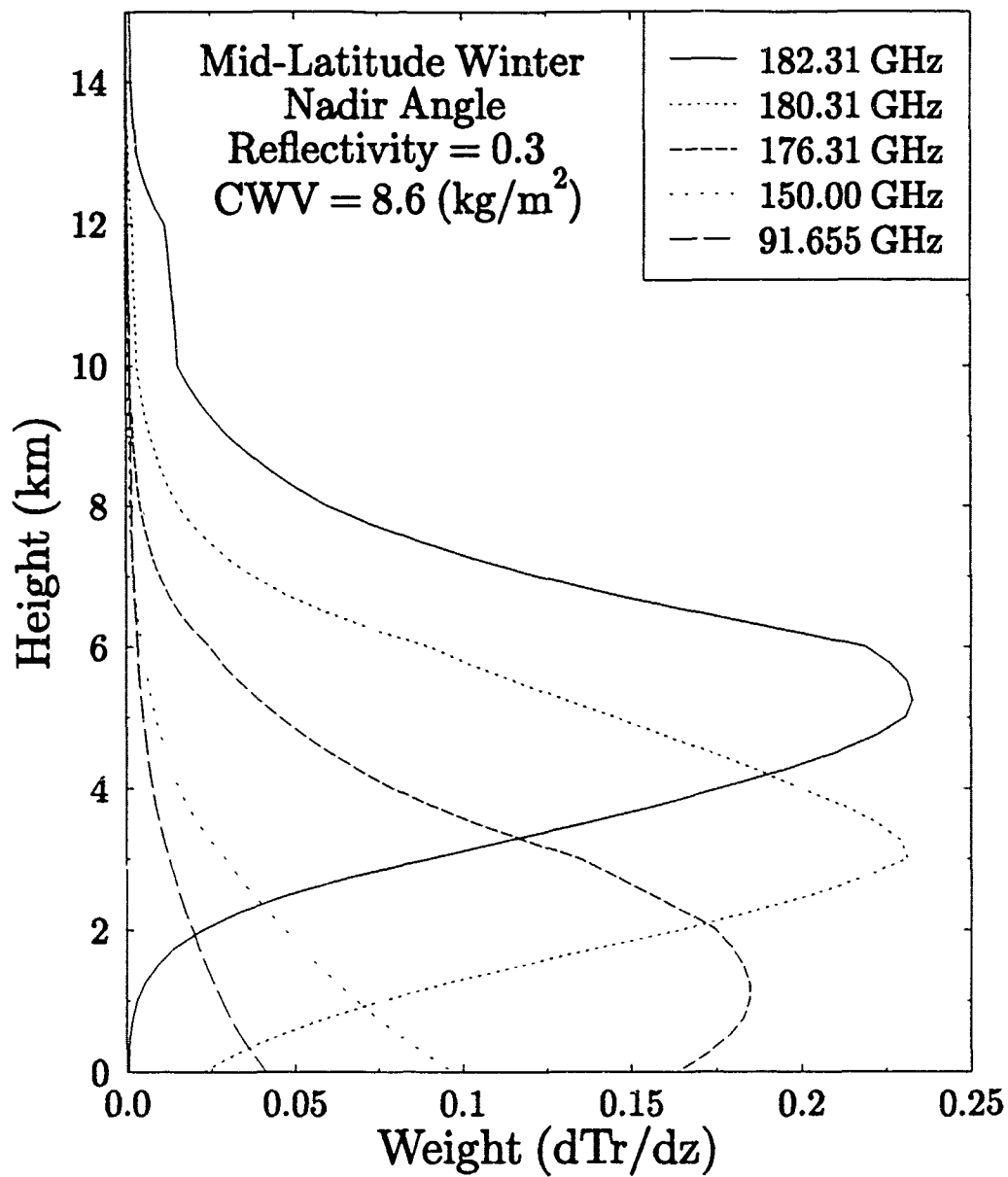


Figure 4.3: The same as Figure 4.1 except for a midlatitude winter atmosphere.

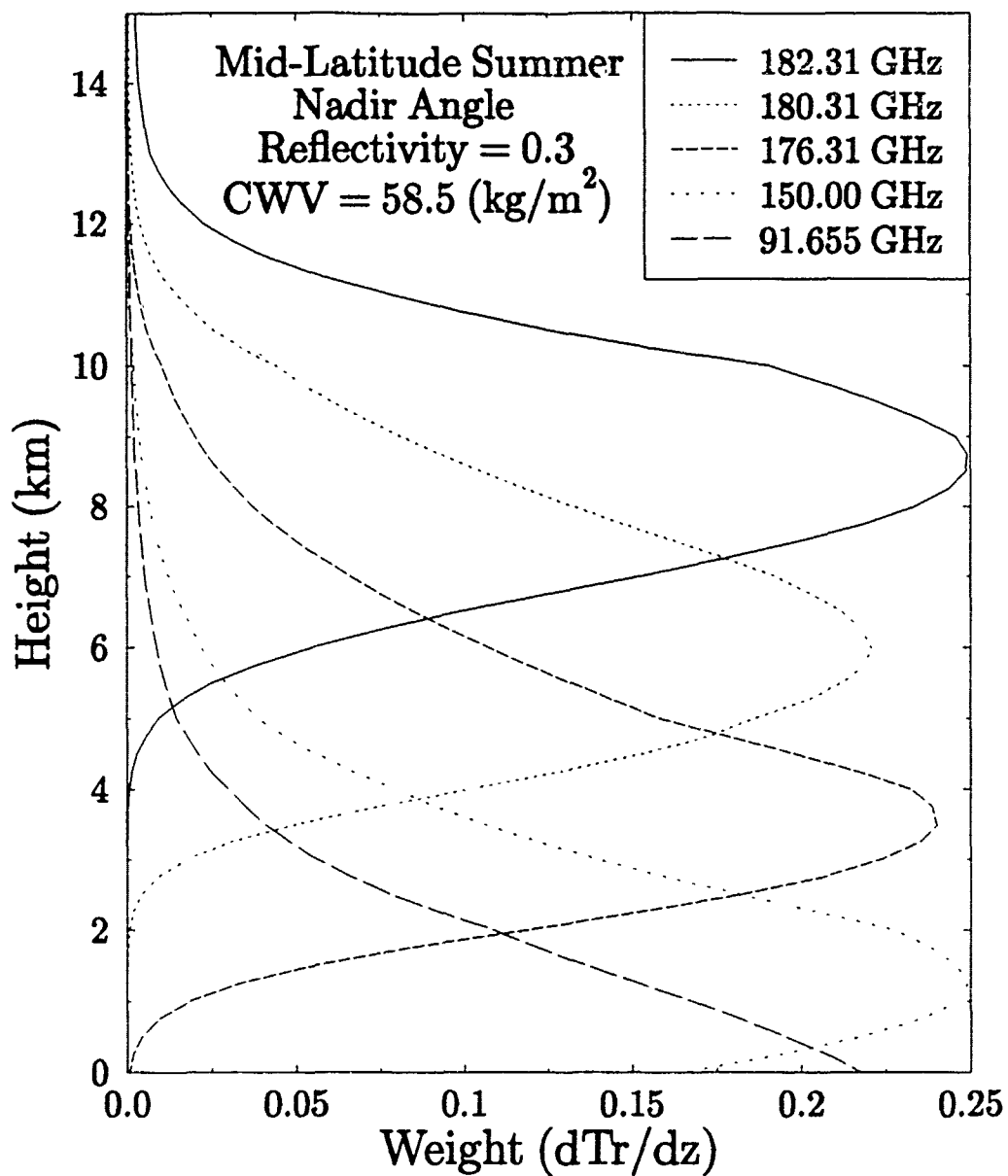


Figure 4.4: The same as Figure 4.2 except with $2 \times$ water vapor profile.

These four figures graphically show how the moisture profiles affect the weighting functions when it is plotted against height (km). Certainly there is a comprehensive change in the weighting functions when the atmospheric water vapor is doubled. This goes back to the discussion earlier about the nonlinearities in the process caused by the absorption factor.

Another way of graphically showing where the atmospheric constituents diminish the emission of the atmosphere and surface is to plot transmission versus altitude. Clear sky atmosphere plots of the transmission corresponding to Figures 4.1–4.3 are shown in Figures 4.5–4.7. Noteworthy is the generally similar appearance of each of the transmission curves and how the levels of the most rapid decrease in transmission with decreasing altitude correspond to the peaks of the weighting functions.

4.2 DEPENDENCE ON BACKGROUND

The surface reflectivity R (or emissivity $\epsilon = 1 - R$) depends on the characteristics of the surface of the earth as viewed by the satellite radiometer. Land and coastal regions have large variations in surface emissivity and hence, the retrieval of moisture profiles can be expected to suffer degradation for these regions as compared with ocean surfaces.

4.2.1 Ocean Background

The emissivity of a smooth ocean surface can be calculated from the dielectric constant of water. Calculations using the dielectric data of Ray (1972) result in a value of ~ 0.7 for the emissivity of calm ocean water at 183 GHz. Lutz *et al.* (1990) have developed an algorithm (from Wilheit, 1990) with an iterative procedure for determining the emissivity for wind-roughened ocean surfaces or land surfaces. The effect of wind roughening procedure degrades the ability to retrieve moisture profiles (versus retrievals over a constant background).

The low emissivity of ocean surfaces is one important aspect which helps with the retrieval of low level moisture. This is because the radiometer senses emission from the warm atmosphere in contrast to a cold background which results in a large brightness temperature contrast. Additionally, the emissivity of a water surface is thought to be

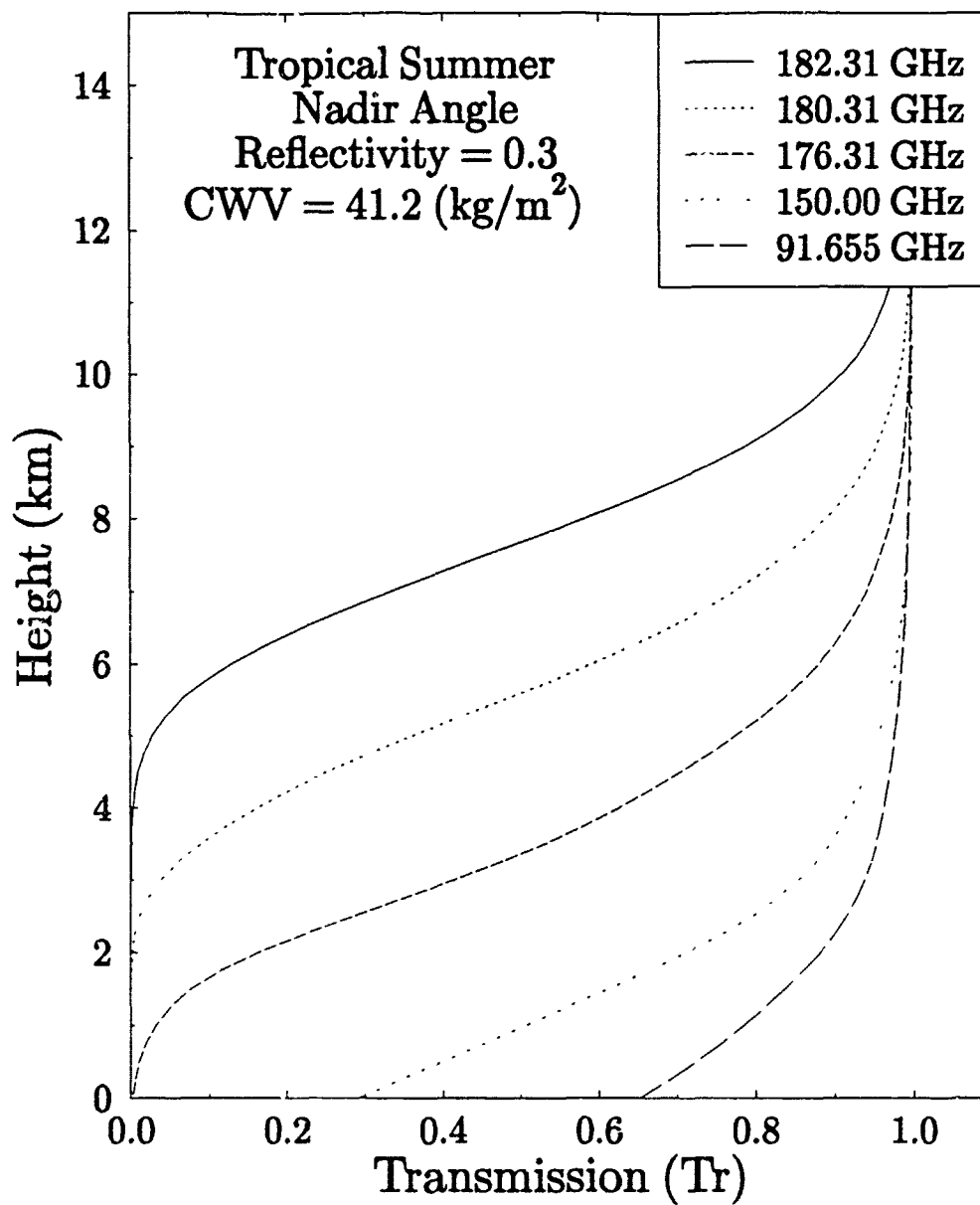


Figure 4.5: Clear sky transmission for the tropical atmosphere.

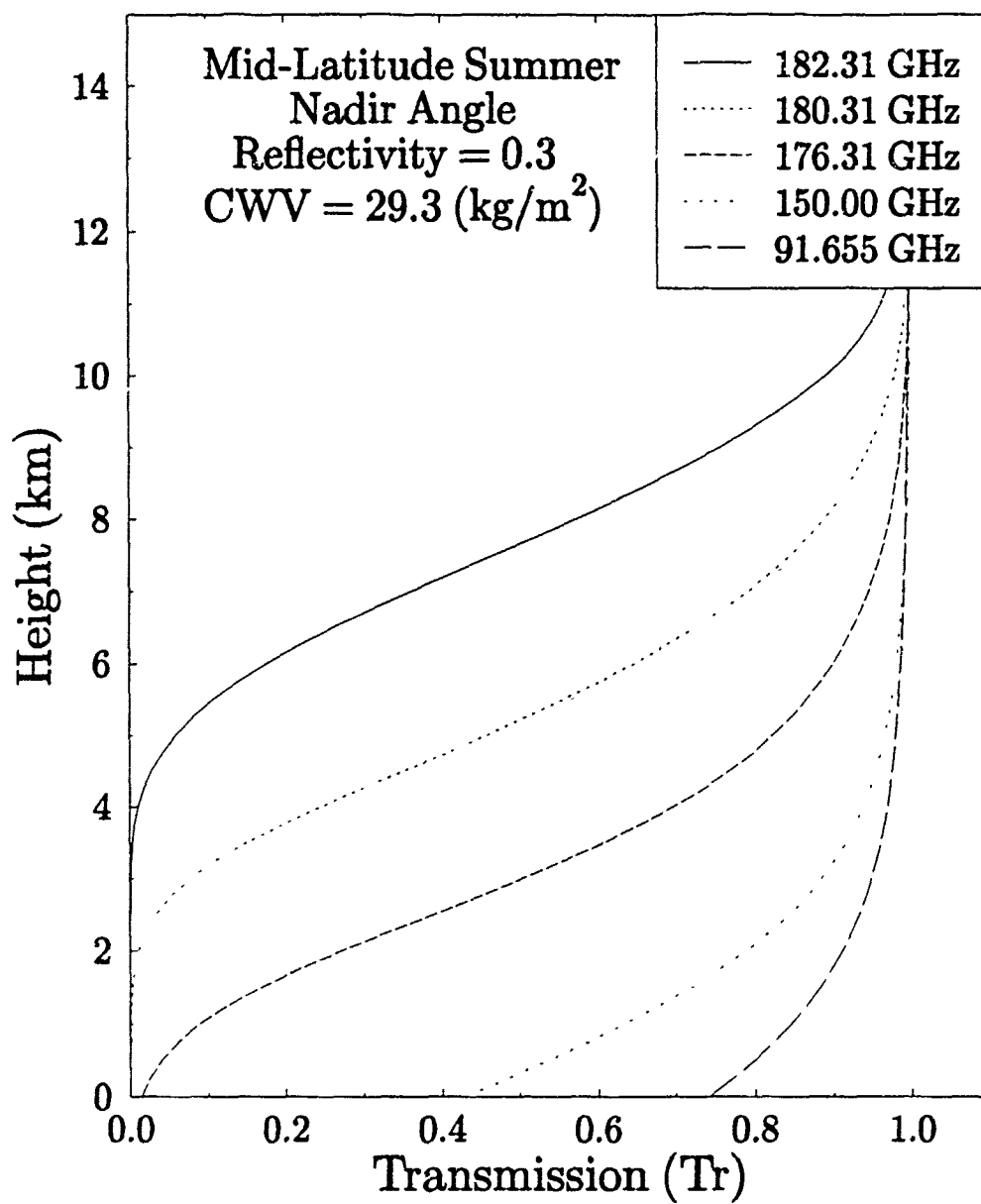


Figure 4.6: Clear sky transmission for the midlatitude atmosphere.

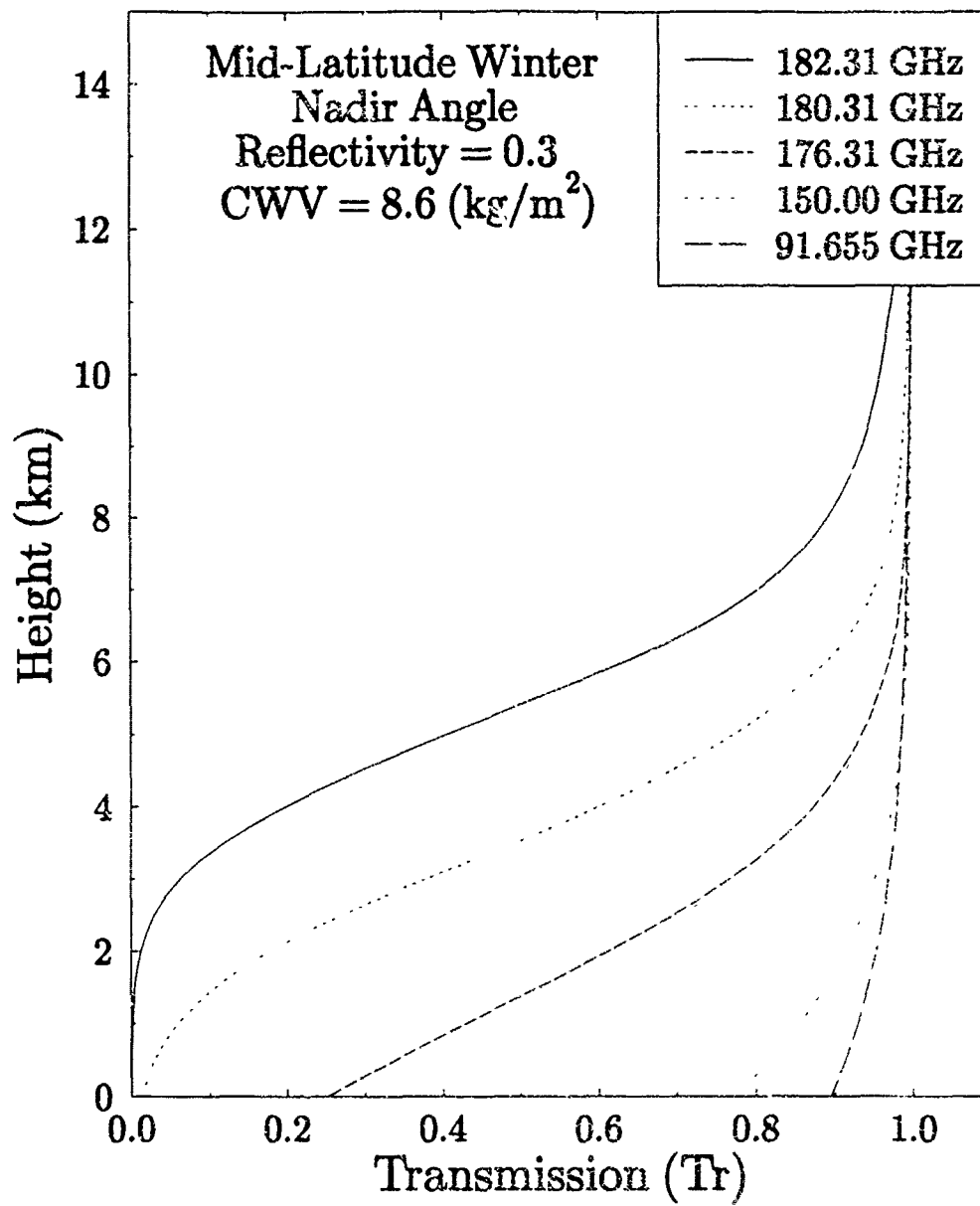


Figure 4.7: Clear sky transmission for the midlatitude winter atmosphere.

rather stable, especially when compared to land surfaces. One problem with the emissivity of the ocean is that it is a weak function of the surface wind speed above it. Various models (e.g. Wilheit, 1979 and Pandey and Kakar, 1982) were developed for determining the emissivity of a wind-roughened ocean surface for earlier instruments which operated at lower frequencies (e.g. SMMR and SSM/I). Currently, there is a dearth of models which are applicable for the region near 183 GHz.

To examine the effect of the emissivity of the ocean's surface, the emissivity of an ocean surface underlying a clear sky midlatitude winter atmosphere was varied between 0.82 and 0.64. These results are shown in Table 4.1.

Table 4.1: Brightness temperatures (K) for emissivities from 0.82 to 0.66 (reflectivities from 0.34 to 0.18) for a midlatitude winter atmosphere.

Midlatitude Winter Brightness Temperatures									
FREQ. (GHz)	Reflectivity								
	0.34	0.32	0.30	0.28	0.26	0.24	0.22	0.20	0.18
180.31	254.99	255.06	255.13	255.20	255.27	255.34	255.41	255.48	255.55
182.31	245.77	245.77	245.77	245.77	245.77	245.77	245.77	245.77	245.77
176.31	243.01	244.40	245.80	247.19	248.59	249.98	251.37	252.77	254.16
150.00	203.81	208.08	212.35	216.62	220.90	225.17	229.44	233.72	237.99
91.655	193.83	198.78	203.74	208.69	213.64	218.60	223.55	228.50	233.46

The channel closest to the absorption line (182.31 GHz) has the same brightness temperature for all emissivities since the atmosphere is so opaque that microwave thermal energy emitted and reflected by the surface does not reach the satellite (i.e. the surface term has no contribution). The 180.31 GHz channel is also basically unaffected by the surface reflectivity. The line wing channel (150 GHz) and the window channel (91.655 GHz) brightness temperatures change appreciably as the emissivity changes according to the values depicted in the table. This result will be discussed later with respect to the operational algorithm in use.

The root mean square (RMS) error calculated pre-launch performance of the T-2 with the *a priori* regression coefficients using the multiple linear regression technique employed

operationally showed the best retrieval statistics occurs over ocean backgrounds with their relatively uniform surface emissivity (Boucher *et al.*, 1993).

4.2.2 Land Background

The emissivity of dry land backgrounds is thought to vary from 0.8 to 1.0 over the range of frequencies of 140 to 200 GHz (Schaerer and Wilheit, 1979). These early values should be compared with those of Wang *et al.* (1992) below. As mentioned above, the Wilheit (1990) algorithm, as amended by Lutz *et al.*, retrieves the land emissivity by an iterative process as part of its computations.

The presence of vegetation cover, however, can change the reflectivity of land surfaces as vegetation generally is an absorptive medium and therefore decreases reflectivity values. Frozen soils also generally have low reflectivity values (~ 0.1). Soils with moisture contents of less than 50% have dielectric constants where the real part is less than 6 which yields a value of R of less than 0.15 (Wang and Schmugge, 1990).

Snow cover presents a different challenge. Wang *et al.* (1992), using the AMMS described in Chapter 1, observed emissivities as low as 0.58 when making flights over Alaska. They surmised that the reason for such low emissivities is due to scattering by snow particles on the ground. Wang *et al.* found the emissivities on these flights generally ranged from 0.6–0.9 which differ from the estimates of Schaerer and Wilheit of more than a decade ago.

Conceptually, low level moisture retrievals would be expected to be more difficult over land because of the high and variable emissivity of this surface. This presents the possible situation where emission from the lower level(s) of the atmosphere and the emission from earth's surface may be nearly at

the same brightness temperature. Isaacs and Deblonde (1985) noted that surface emissivity affects the retrieval accuracy at all levels and not just at the layers near the surface based on the statistical retrieval method they used.

Brightness temperatures for an ocean surface with an emissivity of 0.7 and for a land surface with an emissivity of 1.0 are compared in Table 4.2.

The three channels nearest the absorption line (182.31 GHz channel not shown) are virtually unaffected by the surface emissivity. However, this is certainly not the case for the 150 and 91.655 GHz channels. Radically different brightness temperatures are computed for cases with emissivities of 1.0 and 0.7 for these channels. This is simply the factor of a warm background and a cold background, respectively.

As mentioned above, for the ocean background case in Table 4.1 brightness temperatures for the 150 and 91.655 GHz changed appreciably for small emissivity changes. The operational algorithm retrieves the surface emissivity using the 91.655 GHz channel and a physical retrieval model (Griffin *et al.*, 1993).

4.3 DEPENDENCE ON CLOUDS

Water clouds affect microwave radiation primarily through the processes of absorption and emission. As discussed in the previous chapter, Rayleigh absorption is assumed by the cloud model (MPM92) being used. The process of scattering is usually considered negligible since the single scatter albedo, $\bar{\omega}$, at the microwave/millimeter wavelengths is very small.

To depict the effects of clouds on weighting functions, Figures 4.8–4.12 show the five cloud models for a tropical atmosphere over an ocean ($R = 0.3$ or $\epsilon = 0.7$) background. For the cloud models used, and from the study of the figures shown, the following conclusions are deduced:

1. The channel closest to the absorption line does not 'see' any of the low level water clouds.
2. The 180.31 GHz channel sees only those clouds with cloud tops above 2 km.
3. The weighting functions for the other channels are radically affected by clouds in the FOV.
4. The weighting functions peak sharply at the cloud top.

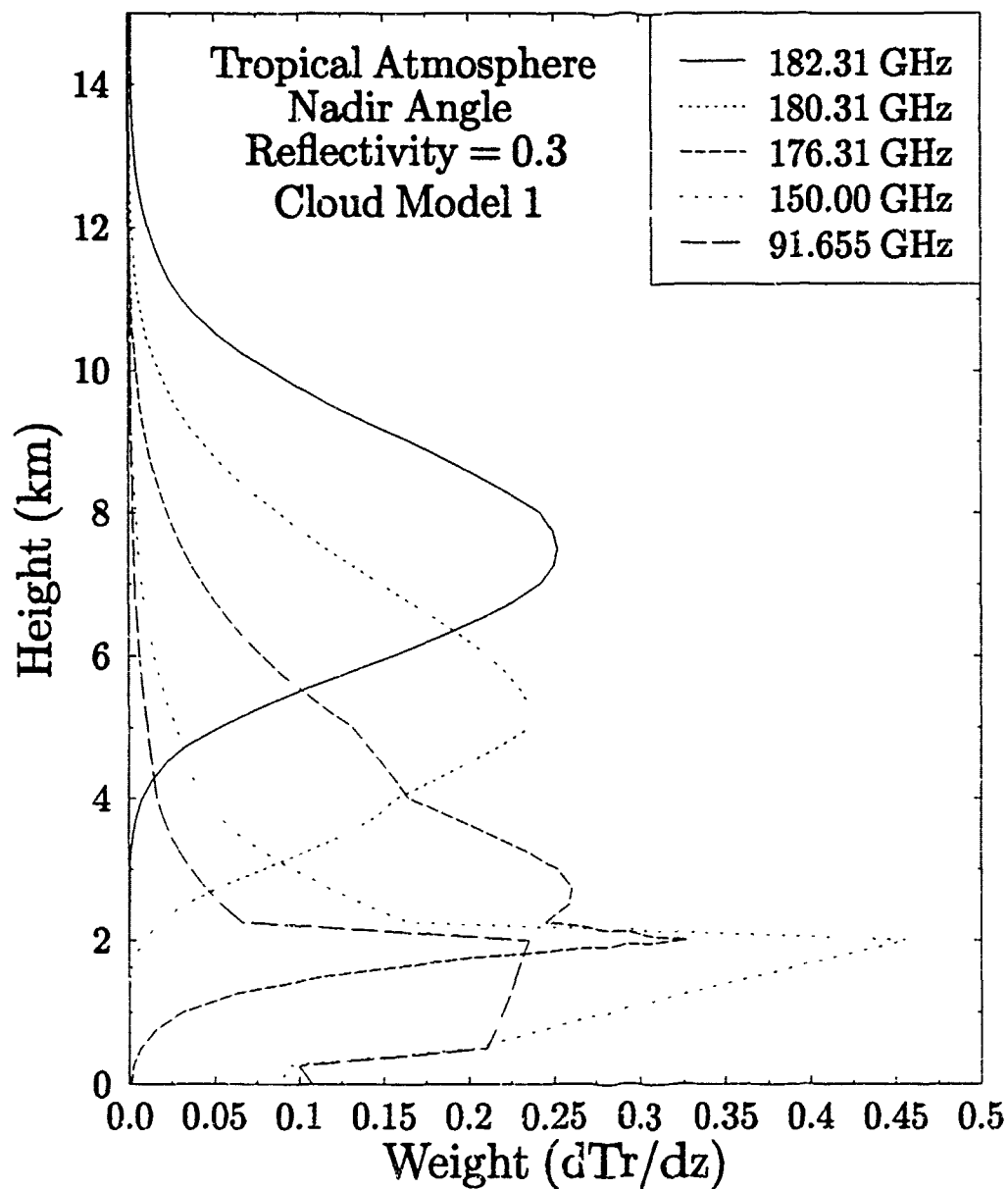


Figure 4.8: Weighting functions as in Figure 4.1 except for stratus cloud ($w = 0.15\text{gm}^{-3}$) from 0.5-2.0 km (cloud model 1).

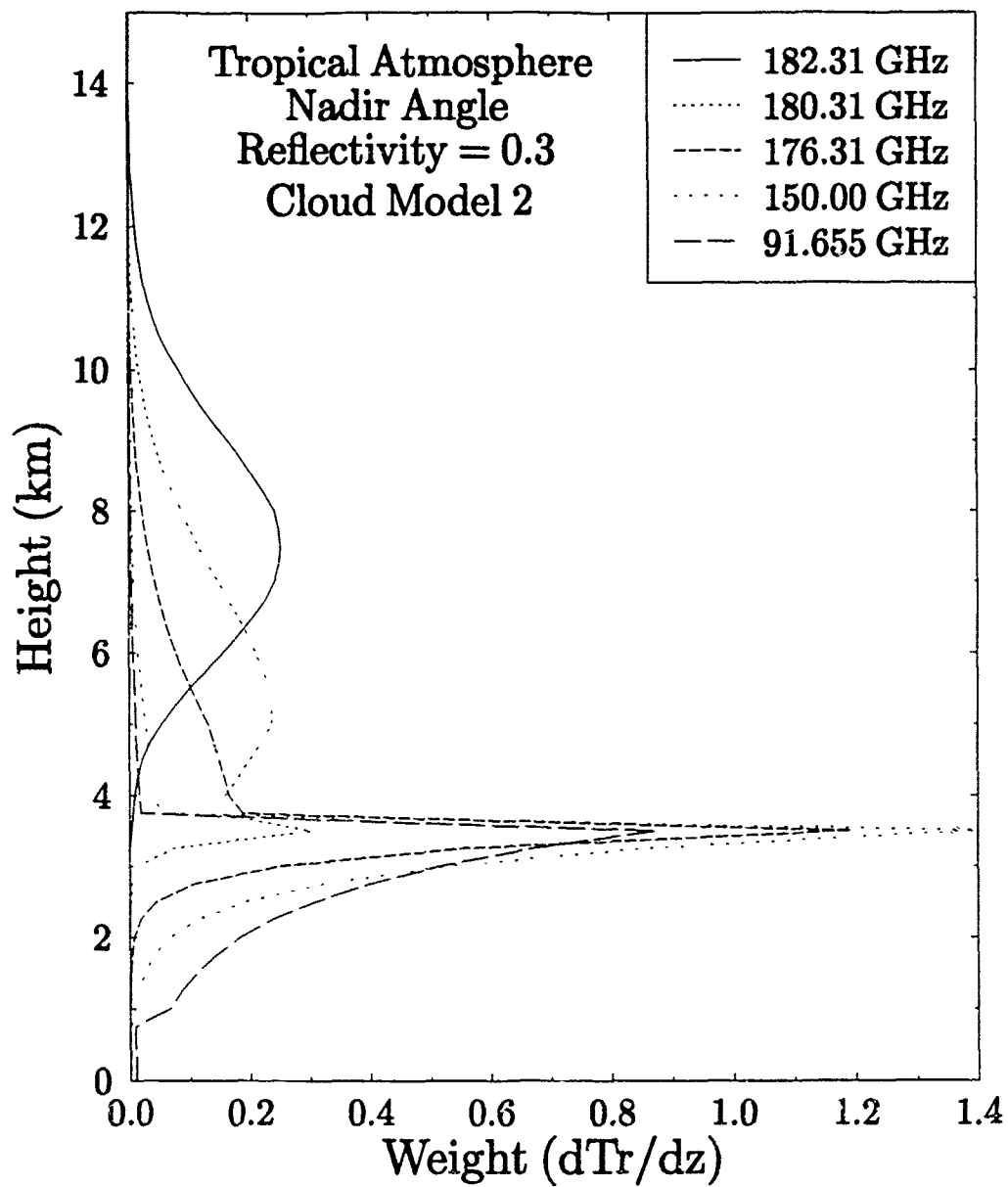


Figure 4.9: The same as Figure 4.8 except for cumulus cloud ($w = 1.0 \text{ gm}^{-3}$) from 1.0-3.5 km (cloud model 2).

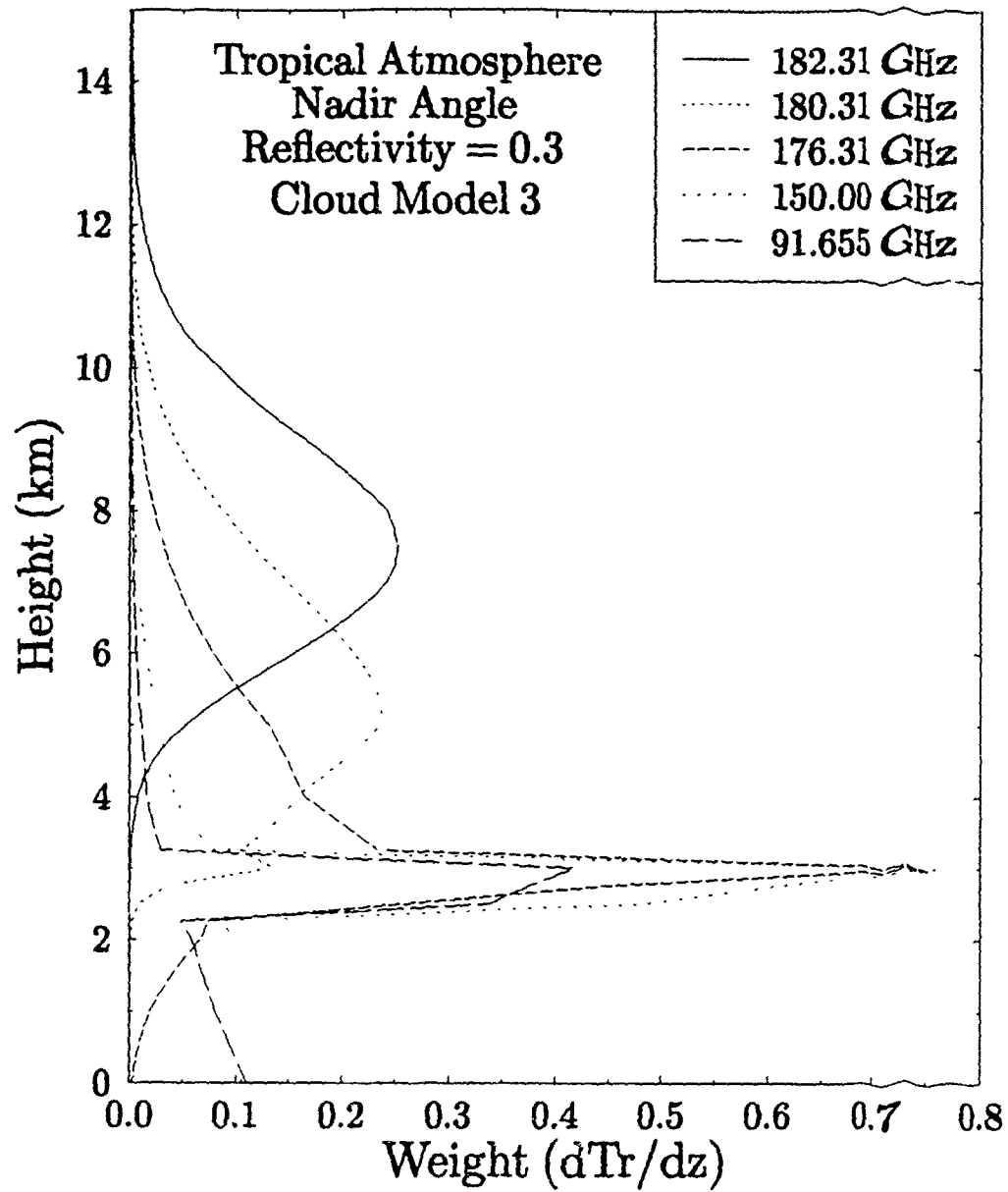


Figure 4.10: The same as Figure 4.8 except for altostratus cloud ($w = 0.40 \text{ gm}^{-3}$) from 2.5-3.0 km (cloud model 3).

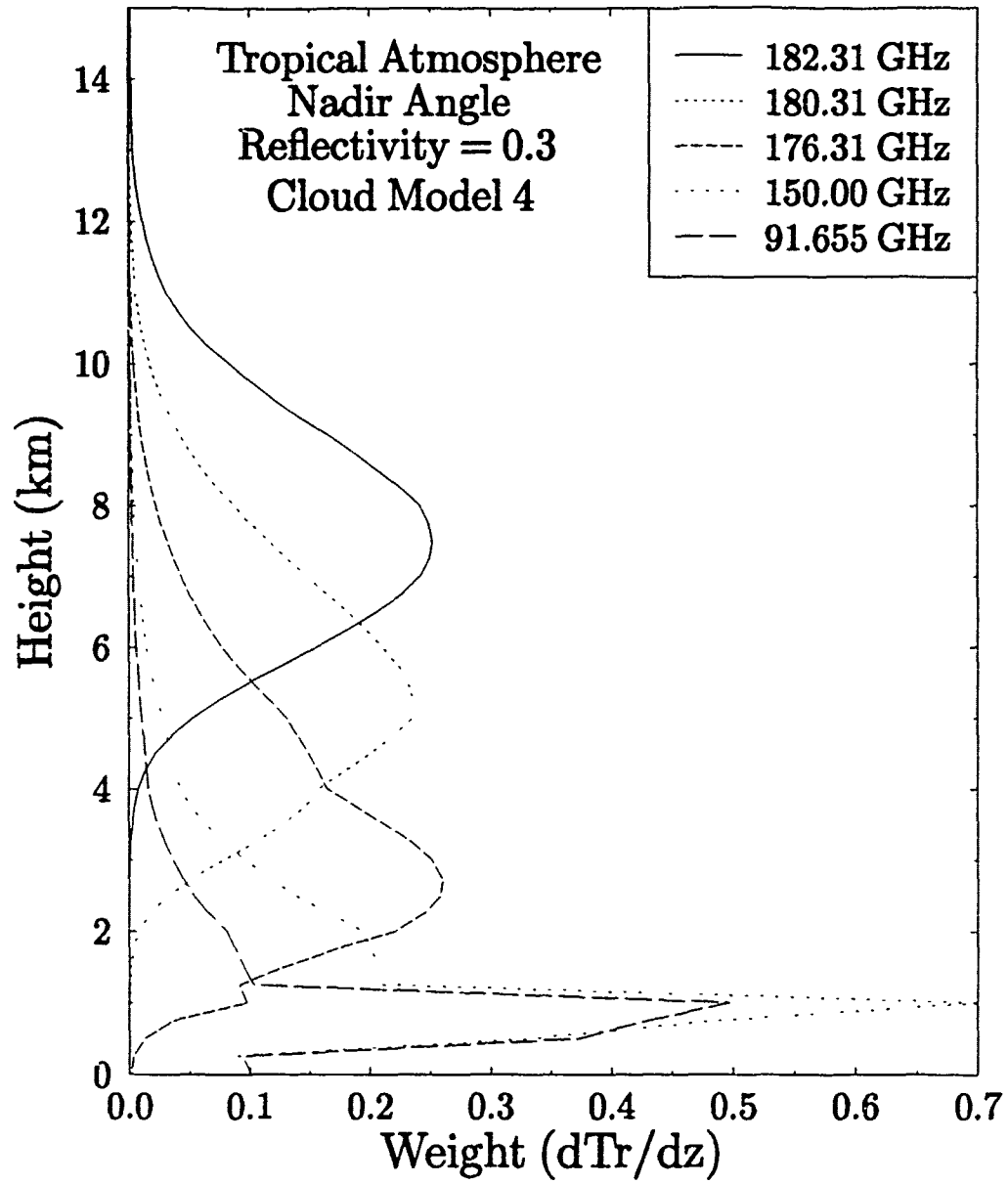


Figure 4.11: The same as Figure 4.8 except for stratocumulus cloud ($w = 0.55 \text{ gm}^{-3}$) from 0.5-1.0 km (cloud model 4).

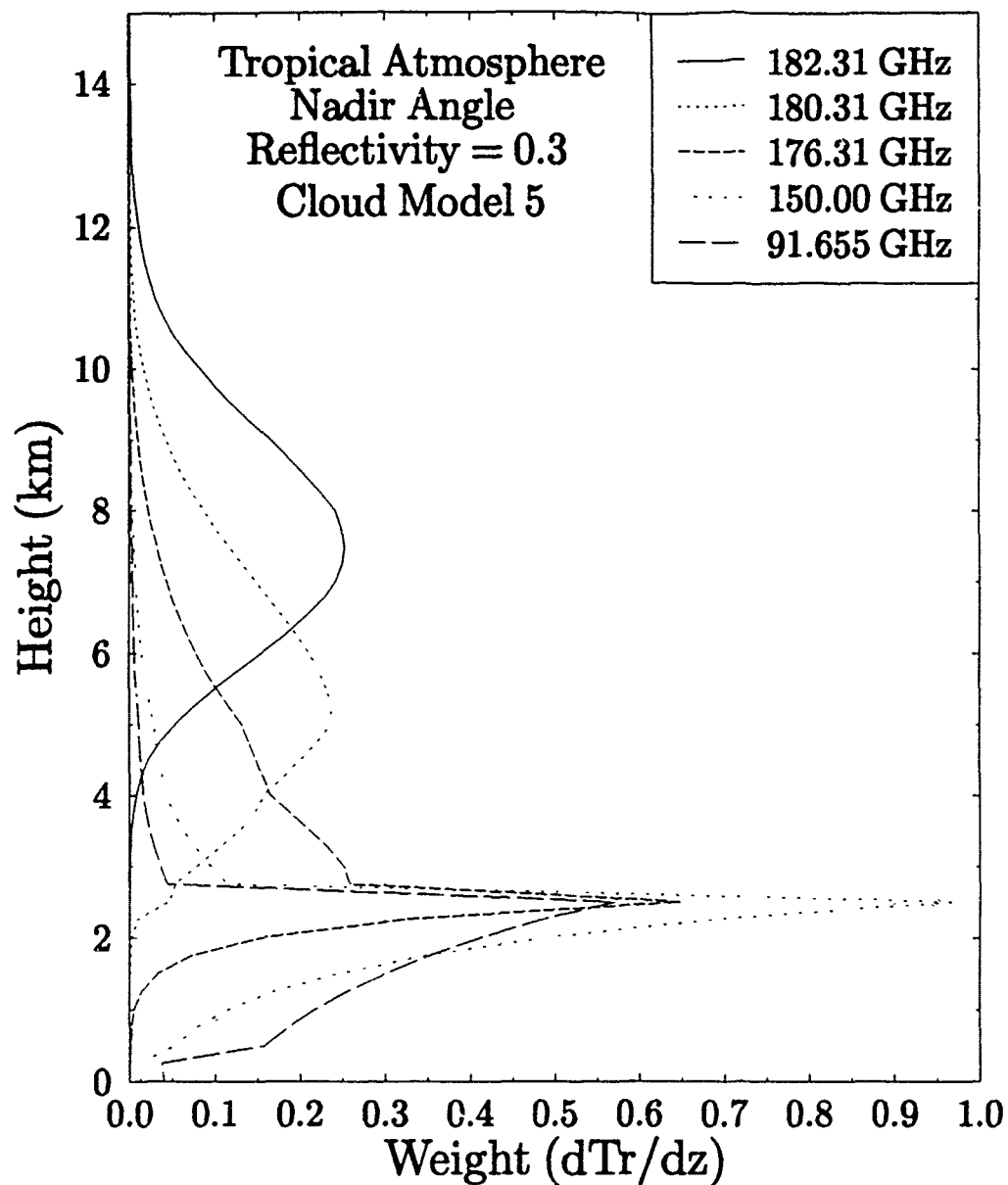


Figure 4.12: The same as Figure 4.8 except for nimbostratus cloud ($w = 0.61 \text{ gm}^{-3}$) from 0.5-2.5 km (cloud model 5).

4.3.1 Dependence on Layer Thickness

The microwave properties of clouds in the Rayleigh absorption regime are defined by several factors. One factor is the thickness of the cloud layer. This is because for a very thin cloud, much of the microwave energy from below is transmitted through the cloud layer. To determine the effect of varying cloud thicknesses on the brightness temperatures at satellite altitude, clouds were inserted into the tropical atmosphere with a constant cloud base of 1 km. Cloud thicknesses were varied from 1 to 5 km by 1 km increments. Table 4.3 shows simulated brightness temperatures for clouds of variable thickness and liquid water content. According to the simulations (summarized in this table), the 150 GHz channel and to a lesser extent the 92 GHz are the most responsive to the presence of clouds. The responsiveness in the 150 GHz channel is expected since it is designed to peak near the surface as depicted in Figure 4.1. Note that brightness temperatures decrease for increasing LWC and increasing cloud thickness (Δz) with a land background. The reason for this is that the clouds diminish the effects of the surface term.

4.3.2 Dependence on Layer Location

It has been seen that the weighting functions for atmospheres containing clouds tend to peak near the cloud top. This gives a good indication of the effects of where a cloud is located in the atmosphere and its influence on brightness temperatures.

To determine the influence of the layer location on brightness temperature, Table 4.4 shows the simulated brightness temperatures for a tropical atmosphere with a constant cloud thickness, reflectivity, and a varying cloud base and liquid water content. The data in this table indicates how the brightness temperatures decrease as a cloud is moved higher into the atmosphere. This is expected since the temperature profile decreases with height and the cloud limits the microwave emissions from below it.

4.3.3 Dependence on Cloud Liquid Water Content

Figures 4.13–4.16 depict brightness temperatures for the five T-2 channels for several cloud models with the LWC varied from 0.0 to 0.50 gm^{-3} . The brightness temperatures for the 3 channels near 183 GHz are basically constant whereas for the 150 and 91.655

Table 4.2: Comparison of brightness temperatures for land ($\epsilon = 1.0$) and ocean ($\epsilon = 0.7$) surfaces.

Brightness Temperature								
Atmospheric case	180.31 GHz		176.31 GHz		150.00 GHz		91.655 GHz	
	Land	Ocean	Land	Ocean	Land	Ocean	Land	Ocean
Clear tropical	264.71	264.71	277.58	277.36	291.19	265.12	295.95	237.72
Clear ML sum.	263.54	263.54	276.32	275.08	290.91	252.62	295.84	229.72
Clear ML winter	256.44	255.31	271.77	249.34	291.92	223.19	295.93	216.26
Cloud model 1	256.89	256.89	269.82	269.81	284.18	272.76	292.04	248.02
Cloud model 2	264.67	264.67	276.89	276.87	289.13	277.67	294.28	253.08
Cloud model 3	262.32	262.32	271.23	271.23	278.64	278.51	283.51	279.32
Cloud model 4	263.92	263.92	275.58	275.52	286.91	273.42	292.59	250.31
Cloud model 5	264.71	264.71	277.22	277.18	289.55	278.92	294.77	255.77

Table 4.3: Brightness temperatures for variable cloud thickness (Δz (km)) and LWC (gm^{-3}) for a fixed cloud base (1 km), emissivity (0.97), and a tropical atmosphere.

BRIGHTNESS TEMPERATURES (K)					
Cloud LWC	Δz (km)	FREQUENCY (GHz)			
		180.31	176.31	150.00	91.655
Cloud Model 1 LWC = 0.15	1	264.67	276.92	287.85	289.91
	2	264.08	276.00	286.20	288.91
	3	263.11	274.26	283.54	287.14
	4	261.99	271.69	280.13	284.67
	5	260.36	268.58	276.24	281.69
Cloud Model 2 LWC = 1.00	1	264.62	275.24	284.30	288.59
	2	263.42	272.68	280.90	285.34
	3	261.25	269.58	275.91	280.37
	4	258.78	265.44	269.86	274.15
	5	255.71	260.65	263.89	267.92
Cloud Model 3 LWC = 0.40	1	264.65	276.50	286.97	289.59
	2	263.90	275.16	284.43	287.69
	3	262.63	272.95	280.49	284.44
	4	261.17	269.61	275.41	279.97
	5	259.13	265.53	269.92	274.90

Table 4.4: Brightness temperatures for variable cloud base and LWC for a fixed emissivity ($\epsilon = 1.0$) and atmosphere (tropical).

BRIGHTNESS TEMPERATURE (K)						
Cloud Base (km)	LWC (gm^{-3})	FREQUENCY (GHz)				
		182.31	180.31	176.31	150.00	91.655
1	0.15	251.24	264.67	276.92	289.34	294.49
1.5	0.15	251.24	264.50	276.57	288.69	294.02
2	0.15	251.23	264.08	276.14	287.99	293.55
3	0.15	251.11	263.13	274.65	286.24	294.43
5	0.15	249.51	260.88	271.16	283.08	290.25
1	1.00	251.24	264.62	275.24	284.54	290.43
1.5	1.00	251.24	264.26	273.99	282.95	288.81
2	1.00	251.23	263.42	272.73	281.44	287.32
3	1.00	251.04	261.25	269.71	276.77	283.11
5	1.00	247.74	255.82	261.20	265.86	273.27

GHz channels brightness temperatures vary with liquid water content, cloud location, and cloud thickness.

Figures 4.15 and 4.16 are identical except for the emissivity (reflectivity). The latter figure shows the effects of the clouds by decreasing the 91.655 and 150 GHz brightness temperatures over a 300 K surface as the cloud liquid water content is increased. Contrast this to Figure 4.15 where the brightness temperature for a low emissivity surface (cold background at 210 K, as discussed above). In this case, the brightness temperatures of the window channels systematically increases as the liquid water path (LWP) is increased.

This yields the observation that clouds generally increase brightness temperatures over oceans and decrease brightness temperatures over land. These effects, however, appear only in the window channels and to a lesser extent in the 183 ± 7 GHz channel, depending on cloud altitude. This response to clouds can also be seen in Table 4.2. The near linear response of the window (especially) and line wing channel (as shown in Figure 4.13) to changes in LWC offers a simple way of retrieving this cloud property by using these channels. Several authors have considered this (including Isaacs *et al.*, 1985).

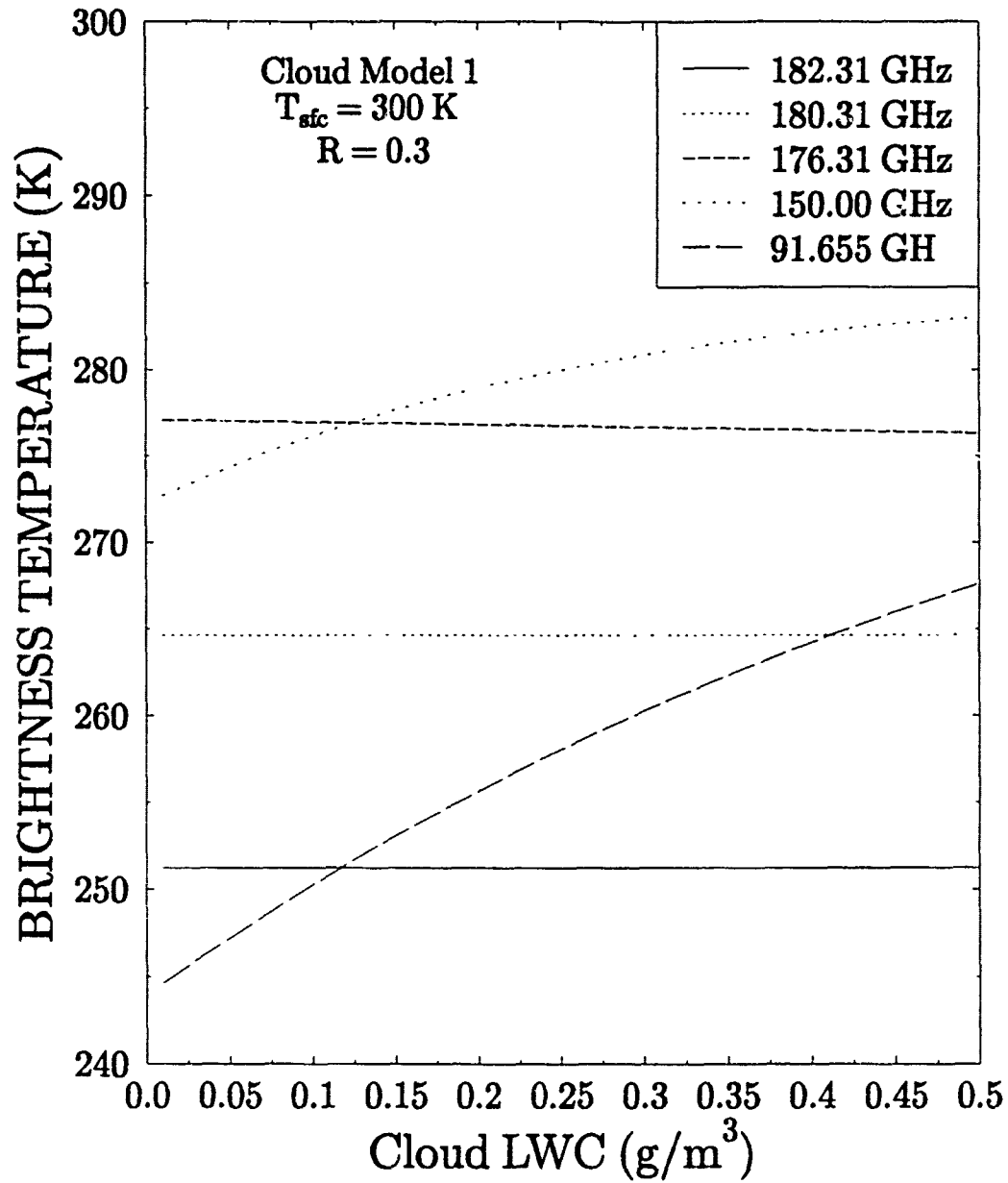


Figure 4.13: Brightness temperatures for Cloud Model 1 and a tropical atmosphere with LWC from 0.01 to 0.50 gm^{-3} .

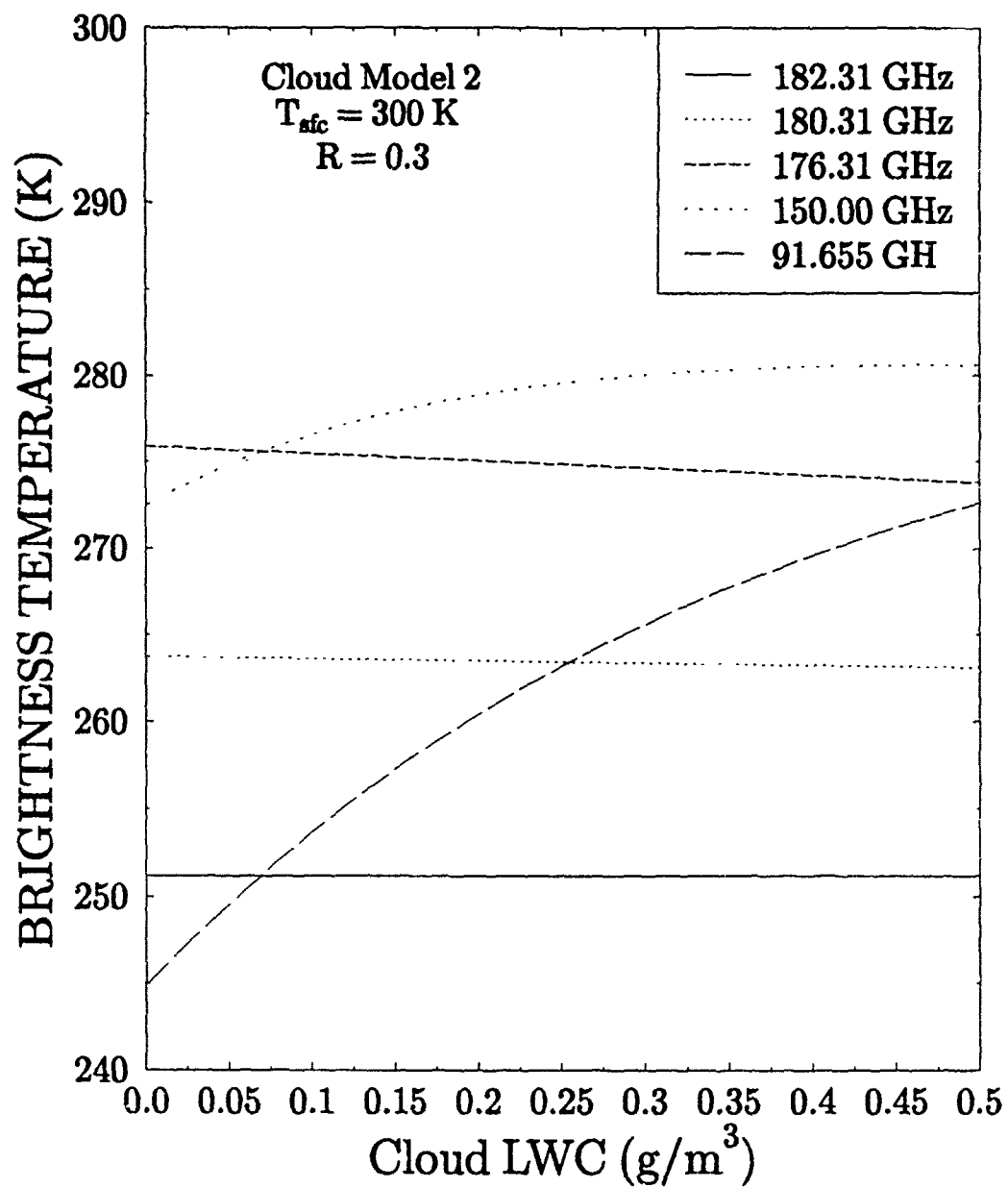


Figure 4.14: Brightness temperatures as in Figure 4.13 except for Cloud Model 2.

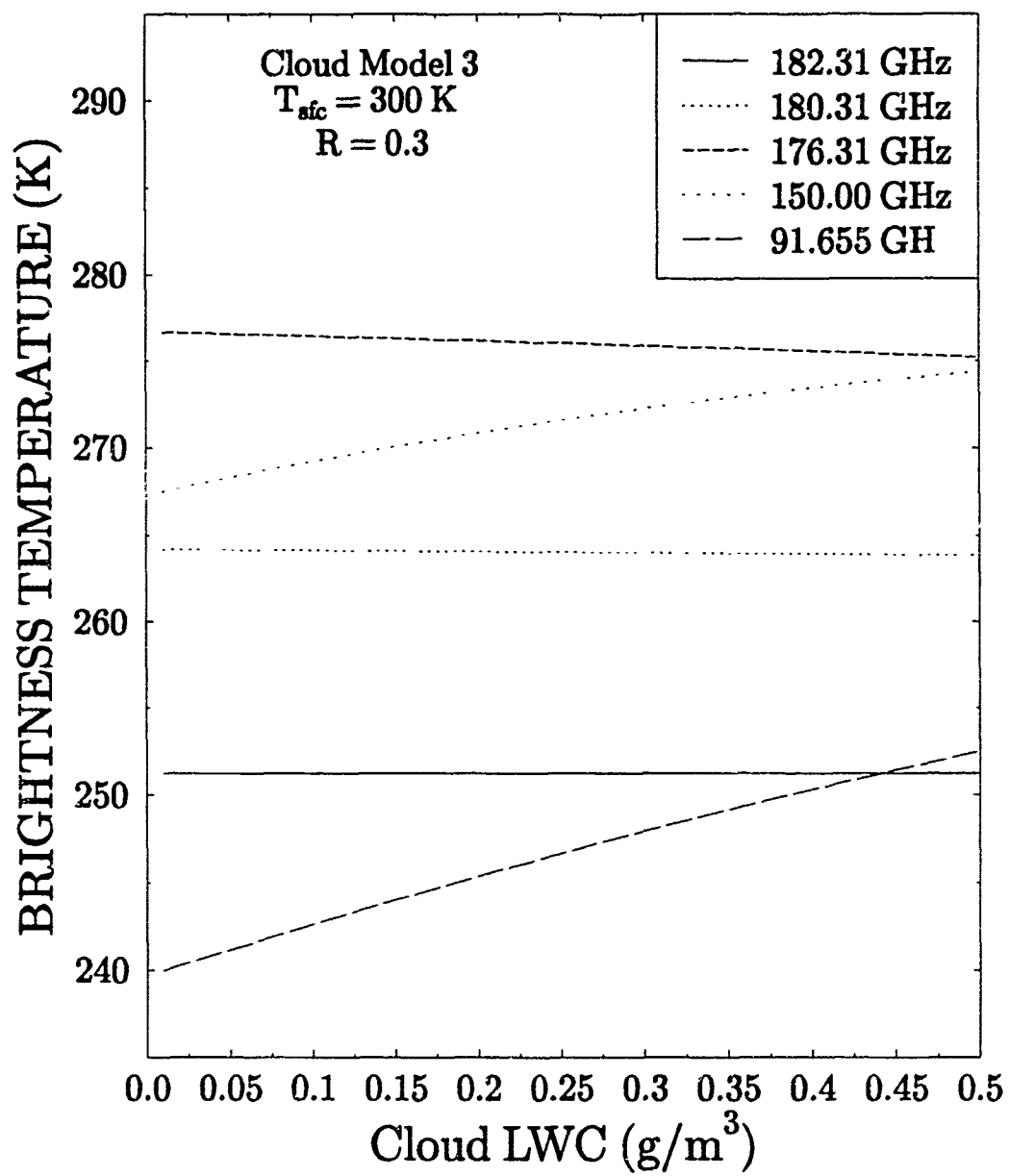


Figure 4.15: Brightness temperatures as in Figure 4.13 except for Cloud Model 3.

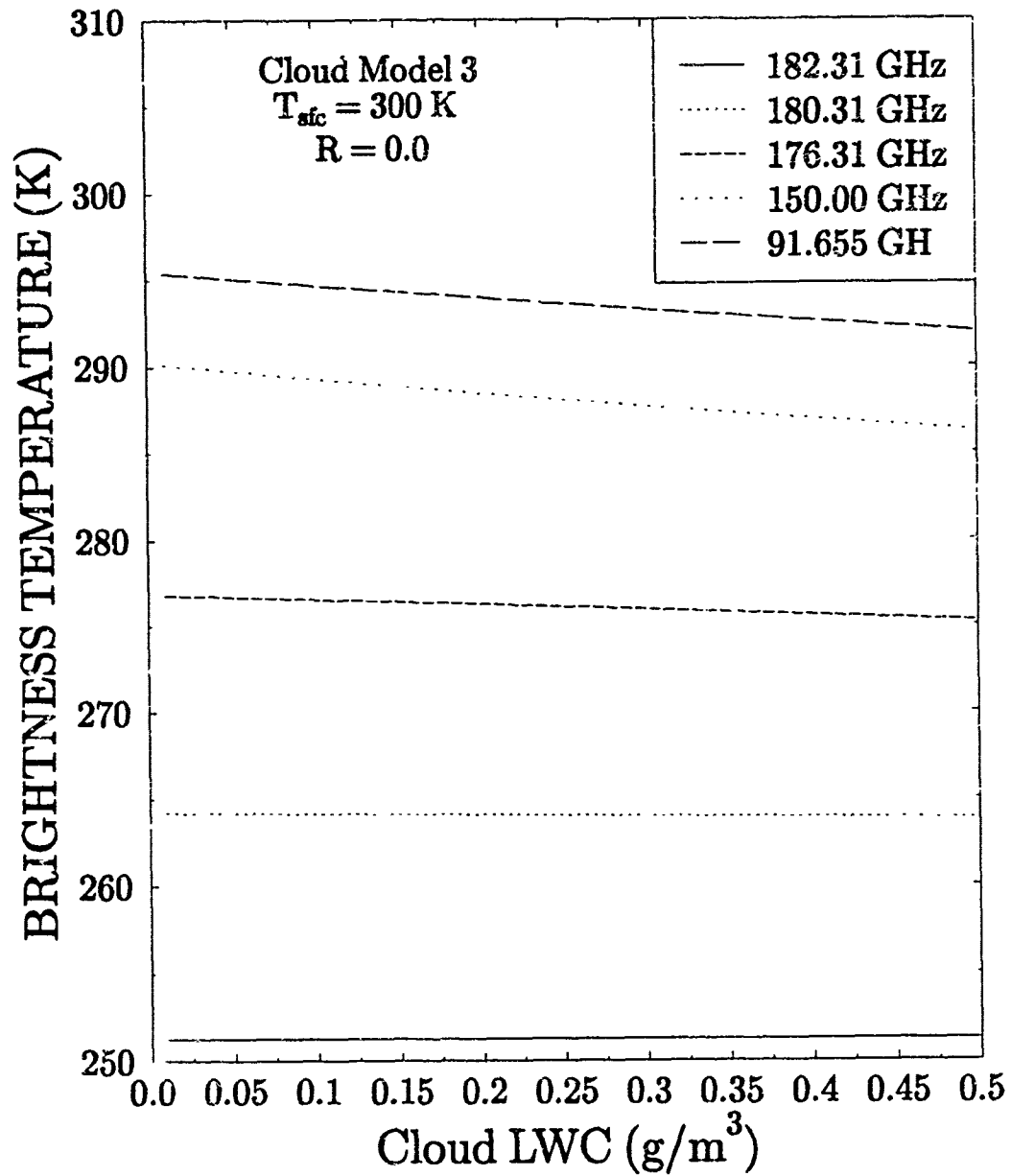


Figure 4.16: Brightness temperatures as in Figure 4.15 except for $R = 0.0$.

4.4 SCAN ANGLE EFFECTS

The effects of scan angle on brightness temperatures can be considered through the use of MPM92. Scan angle affects brightness temperatures since it changes the optical path. As shown in Figure 3.1, the scan angle (or scene station view angle as in Figure 3.1) on the SSM/T-2 varies between 1.5° and 40.5° as the sensor scans across a line. Unfortunately, there is no easy way to correct for this change in brightness temperature for the change in the atmospheric path which is viewed. Figures 4.17 and 4.18 show that the brightness temperature can both increase or decrease as the sensor moves away from nadir. There are competing effects here; limb darkening, occurs when the sensor moves away from nadir and the path length increases and the weighting functions move upwards vertically in the atmosphere. Limb brightening occurs for the wing and window channels which sense near the surface. The temperature of a cold surface is replaced by higher temperatures as the path is extended by viewing away from nadir. This complex problem would likely be handled operationally through the use of regression equations. For example, regression equations are used to solve the scan angle differences for the MSU (Grody, 1983).

4.5 INTERPRETATION OF RESULTS

The SSM/T-2 responds to a variety of atmospheric phenomenon in a manner much different than those instruments which preceded it in the remote sensing of the atmosphere. In this chapter it has been shown that:

1. Weighting functions and brightness temperatures are dependent on the moisture and temperature profile of the atmosphere.
2. The background and its emissivity have a significant effect on the brightness temperatures of the window channels.
3. Backgrounds with higher emissivities result in higher brightness temperatures.
4. Liquid water clouds that form low in the atmosphere have a profound influence on brightness temperatures in the window channels.

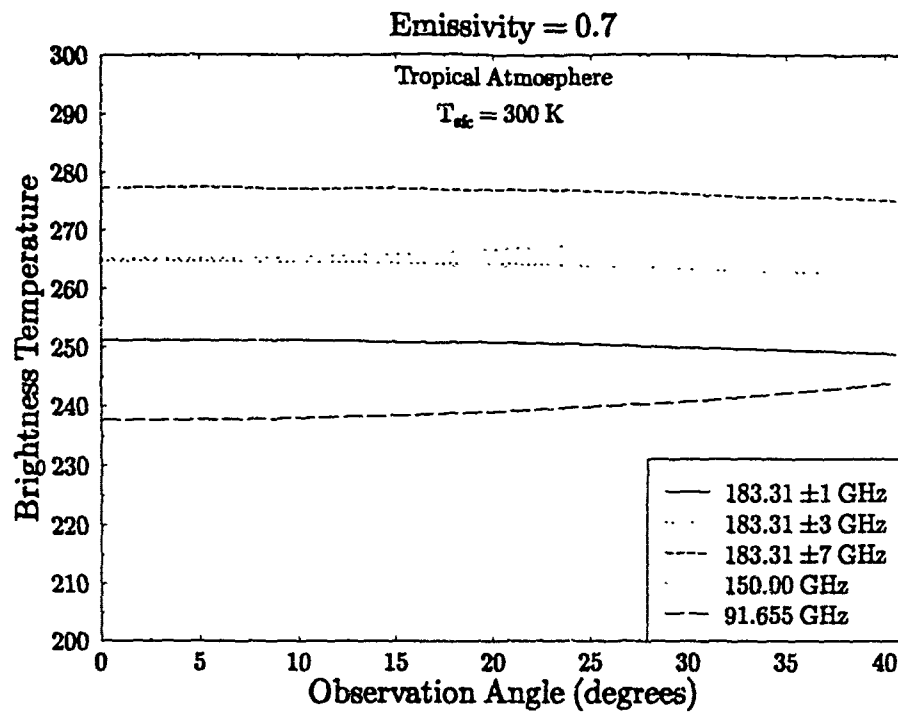


Figure 4.17: Brightness temperatures as a function of observation angle for a tropical atmosphere.

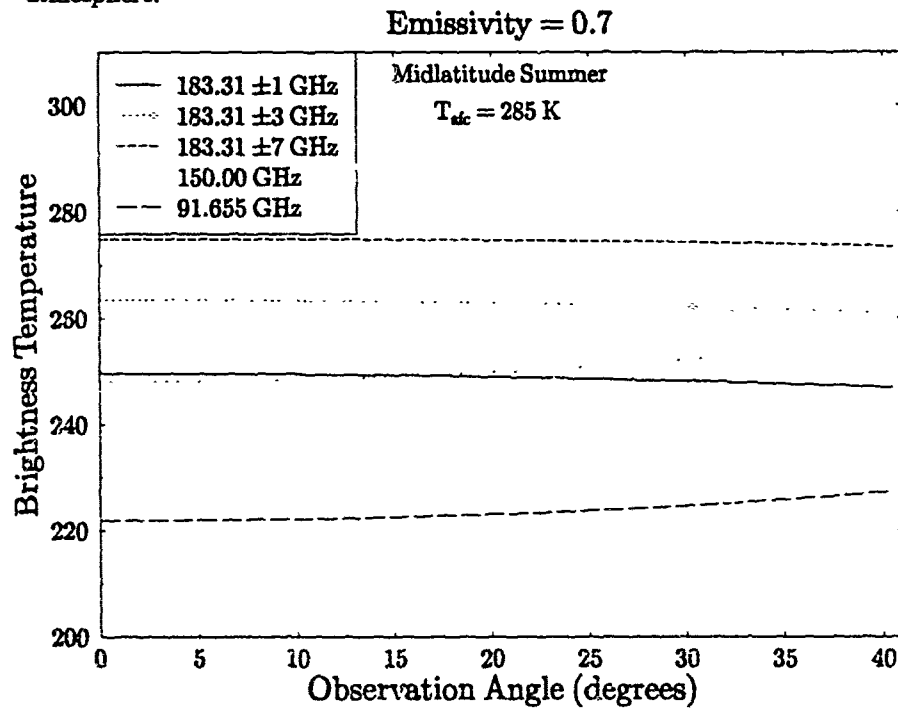


Figure 4.18: The same as Figure 4.17 except for a midlatitude summer atmosphere and $T_{sf} = 285$ K.

- (a) Increasing cloud LWC decreases brightness temperatures.
- (b) Higher clouds correspond to lower brightness temperatures.
- (c) Liquid water content affects the 91 and 150 GHZ channels brightness temperatures greatly.
- (d) Clouds generally increase brightness temperatures over ocean surfaces and decrease brightness temperatures over land.

Certainly water clouds affect brightness temperatures in a systematic manner. Clouds become more difficult to quantify when one considers the possibility of mixed phase clouds, ice clouds, and partial cloud cover.

Chapter 5

WATER VAPOR BURDEN

In this chapter a simple method is described for deriving the column vapor burden from brightness temperatures. It will be demonstrated how the measured brightness temperatures, especially those of 183 ± 1 GHz (Channel 2) and 183 ± 3 GHz (Channel 1), correspond to a level of constant water vapor overburden. This result together with temperature-pressure data are used to establish the burden at a constant pressure. The method is demonstrated using only Channel 2 brightness temperatures.

5.1 WATER VAPOR BURDEN AND THE SSM/T-2 FREQUENCIES

The approach followed is from the study of Rosenkranz *et al.* (1982) who describe the temperature weighting functions for both the oxygen band (e.g. SSM/T-1 frequencies) and for the water vapor absorption line at 183.31 GHz. They define the integrated column water vapor above a given level as the water vapor burden (U) which is proportional to τ , the optical depth. Rosenkranz *et al.* also noted that when weighting functions are expressed as functions of water vapor burden rather than as functions of pressure or temperature, these weighting functions are nearly symmetric in shape and their peaks are invariant with respect to changes in the water vapor profile. These functions are also displaced downward as the frequency varies away from the absorption line at 183 GHz.

Another way of stating this principle is that the water vapor burden may be expressed as:

$$U(h) = \int_h^{\infty} \rho(h') dh', \quad (5.1)$$

where $\rho(h)$ is the water vapor density as a function of height, h . This means that the satellite brightness temperature is a weighted average of the temperature profile. The

weighting is defined by the weighting function, which, when expressed in terms of U , is approximately invariant with respect to changes in $\rho(h)$. Therefore, for a temperature profile with (say) a linear lapse rate near the peak of the weighting function, the brightness temperature and thermometric temperature of the atmosphere will be equal at the peak of the weighting function (Wilheit and al Khalaf, 1993). This leads to the hypothesis that the water vapor burden at the level where the atmospheric temperature (T_t) equals the brightness temperature (T_b) will be constant for a given frequency independent of the water vapor profile.

To test this hypothesis, the 3 atmospheric profiles described in Chapter 3 were used for clear sky temperature/pressure profiles and various water vapor profiles (using the water vapor multiplicative factor) were employed to yield 47 cases. The water vapor burden was calculated using (5.1) where the height h is the altitude where $T_t = T_b$. Table 5.1 shows the results for these water vapor burdens for the brightness temperatures at 183.31 ± 1 GHz for these 47 different atmospheric cases.

Nine cases result in water vapor burdens of less than 0.35 kg/m^2 for the 47 cases in Table 5.1. Certainly, one can argue whether case 7 is a physically realistic atmosphere. The other cases with low water vapor burdens are for small water vapor multiplicative factors. Nonetheless, the hypothesis appears realistic for the 183.31 ± 1 GHz channel. For the cases considered in Table 5.1 a mean water vapor burden of 0.3735 kg/m^2 and a root mean square error (RMSE) value of 0.0256 kg/m^2 .

Water vapor burdens were also calculated for the same 47 cases for 183.31 ± 3 GHz. These results are listed in Table 5.2. Again the values of water vapor burden are reasonably constant with a mean and RMS values of 1.2739 kg/m^2 and 0.3709 kg/m^2 , respectively. The cases with very low water vapor burdens are characterized by optical depths of less than 4, meaning the surface emissivities are influencing the brightness temperatures. Computing these statistics for only the 40 highest cases yields a mean and RMSE of 1.4097 and 0.1486 kg/m^2 , respectively.

In Table 5.2, case 8 has a surface relative humidity of about 14% with the surface temperature near 20°C . Cases 16, 17, and 18 have relative humidities of 25–47% with a

Table 5.1: Water Vapor Overburdens (U) at 183 ± 1 GHz for $T_b = T_e$.

CASE	H ₂ O MULT. FACTOR	TEMPERATURE PROFILE	WATER VAPOR PROFILE	U (kg/m ²)	CWV (kg/m ²)
1	0.50	Tropical	Tropical	.4083	20.61
2	0.75	Tropical	Tropical	.3954	30.91
3	1.0	Tropical	Tropical	.3910	41.21
4	1.25	Tropical	Tropical	.3806	51.51
5	1.50	Tropical	Tropical	.3639	61.82
6	1.75	Tropical	Tropical	.3505	72.12
7	2.00	Tropical	Tropical	.3389	82.42
8	0.25	ML summer	ML summer	.3962	7.32
9	0.50	ML summer	ML summer	.3844	14.64
10	0.75	ML summer	ML summer	.3849	21.95
11	1.0	ML summer	ML summer	.3917	29.27
12	1.25	ML summer	ML summer	.3947	36.59
13	1.50	ML summer	ML summer	.3886	43.91
14	1.75	ML summer	ML summer	.4057	51.23
15	2.00	ML summer	ML summer	.3774	58.54
16	0.40	ML winter	ML winter	.3178	3.42
17	0.50	ML winter	ML winter	.3584	4.27
18	0.75	ML winter	ML winter	.3767	6.41
19	1.00	ML winter	ML winter	.3671	8.54
20	1.25	ML winter	ML winter	.3518	10.68
21	1.50	ML winter	ML winter	.3366	12.81
22	1.75	ML winter	ML winter	.3478	14.95
23	2.00	ML winter	ML winter	.3202	17.08
24	0.40	ML winter	ML summer	.3695	11.71
25	0.50	ML winter	ML summer	.3697	14.64
26	0.75	ML winter	ML summer	.3722	21.95
27	1.00	ML winter	ML summer	.3762	29.27
28	1.25	ML winter	ML summer	.3820	36.59
29	1.50	ML winter	ML summer	.3886	43.91
30	1.75	ML winter	ML summer	.3955	51.23
31	2.00	ML winter	ML summer	.4012	58.54
32	0.40	ML summer	ML winter	.3208	3.42
33	0.50	ML summer	ML winter	.3822	4.27
34	0.75	ML summer	ML winter	.4090	6.41
35	1.00	ML summer	ML winter	.3888	8.54
36	1.25	ML summer	ML winter	.3645	10.68
37	1.50	ML summer	ML winter	.3396	12.81
38	1.75	ML summer	ML winter	.3219	14.95
39	2.00	ML summer	ML winter	.3086	17.08
40	0.40	Tropical	ML summer	.3980	11.71
41	0.50	Tropical	ML summer	.4006	14.64
42	0.75	Tropical	ML summer	.4007	21.95
43	1.00	Tropical	ML summer	.4013	29.27
44	1.25	Tropical	ML summer	.3995	36.59
45	1.50	Tropical	ML summer	.3886	43.91
46	1.75	Tropical	ML summer	.3784	51.23
47	2.00	Tropical	ML summer	.3696	58.54

surface temperature of -1°C and cases 32–34 have relative humidities of 5–11%. Certainly, cases 32–34 would be extremely rare, a surface temperature of about 20°C and a relative humidity near 10% (although these surface conditions are occasionally observed in Colorado, but the surface pressure certainly isn't 1000 mb). The question of whether these atmospheres are realistic or not is debatable but if they happen, it will be very rarely.

There is also more scatter of the data for the ± 3 GHz channel compared to the ± 1 GHz channel. The results in Tables 5.1 and 5.2 correspond well with results of similar studies conducted by Wilheit and al Khalaf (1993).

Figures 5.1 and 5.2 are plots of the water vapor burden for the 47 cases for 183.31 ± 1 and 3 GHz, respectively (these are the data given in Tables 5.1 and 5.2). Figure 5.1 shows how the vapor burdens corresponding to the level at $T_b = T_t$ only slightly varies from atmosphere to atmosphere whereas Figure 5.2 shows that the water vapor burden is much more spread although the outliers are of a debatable, physically, as stated above.

Figures 5.3–5.6 show weighting functions plotted in terms of the burden U for the 183.31 ± 1 , 3, 7 GHz and 150.00 GHz channels, respectively. These figures graphically portray the essence of the hypothesis stated above. While the magnitudes of the weighting function change for each atmospheric profile, the peaks of these functions and their shape are remarkably similar for these different atmospheric profiles. This relative independence of the shape of $W(U)$ on both the temperature and moisture profiles provides a useful way of interpreting the SSM/T-2 brightness temperature distributions such as those shown in Figures 2.2–2.11.

5.2 CHANNEL 2 WATER VAPOR BURDEN MAP

Based on the discussion and results of the previous section, this section presents a retrieval of the water vapor burden for Channel 2 (183.31 ± 1 GHz) on a constant pressure surface. The data used in this retrieval consisted of the T-2 brightness temperatures described above and European Centre for Medium Range Weather Forecasts (ECMWF) monthly mean temperature and pressure analyses for March 1992 (used to simulate the temperature and pressure data which will normally be available from the SSM/T-1 Temperature Sounder). ECMWF monthly mean data were used because temperature data

Table 5.2: Water Vapor Overburden (U) at 183.31 ± 3 GHz for $T_b = T_t$.

CASE	H ₂ O MULT. FACTOR	TEMPERATURE PROFILE	WATER VAPOR PROFILE	U (kg/m ²)	CWV (kg/m ²)
1	0.50	Tropical	Tropical	1.4936	20.61
2	0.75	Tropical	Tropical	1.5346	30.91
3	1.0	Tropical	Tropical	1.5220	41.21
4	1.25	Tropical	Tropical	1.5389	51.51
5	1.50	Tropical	Tropical	1.5669	61.82
6	1.75	Tropical	Tropical	1.5923	72.12
7	2.00	Tropical	Tropical	1.6123	82.42
8	0.25	ML summer	ML summer	0.9340	7.32
9	0.50	ML summer	ML summer	1.1354	14.64
10	0.75	ML summer	ML summer	1.4097	21.95
11	1.0	ML summer	ML summer	1.4589	29.27
12	1.25	ML summer	ML summer	1.4913	36.59
13	1.50	ML summer	ML summer	1.5153	43.91
14	1.75	ML summer	ML summer	1.5346	51.23
15	2.00	ML summer	ML summer	0.2077	58.54
16	0.40	ML winter	ML winter	0.3847	3.42
17	0.50	ML winter	ML winter	0.8060	4.27
18	0.75	ML winter	ML winter	1.0605	6.41
19	1.00	ML winter	ML winter	1.1879	8.54
20	1.25	ML winter	ML winter	1.2347	10.68
21	1.50	ML winter	ML winter	1.2901	12.81
22	1.75	ML winter	ML winter	1.3126	14.95
23	2.00	ML winter	ML winter	1.3126	17.08
24	0.40	ML winter	ML summer	1.1331	11.71
25	0.50	ML winter	ML summer	1.2005	14.64
26	0.75	ML winter	ML summer	1.3006	21.95
27	1.00	ML winter	ML summer	1.3700	29.27
28	1.25	ML winter	ML summer	1.4165	36.59
29	1.50	ML winter	ML summer	1.4555	43.91
30	1.75	ML winter	ML summer	1.4848	51.23
31	2.00	ML winter	ML summer	1.5121	58.54
32	0.40	ML summer	ML winter	0.1346	3.42
33	0.50	ML summer	ML winter	0.2674	4.27
34	0.75	ML summer	ML winter	0.7516	6.41
35	1.00	ML summer	ML winter	1.1167	8.54
36	1.25	ML summer	ML winter	1.3064	10.68
37	1.50	ML summer	ML winter	1.3914	12.81
38	1.75	ML summer	ML winter	1.4259	14.95
39	2.00	ML summer	ML winter	1.4423	17.08
40	0.40	Tropical	ML summer	1.2619	11.71
41	0.50	Tropical	ML summer	1.3509	14.64
42	0.75	Tropical	ML summer	1.4 ⁵⁸	21.95
43	1.00	Tropical	ML summer	1.4916	29.27
44	1.25	Tropical	ML summer	1.5028	36.59
45	1.50	Tropical	ML summer	1.5376	43.91
46	1.75	Tropical	ML summer	1.5730	51.23
47	2.00	Tropical	ML summer	1.6051	58.54

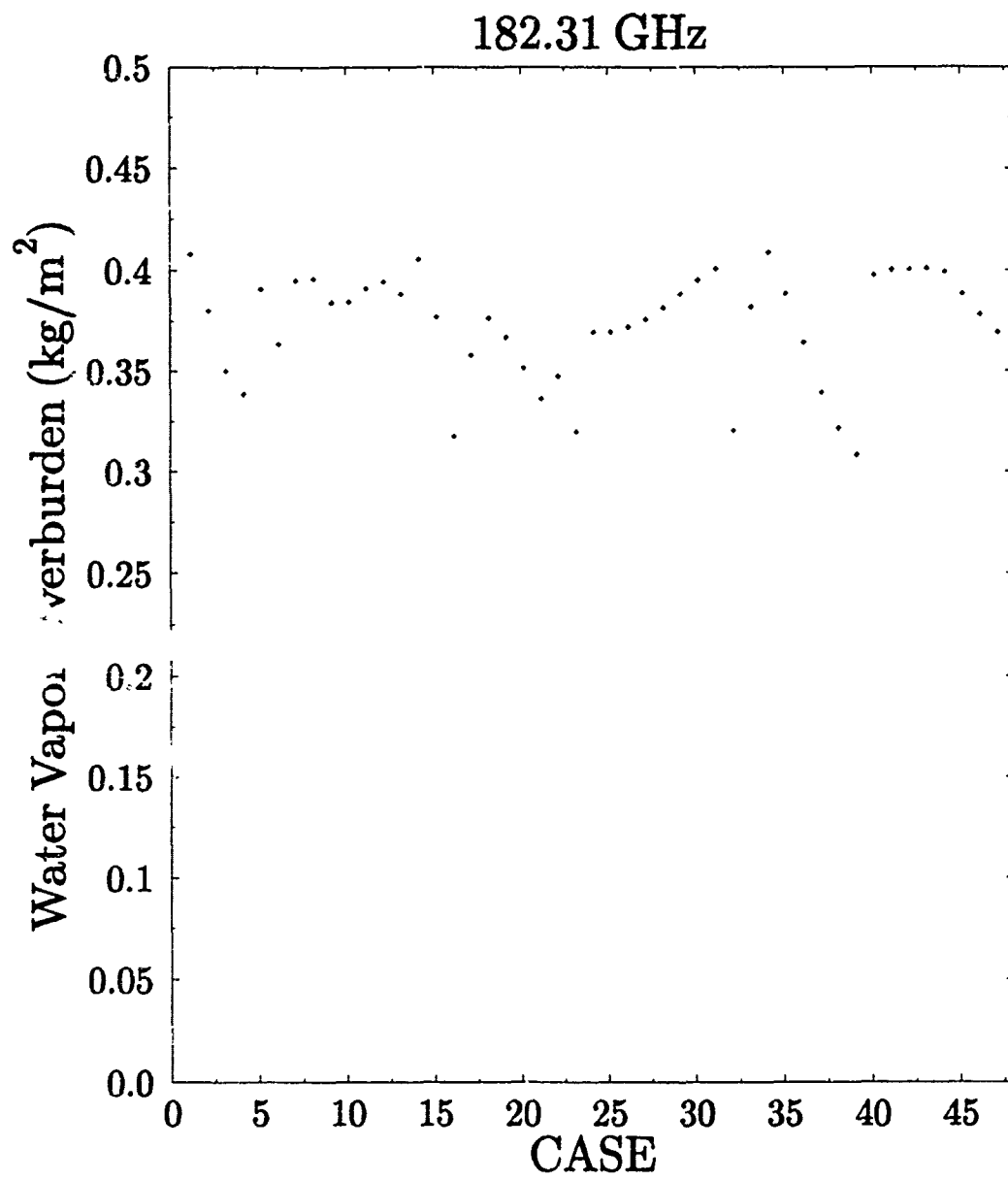


Figure 5.1: Water Vapor Overburdens at 183.31 ± 1 GHz for 47 Atmospheric Cases.

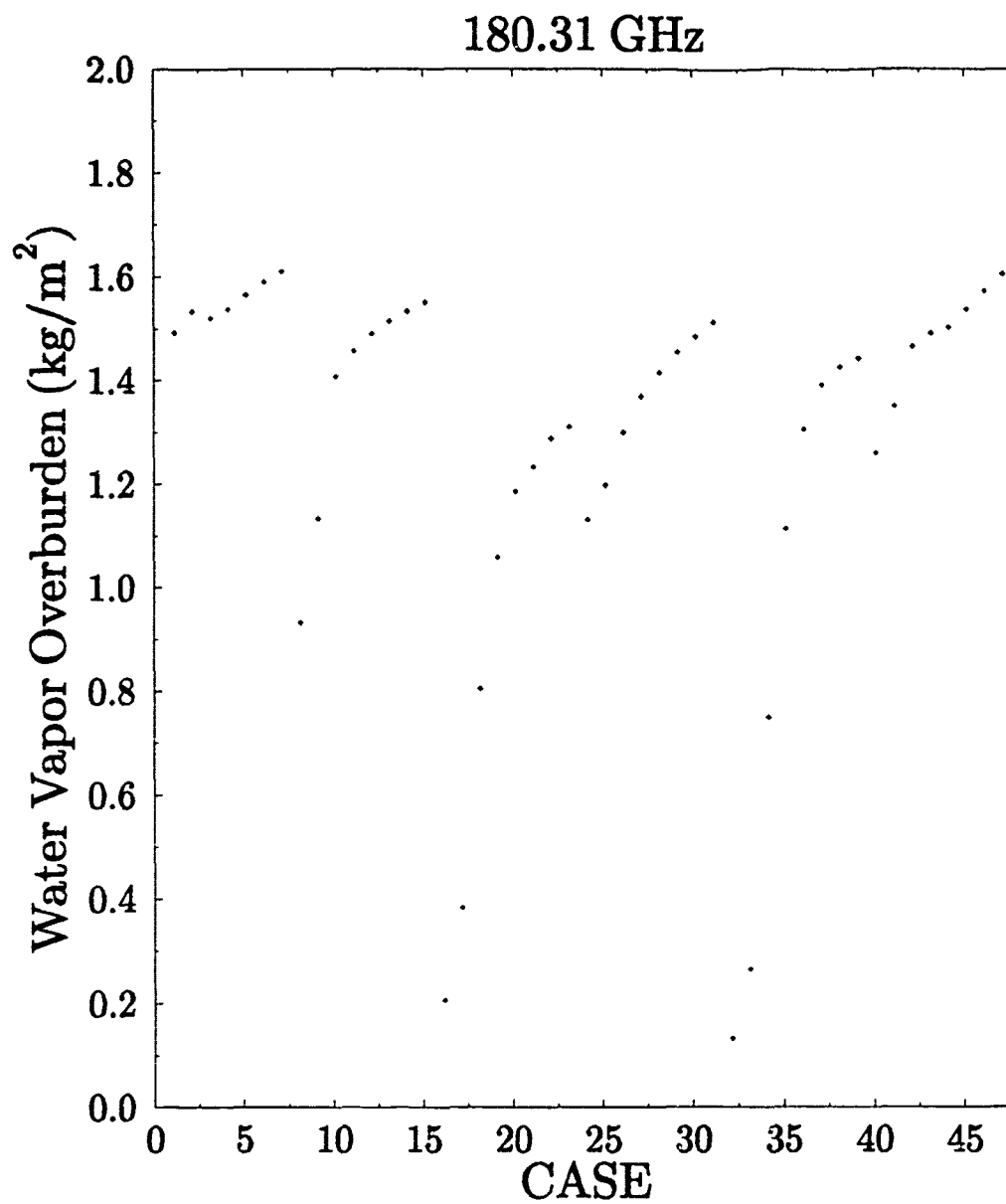


Figure 5.2: Water Vapor Overburden as in Figure 5.1 except at 180.31 GHz.

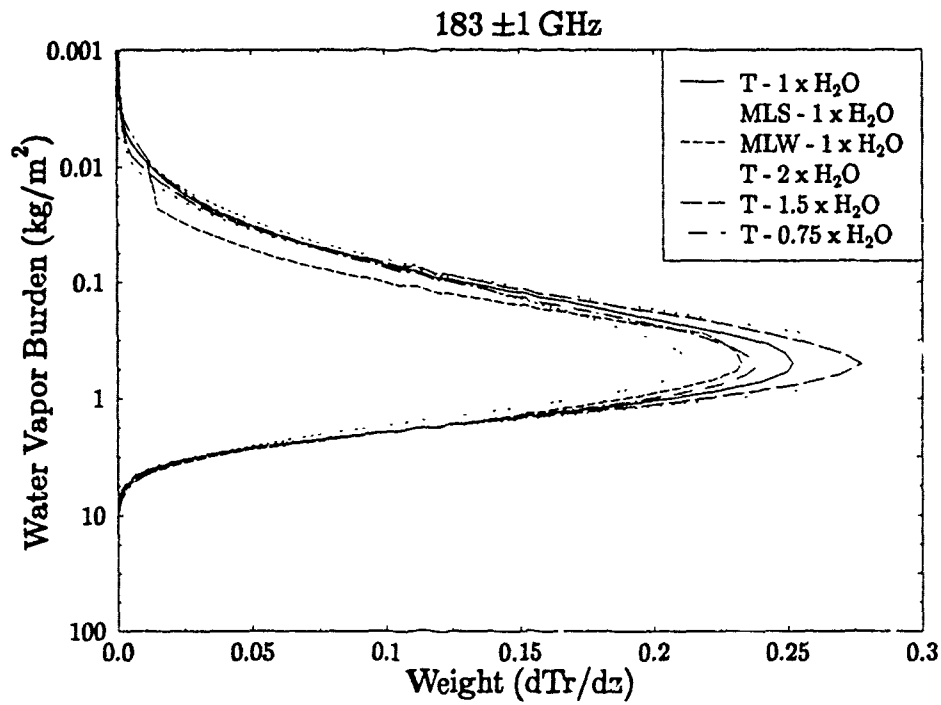


Figure 5.3: Water vapor burden for $183 \pm 1 \text{ GHz}$. Atmospheres are abbreviated as in text.

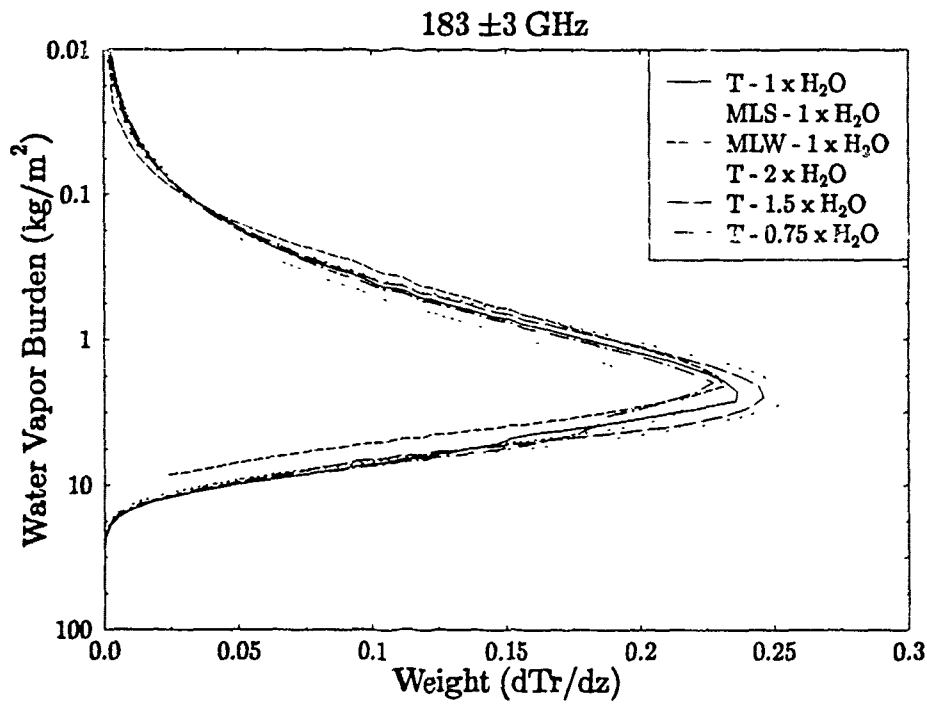


Figure 5.4: Same as in Figure 5.4 except for $183 \pm 3 \text{ GHz}$.

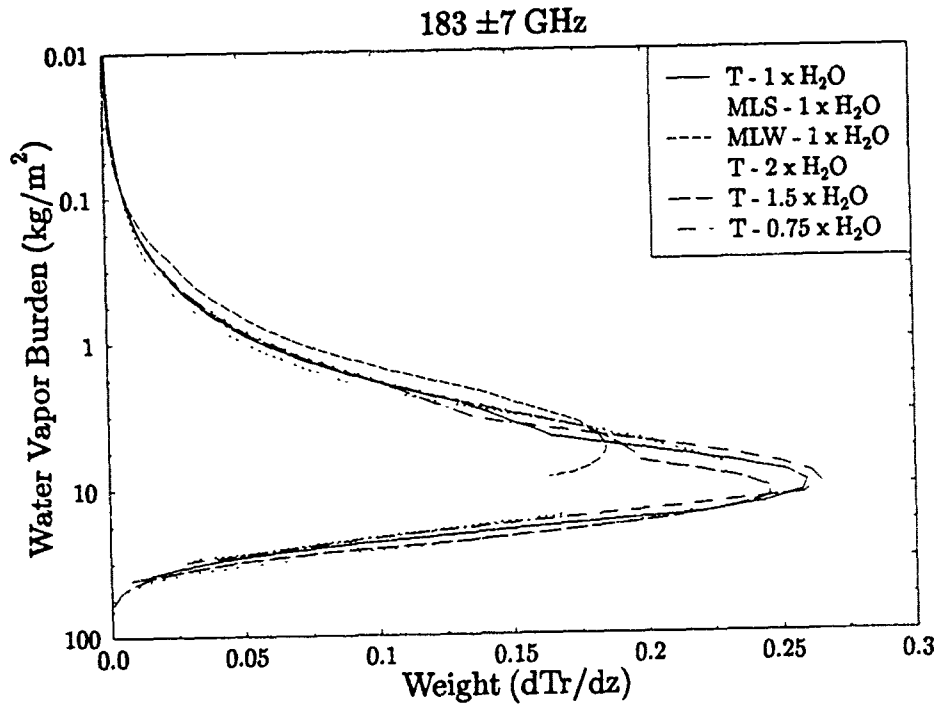


Figure 5.5: The same as Figure 5.3 except for 183.31 ± 7 GHz.

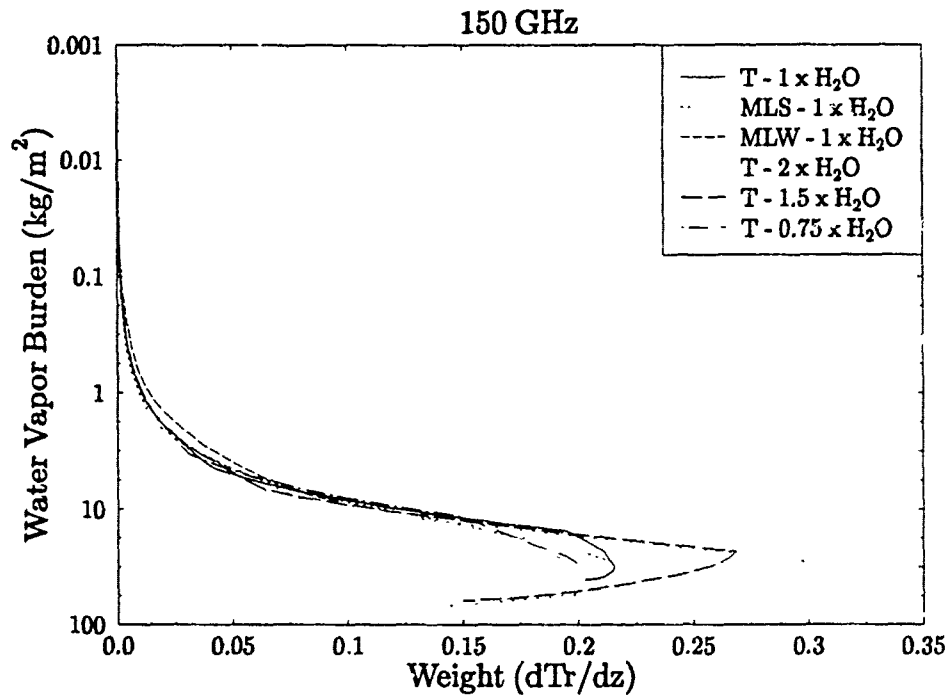


Figure 5.6: The same as Figure 5.3 except for 150 GHz.

coincident with the time of the SSM/T-2 observations was unavailable at the time of this research. The results presented here, especially in the tropics, where synoptic temperature variations are small, will not greatly alter the results presented.

The retrieval starts from the assumption that the brightness temperature and the thermometric temperature of the atmosphere are equal when the vapor burden is 0.3735 kg/m^2 (the mean value from Table 5.1). Using the temperature and pressure data of ECMWF from March 1992, the pressure p^* corresponding to the level where $T_t = T_b$ is derived by interpolation. Maps of p^* represent the contours of the constant U surface. High values of p^* correspond to dry conditions whereas low values of p^* correspond to a moist atmosphere.

A plot of the interpolated p^* derived in this way is presented in Figure 5.7. The pressure varies from high values in the mid-to-high latitudes (varying from 600-500 mb) to regions associated with deep convection in the equatorial regions that have $p^* < 300$ mb. These areas are found in North-central South America, the West Pacific and the South Pacific Convergence Zone (SPCZ), Indonesia extending west into the Indian Ocean, and portions of Central Africa. These regions may be considered to be the ascent region of the Hadley circulation which pumps water vapor from low in the atmosphere to near the tropopause. The subtropical high regions are not as distinct on this map as compared to the brightness temperature maps although some regions do show distinct maxima in p^* such as the Bay of Bengal, and in regions across the northern and southern Pacific. This also is not surprising since the upper level water vapor is carried from the equatorial region at upper levels towards the poles so this water vapor at upper levels would be expected to only drop off slowly. Pressures increase when moving away from the equator. This pressure difference between the tropics and the arctic regions is very large in the Southern Hemisphere whereas this difference is not nearly as great in the Northern Hemisphere.

After calculating this pressure at each grid point, the mean pressure, \bar{p}^* , is computed. A simple method for interpolating the water vapor information contained in Figure 5.7 to a constant pressure surface follows. This surface is selected as the mean pressure \bar{p}^* between 40° North and South latitude which for this case was 393 mb.

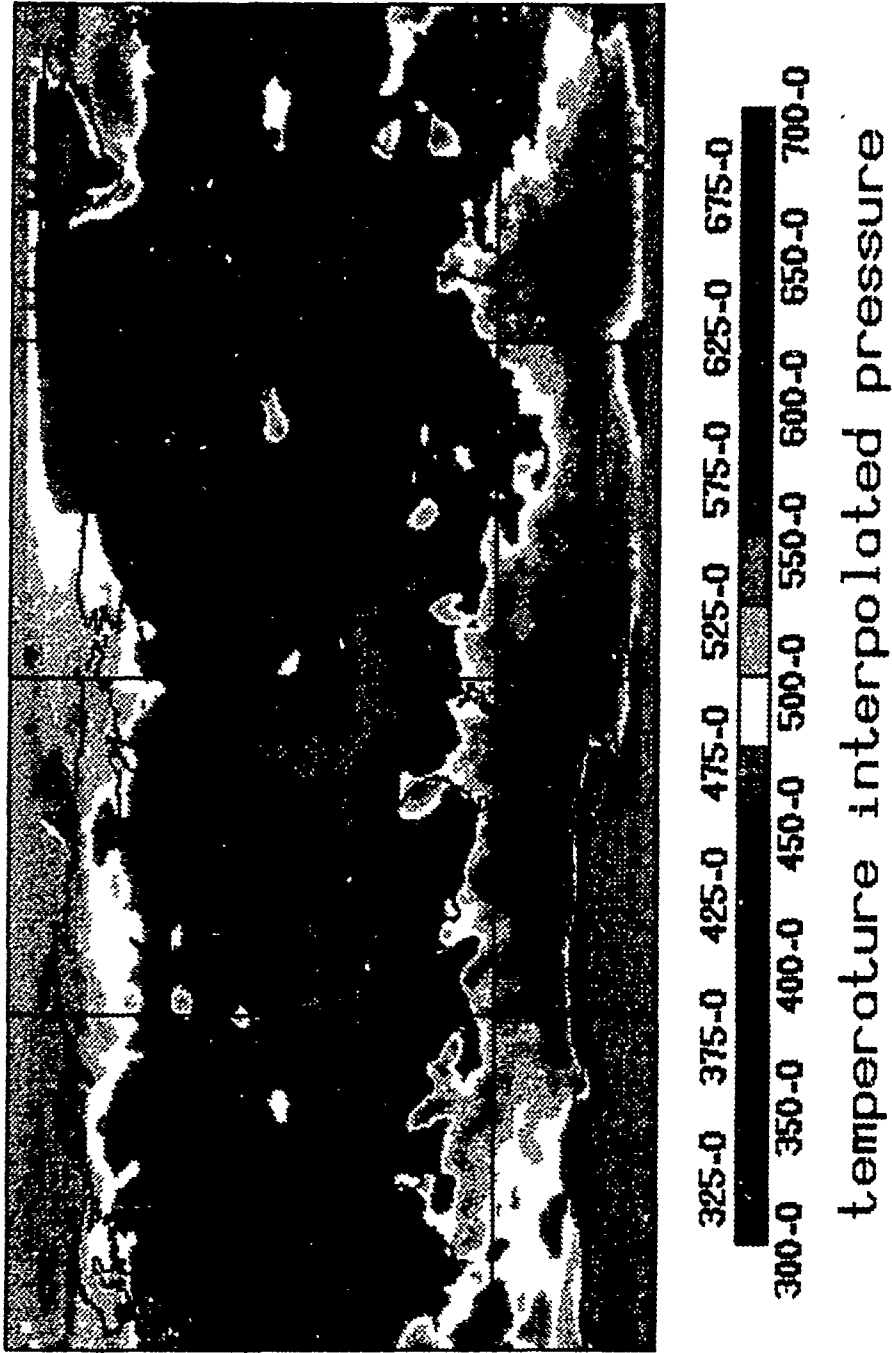


Figure 5.7: Map of pressure, p^* , where $T_i = T_b$.

The water vapor burden for Channel 2, U_2 has a value of 0.37 kg m^{-2} and may be expressed as the integral:

$$U_2 = \frac{1}{g} \int_{p^*}^0 r dp, \quad (5.2)$$

where g is the gravitational constant and r is the mixing ratio. Assuming the mixing ratio can be expressed by: $r = r_s \left(\frac{p}{p_0}\right)^\lambda$ and making the substitution $\tilde{p} = \frac{p}{p_0}$ where p_0 is the surface pressure and r_s the saturation mixing ratio, (5.2) can be rewritten as:

$$U_2 = \frac{r_s p_0}{g} \int_{\tilde{p}^*}^0 \tilde{p}^\lambda d\tilde{p}. \quad (5.3)$$

Finally, making the substitution $\tilde{p}^* = \frac{p^*}{p_0}$ and integrating results in an expression for U_2 :

$$U_2 = \frac{r_s p_0}{g(\lambda + 1)} (\tilde{p}^*)^{\lambda+1}. \quad (5.4)$$

The difference between $U(p^*)$ and $U(\tilde{p}^*)$ at each grid point is now determined and used to adjust the column overburden. This difference, ΔU can be written as (from (5.2)):

$$\Delta U = \frac{r_s p_0}{g} \int_{\tilde{p}^*}^{\tilde{p}} \tilde{p}^\lambda d\tilde{p}, \quad (5.5)$$

which, on integration, becomes:

$$\Delta U = \frac{r_s p_0}{g(\lambda + 1)} [(\tilde{p})^{\lambda+1} - (\tilde{p}^*)^{\lambda+1}] \quad (5.6)$$

On rearrangement using (5.4) for U_2 , (5.6) can be written:

$$\Delta U = \frac{U_2}{(\tilde{p}^*)^{\lambda+1}} [(\tilde{p})^{\lambda+1} - (\tilde{p}^*)^{\lambda+1}]. \quad (5.7)$$

Finally, recalling the definitions for \tilde{p} and \tilde{p}^* and rearranging results in an equation for ΔU which is added to the value of U_2 at each grid point:

$$\Delta U = U_2 \left[\left(\frac{\tilde{p}}{\tilde{p}^*} \right)^{\lambda+1} - 1 \right]. \quad (5.8)$$

Since \tilde{p}^* , the pressure onto which U is to be mapped, is given (393 mb), p^* is derived from the T-2 brightness temperature, and U_2 is known (0.37 kg/m^2), then ΔU can be readily determined and the burden $U(p^*) = U + \Delta U$ then follows. The water vapor overburden U at \tilde{p}^* were derived in this way and mapped (Figure 5.8). The water vapor

burden on the constant pressure surface is very high ($\sim 0.7\text{--}0.8 \text{ kg/m}^2$) in portions of the tropics and extremely low (below 0.2 kg/m^2) in most areas north of Antarctica. These results correlate well with the previous figure. The water vapor burden at $\sim 400 \text{ mb}$ would be expected to be larger at the tropics than towards the poles. Surprising is the magnitude of the differences between these regions.

This process is instructive when one considers that part of the operational output from the T-2 is layer water vapor, as stated in Chapter 2. Performing calculations which yield the water vapor burden on several levels means the layer water vapor mass can also be carried out in this way. Certainly the simplified approach shown above would not be used operationally but it does provide a framework to understand how, in a general sense, the layer vary in the atmosphere and may provide a valuable way of initializing more sophisticated retrieval approaches.



0.10 0.20 0.30 0.40 0.50 0.60 0.70 0.80
 0.05 0.15 0.25 0.35 0.45 0.55 0.65 0.75 0.85

SSM/T-2 Channel 2
 Water Vapor Overburden (kg/m^2)
 March 10-18, 1993

Figure 5.8: Water vapor burden on a constant pressure (393 mb) surface.

Chapter 6

CONCLUSIONS AND SUMMARY

6.1 SUMMARY

The opportunity to be among the first researchers to work with data from the SSM/T-2 Microwave Water Vapor Sounder presented a unique opportunity to examine some of the capabilities of this instrument. Since the SSM/T-2 is a new instrument, the characteristics of this instrument and the other instruments flown on the DMSP spacecraft F-11 were reviewed. The DMSP microwave suite, (SSM/I, SSM/T-1, and SSM/T-2 instruments), and the visible and infrared scanners result in a multi-spectral platform from which observations of the earth may be taken, including the first satellite platform with frequencies near the 183 GHz absorption line.

Remote sensing in the microwave regime has occurred since the 1960's. Techniques for remote sounding in the microwave region have been proposed since the 1970's but only since the launch of the SSM/T-2 has it become possible to profile the distribution of water vapor. Since this sounding approach is solved using weighting functions the properties of these functions for the SSM/T-2 frequencies are examined for a number of different circumstances.

Understanding the response of the measured SSM/T-2 brightness temperatures to a variety of factors (called sensitivity effects, herein) was achieved using a number of models, such as a model of the propagation of microwave radiation through the atmosphere, models of the meteorological state variables of the atmosphere, and simple models of the characteristics of clouds in the atmosphere. Examining how brightness temperatures respond to different atmospheric parameters provides conceptual framework necessary to understand the properties of the SSM/T-2 brightness temperatures and the weighting functions that characterize these temperatures

The T-2 data were analyzed by averaging these data in 1° latitude \times longitude bins over two time periods. Because of the small swath width, the result of discarding data from the 4 scan scenes furthest from nadir on each side, some regions are not sampled during the two time periods in March 1993 (10-14 and 16-18). The global maps of SSM/T-2 brightness temperatures derived for these two time periods were examined and related to the gross characteristics of the general circulation of the atmosphere. Additionally, some information about the surface characteristics of earth and the moisture profiles above the land surfaces are discernible from these brightness temperatures.

Comparisons of brightness temperatures from two regions of the tropical Pacific were presented. One of these regions was located within the TOGA COARE domain and is characterized by deep convection and moist conditions. The second region was over the Eastern Pacific under prevailing subsidence and thus represents conditions of drying.

The concept of the invariance of the weighting functions invariant with respect to water vapor overburden is tested. It is demonstrated that the level where Channel 2 and Channel 1 brightness temperatures match the thermodynamic temperature are levels of approximately equal overburden irrespective of the atmospheric profiles of temperature and moisture.

The pressure p^* , which corresponds to the level where the brightness temperature for Channel 2 equals the thermodynamic temperature, was derived by interpolation from temperature-pressure data. The water vapor burden, for Channel 2, U_2 , was then mapped on a constant pressure surface $\bar{p}^* = 393$ mb.

6.2 CONCLUSIONS

From the analyses of both model simulations and observations performed in this study, the following conclusions were made:

1. Weighting functions at T-2 frequencies (and therefore brightness temperatures) are strongly dependent on the profiles of water vapor. The dependence on temperature is weaker.

2. Background (surface) emissivities strongly affect brightness temperatures at 91 GHz, 150 GHz, and at 183 ± 7 GHz. Scenes characterized by backgrounds with high emissivities are scenes of high brightness temperatures.
3. Liquid water clouds profoundly affect brightness temperatures:
 - (a) Increased cloud liquid water content (LWC) decreases brightness temperatures over high emissivity backgrounds.
 - (b) Clouds generally increase brightness temperatures over low emissivity (i.e. ocean) surfaces and decrease brightness temperatures over high (i.e. land) emissivity surfaces.
4. An observational study of the T-2 brightness temperature maps results in the ability to see some characteristics of the known general circulation of the atmosphere. The subtropical regions with their associated subsidence and hence, high brightness temperatures, are striking features on the T-2 brightness temperature maps for all channels on the 183 GHz absorption line. The South Pacific Convergence Zone (SPCZ) and the Intertropical Convergence Zone (ITCZ) appear on the maps of Channels 1 and 2 which are indicative of high mid-to-upper tropospheric water vapor.
5. Surface characteristics can also be observed in the T-2 brightness temperature maps for the window channels (92 and 150 GHz). Arid land areas possess large emissivities and high brightness temperatures. All the land masses in the Southern Hemisphere appear warm in contrast to the relatively cold adjacent ocean regions.
6. Water vapor burdens are relatively constant for the two SSM/T-2 frequencies nearest the absorption line. The water vapor burden is 0.37 ± 0.02 kg/m² for Channel 2 and 1.4 ± 0.15 kg/m² for Channel 1. The pressure of the surface of constant vapor overburden, introduced here as p^* , varies from around 600 mb in high latitudes to pressures less than 300 mb in regions associated with moist convection.

7. Brightness temperatures and temperature-pressure profiles obtained from ECMWF analyses, combined with the above result, were then mapped onto a constant pressure surface. This provides a simple method for retrieving vapor overburden. The method was illustrated for a constant 393 mb pressure surface.

6.3 DISCUSSION OF FUTURE WORK

Obviously, since the SSM/T-2 represents a new microwave radiometer on a satellite there are a number of sensitivity issues which still need to be examined. The first issue that comes to mind is that both mixed phase and ice clouds are not discussed very much in the literature, except that the influence of ice clouds is negligible at the frequencies of the SSM/T-2. Mixed-phase clouds also represent a significant hurdle in the interpretation of brightness temperatures. Certainly, the ability to model this problem and quantify the effects of ice and mixed phase clouds would increase the ability to retrieve water vapor information.

A validation test of the retrieval scheme introduced here should also be undertaken. This could be accomplished using data from special intensive observation periods (e.g. TOGA COARE) where water vapor information derived from radiosonde observations could be compared with coincident T-2 data.

Improved models of the surface emissivity at the 183 GHz region are also needed. These models should address the emissivities ocean surfaces and sea ice and snow surfaces. The possibility of using the T-2 for snow cover mapping should also be investigated.

The 183 GHz region is under study by NASA in a high priority program to place a Microwave Imager and Sounder on a future geostationary satellite - the GEO-PLATFORM. A microwave sounder of this type would certainly improved the sampling capabilities for mesoscale forecasting.

I feel the immediate future (less than five years) will see an enormous amount of research along the lines of a synergistic approach/unified retrieval. The scanners and radiometers on DMSP spacecraft F-11 provide a data set which is as comprehensive as any. Certainly the SSM/I could be used for the ocean surface wind speeds and this

information could be used to help in the determination of the background emissivity over ocean surfaces for the 183 GHz channels. Additionally, the SSM/I and SSM/T-2 can be used together for column water vapor and cloud liquid water content. Here it may be possible to explore column water vapor over both land and ocean surfaces. Present SSM/I analysis of this column quantity is restricted to ocean areas only. The visible and infrared data from the OLS can be used for cloud type determination (and cloud cover) and the responses of the SSM/T-2 channels can be evaluated to improve the understanding of the effects of clouds in the 183 GHz region.

The SSM/T-2 will serve to only expand the research opportunities to those with a keen interest in water vapor and it will undoubtedly improve the ability of NWP models to forecast the state of the atmosphere. While a great deal of work remains to be done on the use of the 183 GHz absorption line for water vapor profiling, it has been an enlightening opportunity to use the T-2 data.

REFERENCES

Barath, F.T., A.H. Barrett, J. Copeland, D.E. Jones, and A.E. Lilley, 1964: Mariner 2 microwave radiometer experiments and results. *Astron. J.*, **69**, 49-58.

Bates, J.J. and G.L. Stephens, 1991: Global integrated water vapor from satellite data: preliminary results from a GVaP pilot study. Preprints *Fifth Conference on Climate Variations*, Denver, Amer. Meteor. Soc., 303-304.

Bennett, W.H., 1987: Passive microwave sounders for air temperature and water vapor profiling. *NOAA NESDIS Tech. Rep. 35*, NOAA, Wash. D.C., 157-165.

Boucher, D.J., B.H. Thomas, and A.M. Kishi, 1993: Performance of the DMSP SSM/T-2 microwave radiometer: a comparison between sensor derived, model analyzed, and radiosonde measured moisture variables. Preprints *8th Symp. on Meteorological Observations and Instrumentation*, Anaheim, CA, Amer. Meteor. Soc., J150-J152.

Curtis, J.A., and B.W. Shipley, 1987: Air Force microwave programs: status and future plans. *NOAA NESDIS Tech. Rep. 35*, NOAA, Wash. D.C., 16-20.

Eyre, J. and H. Woolf, 1988: Transmittance of atmospheric gases in the microwave region: a fast model. *Appl. Opt.*, **27**, 3244-3249.

Falcone, V.J., L.W. Abreu, and E.P. Shettle, 1979: Atmospheric attenuation of millimeter and submillimeter waves: models and computer code. *Rep. AFGL-TR-79-0253*, 79pp., Air Force Geophysics Lab., Hanscom Air Force Base, Bedford MA.

Falcone, V.J. and R.G. Isaacs, 1987: The DMSP Microwave Suite. *NOAA NESDIS Tech Rep. 35*, NOAA, Wash. D.C., 174-185.

Fleming, H.E., N.C. Grody, and E.J. Kratz, 1991: The forward problem and corrections for the SSM/T satellite microwave temperature sounder. *IEEE Trans. Geosci. Remote Sensing*, **29**, 571-583.

Gaut, N.E., M.G. Fowler, R.G. Isaacs, D.T. Chang, and E.C. Reifstein, 1975: Studies of microwave remote sensing of atmospheric parameters. *Rep. AFCRL-TR-75-0007*, 75 pp., Air Force Cambridge Res. Lab., Bedford, MA.

Griffin, M.K., V.J. Falcone, J.F. Morrissey, R.G. Isaacs, J.D. Pickle, R. Kakar, J. Wang, and P. Racette, 1993: The Special Sensor Microwave Water Vapor Sounder (SSM/T-2): calibration study. Preprints *8th Symp. on Meteorological Observations and Instrumentation*, Anaheim CA, Amer. Meteor. Soc., J144-J149.

Grody, N.C., 1983: Severe storm observations using the Microwave Sounding Unit. *J. Climate Appl. Meteor.*, **22**, 609-625.

Hillger, D.W., and T.H. Vonder Haar, 1981: Retrieval and use of high resolution moisture and stability fields from NIMBUS 6 HIRS radiances in pre-convective situations. *Mon. Wea. Rev.*, **109**, 1788-1806.

Hoffman, R.N., C. Grassotti, R.G. Isaacs, J.F. Louis, T. Nehr Korn, and D.C. Norquist, 1990: Assessment of the impact of simulated satellite lidar wind and retrieved 183 GHz water vapor observations on a global data assimilation system. *Mon. Wea. Rev.*, **118**, 2513-2542.

Hollinger, J.P., J.L. Peirce, and G.A. Poe, 1990: SSM/I Instrument Evaluation. *IEEE Trans. Geosci. Remote Sensing*, **28**, B781-789.

Houghton, J.T., G.J. Jenkins, and J.J. Ephraums, eds., 1990: *Climate Change. The IPCC Scientific Assessment*. 365 pp., Cambridge University Press, Cambridge.

Isaacs, R.G., 1987: Review of 183 GHz moisture profiler retrieval studies. *Rep. AFGL-TR-87-0127*, 52 pp., Air Force Geophysics Lab., Hanscom Air Force Base, Bedford, MA.

Isaacs, R.G., and G. Deblonde, 1985: Water vapor profile retrievals at 183 GHz: land vs. ocean and clear vs. cloudy. *Rep. AFGL-TR-85-0095*, 88 pp., Air Force Geophysics Lab., Hanscom Air Force Base, Bedford, MA.

Isaacs, R.G., G. Deblonde, R.D. Worsham and M. Livshits, 1985: Millimeter wave moisture sounder feasibility study: the effect of cloud and precipitation on moisture retrievals. *Rep. AFGL-TR-85-0040*, 60 pp., Air Force Geophysics Lab., Hanscom Air Force Base, Bedford, MA.

Isaacs, R.G., and G. Deblonde, 1987: Millimeter wave moisture sounding: the effect of clouds. *Radio Sci.*, **22**, 367-377.

Jackson, D.L., 1992: On the role of SSM/I precipitable water over the globe and tropical pacific. M.S. Thesis, Colorado State University, Ft. Collins, 112 pp.

Kakar, R.K., 1983: Retrieval of clear sky moisture profiles using the 183 GHz water vapor line. *J. Climate Appl. Meteor.*, **22**, 1282-1289.

Kakar, R.K. and B.H. Lambrigtsen, 1984: A statistical method for the retrieval of atmospheric moisture profiles by microwave radiometry. *J. Climate Appl. Meteor.*, **23**, 1110-1114.

Liebe, H.J., 1989: MPM89 - an atmospheric mm-wave propagation model. *Int. J. IR & MM Waves*, **10**, 631-650.

Liebe, H.J., T. Manabe, and G.A. Hufford, 1989: Millimeter-wave attenuation and delay rates due to fog/cloud conditions. *IEEE Trans. Antennas Propagat.*, **AP-37(12)**, 1617-1623.

Lindzen, R.S., 1990: Some coolness concerning global warming. *Bull. Amer. Meteor. Soc.*, **71**, 288-299.

Liou, K.N., P.T. Nipko, G.C. Aufderhaar, and H.Y. Yeh, 1979: Development of the microwave radiative transfer program for cloudy atmospheres: application to DMSP SSM/T channels. *Rep. AFGL-TR-80-0051*, 120pp, Air Force Geophysics Lab., Hanscom Air Force Base, Bedford MA.

Lutz, R., T.T. Wilheit, J.R. Wang, and R.K. Kakar, 1991: Retrieval of atmospheric water vapor profiles using radiometric measurements at 183 and 90 GHz. *IEEE Trans. Geosci. Remote Sensing*, **GE-29**, 602-609.

McClatchey, R.A., R.W. Fenn, J.E.A. Selby, F.E. Volz, and J.S. Garing, 1972: Optical properties of the atmosphere. *Environ. Res. Pap.* **411**, 198 pp., Air Force Cambridge Res. Lab., Bedford, MA.

Pandey, P.C., and R.K. Kakar, 1982: An empirical microwave emissivity model for a foam-covered sea. *IEEE J. Oceanic Eng.*, **OE-7(3)**, 135-140.

Peixoto, J.P., and A.H. Oort, 1983: The atmospheric branch of the hydrological cycle and climate. in *Variations on the Global Water Budget*, D. Reidel, Norwell, Mass., 5-65.

Prabhakara, C. and G. Dalu, 1980: Passive remote sensing of the water vapor in the troposphere and its meteorological significance. In *Atmospheric Water Vapor*, edited by A. Deepak, T.D. Wilkenson, and L.H. Ruhnke, Academic Press, New York, 355-374.

Prabhakara, C., H.D. Chang, and A.T.C. Chang, 1982: Remote sensing of precipitable water over the oceans from Nimbus 7 microwave measurements. *J. Appl. Meteor.*, **21**, 59-68.

Ray, P.S., 1972: Broadband complex refractive indices of ice and water. *Appl. Opt.*, **11**, 1835-1844.

Racette, P.E., L.R. Dod, J.C. Shiue, R.F. Adler, D.M. Jackson, A.J. Gasiewski, and D.S. Zacharias, 1992: Millimeter-wave imaging radiometer for cloud, precipitation, and atmospheric water vapor studies. *IGARSS-92 Proceedings*, Houston TX.

Rosenkranz, P.W., M.J. Komichak, and D.H. Staelin, 1982: A method for estimation of atmospheric water vapor profiles by microwave radiometry. *J. Appl. Meteor.*, **21**, 1364-1370.

Schaerer, G. and T.T. Wilheit, 1979: A passive microwave technique for profiling of atmospheric water vapor. *Radio Sci.*, **14**, 371-375.

Schwartz, B.E. and C.A. Doswell III, 1991: North American radiosonde observations: problems, concerns, and a call to action. *Bull. Amer. Meteor. Soc.*, **72**, 1885-1896.

Smith, W.L., H.M. Woolf, C.M. Hayden, D.Q. Wark, and L.M. McMillan, 1979: The TIROS-N Operational Vertical Sounder. *Bull. Amer. Meteor. Soc.*, **60**, 1177-1187.

Smith, W.L., 1983: The retrieval of atmospheric profiles from VAS geostationary radiance observations. *J. Atmos. Sci.*, **40**, 2025-2035.

Spencer, R.W., J.R. Christy, and N.C. Grody, 1990: Global atmospheric temperature monitoring with satellite microwave measurements: method and results. *J. Clim.*, **3**, 111-128.

Staelin, D.H., K.F. Kunzi, R.L. Pettyjohn, R.K.L. Poon, R.W. Wilcox, and J.W. Walters, 1976: Remote sensing of atmospheric water vapor and liquid water with the Nimbus-5 microwave spectrometer. *J. Appl. Meteor.*, **15**, 1204-1214.

Stephens, G.L., and S. A. Tjemkes, 1992: Water vapour and its role in the earth's greenhouse. *Aust. J. Phys.*, submitted.

Stephens, G.L., 1993: *The Remote Sensing of the Lower Atmosphere: An Introduction*, Oxford, Oxford University Press, in press.

Twomey, S., 1977: *Introduction to the mathematics of inversion in remote sensing and indirect measurements*. 243 pp., Elsevier Scientific Publishing Company, Amsterdam.

Wang, J.R., and T.J. Schmugge, 1980: An empirical model for the complex dielectric permittivity of soils as a function of water content. *IEEE Trans. Geosci. Remote Sens.*, **GE-18**, 288-295.

Wang, J.R., J.L. King, T.T. Wilheit, G. Szejwach, L.H. Gessell, R.A. Nieman, D.S. Niver, B.M. Krupp, and J.A. Gagliano, 1983: Profiling atmospheric water vapor by microwave radiometry. *J. Climate Appl. Meteor.*, **24**, 779-788.

Wang, J.R., W.C. Boncyk, L.R. Dod, and A.K. Sharma, 1992: Retrieval of total precipitable water over high latitude regions using radiometric measurements near 90 and 183 GHz. *J. Appl. Meteor.*, **31**, 1368-1378.

Waters, J.W., 1976: Absorption and emission by atmospheric gases, in *Methods of Experimental Physics*, **12**, Academic, New York, pp. 142-176.

Wilheit, T.T., 1979: A model for the microwave emissivity of the ocean's surface as a function of wind speed. *IEEE Trans. Geosci. Electron.*, **GE-17**, 244-249.

Wilheit, T.T., 1990: An algorithm for retrieving water vapor profiles in clear and cloudy atmospheres from 183 GHz radiometric measurements: simulation studies. *J. Appl. Meteor.*, **29**, 508-515.

Wilheit, T.T., and A. al Khalaf, 1993: A simplified interpretation of the radiances from the SSM/T-2. *Meteorology and Atmospheric Physics*, submitted.

Wittmeyer, I.L., 1990: Satellite based estimates of global precipitable water and poleward latent heat transport. M.S. Thesis, Colorado State University, Ft. Collins, 76 pp.

Wittmeyer, I.L. and T.H. Vonder Haar, 1993: Analysis of the global ISCCO TOVS water vapor climatology. *J. Climate*, accepted.

THESIS

**AN ANALYSIS OF SIMULATED AND ACTUAL DMSP SSM/T-2 BRIGHTNESS
TEMPERATURES**

Submitted by

FRANK A. LEUTE IV

Department of Atmospheric Science

In partial fulfillment of the requirements

for the degree of Master of Science

Colorado State University

Fort Collins, Colorado

Summer, 1993

COLORADO STATE UNIVERSITY


May 13, 1993

WE HEREBY RECOMMEND THAT THE THESIS PREPARED UNDER OUR SUPERVISION BY FRANK A. LEUTE IV ENTITLED AN ANALYSIS OF SIMULATED AND ACTUAL DMSP SSM/T-2 BRIGHTNESS TEMPERATURES BE ACCEPTED AS FULFILLING IN PART REQUIREMENTS FOR THE DEGREE OF MASTER OF SCIENCE.

Committee on Graduate Work

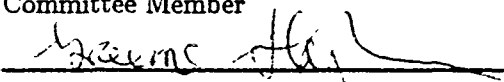


Committee Member

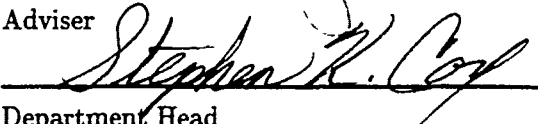


Committee Member

Committee Member



Adviser



Department Head

ABSTRACT OF THESIS

AN ANALYSIS OF SIMULATED AND ACTUAL DMSP SSM/T-2 BRIGHTNESS TEMPERATURES

Defense Meteorological Satellite Program (DMSP) Special Sensor Microwave/T-2 (SSM/T-2 or T-2) global brightness temperature maps are related to some of the known observed general circulation features of the atmosphere and surface characteristics of Earth. The brightness temperatures from two regions with different large scale circulations are compared and contrasted.

The concept of the invariance of the weighting functions with respect to water vapor overburden is tested. It is demonstrated that the levels where the 183 ± 1 and 3 GHz brightness temperatures match the thermodynamic temperature are levels of approximately equal overburden. Water vapor overburden (integrated water vapor above a given level) was retrieved and mapped on a constant pressure surface from T-2 brightness temperatures and atmospheric temperature-pressure data. A simple physical retrieval scheme based on the approximately equal overburden, irrespective of the moisture profile, for the 183 ± 1 GHz frequency was developed and demonstrated. This simple retrieval could be used to initialize more sophisticated retrievals.

Simulation studies of some factors which affect brightness temperatures at the SSM/T-2 frequencies were conducted and the results discussed. These factors included moisture profiles, backgrounds with different emissivities, and low level water clouds.

FRANK A. LEUTE IV
Department of Atmospheric Science
Colorado State University
Fort Collins, Colorado 80523
Summer, 1993

ACKNOWLEDGEMENTS

I would like to thank my advisor, Dr. Graeme Stephens, for his assistance, guidance, and most especially his patience over the last two years. I would like to extend my gratitude to Dr. Thomas Vonder Haar and Dr. V. Chandrasekar for their evaluation of this thesis.

I extend my sincere gratitude to Mr. Bruce Thomas of Aerospace Corporation, Omaha, for providing the SSM/T-2 data used in this thesis. I would like to thank Col. Carl Bjerkaas, Mr. Vincent Falcone, and Capt. Don Rhudy for obtaining the release of the SSM/T-2 data from Aerospace. I extend a heartfelt thank you to Ian Wittmeyer for his invaluable programming and plotting assistance. I could not have finished this study without the assistance of Tim Schneider, Darren Jackson, Frank Evans, Tak Wong and Tom Greenwald. They provided me technical assistance with computer operations and data acquisition. I thank Sue Lini and Heather Jensen for their administrative assistance.

I conclude by thanking my wife, Tara, for her love, encouragement, support, and understanding.

Aspects of this work were supported by NOAA Grant NA90AA-D-AC822, NOAA Grant NA90 RAH 00077, and NASA grant NAG8-876.

CONTENTS

1 INTRODUCTION	1
1.1 BACKGROUND	1
1.2 MICROWAVE/MILLIMETER WAVE SATELLITE RETRIEVALS	4
1.3 USE OF THE 183 GHz ABSORPTION LINE	6
1.4 MOTIVATION, OBJECTIVES, AND THESIS OUTLINE	8
1.4.1 Motivation	8
1.4.2 Objectives	8
1.4.3 Thesis Outline	8
2 THE DMSP SSM/T-2 AND T-1 INSTRUMENTS AND DATA ANALYSIS	10
2.1 DMSP Block 5D Satellite Characteristics	10
2.1.1 SSM/T-2 Channel Characteristics	11
2.1.2 T-2 Output Parameters	13
2.1.3 SSM/T-1 Channel Characteristics	13
2.1.4 SSM/T-2 and T-1 Scan Patterns	14
2.2 SSM/T-2 DATA	15
2.3 T-2 BRIGHTNESS TEMPERATURE MAPS	15
2.3.1 Channel 1 Brightness Temperature Maps	17
2.3.2 Channel 2 Brightness Temperature Maps	18
2.3.3 Channel 3 Brightness Temperature Maps	18
2.3.4 Channel 4 Brightness Temperature Maps	18
2.3.5 Channel 5 Brightness Temperature Maps	19
2.4 CHANNEL COHERENCE	20
3 MICROWAVE RADIATIVE TRANSFER AND WEIGHTING FUNCTIONS	38
3.1 THE RADIATIVE TRANSFER EQUATION FOR MICROWAVE REMOTE SENSING	39
3.1.1 Brightness Temperatures	39
3.2 WEIGHTING FUNCTIONS	42
3.2.1 Relative Humidity-based Weighting Functions	42
3.2.2 Transmission-based Weighting Functions	43
3.3 ATMOSPHERIC PROFILES, PROPAGATION MODEL, AND CLOUD MODELS	44
3.3.1 Atmospheric Profiles	46
3.3.2 The Propagation Model	46
3.3.3 Cloud Models	47

4 SENSITIVITY EFFECTS FOR THE DMSP SSM/T-2	48
4.1 DEPENDENCE ON MOISTURE PROFILES	48
4.2 DEPENDENCE ON BACKGROUND	54
4.2.1 Ocean Background	54
4.2.2 Land Background	59
4.3 DEPENDENCE ON CLOUDS	60
4.3.1 Dependence on Layer Thickness	66
4.3.2 Dependence on Layer Location	66
4.3.3 Dependence on Cloud Liquid Water Content	66
4.4 SCAN ANGLE EFFECTS	73
4.5 INTERPRETATION OF RESULTS	73
5 WATER VAPOR BURDEN	76
5.1 WATER VAPOR BURDEN AND THE SSM/T-2 FREQUENCIES	76
5.2 CHANNEL 2 WATER VAPOR BURDEN MAP	79
6 CONCLUSIONS AND SUMMARY	90
6.1 SUMMARY	90
6.2 CONCLUSIONS	91
6.3 DISCUSSION OF FUTURE WORK	93

LIST OF FIGURES

1.1	Hypotheses on water vapor feedback mechanisms (Stephens, personal communication). The left portion of the diagram is the feedback as presently perceived, with increasing temperature leading to increased water vapor largely in the boundary layer. The right portion of the diagram is the additional modification to the feedback by increasing the upper tropospheric moisture through convection.	3
2.1	Footprint patterns for the SSM/T-2 and SSM/T-1 (D. Khady, personal communication).	16
2.2	Channel 1 brightness temperature map for 10-14 March 1993.	21
2.3	Channel 1 brightness temperature map for 16-18 March 1993.	22
2.4	Channel 2 brightness temperature map for 10-14 March 1993.	23
2.5	Channel 2 brightness temperature map for 16-18 March 1993.	24
2.6	Channel 3 brightness temperature map for 10-14 March 1993.	25
2.7	Channel 3 brightness temperature map for 16-18 March 1993.	26
2.8	Channel 4 brightness temperature map for 10-14 March 1993.	27
2.9	Channel 4 brightness temperature map for 16-18 March 1993.	28
2.10	Channel 5 brightness temperature map for 10-14 March 1993.	29
2.11	Channel 5 brightness temperature map for 16-18 March 1993.	30
2.12	Channel 5 versus Channel 4 brightness temperatures for the two Pacific areas.	32
2.13	Channel 5 versus Channel 3 brightness temperatures for the two Pacific areas.	33
2.14	Same as Figure 2.12 except Channel 5 vs. Channel 1.	34
2.15	Channel 4 versus Channel 2 brightness temperatures for the two Pacific areas.	35
2.16	Same as Figure 2.12 except Channel 4 vs. Channel 1.	37
3.1	Brightness temperature spectra from 1-200 GHz for cases (1) tropical atmosphere with no water vapor and reflectivity (R) = 0.3; (2) tropical atmosphere ($CWV = 41.2\text{g/m}^2$) and $R = 0.3$; (3) tropical atmosphere with a cloud ($LWC = 0.5\text{g/m}^2$) from 1-2 km and $R = 0.3$ and case (4) same as case (2) except $R = 0.0$. The locations of the SSM/I and SSM/T-2 channels are indicated by "1" and "2", respectively.	40
3.2	Clear sky weighting functions for the SSM/T-1 channels 1-4 for a tropical atmosphere, reflectivity = 0.03, and a column water vapor (CWV) = 41.2 kg/m^2	45
4.1	Clear sky weighting functions for the SSM/T-2 channels for a tropical atmosphere over an ocean background with a reflectivity factor of 0.3 and a thermometric temperature of 300 K.	50
4.2	The same as Figure 4.1 except for a midlatitude summer atmosphere.	51
4.3	The same as Figure 4.1 except for a midlatitude winter atmosphere.	52

4.4	The same as Figure 4.2 except with $2 \times$ water vapor profile.	53
4.5	Clear sky transmission for the tropical atmosphere.	55
4.6	Clear sky transmission for the midlatitude atmosphere.	56
4.7	Clear sky transmission for the midlatitude winter atmosphere.	57
4.8	Weighting functions as in Figure 4.1 except for stratus cloud ($w = 0.15 \text{ gm}^{-3}$) from 0.5-2.0 km (cloud model 1).	61
4.9	The same as Figure 4.8 except for cumulus cloud ($w = 1.0 \text{ gm}^{-3}$) from 1.0-3.5 km (cloud model 2).	62
4.10	The same as Figure 4.8 except for altostratus cloud ($w = 0.40 \text{ gm}^{-3}$) from 2.5-3.0 km (cloud model 3).	63
4.11	The same as Figure 4.8 except for stratocumulus cloud ($w = 0.55 \text{ gm}^{-3}$) from 0.5-1.0 km (cloud model 4).	64
4.12	The same as Figure 4.8 except for nimbostratus cloud ($w = 0.61 \text{ gm}^{-3}$) from 0.5-2.5 km (cloud model 5).	65
4.13	Brightness temperatures for Cloud Model 1 and a tropical atmosphere with LWC from 0.01 to 0.50 gm^{-3}	69
4.14	Brightness temperatures as in Figure 4.13 except for Cloud Model 2.	70
4.15	Brightness temperatures as in Figure 4.13 except for Cloud Model 3.	71
4.16	Brightness temperatures as in Figure 4.15 except for $R = 0.0$	72
4.17	Brightness temperatures as a function of observation angle for a tropical at- mosphere.	74
4.18	The same as Figure 4.17 except for a midlatitude summer atmosphere and T_{sfc} $= 285 \text{ K}$	74
5.1	Water Vapor Overburdens at $183.31 \pm 1 \text{ GHz}$ for 47 Atmospheric Cases.	81
5.2	Water Vapor Overburden as in Figure 5.1 except at 180.31 GHz	82
5.3	Water vapor burden for $183 \pm 1 \text{ GHz}$. Atmospheres are abbreviated as in text.	83
5.4	Same as in Figure 5.4 except for $183 \pm 3 \text{ GHz}$	83
5.5	The same as Figure 5.3 except for $183.31 \pm 7 \text{ GHz}$	84
5.6	The same as Figure 5.3 except for 150 GHz	84
5.7	Map of pressure, p^* , where $T_t = T_b$	86
5.8	Water vapor burden on a constant pressure (393 mb) surface.	89

LIST OF TABLES

2.1	SSM/T-2 Channel Characteristics (after Griffin <i>et al.</i> , 1993).	12
2.2	SSM/T-1 Channel Characteristics.	14
3.1	Cloud Type Characteristics (after Isaacs and Deblonde, 1987)	47
4.1	Brightness temperatures (K) for emissivities from 0.82 to 0.66 (reflectivities from 0.34 to 0.18) for a midlatitude winter atmosphere.	58
4.2	Comparison of brightness temperatures for land ($\epsilon = 1.0$) and ocean ($\epsilon = 0.7$) surfaces.	67
4.3	Brightness temperatures for variable cloud thickness (Δz (km)) and LWC (gm^{-3}) for a fixed cloud base (1 km), emissivity (0.97), and a tropical atmosphere.	67
4.4	Brightness temperatures for variable cloud base and LWC for a fixed emissivity ($\epsilon = 1.0$) and atmosphere (tropical).	68
5.1	Water Vapor Overburdens (U) at 183.31 ± 1 GHz for $T_b = T_t$	78
5.2	Water Vapor Overburden (U) at 183.31 ± 3 GHz for $T_b = T_t$	80

Chapter 1

INTRODUCTION

1.1 BACKGROUND

Water vapor plays a vital role in establishing our present-day climate. It is the most significant contributor to the observed greenhouse effect of the planet (Stephens and Tjemkes, 1992). Water vapor links the processes of evaporation, cloud formation, and precipitation. Latent heat release plays a large role in the dynamical flow fields of the tropical atmosphere and knowledge of the distribution, transport, and divergence of water in all phases is critical to work pertaining to the difficult problem of cloud feedback and its role in climate change (Stephens, personal communication).

The source of water vapor is primarily at the earth's surface whereas its sink is in the process of precipitation. Combining these sources and sinks with the atmospheric circulation means the distribution of water vapor in the atmosphere is highly variable both in spatial and temporal scales (Prabhakara and Dalu, 1980). Thus, it is necessary to establish a dense network for observing water vapor and its distribution. Present day observations are largely based in the use of radiosonde data and these data lack in the necessary global coverage needed for understanding the role of water vapor in climate.

Water vapor also affects the exchange of radiation between the atmosphere and space directly by its influence in atmospheric emission and indirectly by its role in cloud formation processes (Bates and Stephens, 1991). GEWEX (the Global Energy and Water Cycle Experiment, part of the World Climate Research Program) has the basic theme of developing a quantitative understanding of how water shapes the energy budget of the climate system of earth. The connections and relationships between the global hydrological cycle and the energy budget are critical to the question (and potential problem) of climate

change (Stephens and Tjemkes, 1992). The typical climate change scenario ($2 \times \text{CO}_2$) predicts a global warming of approximately twice (or treble, depending on the model) the CO_2 -induced warming with water vapor feedback than without this feedback (Houghton *et al.*, 1990). The first part of the water vapor feedback is due to the direct greenhouse effects of doubled CO_2 which directly leads to increased sea surface temperature (SST). The increased SST increases evaporation in the boundary layer which increases humidity in the boundary layer. The increase of water vapor in the boundary layer through its greenhouse effect increases the SST. The second part of the feedback process was hypothesized by Lindzen (1990). Water vapor feedback is also thought to be modulated by the changes in the vertical distribution of water vapor. Lindzen argues that the increased warming near the ground results in increased and deeper cumulus convection. This increased cumulus convection, he claims, leads to drying of the upper troposphere (above 5 km) and elevation of the altitude at which convected heat is deposited. Since greenhouse absorption is most important above 5 km these cumulus effects are negative and hence, should diminish the effect of CO_2 warming. In contrast to this view, present day climate models actually produce a moistening of the upper troposphere associated with this convection. Both hypotheses are depicted in Figure 1.1 (Stephens, personal communication). Attempts to study quantitatively the distribution and transport of water vapor in the atmosphere have been made using the global radiosonde network (e.g. Peixoto and Oort, 1983). Unfortunately, these studies have met limited success since these radiosonde observations are confined mainly to land areas since this is where the radiosonde stations are primarily located. Important atmospheric phenomenon restricted to oceanic areas are thus largely ignored (e.g. many aspects of El Niño, including westerly wind bursts and the location of moisture convergence/divergence). Early work on transports based on infrared (IR) water vapor data have been reported by Wittmeyer (1990). However, Wittmeyer and Vonder Haar (1993) and others report serious adverse cloud impacts in baroclinic zones. Schwartz and Doswell (1991) contend that more observations are essential in both time and space to improve mesoscale weather forecasting and further, that remote sensing systems have yet to approach the radiosonde's capability to resolve the vertical thermodynamic structure of the atmosphere. While the later may or may not remain true in the age

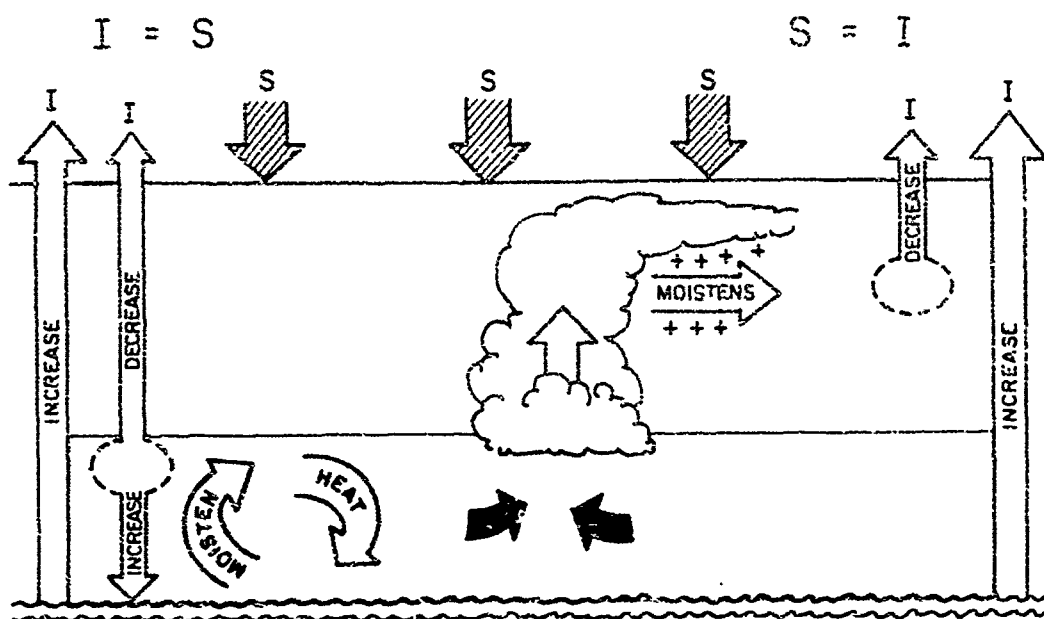


Figure 1.1: Hypotheses on water vapor feedback mechanisms (Stephens, personal communication). The left portion of the diagram is the feedback as presently perceived, with increasing temperature leading to increased water vapor largely in the boundary layer. The right portion of the diagram is the additional modification to the feedback by increasing the upper tropospheric moisture through convection.

of new microwave (millimeter wave) instruments, the former may be improved drastically by these new remote sensing systems. Certainly, the future lies, in many respects, in the advancement of the capabilities of remote sensing and the application of these capabilities to the measurement of atmospheric phenomena.

Satellites are used for many applications of remote sensing. The theory and practice of remote sensing spans many disciplines and is intimately related to inversion theory (see Twomey, 1977). The deployment of satellites expanded the opportunities for deriving the distribution of water vapor over the entire globe (as opposed to the limitations with land- and ship-based radiosondes). Moreover, many of the satellites launched in the 1970s and 1980s were restricted to measurements of the total precipitable water. The launch of the Special Sensor Microwave/Water Vapor Sounder (SSM/T-2 or T-2 which is described in more detail in the next chapter) heralds a new era in water vapor studies with its apparent capability of profiling atmospheric water vapor although not with the vertical resolution of current radiosondes.

Observing system simulation experiments (OSSEs) were carried out by Hoffman *et al.* (1990) to attempt to determine the impact of the Special Sensor Microwave/Temperature (SSM/T) sensors, in addition to other sensors. In these experiments the addition of the SSM/T-2 and SSM/T-1 data improves moisture analysis, especially in the tropics and the extratropics of the Southern Hemisphere. Root mean square (RMS) errors for relative humidity forecasts were decreased from 29% to 22% in the OSSEs with the SSM/T-2 data included. In the Southern Hemisphere, the SSM data improved the 500 hPa height forecasts by 12 hours.

1.2 MICROWAVE/MILLIMETER WAVE SATELLITE RETRIEVALS

The potential benefits of using passive microwave sensors to measure atmospheric parameters was first recognized in the 1940's. Nonetheless, it was only during the early 1960's when the first microwave radiometer was used on a spacecraft for the purpose of atmospheric remote sensing. The U.S. Mariner 2 Venus Probe in 1962 took the first satellite microwave emission observations of a planetary atmosphere. The two-channel

radiometer determined an upper limit on water vapor in Venus' atmosphere and retrieved a planetary surface temperature near 600°K (Barath *et al.*, 1964). The first U.S. satellite to make microwave observations of the earth's atmosphere was Nimbus 5 in 1972.

Microwave temperature retrieval on satellites operated by National Oceanic and Atmospheric Administration (NOAA) began with the Nimbus 5 (Nimbus E) Satellite Microwave Spectrometer and continued with the Nimbus 6 Scanning Microwave Spectrometer (SCAMS). The SCAMS used three channels (52.85 GHz, 53.85 GHz, and 55.45 GHz) in the oxygen absorption band between 50 and 60 GHz. The follow-on to the SCAMS is the Microwave Sounding Unit (MSU). It serves as a complement to the infrared temperature sounding unit called the High Resolution Infrared Sounder 2 (HIRS/2). The MSU has four channels (50.30 GHz, 53.74 GHz, 54.96 GHz, and 57.95 GHz) in the oxygen absorption band. The MSU is a 'Dicke' radiometer where the output of the receiver is proportional to the difference between the brightness temperature of the scene being viewed and the temperature of the internal radiation source. The primary purpose of the MSU is to make temperature soundings in the presence of clouds although MSU brightness temperature data are also currently being analyzed to understand certain aspects of the Earth's climate (Spencer *et al.*, 1990).

Water vapor retrieval from satellites occurs primarily in two regions of the electromagnetic spectrum, the infrared and microwave/millimeter wave regions. The HIRS/2 component of the polar orbiting TIROS-N operational vertical sounder (TOVS) (Smith *et al.*, 1979; Hillger and Vonder Haar, 1981) and the VISSR atmospheric sounder (VAS) on Geostationary Operational Environmental Satellites (GOES) (Smith, 1983) are examples of infrared instruments. These instruments use the absorption in the 6.7 μm infrared vibration band. They have had limited success in obtaining operationally useful water vapor profiles, in part because of the limitation of all infrared sensors that moisture sounding is impossible at levels below cloud top.

The appeal of microwave/millimeter wave sounding is that temperature retrievals suffer limited, if any, degradation due to the presence of clouds. For years the concept of using microwave remote sensing for water vapor retrieval was discussed. The first

efforts focused on the use of the weak H_2O rotational line at 22.235 GHz for sensing total precipitable water. The Nimbus 5 (Nimbus E) Satellite Microwave Spectrometer (NEMS) used channels at 22.235 and 31.4 GHz to measure atmospheric water vapor and liquid water over the oceans, even in the presence of many types of clouds. NEMS also measured the atmospheric temperature profile (as mentioned above) from 0-20 km (Staelin *et al.*, 1976).

Millimeter wavelengths also possess the advantage of low emissivity values for the ocean surface versus infrared wavelengths. The low emissivity values provide a relatively cold background that provides enough contrast to allow the retrieval of low level moisture fields (Hoffman *et al.*, 1990). The accuracy of these low level retrieved values decreases with high surface wind speeds due to the formation of foam on the ocean surface. This foam causes the emissivity of the ocean to increase, thus effectively reducing the contrast of this background surface. Additionally, millimeter wavelengths are able to sense through clouds so we can measure water vapor in the atmosphere below the clouds.

The Special Sensor Microwave/Imager (SSM/I) which has been carried on DMSP satellites since 1987 is also used to retrieve precipitable water. Jackson (1992) presents a review of several of the methods used for retrieval of precipitable water with the SSM/I. The SSM/I also makes use of the water vapor line at 22.235 GHz.

1.3 USE OF THE 183 GHz ABSORPTION LINE

The water vapor rotation absorption line feature at 183.31 GHz is about 20 times stronger than the rotation feature at 22.235 GHz (Waters, 1976). For this reason some researchers have discussed, in both abstract and definitive terms, its potential use to profile atmospheric water vapor since the 1970's.

Gaut *et al.* (1975) performed a study of a variety of microwave remote sensing systems to satisfy Air Force meteorological data requirements. The simulation and retrieval exercises investigated the following parameters: (a) total integrated water vapor, (b) the vertical distribution of water vapor, (c) temperature profile, and (d) the integrated and vertical distribution of cloud liquid water. While emphasizing channels below 60 GHz,

higher frequency channels (including those in the vicinity of 183 GHz) were also evaluated. The higher frequency channels were explored because: (a) it was desired to remove the effects of variable surface emissivity over land at the lower frequencies used to obtain water vapor information, (b) it was hypothesized that the higher frequency channels could provide information on cloud vertical structure, and (c) higher frequency channels were expected to be more sensitive to the integrated water vapor of clouds with relatively small liquid water content (Isaacs, 1987).

The pioneering work in the theory of using the 183 GHz rotation line for atmospheric remote sensing was written by Schaerer and Wilheit (1979). Several authors (Kakar, 1983; Kakar and Lambrechtsen, 1984; and Rosenkranz *et al.*, 1982) have since discussed various methods for the retrieval of clear sky atmospheric moisture profiles using channels around the 183 GHz line.

Subsequently, the theory has been extended to include clouds in the instrument field of view (FOV). Isaacs and Deblonde (1987) examined some of the effects of beam-filling liquid water clouds on millimeter wave moisture retrievals. They compared retrieved soundings with radiosondes from clear sky and cloudy conditions in simulation studies. Wilheit (1990) performed similar simulation studies expanding on the work he did previously with Schaerer. Both of these simulation studies were limited by the constraint of only one cloud layer.

Wang *et al.* (1983) showed experimentally that the 183 GHz line could be used for profiling atmospheric water vapor. They used an instrument, the Advanced Microwave Moisture Sounder (AMMS), from an airborne platform and this work was for clear sky cases. Lutz *et al.* (1991) used the algorithm developed by Wilheit for profiling atmospheric water vapor even in the presence of clouds. This work again used measurements from the AMMS. They showed the retrieved profiles were in general agreement with those from radiosonde data. Lutz *et al.* also noted that the algorithm did not perform very well in the vicinity of surface fronts. With the concept proven by these aircraft studies the next step was to put a moisture sounder on a satellite.

1.4 MOTIVATION, OBJECTIVES, AND THESIS OUTLINE

1.4.1 Motivation

The attraction for working with SSM/T-2 data is the opportunity to work data from the newest microwave instrument, also the first with frequencies near 183 GHz, on an Air Force meteorological satellite. The work on data from this instrument has barely begun and the ability to learn about some of the capabilities of the SSM/T-2 is a special opportunity. The ability to retrieve moisture soundings over the entire globe regularly is also appealing to the needs of GEWEX and other major global climate research programs. The T-2 will also help improve the output of numerical weather prediction models. Additionally, during the testing of the capabilities of an instrument a researcher may also learn of its limitations, whether they be inherent or due to the advancement of the science.

1.4.2 Objectives

This thesis attempts to achieve the following objectives:

1. Develop an understanding of many of the sensitivity factors which affect the microwave brightness temperatures, specifically for the SSM/T-2 frequencies.
2. Relate T-2 brightness temperature features to characteristics of the general circulation of the atmosphere and characteristics of the earth's surface.
3. Develop a simple physical retrieval of columnar water vapor which may be used to assist in the interpretation of the T-2 data and which may be used in initializations of more complex schemes. This retrieval scheme assumes the thermodynamic temperature and brightness temperature are equal at a level of approximately equal water vapor overburden (column water vapor above this level) irrespective of the temperature and moisture profiles.

1.4.3 Thesis Outline

Chapter 2 overviews the characteristics of the satellites which carry the SSM/T-2 and the characteristics of the instruments flown on these satellites. Chapter 2 also presents

brightness temperature maps for two T-2 data periods and an analysis of these data is presented. Chapter 2 concludes with scatter plots of brightness temperatures from two regions which demonstrate distinctly different temperature and moisture properties. Chapter 3 develops the radiative transfer equation as it applies to microwave remote sensing. It continues with a discussion of retrievals, first temperature (briefly) and then water vapor and introduces the concepts of weighting functions. Chapter 3 concludes with a description of various models (atmospheric propagation, atmospheric temperature/pressure, and cloud) used in the simulations discussed in this work. Chapter 4 analyzes the response of the DMSP SSM/T-2 channels to a variety of factors (what is called the forward problem) including: the profile of atmospheric moisture, the presence of clouds, the characteristics of clouds, and the background against which the atmosphere is viewed. The analysis of cloud effects here is limited only to low level water clouds. The possible effects of ice scattering at 183 GHz is not considered in this study although it may be important under some circumstances. Chapter 5 introduces the concept of water vapor burden and through the use of figures and tables, it is shown that the vapor burden is (nearly) constant at a given frequency near the 183 GHz absorption line and is only slightly dependent on the moisture and temperature profile. The water vapor burden is mapped onto a constant pressure surface thus providing the water vapor burden above this surface. Chapter 6 presents conclusions based on the work contained herein and a discussion about possible applications of the SSM/T-2 instrument and the possibilities of unified retrievals using other instruments from the DMSP microwave suite.

Chapter 2

THE DMSP SSM/T-2 AND T-1 INSTRUMENTS AND DATA ANALYSIS

2.1 DMSP Block 5D Satellite Characteristics

DMSP Block 5D Satellites operate in a sun-synchronous, near-polar orbit with a nominal altitude of 800 km. The inclination angle of the orbit is 98.8° and an orbit period of 102.0 min. The orbit produces 14.1 orbit revolutions of the satellite per day. The combination of these parameters produces data void areas, diamond-shaped in appearance near the equator, in a 24 hour period. This missing coverage has obvious drawbacks when the data are to be applied to study the tropics (such as in the use of SSM/I to monitor tropical cyclone intensity and position). These data void regions shift with each orbit and complete coverage of the tropical regions is achieved after 72 hours. The orbit inclination also results in circular sectors of 280 km at both poles that are never sampled. The swath width for the SSM/I and SSM/T channels is 1400 km perpendicular to the satellite subtrack. The SSM/I is a conically scanning radiometer (with a constant scan angle of 45 degrees aft of the satellite) as compared to the SSM/T radiometers which are cross-track scanning sounders (which scan in a fashion similar to the OLS described below).

The primary instrument on the DMSP satellites is the Operational Linescan System (OLS) which is a four channel imager. The OLS visible channel for very high resolution has a resolution of 600 m. Since the bandwidth of this channel is very broad, the instrument receives more radiation from a given scene (e.g. as compared to the imagers on NOAA polar orbiter satellites) and hence has a greater sensitivity. The maximum swath width for the OLS is 2500 km. The OLS produces the visible and IR imagery used for many operational requirements by forecasters in the Department of Defense (DOD).

The F8 DMSP spacecraft, launched in 1987, was the first satellite with the Special Sensor Microwave/Imager (SSM/I). The SSM/I is a seven-channel passive microwave radiometer which operates at four frequencies. It receives both vertically and horizontally linearized radiation at 19.3, 37.0, and 85.5 GHz and vertical only at 22.2 GHz (Hollinger *et al.*, 1990). Data from this instrument are used for the determination of the following environmental parameters:

1. Ocean surface wind speeds.
2. Ice coverage, age and extent.
3. Cloud water content.
4. Integrated water vapor (precipitable water).
5. Precipitation over water.
6. Soil moisture.
7. Land surface temperature.
8. Snow water content.
9. Cloud amount.

The SSM/I is also flown on F11 together with the SSM/T-2 and SSM/T-1. These instruments being on the same satellite offer the possibility of a synergistic (also called a unified) approach to atmospheric retrieval where deficiencies of one instrument perhaps can be diminished or removed through the use of another instrument.

2.1.1 SSM/T-2 Channel Characteristics

The Defense Meteorological Satellite Program (DMSP) Special Sensor Microwave (also called Millimeter Wave) Water Vapor Sounder (SSM/T-2) currently flies on the F-11 satellite which was launched on November 28, 1991. The SSM/T-2 possesses 5 channels: three dual-pass bands located on the 183 GHz (1.64 mm) water vapor absorption line, one

on the line's wing (150 GHz), and a window channel (91.655 GHz). The local descending nodal crossing time of F-11 is approximately 0514. The T-2 is a total-power radiometer which measures the total power seen by the antenna over the signal processing integration time. The objective of the SSM/T-2 is to provide global measurements of the vertical profile of water vapor to support Air Force applications including the input of these profiles to numerical weather forecast models. The characteristics of the SSM/T-2 channels are shown in Table 2.1 (including the noise equivalent temperature uncertainty, NEDT).

Table 2.1: SSM/T-2 Channel Characteristics (after Griffin *et al.*, 1993).

Chan. No.	Center Frequency (GHz)	Nadir FOV (km)	Beam Acceptance (degrees)	Peak Altitude (hPa)	Pol.	NEDT ($^{\circ}$ K)	Response
1	183.31 ± 3	48	3.3	650	V	0.6	water vapor
2	183.31 ± 1	48	3.3	500	V	0.8	water vapor
3	183.31 ± 7	48	3.3	800	V	0.6	water vapor
4	91.655	88	6.0	Surface	V	0.6	surface
5	150.0	54	3.7	1000	V	0.6	surface

The T-2 was originally designed to be a four channel instrument (minus the channel near 92 GHz). The work of Isaacs and Deblonde (1985) showed that retrievals were not very accurate under some conditions (specifically, tropical atmospheres) without the 91.655 GHz channel.

The T-2 views both an internal hot-load target ($\sim 30^{\circ}$ K) and cosmic background radiation for calibration measurements. The T-2 also underwent a calibration study led by the Geophysics Directorate of the Air Force's Phillips Laboratory. This calibration study included independent measurements and model calculation studies. These independent measurements were performed by the NASA Millimeter-wave Imaging Radiometer (MIR) carried on the NASA ER-2 aircraft (Racette *et al.*, 1992). The MIR and T-2 contain essentially the same channels with the exception of the window channel which for the MIR is located at 89 GHz. The NASA ER-2 equipped with the MIR undeflew selected DSMP satellite passes including ocean, coastal, and land background cases. RMS differences of 0.7-1.4 $^{\circ}$ K were measured between the T-2 and the MIR.

Radiative transfer model calculations were also conducted (at coincident times and locations with the model of Eyre and Woolf (1988)) using radiosonde data and estimates of the surface emittances. Although the comparisons of the model calculations with the T-2 data showed collocated RMS differences of 6.5°K, the calibration team concluded based on the data they had obtained that the SSM/T-2 suffers no significant bias in its calibration (Griffin *et al.*, 1993).

2.1.2 T-2 Output Parameters

The following parameters are derived from T-2 data using the operational retrieval retrieval scheme of A. Stogryn (Boucher *et al.*, 1993):

1. Relative humidity at 1000, 850, 700, 500, 400, and 300 mb levels.
2. Specific humidity at 1000, 850, 700, 500, 400 and 300 mb levels.
3. Water vapor mass (kg/m^2) between levels surface-1000, 1000-850, 850-700, 700-500, 500-300, and above 300 mb.

Although these parameters are produced operationally, the actual retrieval of data on water vapor from T-2 data is complex for reasons described in the next chapter and there remains considerable scope for research in understanding these complexities.

2.1.3 SSM/T-1 Channel Characteristics

The Special Sensor Microwave/Temperature Sounder (SSM/T-1) was developed and built by Aerojet ElectroSystems Company for the U.S. Air Force Space Systems Division Defense Meteorological Satellite Program (DMSP). The design methodology was a top-down systems development approach. The SSM/T-1, first launched in 1978, was designed to support Air Force and Department of Defense operational weather forecasting, specifically the data required by the Air Force Global Weather Central (AFGWC) numerical weather prediction (NWP) models. To incorporate the T-1 data, the T-1 is designed to emulate radiosonde temperature and pressure measurements, i.e. retrieve temperatures at the standard pressure levels, thicknesses between these levels, and the temperature and

pressure of the tropopause. Channel selection was such that the weighting functions are distributed as evenly as possible throughout the atmosphere (Falcone and Isaacs, 1987). Weighting functions for channels 1-4 of the T-1 were shown in Figure 3.1. The channel characteristics for the SSM/T-1 are shown in Table 2.2.

Table 2.2: SSM/T-1 Channel Characteristics.

Center Frequency (GHz)	Nadir FOV (km)	Beam Acceptance (degrees)	Peak Altitude (km)	NEDT (°K)	Response
50.5	204	14	0	0.6	surface
53.2	204	14	2	0.4	T at 2 km
54.35	204	14	6	0.4	T at 6 km
54.9	204	14	10	0.4	T at 10 km
58.4	204	14	30	0.5	T at 30 km
58.825	204	14	16	0.4	T at 16 km
59.4	204	14	22	0.4	T at 22 km

The SSM/T-1 is a passive 'Dicke' radiometer which scans in a cross-track fashion. The radiometer has a scan time of 32 seconds and a dwell time for each scene of 2.7 seconds; the instrument takes 0.3 seconds between each scene and the warm and cold calibrations occur during the remaining time. The SSM/T-1 operates in an oxygen absorption band using seven frequencies between 50 and 60 GHz and is similar to the MSU which was described above. The variation of the dry air absorption at each of these frequencies provides the basis for the retrieval of temperature profiles (Curtis and Shipley, 1987).

2.1.4 SSM/T-2 and T-1 Scan Patterns

The scan pattern for the SSM/T-2 is similar to the SSM/T-1. Since the SSM/T-2 operates at a longer wavelength than the SSM/T-1 and hence has a smaller footprint, or field of view, the SSM/T-2 samples four times as many scene stations (28 versus 7) per scan revolution, and must scan four times as fast to provide coincident samples. The result is that the SSM/T-2 produces 16 times as many total stations scenes. The footprint pattern is shown in Figure 2.1. The reason for coincident samples is that to produce water

vapor retrievals the T-2 operational algorithm also requires four of the seven measured T-1 frequency channels (Channels 1-4) to provide the requisite temperature sounding. The pattern in Figure 2.1 is changed by the presence of a glare obstructor or GLOB, on the satellite. The GLOB is designed to protect the OLS from solar insolation which could degrade the instrument but this also means that 1 scene of T-1 data and 4 scenes of T-2 data on the sun side of the satellite are degraded and therefore not used.

2.2 SSM/T-2 DATA

The SSM/T-2 data used for this thesis was kindly provided by Mr. Bruce Thomas of the DMSP Omaha Field Office of Aerospace Corporation. The data were obtained for approximately 78 revolutions of satellite F-11 in March 1993. The data package received from Aerospace Corporation consisted of T-2, T-1, and SSM/I data in a VMS back-up save set format. All data received from Aerospace were in sensor data record (SDR) format (also known as antenna pattern corrected temperatures).

The T-2 data set consists of 13 words in each record. Word 1 contains information on the scan scene (which provides the scan angle for the sensor) and the background against which the sensor is viewing (land, ocean, sea ice, or coast). The reason for the differentiation between backgrounds is to have a mechanism to help facilitate the determination of the surface emission for each viewing scene. A discussion of emissions for various backgrounds is included in Chapter 4. Word 2 contains the Julian hour (referenced to 00 UTC 31 December 1967), and words 3 and 4 are the Julian minute and second, respectively. Word 5 is the longitude (from 0.-360° East) and word 6 is the latitude ($\pm 90^\circ$) which together determine the earth location of the scan scene. Word 7 provides the terrain height (m) and word 8 is the 1000hPa height (m) from the operational forecasting model at AFGWC. Words 9-13 are the sensor data records (SDRs) for the five T-2 channels (Kelvin) (B. Thomas, personal communication).

2.3 T-2 BRIGHTNESS TEMPERATURE MAPS

The T-2 brightness temperatures fields for the available data from March 1993 were mapped and contoured. Since the 4 scan scenes on one side of the swath are unusable

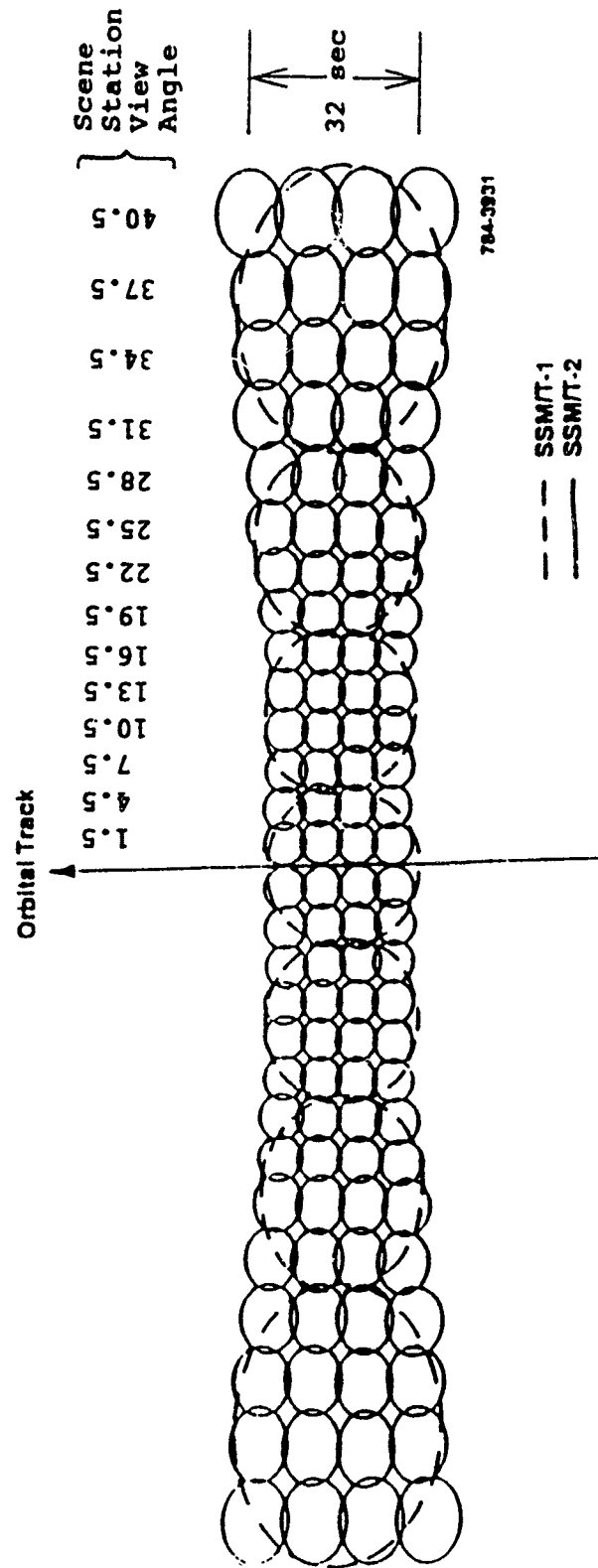


Figure 2.1: Footprint pattern for the SSM/T-2 and T-1. (D. Rhudy, personnel communication).

because of the shielding by the GLOB as mentioned above and because of the brightness temperature changes as a function of scan scene angle (discussed in further detail in Chapter 4), the outer 4 scenes on the other side of the scan were also removed. This results in a scan line that is considerably less than the 1400 km swath width mentioned above but it does mean a data set which is more representative requiring no corrections to the T-2 brightness temperatures for angle effects. The result of this is that there are areas during the two periods which are not sampled and these areas are represented by gray in the colored diagrams.

Data were binned into 1 degree latitude \times longitude bins and then averaged. Since resolution at nadir is about 50 km, bins twice the size of nadir resolution should be representative for the data.

2.3.1 Channel 1 Brightness Temperature Maps

Channel 1, at 183.31 ± 3 GHz, is used for the determination of mid-upper tropospheric water vapor and relative humidity information. As shown below (in Figures 4.1-4.3), the peak of the weighting function for this channel lies between 3-6 km for the three McClatchey atmospheres. Figures 2.2 and 2.3 are the Channel 1 brightness temperatures for the periods 10-14 March and 16-18 March 1993, respectively.

The areas in red which are located both north and south of the equator (e.g. roughly 20-25° from the equator) delineate the location of subsidence associated with the subtropical highs. This prominent feature is also prevalent in the distributions for other frequencies. The subtropical high in the North Atlantic extends from western Africa westward all the way to the Caribbean Sea.

Figure 2.3 suggests a more coherent and stronger ITCZ in the Pacific Ocean (the white and green color shading with several purple pixels). The South Pacific Convergence Zone (SPCZ) (from the central South Pacific extending northwest to east of New Guinea) is also more distinct in this figure. Both features appear cold (and thus moist) in contrast to the the warm (and thus dry) subsiding air poleward of these features.

2.3.2 Channel 2 Brightness Temperature Maps

The weighting functions of Channel 2 peak highest in the atmosphere (Figures 4.1-4.3 with peaks between 5-8 km) and measurements provided by Channel 2 thus applies to upper tropospheric moisture. Figure 2.4 and 2.5 are the Channel 2 brightness temperature maps for the two time periods described above. Maps for this channel have less spread of brightness temperatures than for Channel 1. Channel 2 shows several areas with high brightness temperatures over the oceans and these are: (1) in the central North Pacific near 10-15° latitude and near the date line, (2) in the eastern North Pacific south of Baja, California, (3) in the eastern North Atlantic off the west coast of Africa, (4) in the South Atlantic off the coast of Brazil and (5) near Madagascar in the Indian Ocean. These brightness temperatures indicate that the atmosphere is very dry in the upper levels and these regions are also over the subsidence regions indicated in Figures 2.2 and 2.3. The coldest brightness temperatures over the tropical oceans occur near Fiji in the western Pacific and in the central Indian Ocean. The cold brightness temperatures indicate deep convection in these areas and elevated amounts of upper tropospheric moisture.

2.3.3 Channel 3 Brightness Temperature Maps

Channel 3, located at 183.31 ± 7 GHz, senses levels of water vapor that occur deeper into the atmosphere according to the location of the weighting function maxima for this channel that are depicted in Chapter 4. Figure 2.6 and 2.7 are the brightness temperature maps for 10-14 March and 16-18 March, respectively. Once again, there exists coherence in the subsidence regions such that the broad areas of red color are the regions of subtropical high pressures underlying those dry regions noted in reference to the maps of Channels 1 and 2 brightness temperature. Similarly, the moist tropical regions where the deepest convection occurs appear relatively cold (indicated by white-green colors).

2.3.4 Channel 4 Brightness Temperature Maps

Channel 4, the window channel at 91.655 GHz, primarily senses the surface of the earth. Figures 2.8 and 2.9 are show the brightness temperatures from Channel 4 for the time periods described above. The red color across the land masses (especially Australia)

in the southern hemisphere point to clear skies (at least predominantly), a warm surface and a high emissivity for these land masses. This is not surprising when considering that the land has had the entire summer to become warm and dry. The lower emissivity of the adjacent ocean surfaces results in much lower brightness temperatures and it is easy to differentiate between land masses and ocean surfaces.

East of Japan there are four curved features with brightness temperatures warmer than the surrounding region. Daily maps of brightness temperatures (not shown) indicate this feature is a mesoscale storm system which has been viewed by the T-2 on successive satellite passes (over several days). The cloud features associated with this low-pressure system show up as warm brightness temperatures over the cold ocean background, resembling a comma cloud.

Regions of the tropical oceans show little structure. The yellow and brown colors extend farther south in the Southern Hemisphere as compared to the northern extent in the Northern Hemisphere due to warmer sea surface temperatures and low level moisture over these oceans, since the weighting functions corresponding to this channel peak at/near the surface. Since SSTs typically lag by about two months, SSTs in the southern oceans should be just beginning their fall from the yearly temperature maximum.

2.3.5 Channel 5 Brightness Temperature Maps

Channel 5, at 150 GHz, is located on the line wing of the absorption line at 183.31 GHz. As shown in Chapter 4, the weighting function for this channel peaks in the lower troposphere or at the earth's surface (depending on the moisture profile of the atmosphere). Figures 2.10 and 2.11 are the brightness temperature maps for the periods 10–14 and 16–18 March 1993. The maps hint at the ITCZ and associated convection (with the light yellow and white pixels) in the tropical oceans. Otherwise, there is not a great deal of structure to the temperature differences that hasn't already been said in the previous subsections.

Figure 2.11 does indicate a stronger SPCZ than does Figure 2.10. Australia has high brightness temperatures over the entire country likely indicating a high emissivity for the land and a dry atmosphere above it. Again, the land surfaces are easily found in the brightness temperature maps due to the emissivity contrasts with ocean surfaces.

The brightness temperature maps in Figure 2.2-2.11 provide an opportunity to examine some of the general circulation features of the atmosphere and to see the surface characteristics of ocean and land masses at the frequencies of the SSM/T-2.

2.4 CHANNEL COHERENCE

A helpful way of analyzing and understanding the properties of the T-2 channel brightness temperatures is to consider the relationships between channels. Here we consider two regions which are characterized by distinctly different large scale circulation features and thus different temperature and moisture properties.

The two areas selected are located over the Pacific Ocean. The first area corresponds approximately to the TOGA COARE (Coupled Ocean-Atmosphere Response Experiment) domain and is defined as the area 160-170° East longitude and 0-10° South latitude. This area is largely under the control of deep convection and ascent as part of the Hadley and Walker circulations and represents a region of relatively high moisture content at all levels. The brightness temperatures from this area are compared and contrasted with an area in the Eastern Pacific defined by the coordinates 110-120° West longitude and 10-20° North latitude. This East Pacific area is located in a region dominated by a subtropical high with its (assumed) associated strong subsidence and lower column water vapor. Time constraints did not permit a detailed analysis of the cloudiness over these regions during this study.

The brightness temperatures for these regions and for the 5 channels are plotted against each other in the form of scatter diagrams. Figure 2.12 shows Channel 5 versus Channel 4 for the two Pacific regions. The East Pacific (EP) region shows a very small scatter for the brightness temperature data. The Channel 4 temperatures are relatively low (as compared to the Channel 5) since this channel is designed to see the surface. As discussed in Chapter 4, the emissivity of the ocean surface is relatively low (~ 0.7) and it provides a cold background. Channel 5, on the line wing, provides both surface effects and the effects of low level water vapor. The brightness temperature indicates an emission temperature near 280 K. The West Pacific (WP) area shows a window brightness



226-0 234-0 242-0 250-0 258-0 266-0 274-0 282-0
 222-0 230-0 238-0 246-0 254-0 262-0 270-0 278-0 286-0

SSM/T-2 Channel 1
 1 Degree Bin Averages
 March 10-14, 1993

Figure 2.2: Channel 1 brightness temperature map for 10-14 March 1993.



SSM/T-2 Channel 1
 1 Degree Bin Averages
 March 16-18, 1993

Figure 2.3: Channel 1 brightness temperature map for 16-18 March 1993.



220-0 228-0 236-0 244-0 252-0 260-0 268-0 276-0
 216-0 224-0 232-0 240-0 248-0 256-0 264-0 272-0 280-0

SSM/T-2 Channel 1 2
 1 Degree Bin Averages
 March 10-14, 1993

Figure 2.4: Channel 2 brightness temperature map for 10-14 March 1993.



220-0 228-0 236-0 244-0 252-0 260-0 268-0 276-0
 216-0 224-0 232-0 240-0 248-0 256-0 264-0 272-0 280-0

SSM/T-2 Channel 2
 1 Degree Bin Averages
 March 16-18, 1993

Figure 2.5: Channel 2 brightness temperature map for 16-18 March 1993.



204-0 216-0 228-0 240-0 252-0 264-0 276-0 288-0
 198-0 210-0 222-0 234-0 246-0 258-0 270-0 282-0 294-0

SSM/T-2 Channel 3
 1 Degree Bin Averages
 March 10-14, 1993

Figure 2.6: Channel 3 brightness temperature map for 10-14 March 1993.



204.0 216.0 228.0 240.0 252.0 264.0 276.0 288.0
 198.0 210.0 222.0 234.0 246.0 258.0 270.0 282.0 294.0

SSM/T-2 Channel 3
 1 Degree Bin Averages
 March 16-18, 1993

Figure 2.7: Channel 3 brightness temperature map for 16-18 March 1993.



192-8 206-3 219-8 233-3 246-8 260-3 273-8 287-3
 186-0 199-5 213-0 226-5 240-0 253-5 267-0 280-5 294-0

SSM/T-2 Channel 4
 1 Degree Bin Averages
 March 10-14, 1993

Figure 2.8: Channel 4 brightness temperature map for 10-14 March 1993.



Figure 2.9: Channel 4 brightness temperature map for 16-18 March 1993.



190-0 206-0 222-0 238-0 254-0 270-0 286-0 302-0
 182-0 198-0 214-0 230-0 246-0 262-0 278-0 294-0 310-0

SSM/T-2 Channel 5
 1 Degree Bin Averages
 March 10-14, 1993

Figure 2.10: Channel 5 brightness temperature map for 10-14 March 1993.



190-0 206-0 222-0 238-0 254-0 270-0 286-0 302-0
 182-0 198-0 214-0 230-0 246-0 262-0 278-0 294-0 310-0

SSM/T-2 Channel 5
 1 Degree Bin Averages
 March 16-18, 1993

Figure 2.11: Channel 5 brightness temperature map for 16-18 March 1993.

temperature of 10-15 degrees higher than the East Pacific area. This likely occurs due to more emission by the water vapor (near the surface, emitting at a high temperature) in the wetter atmosphere in the West Pacific. The scatter of data from the West Pacific indicates that the area contains many inhomogeneities. Possible reasons for this scatter will be discussed later.

Figure 2.13 depicts the brightness temperatures of the 150 GHz channel and the 183 ± 7 GHz channel. Since these two channels are adjacent to each other, it is expected that the two channels would be well correlated. For the East Pacific area, the Channel 3 and 5 temperatures are nearly equal, with most of the Channel 3 temperatures within 10° of 280 K. For the WP region, Channel 3 becomes opaque more quickly and therefore, most of the temperatures are below 275 K. The vertical correlation of brightness temperature (and therefore water) shows up very well for the WP region. An almost linear relationship between these two channels is inferred by the data.

Figure 2.14 is the scatter plot of the brightness temperatures of Channels 1 and 5. The EP area again exhibits higher brightness temperatures for channels which peak above the surface, implying a dry upper atmosphere. Additionally, there is not much scatter of the data for this region, implying a profile which is nearly invariant. Channel 1 brightness temperatures for the WP region are about 20° colder than the EP region. This indicates that this channel is sensing water vapor at a colder temperature which means a higher altitude.

Perhaps the best depiction of the differences in the two areas is shown in Figure 2.15. This figure plots the window channel (Channel 4) against the channel closest to the absorption line (Channel 2). Figure 2.15 shows that the EP area has a high Channel 2 brightness temperature, implying the channel peaks well down in the atmosphere. The WP area has noticeably lower brightness temperatures for Channel 2, indicating a peak of the channel higher in the vertical (and consequently, at a lower thermometric temperature than for the EP). Channel 4 brightness temperatures are governed by the low emissivity of the cold ocean surface in the EP and the higher thermal temperature of the surface and lower atmosphere combined for the WP region.

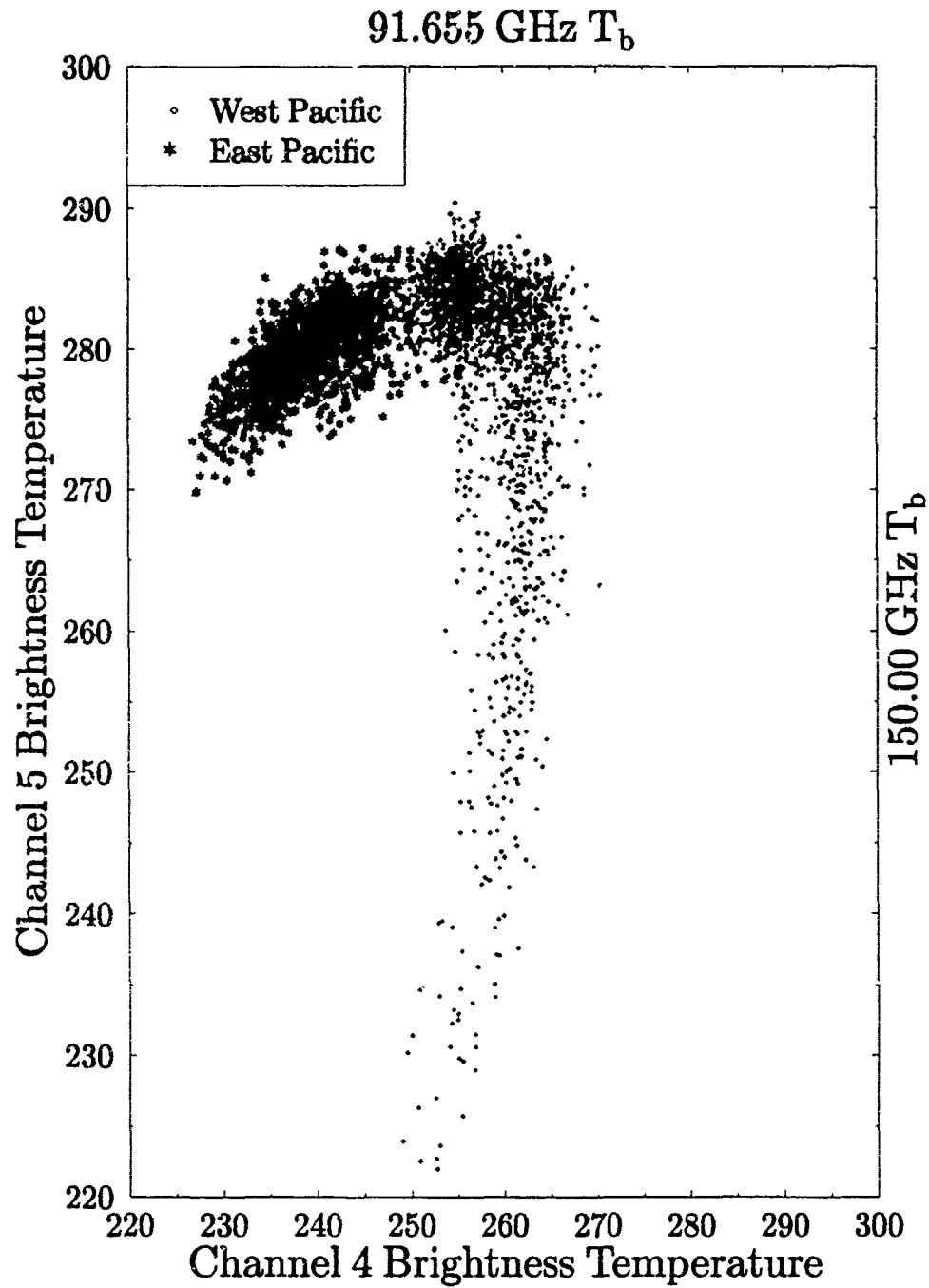


Figure 2.12: Channel 5 versus Channel 4 brightness temperatures for the two Pacific areas.

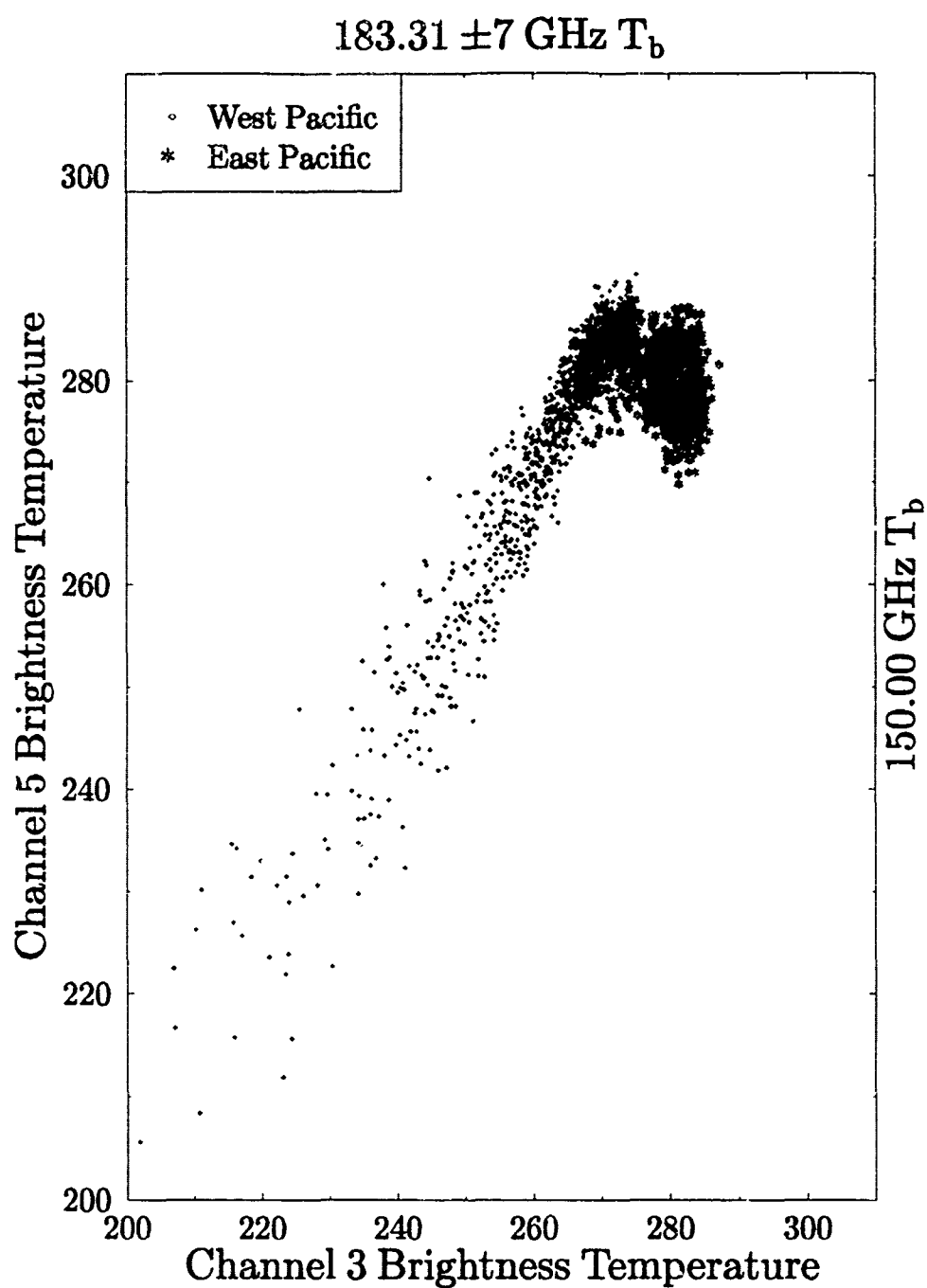


Figure 2.13: Channel 5 versus Channel 3 brightness temperatures for the two Pacific areas.

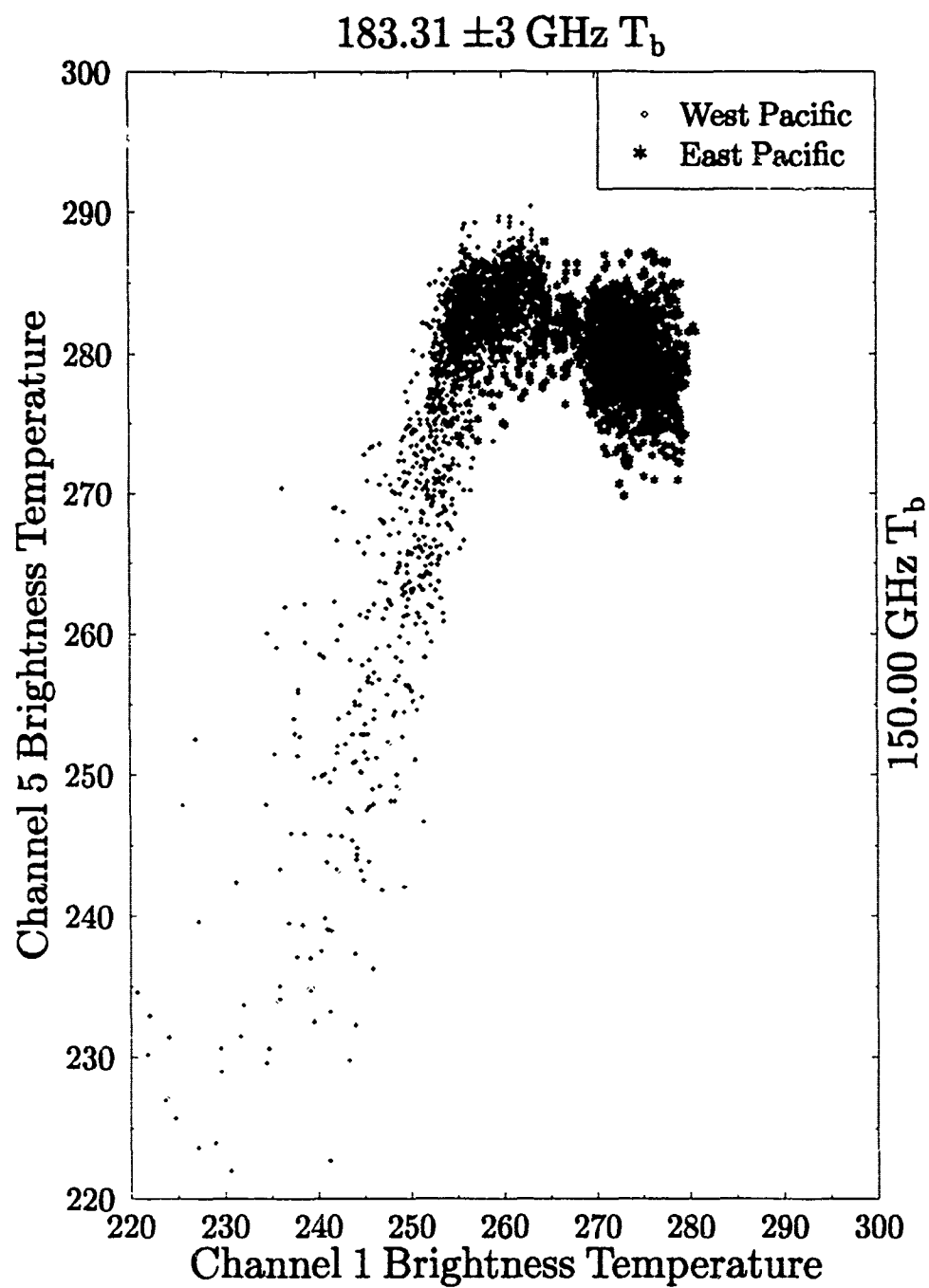


Figure 2.14: Same as Figure 2.12 except Channel 5 vs. Channel 1.

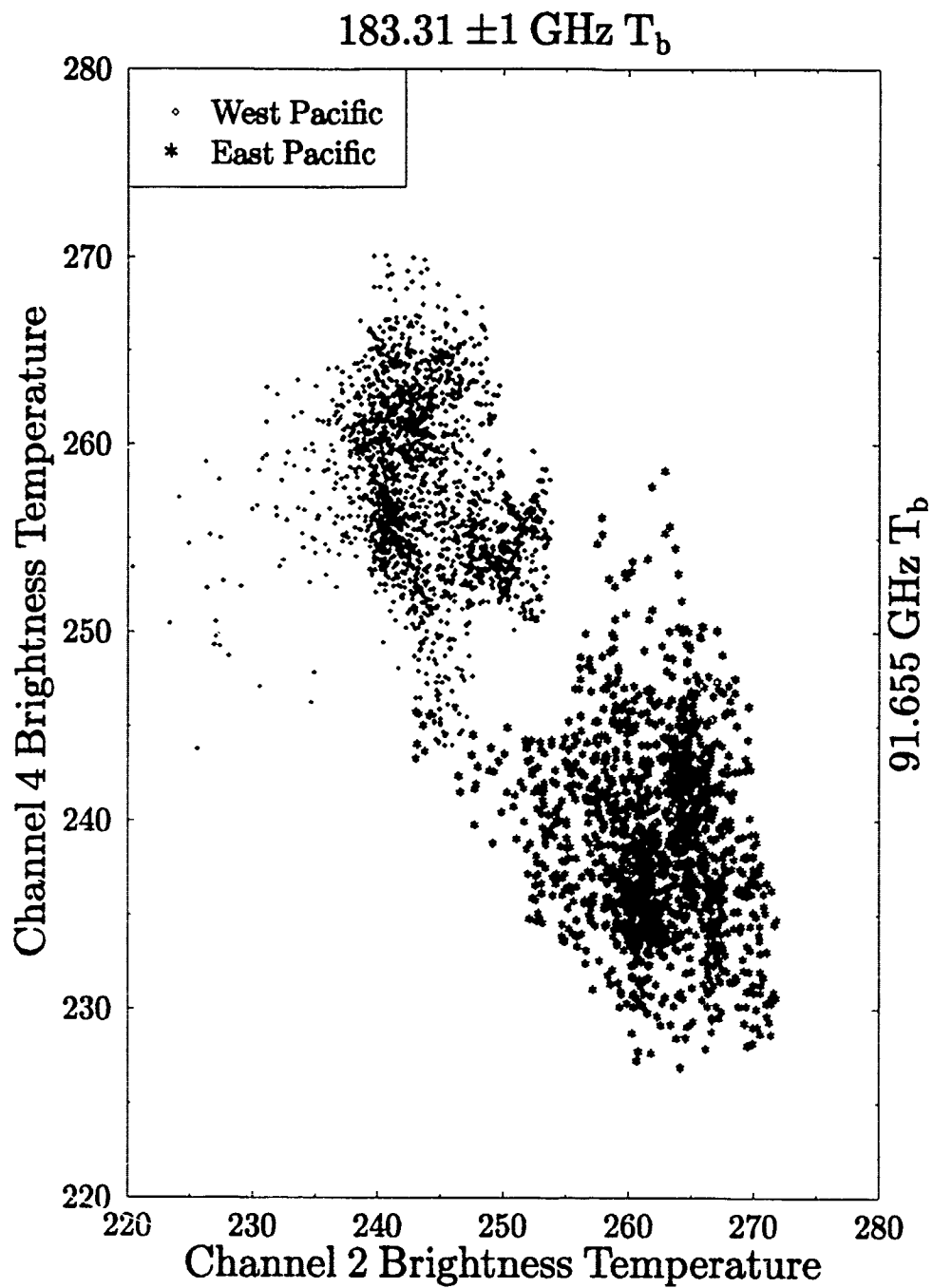


Figure 2.15: Channel 4 versus Channel 2 brightness temperatures for the two Pacific areas.

Figure 2.16 also shows a distinct difference in the brightness temperatures for the two Pacific areas. This figure depicts the brightness temperatures for Channel 4 versus Channel 1. The explanation of these features is basically the same as the previous paragraph as the Channel 1, mid-upper tropospheric peak for the weighting function, brightness temperature is high for the region with subsidence and is low for the region with an abundance of water vapor. Conversely, the Channel 4 brightness temperatures are high for the WP and relatively low for the EP. SST differences certainly play a part in these brightness temperature differences, with higher SSTs (which means higher brightness temperatures) for the WP. Additionally, water vapor near the surface and cloud effects also contribute to the higher brightness temperatures in the WP region.

The effect of ice and mixed phase and partial cloud cover clouds cannot be quantitatively nor qualitatively examined from these figures or from the brightness temperature maps. This is an area where future research is needed.

In this section it has been shown that:

1. Areas with distinctly different moisture profiles (such as regions of large scale subsidence versus moist ascent) can be uniquely identified through the use of brightness temperature plots.
2. Surface characteristics can be inferred from the brightness temperature plots.

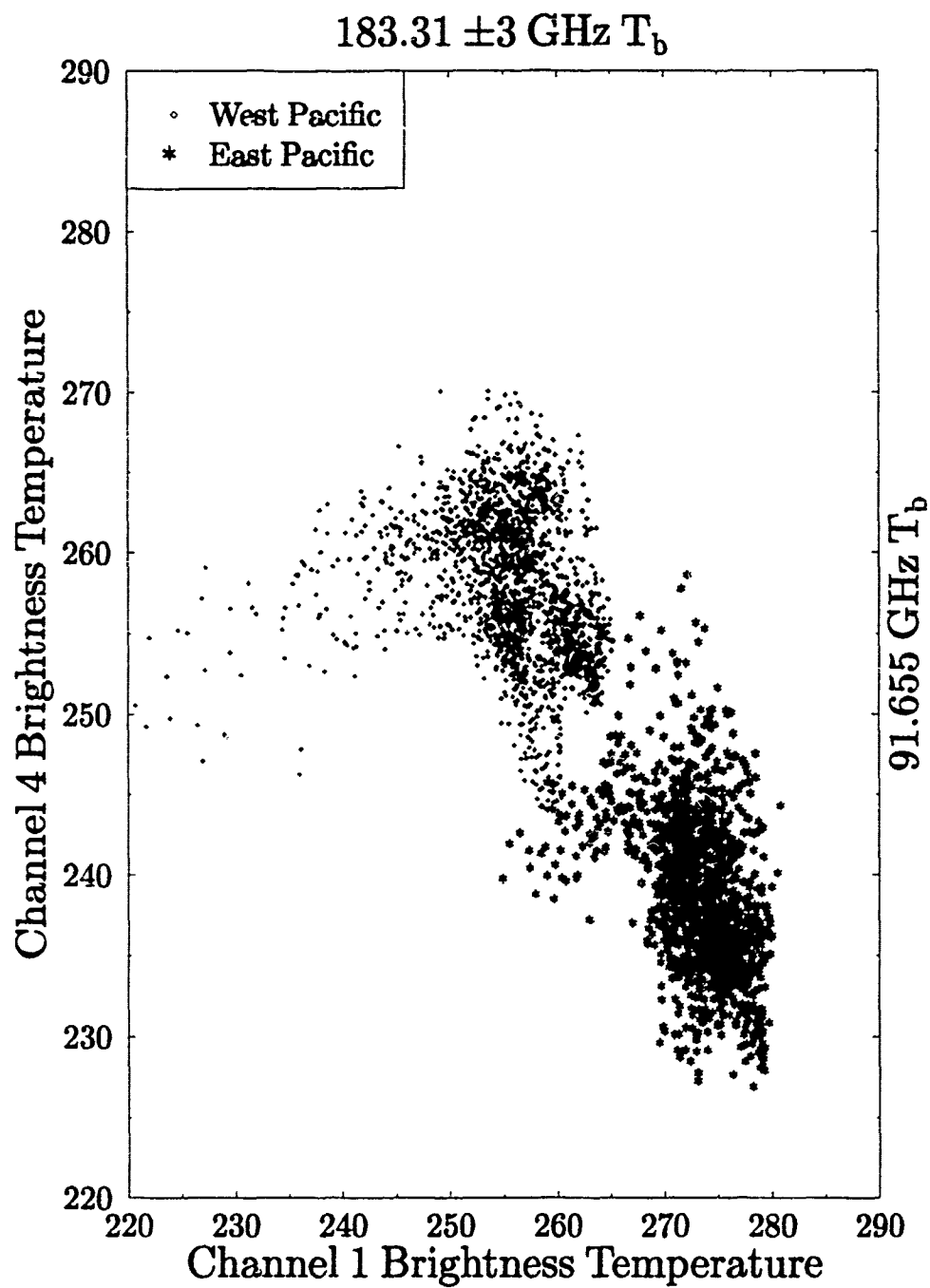


Figure 2.16: Same as Figure 2.12 except Channel 4 vs. Channel 1.

Chapter 3

MICROWAVE RADIATIVE TRANSFER AND WEIGHTING FUNCTIONS

Emission from the atmosphere and the Earth's surface provide the source of radiation received at satellite altitude by microwave instruments. Radiation detected by these instruments is changed by the processes of absorption, emission and scattering within the atmosphere. These processes depend on the properties of the Earth's surface, atmospheric constituents especially water vapor and the concentration of hydrometeors and information about these properties can be retrieved from measurements of this radiation (Stephens, 1993). As stated, detection of atmospheric water vapor, and specifically its vertical profile is the objective of the SSM/T-2 Millimeter Wave Moisture Sounder.

For the frequencies of interest, clear sky absorption arises primarily from water vapor and to a lesser extent oxygen absorption (Waters, 1976.) Ozone also absorbs in this region, but to a much lesser extent than water vapor and oxygen, and ozone absorption has a negligible effect on brightness temperatures. Cloud droplets also absorb in the microwave/millimeter wave region.

Figure 3.1 provides a physical perspective on microwave emission and shows some of the effects of water vapor, surface reflectance, and cloud liquid water on this emission. Case (2) shows the emission spectra found over a cold surface (e.g. ocean) versus case (4) which presents the spectra found over a warm surface (e.g. land). The difference in spectra between case 1 and case 2 shows how water vapor changes the brightness temperatures. These effects lead to temperature decreases over land (warm background) and increases over ocean (cold background). Similarly, the change in spectra between cases 2 and 3 show the effects of cloud droplet (Rayleigh) absorption. Finally, the spectra change from case

2 to case 4 is an example of how surface characteristics may change intensities measured by a satellite radiometer.

3.1 THE RADIATIVE TRANSFER EQUATION FOR MICROWAVE REMOTE SENSING

The radiative transfer equation describes how, in a mathematical sense, radiation is transferred from one layer to another. The generalized form of this equation which includes the effects of both absorption and emission of energy is written as:

$$dI = -k_\nu[I - B]ds, \quad (3.1)$$

where I is the intensity, k_ν is the volume absorption coefficient, and B is the emission represented by Planck's function. Equation (3.1) neglects scattering, which is common for many problems in microwave radiative transfer and it also assumes the condition of local thermodynamic equilibrium. The principles of emission-based sensing are used for many atmospheric applications including the remote sensing of sea surface temperature (SST), column water vapor, cloud liquid water content, precipitation rate, temperature profiles, and clouds.

3.1.1 Brightness Temperatures

At the wavelength of microwave/millimeter wave radiometers, the Rayleigh-Jeans distribution applies — that is, radiant energy and temperature are synonymous. This temperature is referred to as the brightness temperature, and, for satellite radiometers is a measure of the upwelling thermal microwave radiation from the medium (in this case the atmosphere) below. Using the Rayleigh-Jeans approximation, assuming specular reflection and for a nadir viewing radiometer, this brightness temperature, $T_b(\nu)$, can be expressed as:

$$T_b(\nu) = \int_0^\infty \exp(-\tau(h, \infty))\gamma(\nu, h)T(h)dh + \exp(-\tau(0, \infty)) \times \\ \left[(1 - R)T_{sf} + R \int_0^\infty \exp(-\tau(0, h))\gamma(\nu, h)T(h)dh \right] + R \exp(-2\tau(0, \infty))T_{cb}, \quad (3.2)$$

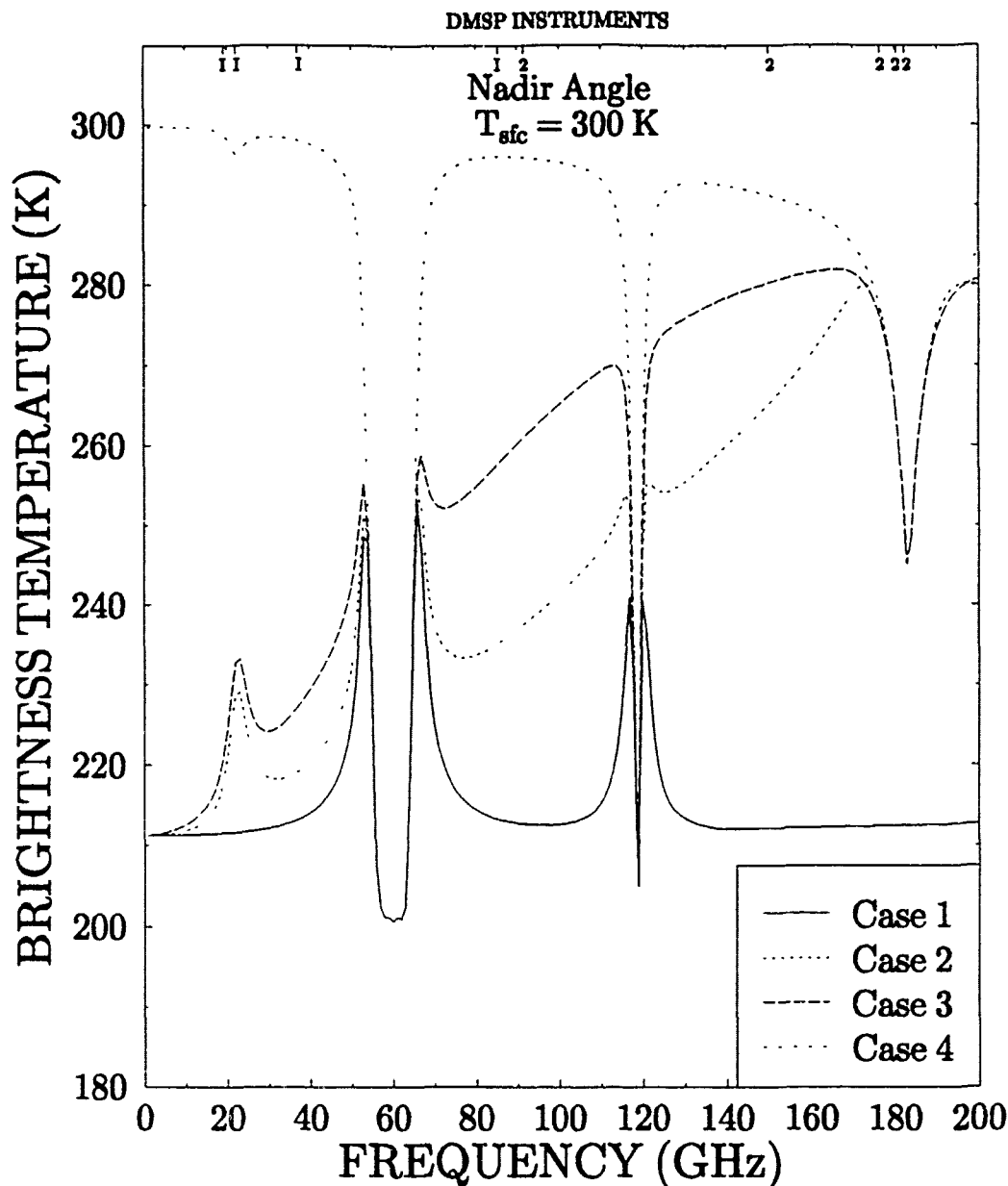


Figure 3.1: Brightness temperature spectra from 1–200 GHz for cases (1) tropical atmosphere with no water vapor and reflectivity (R) = 0.3; (2) tropical atmosphere ($CWV = 41.2\text{g/m}^2$) and $R = 0.3$; (3) tropical atmosphere with a cloud ($LWC = 0.5\text{g/m}^2$) from 1–2 km and $R = 0.3$ and case (4) same as case (2) except $R = 0.0$. The locations of the SSM/I and SSM/T-2 channels are indicated by “1” and “2”, respectively.

where $\tau(z, y) = \int_z^y \gamma(\nu, x) dx$ represents the optical depth between heights z and y , R is the reflectivity of the surface ($(1-R)$ is the emissivity (ϵ) of the surface), $\gamma(\nu, h)$ the volume absorption coefficient of the atmosphere at a height h for a frequency ν , $T(h)$ the temperature profile of the atmosphere, T_{sf} the thermometric temperature of the surface, and T_{cb} the cosmic background (2.7°K) temperature. Each term on the right hand side of (3.2) has a related physical description. The first term is the contribution to the brightness temperature due to upward emission by the atmosphere. The second term is the 'surface term' which is the radiation emitted by the Earth's surface which reaches the satellite. The third term is the downwelling radiation of the atmosphere which is reflected by the Earth's surface to the satellite. The last term is the cosmic background temperature which is reflected by the earth's surface to the satellite. The angular dependence of quantities has been omitted here and is taken to be understood.

There is some debate as to the necessity of the cosmic background term. Some researchers state that this term can be ignored whereas Kakar (1983) argues that for a channel on the wing of the absorption line (e.g. such as the 150 GHz channel of the SSM/T-2) that this term would add approximately 0.5°K to the measured brightness temperature. The term is retained in the radiative transfer model introduced below and used to produce the results of subsequent chapters.

In calculating brightness temperatures from (3.2), the state of the polarization of radiation has not been considered. The main sources of polarization arise from reflection by the surface and by scattering from irregular particles in the atmosphere. The latter effects are ignored and only the effects of polarization due to surface reflection are considered. By ignoring any cross polarization effects within the atmosphere, (3.2) becomes the radiative transfer equation for the vertical state of polarization assuming R represents the surface reflectivity for vertical polarization. In any event, the effects of surface reflectivity are minimal for Channels 1 and 2, and thus the effects of polarization are of little consequence for the study described in this thesis.

3.2 WEIGHTING FUNCTIONS

For atmospheric temperature profiling, (3.1) may be expressed in the form:

$$T_b(\infty) = \int_0^{\infty} K(\nu, h)T(h)dh + A, \quad (3.3)$$

where A represents terms independent of the temperature profile and $K(\nu, h)$, the temperature weighting function, is weakly dependent on the temperature profile. These weighting functions are a basis for selection of channels for temperature profiling instruments and, in some cases, a basis for the temperature profile retrieval itself.

Smith *et al.* (1979) show weighting functions for the TOVS instrument suite. The MSU operates in the same oxygen absorption band as the SSM/T-1 instrument. The depicted weighting functions (shown in Figure 3.2) give a demonstration of the vertical resolution of each of the channels. The weighting functions appear in the integral equations relating temperature to the measured radiances (as in (3.3)).

3.2.1 Relative Humidity-based Weighting Functions

This discussion of constituent retrievals follows from the work of Schaerer and Wilheit (1979). Constituent retrievals are unfortunately a nonlinear problem because the absorption coefficient appears both in the transmission factor ($\exp(-\int \gamma dx)$) and in the radiation factor $\gamma(h)T(H)$ of (3.2). Therefore, the effect of $\gamma(\nu, h)$ at one height is dependent on $\gamma(\nu, h)$ at all other heights and so the problem of constituent retrieval is also a non-local one.

Similarly, (3.1) can be expressed as (Schaerer and Wilheit (1979)):

$$T_b(\infty) = \int_0^{\infty} G(h)\gamma(h)dh + B, \quad (3.4)$$

where B represents terms independent of $\gamma(h)$; however, no insight comparable to the temperature profiling example evolves since $G(h)$ is strongly dependent on $\gamma(h)$. Nonetheless, (3.4) can still be linearized. A small change in the brightness temperature $\Delta T_b(\infty)$ due to a small change in the absorption as a function of height, i.e. $\Delta \gamma(h)$, can be expressed as:

$$\Delta T_b(\infty) = \int_0^{\infty} G[h, \gamma(h), T(h)]\Delta \gamma(h)dh. \quad (3.5)$$

After some manipulation we find an expression for $G(h, \gamma(h), T(h))$:

$$G(h, \gamma(h), T(h)) = \exp(-\tau(h, \infty))[T(h) - T_{b\uparrow}(h)] + R \exp(-\tau(0, \infty)) \exp(-\tau(0, h))[T(h) - T_{b\downarrow}(h)], \quad (3.6)$$

where $T_{b\uparrow}$ and $T_{b\downarrow}$ are the upwelling and downwelling brightness temperatures at height h , respectively. The weighting function with respect to absolute water vapor, $\rho(h)$, is:

$$G_\rho(h) = G(h) \frac{\partial \gamma(h)}{\partial \rho(h)} \quad (3.7)$$

and with respect to relative humidity, $RH(h)$:

$$G_{RH}(h) = G(h) \frac{\partial \gamma(h)}{\partial \rho(h)} \frac{\partial \rho(h)}{\partial RH(h)} = G(h) \frac{\partial \gamma(h)}{\partial \rho(h)} \rho_{sat}(h) \quad (3.8)$$

where $\rho_{sat}(h)$ is the saturation vapor pressure of water at a height h . In this way, weighting functions based on the relative humidity profile $RH(h)$ are produced; these being related to brightness temperature changes by

$$\Delta T_{b\uparrow} = \int_0^\infty G_{RH}(h) \Delta RH(h) dh. \quad (3.9)$$

3.2.2 Transmission-based Weighting Functions

Transmission-based weighting functions assume a different yet comparable form and are similar to those used for temperature retrievals. Isaacs and Deblonde (1987) used these weighting functions for their study of cloud effects on 183 GHz retrievals. These weighting functions are also the same as those used for infrared measurement techniques where both vertical profiles of water vapor and total precipitable water are derived (Prabhakara and Dalu, 1980).

Define $T(\tau, \mu) = \exp(-\tau/\mu)$ as the transmittance of the atmosphere. Neglecting the dependence on the zenith angle (as above), the derivative of the transmittance becomes: $dT = \exp(-\tau)d\tau$ or $dT = \exp(-\tau)(-\gamma dh)$. Using the Rayleigh-Jeans limit, (3.2) becomes:

$$T_{b\uparrow}(\infty) = T(\tau_o)T_{sf}(1 - R) + \int_1^0 T(\tau)dT(\tau) + T(\tau)R \int_1^0 T(\tau)dT(\tau) + T^2(\tau_o)RT_{cb} \quad (3.10)$$

where τ_o is the optical depth from the satellite to the surface. By grouping common factors together, Equation 3.10 can be simplified to:

$$T_{b1}(\infty) = [T_{sf}(1 - R) + RT(\tau_o)T_{cb}]T(\tau_o) + [1 + T(\tau)R] \int_1^0 T(\tau)dT(\tau) \quad (3.11)$$

where there is now only one integral term.

Defining a weighting function $W(Z)$ for a vertical coordinate Z as $W(Z) = \frac{dT(Z)}{dZ} = T(Z)\gamma(Z)$ then the previous equation can be written:

$$T_{b1}(Z_\infty) = [T(Z_o)(1 - R) + RT(Z_o)T_\infty]T(Z_o) + [1 + T(Z)R] \int_{Z_o}^{Z_\infty} T(Z)W(Z)dZ. \quad (3.12)$$

Weighting functions derived in this manner are convenient since they closely resemble the weighting functions often used for temperature retrievals. Transmission is a quantity easily calculated in a propagation model, and these models permit the calculation of the derivative of transmission with height and hence, the weighting functions themselves.

As an example of transmission-based temperature weighting functions, Figure 3.2 shows weighting functions plotted for channels 1-4 of the SSM/T-1 temperature sounder for a tropical atmosphere with a thermometric temperature of 300 K. Figure 3.2 is comparable to Figure 2, Liou *et al.* (1979) and the MSU channels of Figure 1, Smith *et al.* (1979).

Weighting functions from the two different methods appear very similar when plotted. Plots of the transmission-based weighting functions are for the SSM/T-2 are discussed later in Chapter 4.

3.3 ATMOSPHERIC PROFILES, PROPAGATION MODEL, AND CLOUD MODELS

To simulate microwave brightness temperature requires the use of models to represent various aspects of the atmosphere and the propagation of microwave energy through the atmosphere. We use simulations of the brightness temperatures to understand how they vary with changing atmospheric properties and to study these effects in isolation. The selection of the models described below was made for a variety of reasons including the use of a model(s) in similar studies done previously, the most current model available, the computational efficiency of the model, and its simplicity.

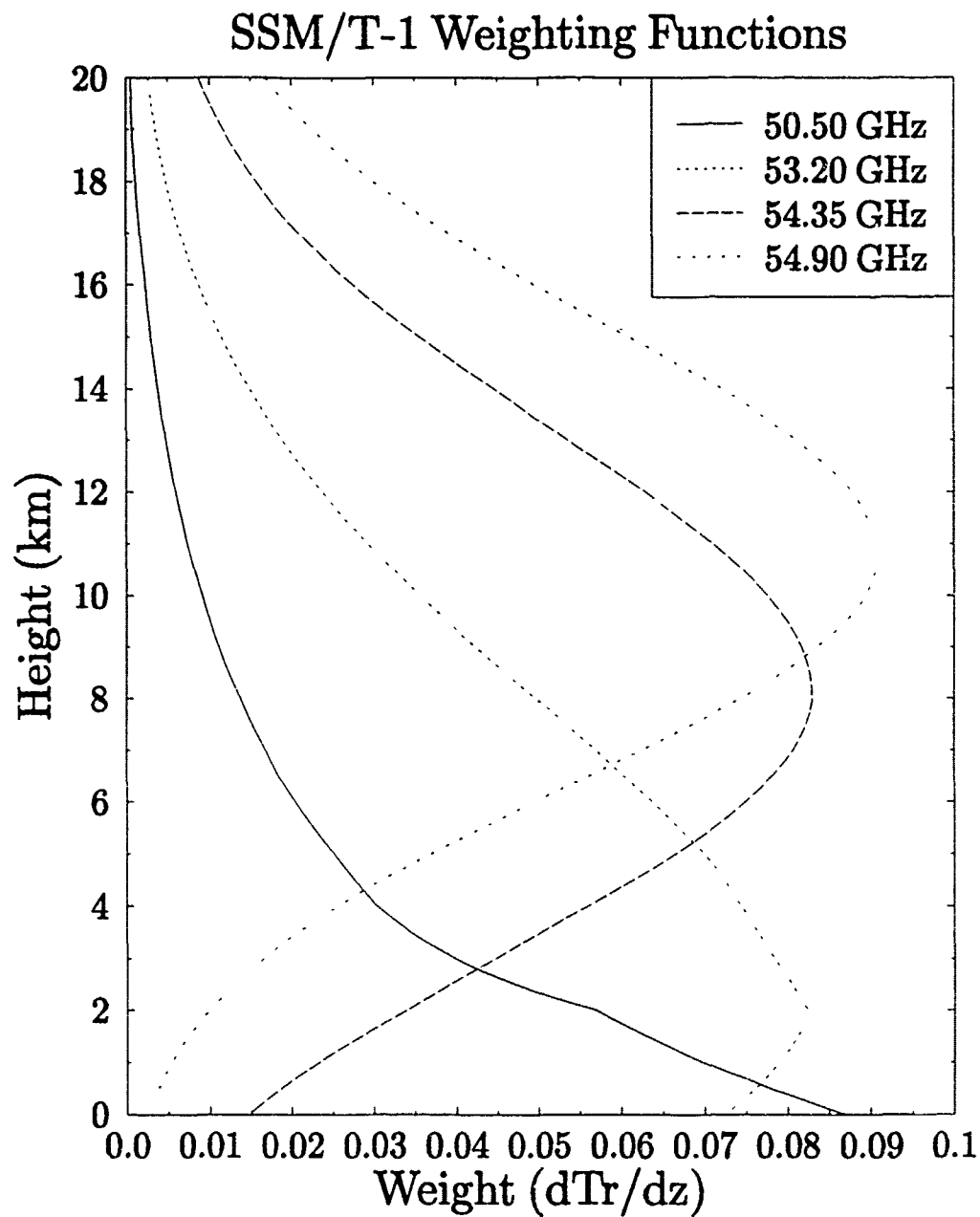


Figure 3.2: Clear sky weighting functions for the SSM/T-1 channels 1-4 for a tropical atmosphere, reflectivity = 0.03, and a column water vapor (CWV) = 41.2 kg/m².

3.3.1 Atmospheric Profiles

McClatchey *et al.* (1972) standard atmosphere profiles of mid-latitude winter, mid-latitude summer, and tropical atmospheres were used as the reference for height (km), pressure (mb or hPa), temperature ($^{\circ}\text{K}$ or K), density (gm^{-3}) and water vapor density (gm^{-3}). The radiative transfer code also included a feature which would allow the water vapor density to be increased or decreased by a common factor throughout the atmosphere. This is used to increase the number of different atmospheres for the simulations discussed in Chapter 5.

3.3.2 The Propagation Model

The Liebe millimeter wave propagation model (MPM92) (which is an updated version of MPM89 (Liebe, 1989) and Liebe, personal communication) allows the specification of an input atmospheric profile. The atmospheric profile provides the necessary meteorological parameters to allow the computation of the volume absorption coefficient, γ . Knowledge of the volume absorption coefficient then allows the computation of the optical depth, τ . From the optical depth the calculation of the transmittance is straightforward and the transmission-based weighting function follows as described above.

The MPM92 model accounts for dry air attenuation, oxygen and water vapor line absorption, water vapor continuum, and Rayleigh cloud droplet absorption. The Zeeman effect for oxygen for pressures less than 0.7 kPa and Doppler broadening for water vapor are also included. One distinct advantage of MPM92 is the small number of lines used in the model. The model uses 44 O_2 and 30 H_2O local line contributions versus the over 500 contributing spectral lines for frequencies below 1 THz. The small number of lines in MPM92 require considerably less computation time than do other codes (i.e. RAD-TRAN). Versions of MPM have been used by various researchers (e.g. Wang *et al.* (1992) and Fleming *et al.* (1991)) to study atmospheric propagation at millimeter/microwave wavelengths.

3.3.3 Cloud Models

To simulate cloud effects within the field of view (FOV) of the radiometer, a set of cloud models was chosen to be incorporated within the atmospheric attenuation profiles. The cloud models chosen (after Isaacs and Deblonde, 1987) are from the Air Force Geophysics Laboratory FASCODE model (Falcone *et al.*, 1979). Cloud parameters for the five cloud models are given in Table 3.1.

Table 3.1: Cloud Type Characteristics (after Isaacs and Deblonde, 1987)

Cloud Model	Type	Mode Radius, μm	Liquid Water Content, gm^{-3}	Vertical Extent, km
1	Stratus	2.7	0.15	0.5-2.0
2	Cumulus	6.0	1.00	1.0-3.5
3	Altostratus	4.5	0.40	2.5-3.0
4	Stratocumulus	6.25	0.55	0.5-1.0
5	Nimbostratus	3.0	0.61	0.5-2.5

Cloud attenuation was calculated using the Rayleigh absorption approximation of Mie's forward scattering function (Liebe, 1989). Cloud liquid water content (w , gm^{-3}) and frequency are the required variables. Cloud attenuation (calculated by Liebe's MPM92 model) was added to the clear sky absorption for each layer of the atmosphere for the entire cloud layer as specified by the cloud model. The MPM model assumes that the cloud fills the entire FOV and that there is only one cloud layer. These assumptions will tend to overestimate and underestimate the effects of clouds, respectively.

Chapter 4

SENSITIVITY EFFECTS FOR THE DMSP SSM/T-2

This chapter is devoted primarily to the discussion of forward radiative transfer simulations of the SSM/T-2 brightness temperatures and how these temperatures respond to a variety of different atmospheric parameters. The approach is to build an understanding of this radiative transfer problem before tackling the inverse problem — that of retrieving moisture information from brightness temperature measurements. There are a number of factors which influence brightness temperatures and hence, the retrieval of moisture profiles using 3 channels near 183 GHz and a window channel near 92 and a line wing channel at 150 GHz. These factors will be referred to as sensitivity factors and include: the thermometric temperature and its vertical profile, the surface reflectivity (emissivity), the humidity (moisture) profile, the characteristics of clouds (both water clouds and perhaps ice clouds), the surface elevation, the channel noise, and scan angle. The influence of some of these factors on T-2 simulated brightness temperatures is now examined.

4.1 DEPENDENCE ON MOISTURE PROFILES

For the simulation studies described below, three basic atmospheric profiles are used: a tropical (T) profile, a midlatitude (MLS) summer profile, and a midlatitude winter (MLW) profile (McClatchey *et al.*, 1972). The water vapor density data for each profile will also be multiplied by a constant factor at each level to provide a method of varying the column water vapor (CWV) amount. Since each moisture profile is characterized by a different column water vapor amount, since each atmosphere has a different temperature profile, the simulated channel brightness temperatures of T-2 will respond differently to each profile.

The clear sky weighting function profiles for an ocean background with an emissivity of 0.7 are shown in Figures 4.1–4.3 with altitude as the ordinate and the weighting function $\frac{dT}{dz}$ (or $\frac{dT_r}{dz}$ as designated in the figures) as the abscissa. These profiles are plotted for the nadir angle and for values the column water vapor CWV (kg m^{-2}) as given.

Comparing these figures it can easily be seen how the amount of moisture in the atmosphere affects the location of the peaks of the weighting functions. For example, for the tropical and midlatitude summer atmospheres the 182.31 GHz channel peaks between 7 and 8 km whereas for the midlatitude winter atmosphere the channel peaks between 5 and 6 km. Similar effects are seen for the other channels where the more moisture in the atmosphere the higher in the atmosphere the channel peaks. Even the ‘window’ channel (91.655 GHz) sees the effects of moisture in the atmosphere and this serves as a reminder that the ‘window’ is not entirely transparent.

It can also be seen from Figures 4.1–4.3 the broadness of the weighting functions as depicted for these cases. This broadness is an obvious limitation of the system in that the resolution for retrievals is limited by the lack of sharpness of these weighting functions. The resolution of the T-2 was expected to be on the order of 2–3 km based on the weighting functions of this type (e.g. Schaerer and Wilheit, 1979).

Additionally, from Figures 4.1–4.3 it is relatively easy to develop some intuition as to the purpose of each channel, at least for clear-sky conditions. The two channels closest to the 183 GHz line relate to the measurement upper tropospheric moisture; the line wing channel (150 GHz) to low level moisture; and the window channel senses low level moisture and surface characteristics, including the emissivity and perhaps the thermometric (‘skin’) temperature. The remaining channel is relevant to midtropospheric moisture determinations.

As a final examination of how moisture changes the weighting functions of the SSM/T-2, the midlatitude summer profile will again be used. In this case, the specific humidity is increased by a factor of two throughout the entire atmosphere (20 km). Figure 4.4, compared to Figure 4.2, shows how the increased moisture at all levels moisture changes the weighting functions significantly.

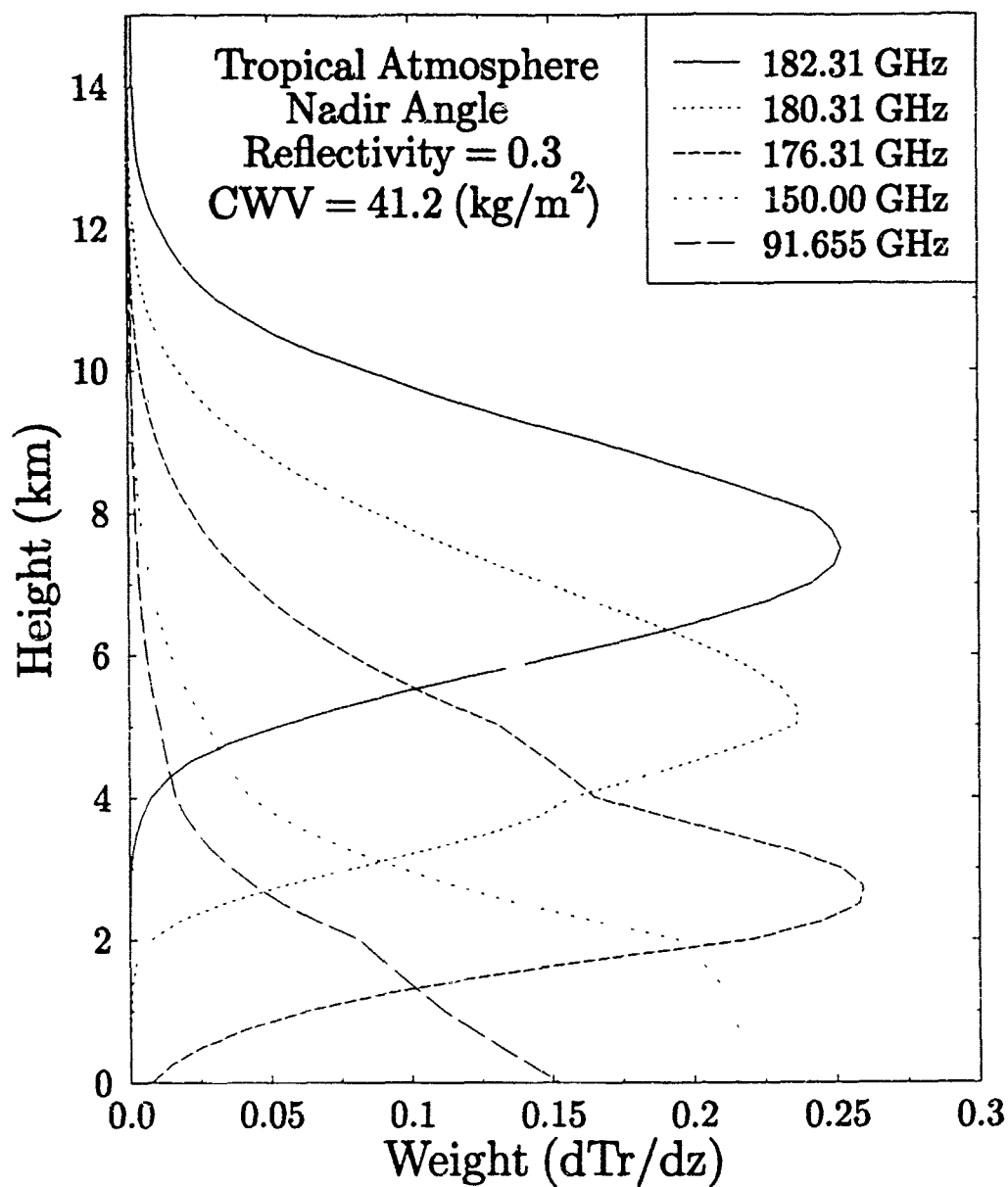


Figure 4.1: Clear sky weighting functions for the SSM/T-2 channels for a tropical atmosphere over an ocean background with a reflectivity factor of 0.3 and a thermometric temperature of 300 K.

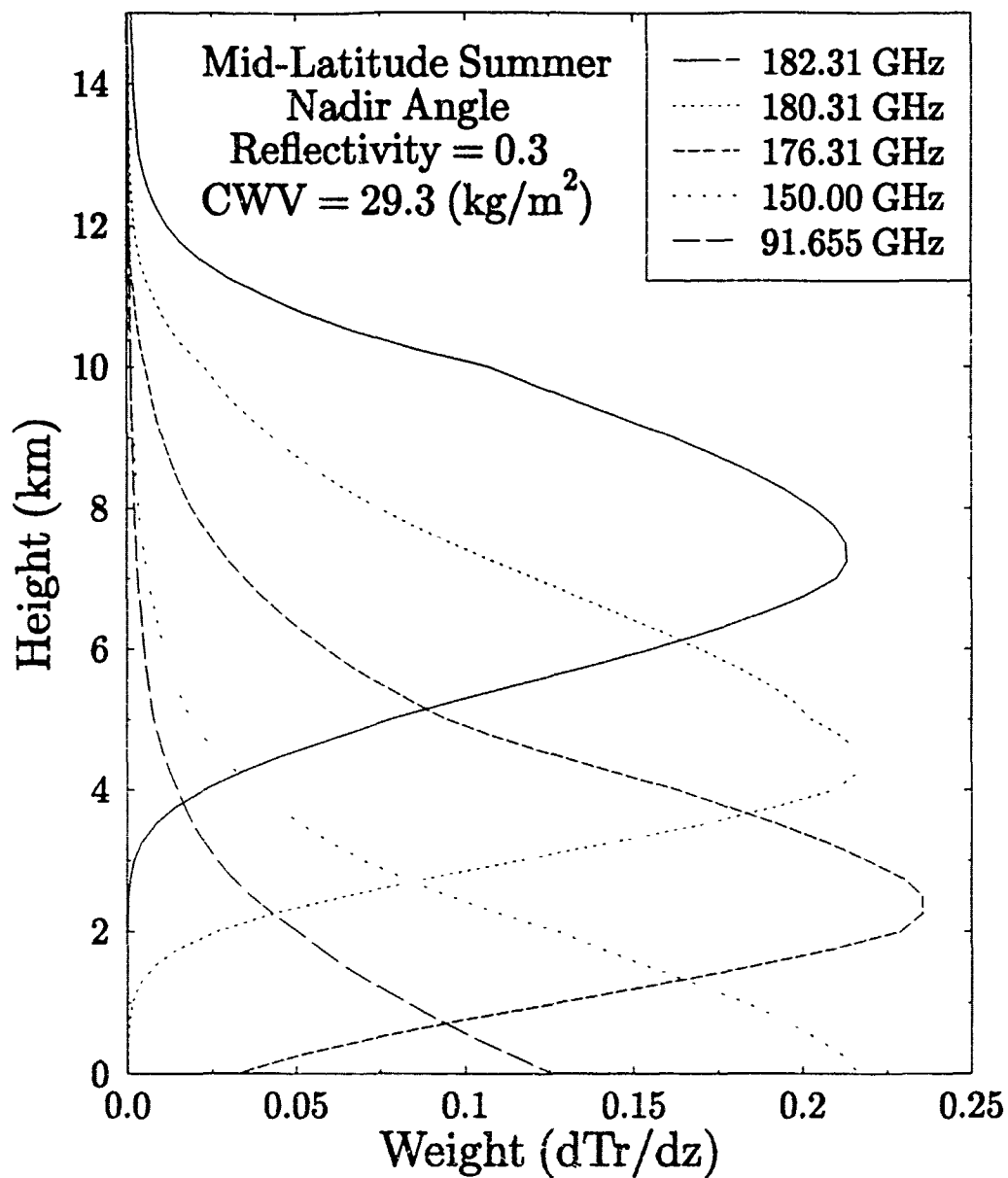


Figure 4.2: The same as Figure 4.1 except for a midlatitude summer atmosphere.

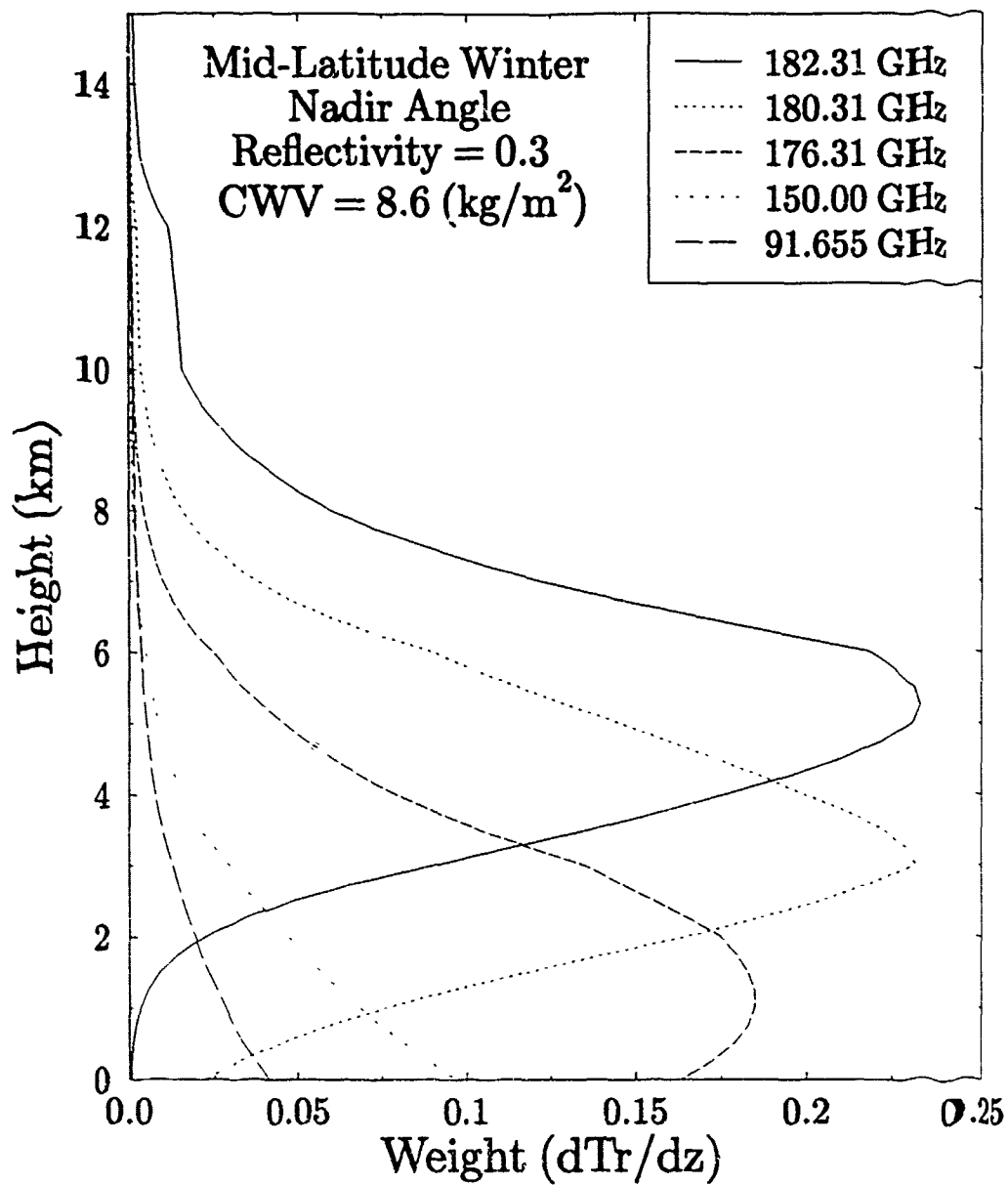


Figure 4.3: The same as Figure 4.1 except for a midlatitude winter atmosphere-

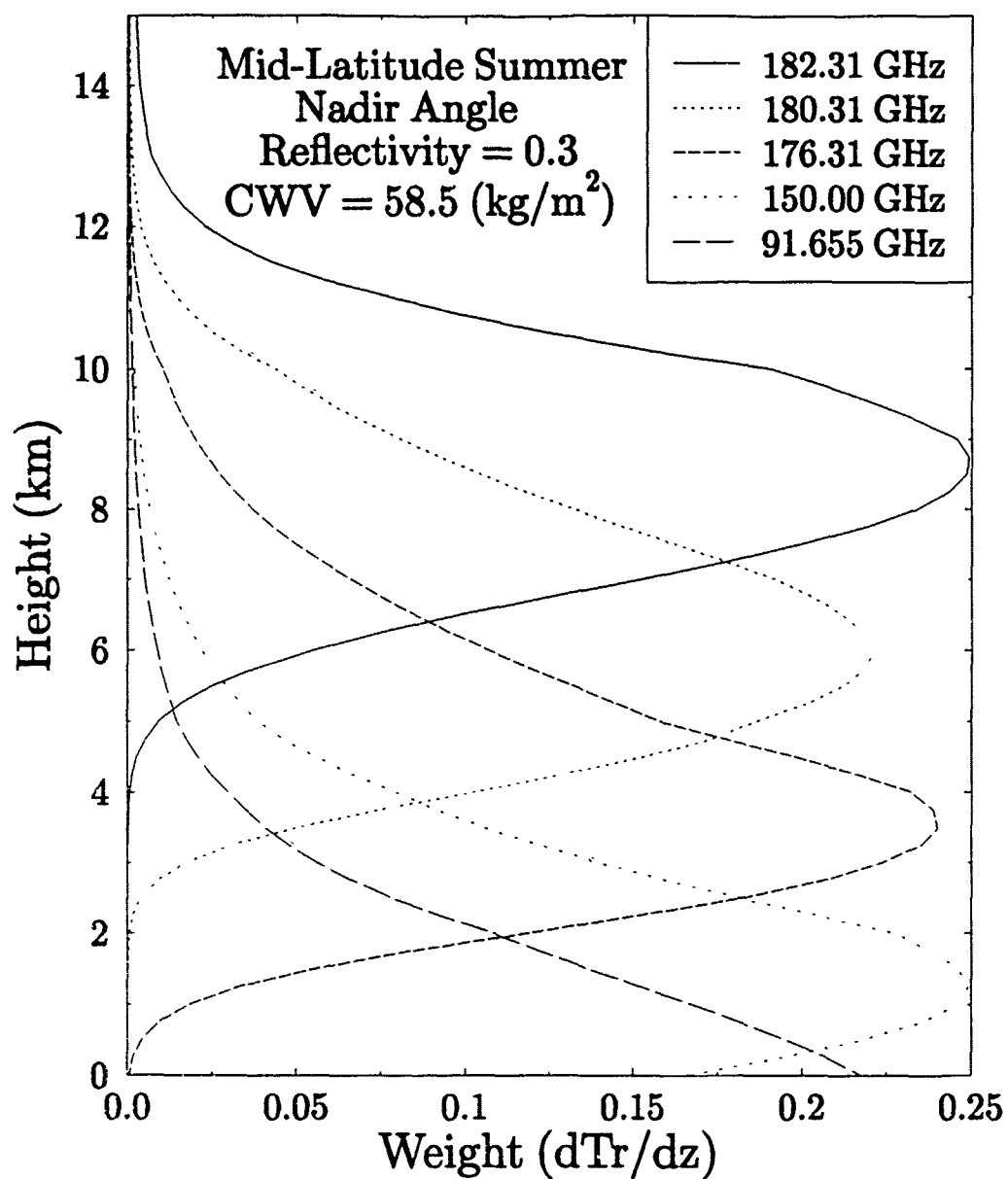


Figure 4.4: The same as Figure 4.2 except with $2 \times$ water vapor profile.

These four figures graphically show how the moisture profiles affect the weighting functions when it is plotted against height (km). Certainly there is a comprehensive change in the weighting functions when the atmospheric water vapor is doubled. This goes back to the discussion earlier about the nonlinearities in the process caused by the absorption factor.

Another way of graphically showing where the atmospheric constituents diminish the emission of the atmosphere and surface is to plot transmission versus altitude. Clear sky atmosphere plots of the transmission corresponding to Figures 4.1–4.3 are shown in Figures 4.5–4.7. Noteworthy is the generally similar appearance of each of the transmission curves and how the levels of the most rapid decrease in transmission with decreasing altitude correspond to the peaks of the weighting functions.

4.2 DEPENDENCE ON BACKGROUND

The surface reflectivity R (or emissivity $\epsilon = 1-R$) depends on the characteristics of the surface of the earth as viewed by the satellite radiometer. Land and coastal regions have large variations in surface emissivity and hence, the retrieval of moisture profiles can be expected to suffer degradation for these regions as compared with ocean surfaces.

4.2.1 Ocean Background

The emissivity of a smooth ocean surface can be calculated from the dielectric constant of water. Calculations using the dielectric data of Ray (1972) result in a value of ~ 0.7 for the emissivity of calm ocean water at 183 GHz. Lutz *et al.* (1990) have developed an algorithm (from Wilheit, 1990) with an iterative procedure for determining the emissivity for wind-roughened ocean surfaces or land surfaces. The effect of wind roughening procedure degrades the ability to retrieve moisture profiles (versus retrievals over a constant background).

The low emissivity of ocean surfaces is one important aspect which helps with the retrieval of low level moisture. This is because the radiometer senses emission from the warm atmosphere in contrast to a cold background which results in a large brightness temperature contrast. Additionally, the emissivity of a water surface is thought to be

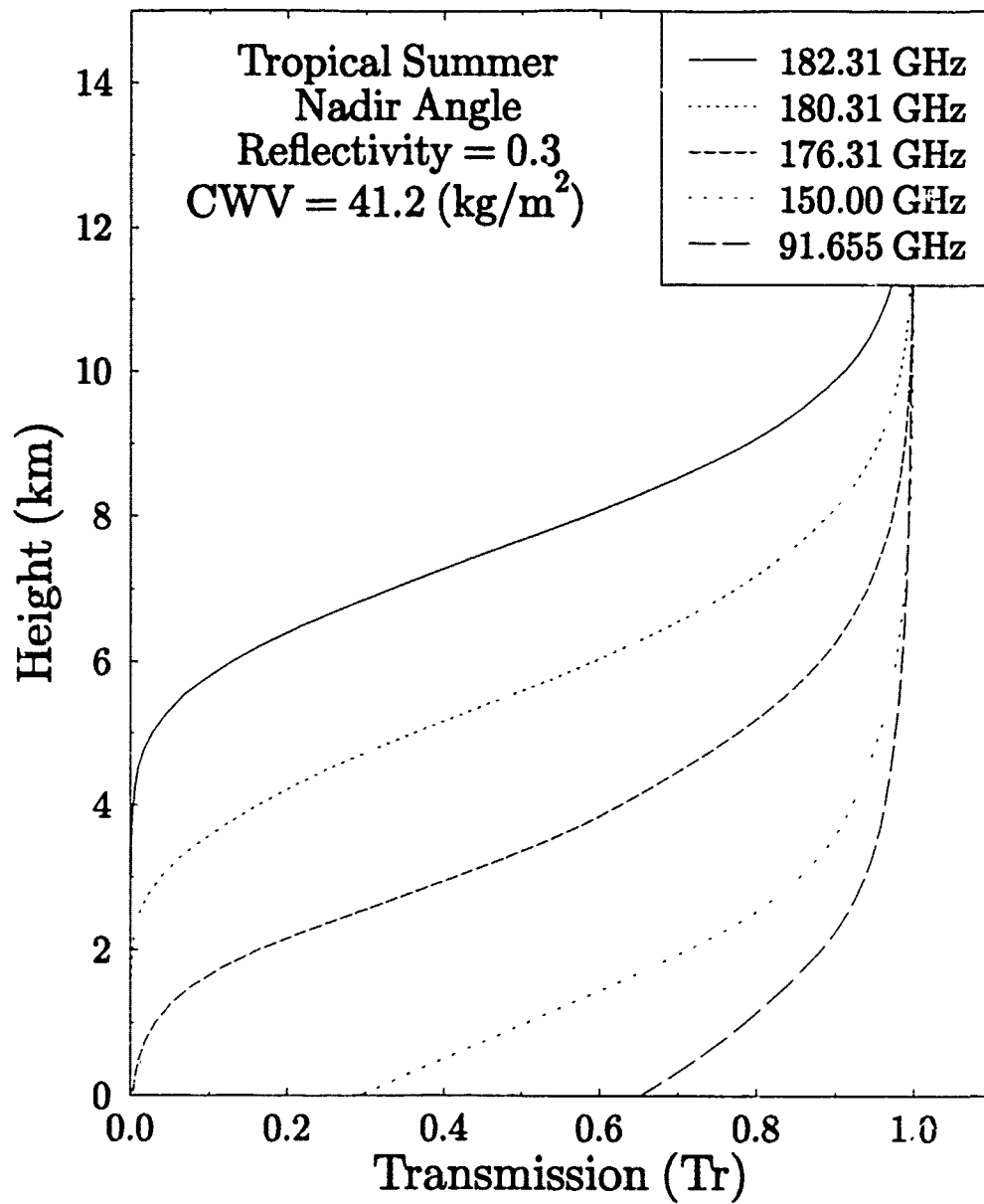


Figure 4.5: Clear sky transmission for the tropical atmosphere.

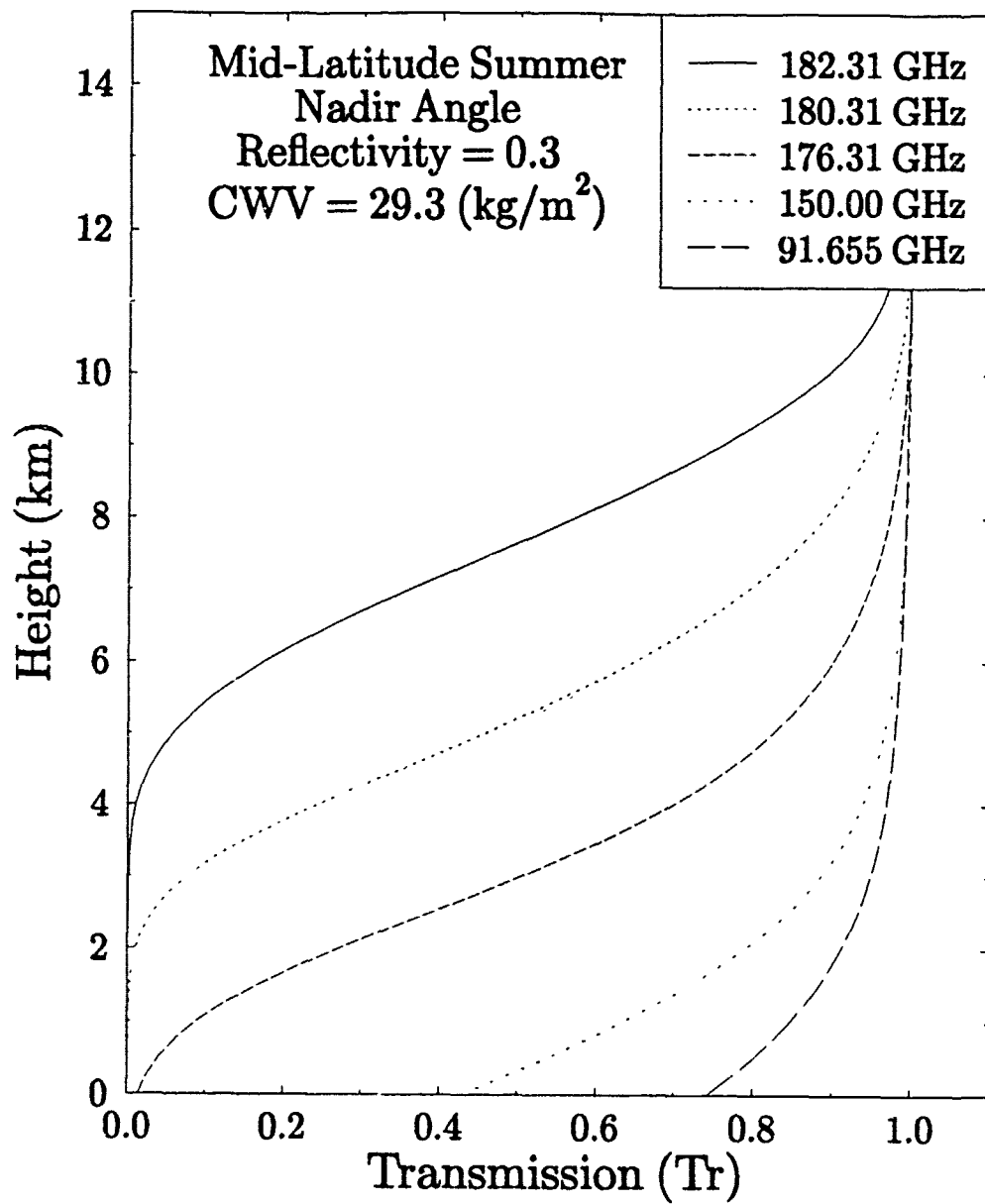


Figure 4.6: Clear sky transmission for the midlatitude atmosphere.

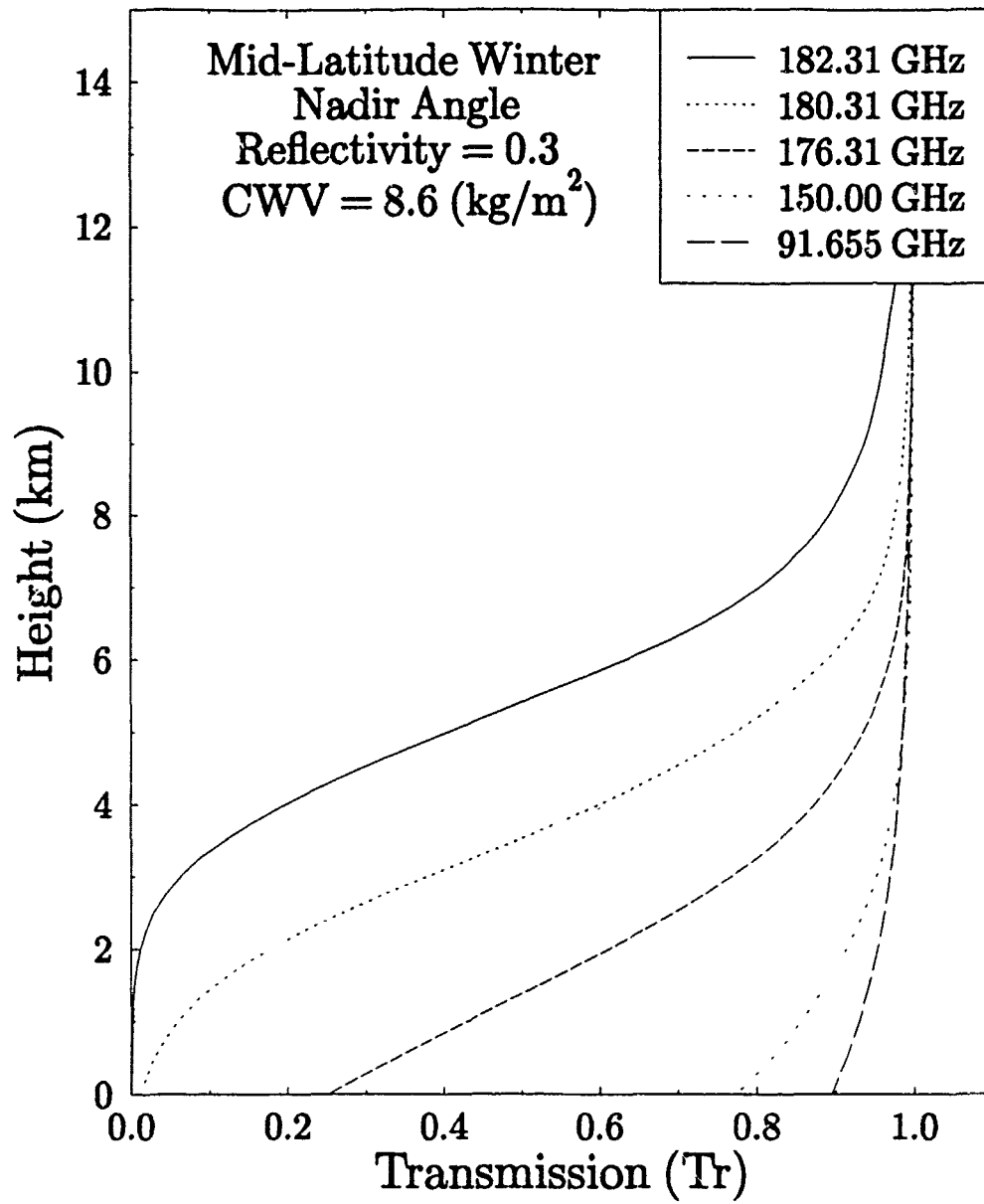


Figure 4.7: Clear sky transmission for the midlatitude winter atmosphere.

rather stable, especially when compared to land surfaces. One problem with the emissivity of the ocean is that it is a weak function of the surface wind speed above it. Various models (e.g. Wilheit, 1979 and Pandey and Kakar, 1982) were developed for determining the emissivity of a wind-roughened ocean surface for earlier instruments which operated at lower frequencies (e.g. SMMR and SSM/I). Currently, there is a dearth of models which are applicable for the region near 183 GHz.

To examine the effect of the emissivity of the ocean's surface, the emissivity of an ocean surface underlying a clear sky midlatitude winter atmosphere was varied between 0.82 and 0.64. These results are shown in Table 4.1.

Table 4.1: Brightness temperatures (K) for emissivities from 0.82 to 0.66 (reflectivities from 0.34 to 0.18) for a midlatitude winter atmosphere.

Midlatitude Winter Brightness Temperatures									
FREQ. (GHz)	Reflectivity								
	0.34	0.32	0.30	0.28	0.26	0.24	0.22	0.20	0.18
180.31	254.99	255.06	255.13	255.20	255.27	255.34	255.41	255.48	255.55
182.31	245.77	245.77	245.77	245.77	245.77	245.77	245.77	245.77	245.77
176.31	243.01	244.40	245.80	247.19	248.59	249.98	251.37	252.77	254.16
150.00	203.81	208.08	212.35	216.62	220.90	225.17	229.44	233.72	237.99
91.655	193.83	198.78	203.74	208.69	213.64	218.60	223.55	228.50	233.46

The channel closest to the absorption line (182.31 GHz) has the same brightness temperature for all emissivities since the atmosphere is so opaque that microwave thermal energy emitted and reflected by the surface does not reach the satellite (i.e. the surface term has no contribution). The 180.31 GHz channel is also basically unaffected by the surface reflectivity. The line wing channel (150 GHz) and the window channel (91.655 GHz) brightness temperatures change appreciably as the emissivity changes according to the values depicted in the table. This result will be discussed later with respect to the operational algorithm in use.

The root mean square (RMS) error calculated pre-launch performance of the T-2 with the *a priori* regression coefficients using the multiple linear regression technique employed

operationally showed the best retrieval statistics occurs over ocean backgrounds with their relatively uniform surface emissivity (Boucher *et al.*, 1993).

4.2.2 Land Background

The emissivity of dry land backgrounds is thought to vary from 0.8 to 1.0 over the range of frequencies of 140 to 200 GHz (Schaerer and Wilheit, 1979). These early values should be compared with those of Wang *et al.* (1992) below. As mentioned above, the Wilheit (1990) algorithm, as amended by Lutz *et al.*, retrieves the land emissivity by an iterative process as part of its computations.

The presence of vegetation cover, however, can change the reflectivity of land surfaces as vegetation generally is an absorptive medium and therefore decreases reflectivity values. Frozen soils also generally have low reflectivity values (~ 0.1). Soils with moisture contents of less than 50% have dielectric constants where the real part is less than 6 which yields a value of R of less than 0.15 (Wang and Schmugge, 1990).

Snow cover presents a different challenge. Wang *et al.* (1992), using the AMMS described in Chapter 1, observed emissivities as low as 0.58 when making flights over Alaska. They surmised that the reason for such low emissivities is due to scattering by snow particles on the ground. Wang *et al.* found the emissivities on these flights generally ranged from 0.6–0.9 which differ from the estimates of Schaerer and Wilheit of more than a decade ago.

Conceptually, low level moisture retrievals would be expected to be more difficult over land because of the high and variable emissivity of this surface. This presents the possible situation where emission from the lower level(s) of the atmosphere and the emission from earth's surface may be nearly at

the same brightness temperature. Isaacs and Deblonde (1985) noted that surface emissivity affects the retrieval accuracy at all levels and not just at the layers near the surface based on the statistical retrieval method they used.

Brightness temperatures for an ocean surface with an emissivity of 0.7 and for a land surface with an emissivity of 1.0 are compared in Table 4.2.

The three channels nearest the absorption line (182.31 GHz channel not shown) are virtually unaffected by the surface emissivity. However, this is certainly not the case for the 150 and 91.655 GHz channels. Radically different brightness temperatures are computed for cases with emissivities of 1.0 and 0.7 for these channels. This is simply the factor of a warm background and a cold background, respectively.

As mentioned above, for the ocean background case in Table 4.1 brightness temperatures for the 150 and 91.655 GHz changed appreciably for small emissivity changes. The operational algorithm retrieves the surface emissivity using the 91.655 GHz channel and a physical retrieval model (Griffin *et al.*, 1993).

4.3 DEPENDENCE ON CLOUDS

Water clouds affect microwave radiation primarily through the processes of absorption and emission. As discussed in the previous chapter, Rayleigh absorption is assumed by the cloud model (MPM92) being used. The process of scattering is usually considered negligible since the single scatter albedo, $\tilde{\omega}$, at the microwave/millimeter wavelengths is very small.

To depict the effects of clouds on weighting functions, Figures 4.8–4.12 show the five cloud models for a tropical atmosphere over an ocean ($R = 0.3$ or $\epsilon = 7$) background. For the cloud models used, and from the study of the figures shown, the following conclusions are deduced:

1. The channel closest to the absorption line does not 'see' any of the low level water clouds.
2. The 180.31 GHz channel sees only those clouds with cloud tops above 2 km.
3. The weighting functions for the other three channels are radically affected by clouds in the FOV.
4. The weighting functions peak sharply at the cloud top.

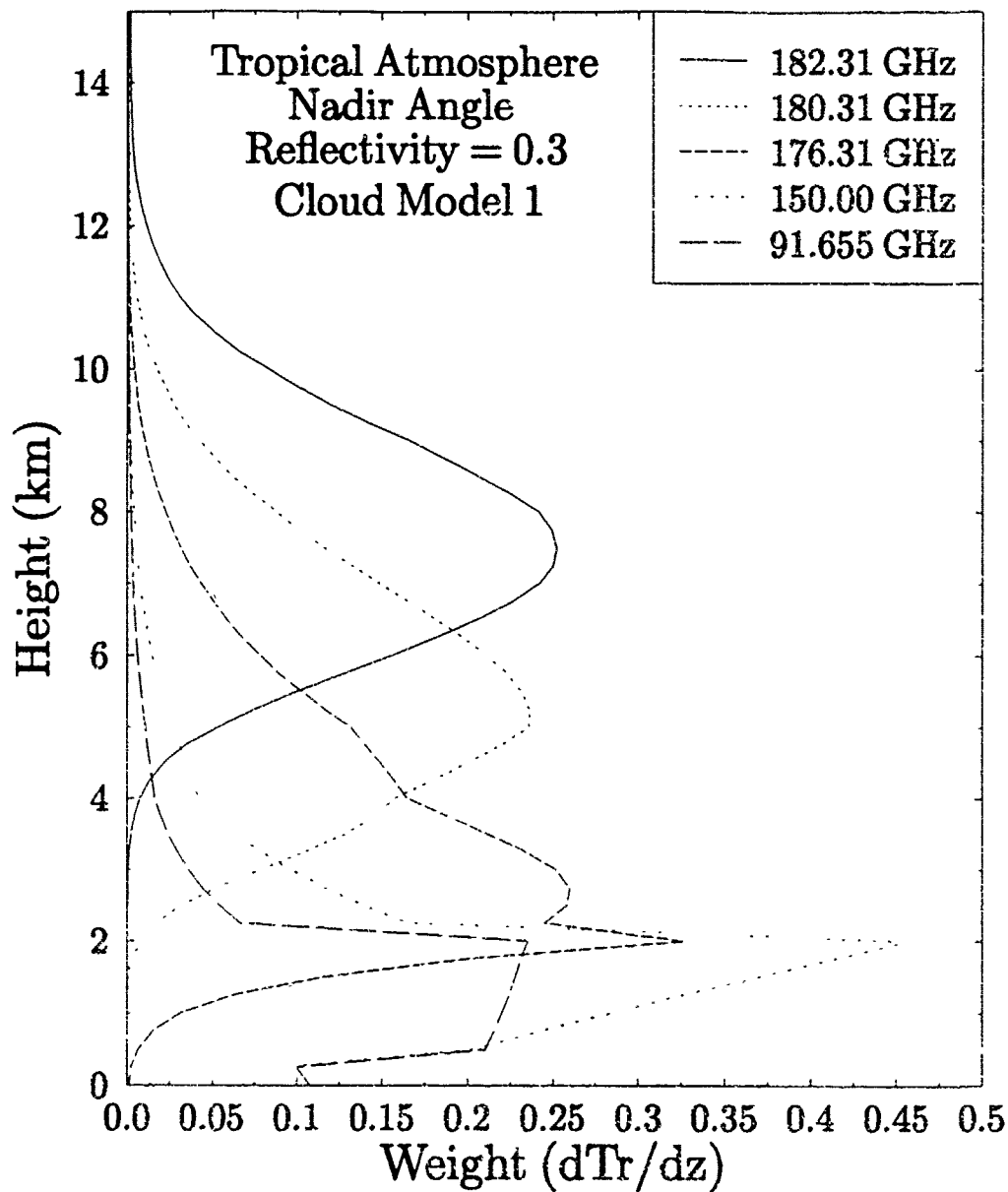


Figure 4.8: Weighting functions as in Figure 4.1 except for stratus cloud ($w = 0.15\text{gm}^{-3}$) from 0.5-2.0 km (cloud model 1).

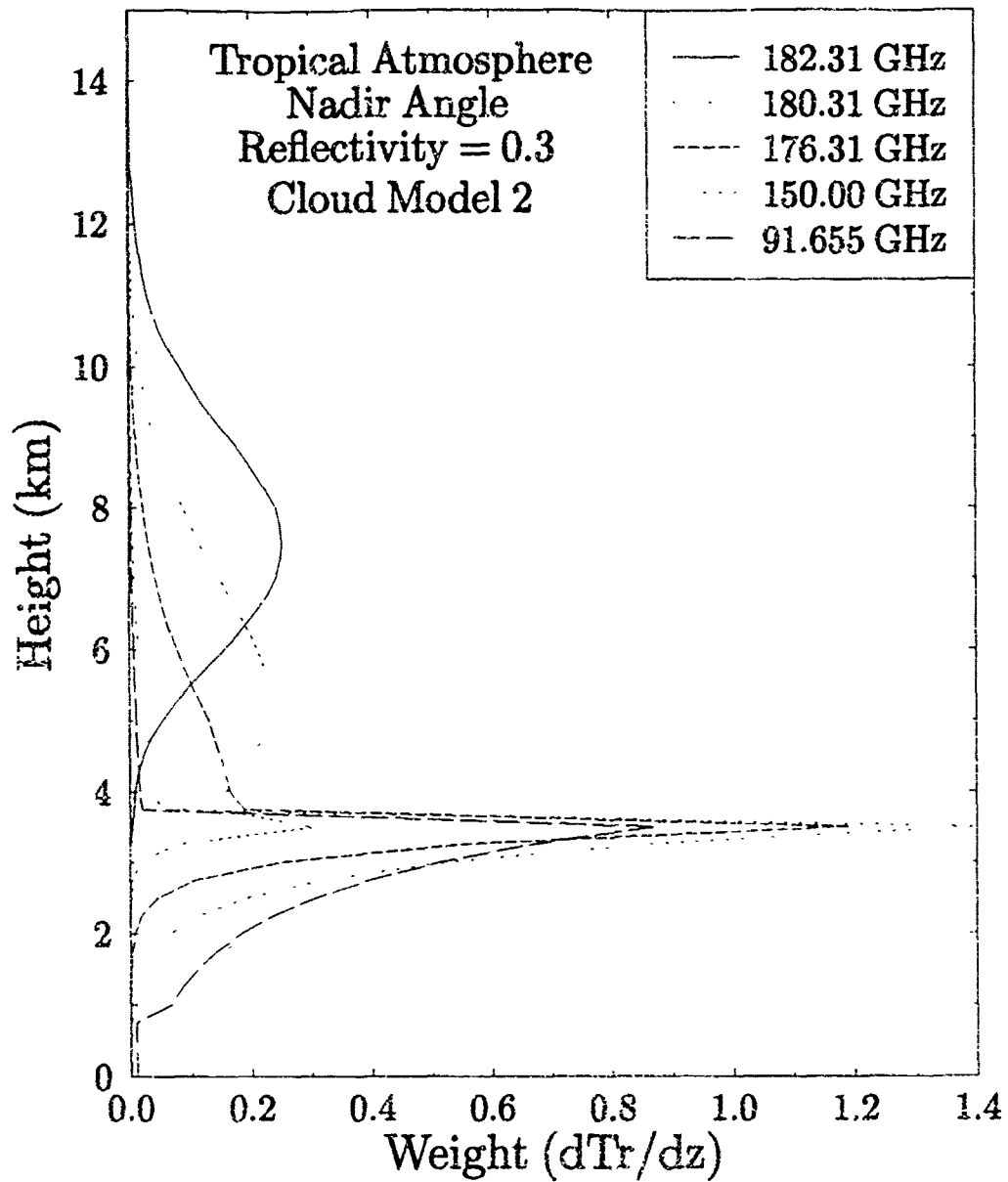


Figure 4.9: The same as Figure 4.8 except for cumulus cloud ($w = 1.0 \text{ gm}^{-3}$) from 1.0-3.5 km (cloud model 2).

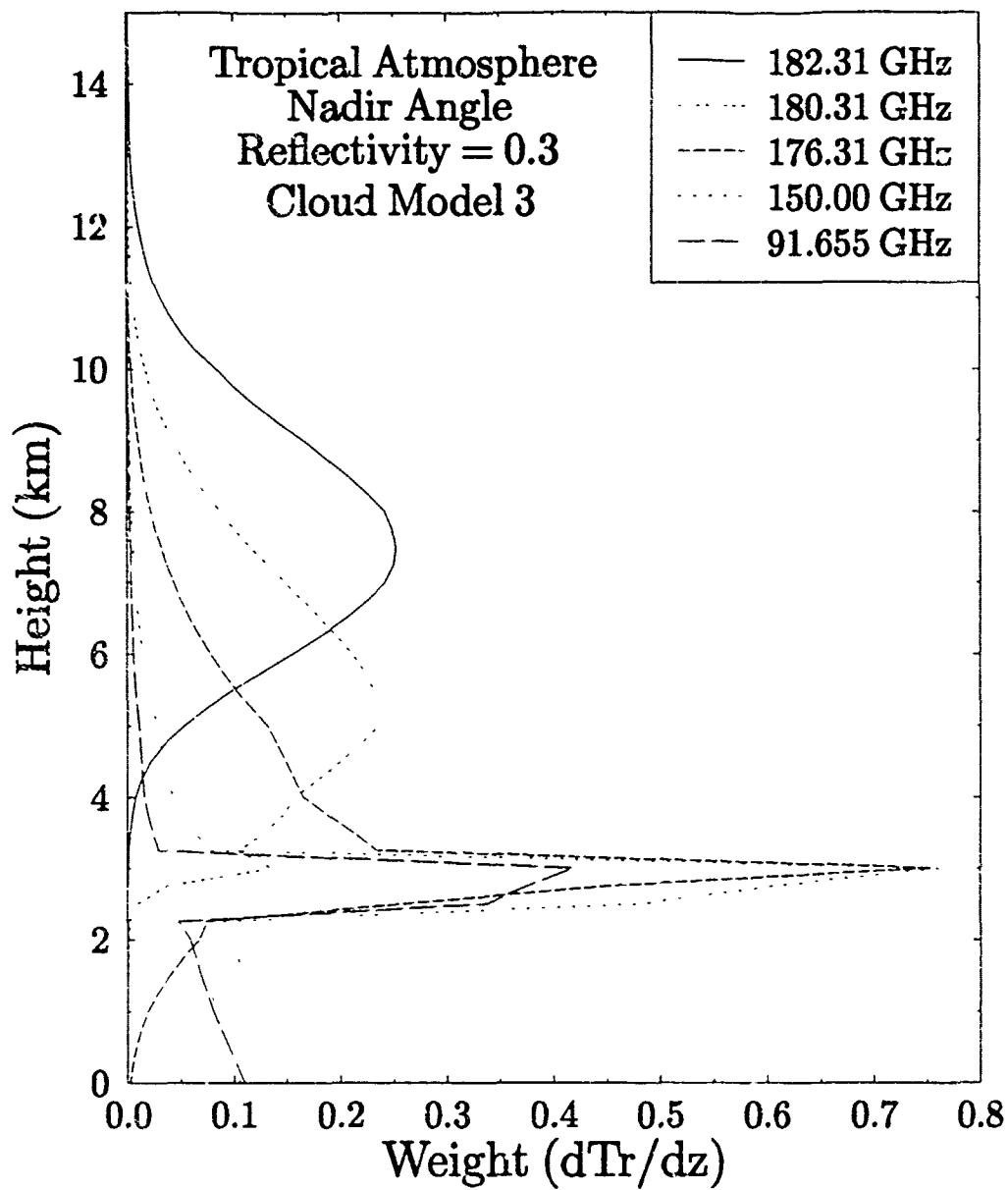


Figure 4.10: The same as Figure 4.8 except for altostratus cloud ($w = 0.40 \text{ gm}^{-3}$) from 2.5-3.0 km (cloud model 3).

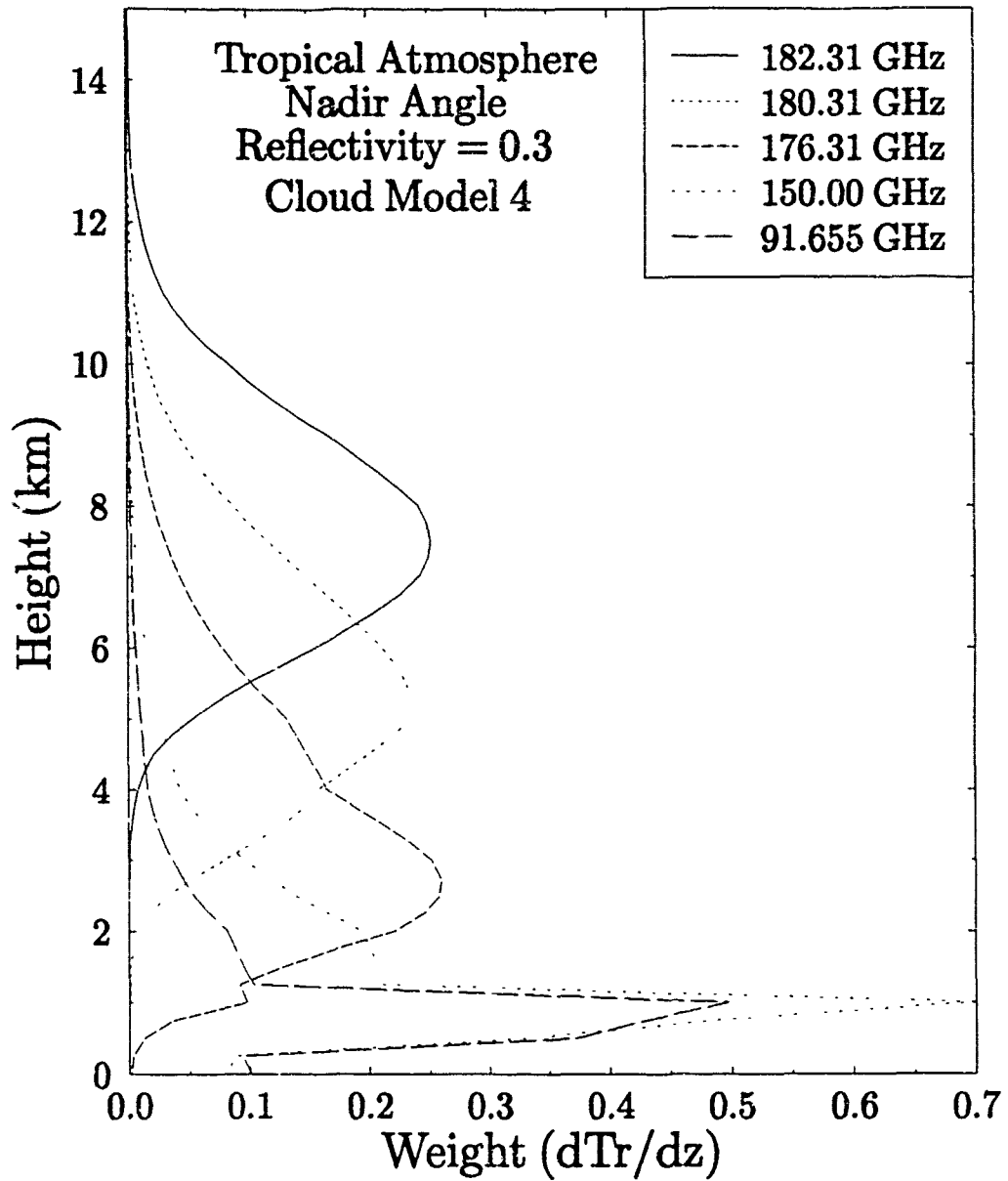


Figure 4.11: The same as Figure 4.8 except for stratocumulus cloud ($w = 0.55 \text{ gm}^{-3}$) from 0.5-1.0 km (cloud model 4).

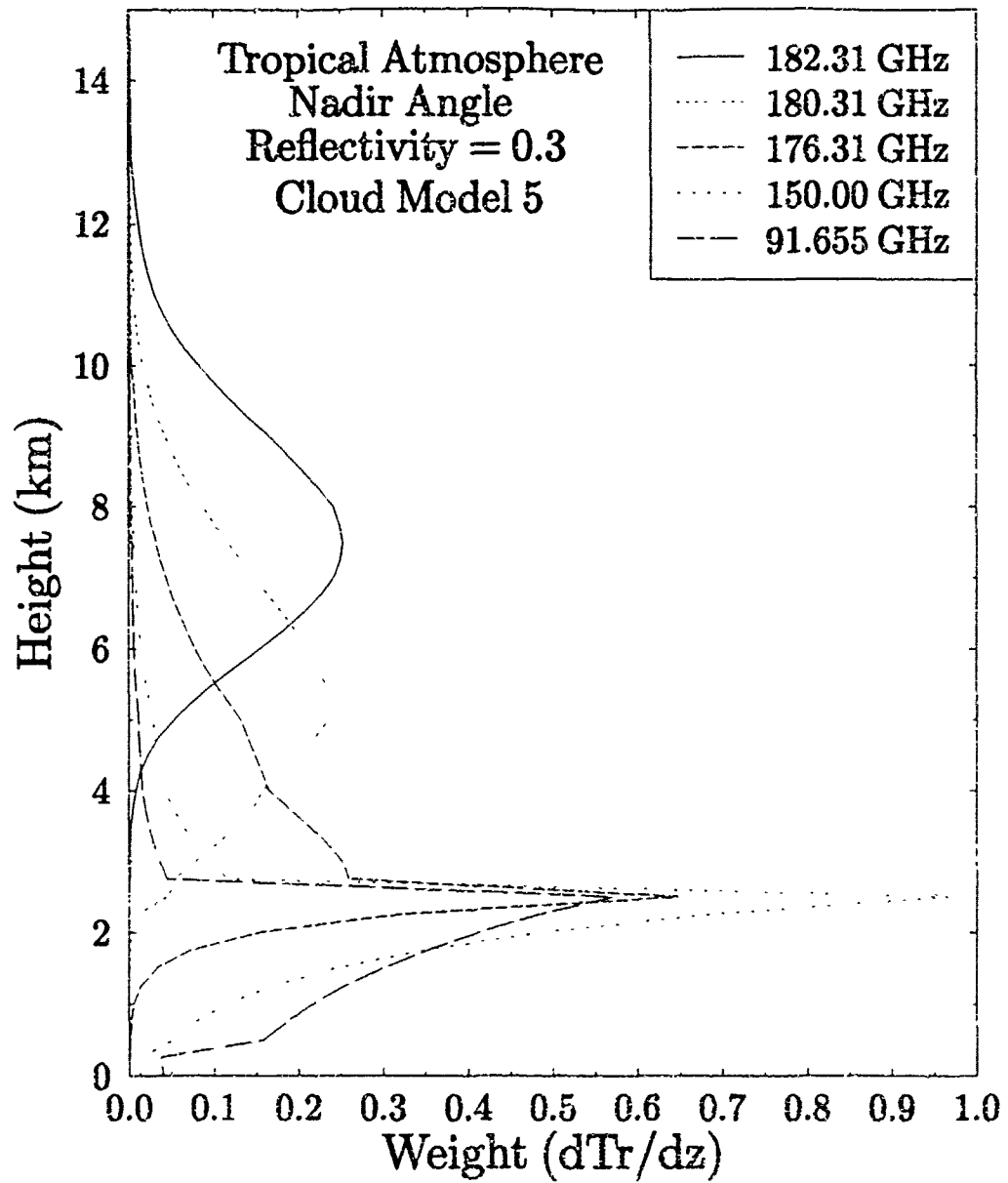


Figure 4.12: The same as Figure 4.8 except for nimbostratus cloud ($w = 0.61 \text{ gm}^{-3}$) from 0.5-2.5 km (cloud model 5).

4.3.1 Dependence on Layer Thickness

The microwave properties of clouds in the Rayleigh absorption regime are defined by several factors. One factor is the thickness of the cloud layer. This is because for a very thin cloud, much of the microwave energy from below is transmitted through the cloud layer. To determine the effect of varying cloud thicknesses on the brightness temperatures at satellite altitude, clouds were inserted into the tropical atmosphere with a constant cloud base of 1 km. Cloud thicknesses were varied from 1 to 5 km by 1 km increments. Table 4.3 shows simulated brightness temperatures for clouds of variable thickness and liquid water content. According to the simulations (summarized in this table), the 150 GHz channel and to a lesser extent the 92 GHz are the most responsive to the presence of clouds. The responsiveness in the 150 GHz channel is expected since it is designed to peak near the surface as depicted in Figure 4.1. Note that brightness temperatures decrease for increasing LWC and increasing cloud thickness (Δz) with a land background. The reason for this is that the clouds diminish the effects of the surface term.

4.3.2 Dependence on Layer Location

It has been seen that the weighting functions for atmospheres containing clouds tend to peak near the cloud top. This gives a good indication of the effects of where a cloud is located in the atmosphere and its influence on brightness temperatures.

To determine the influence of the layer location on brightness temperature, Table 4.4 shows the simulated brightness temperatures for a tropical atmosphere with a constant cloud thickness, reflectivity, and a varying cloud base and liquid water content. The data in this table indicates how the brightness temperatures decrease as a cloud is moved higher into the atmosphere. This is expected since the temperature profile decreases with height and the cloud limits the microwave emissions from below it.

4.3.3 Dependence on Cloud Liquid Water Content

Figures 4.13–4.16 depict brightness temperatures for the five T-2 channels for several cloud models with the LWC varied from 0.0 to 0.50 gm^{-3} . The brightness temperatures for the 3 channels near 183 GHz are basically constant whereas for the 150 and 91.655

Table 4.2: Comparison of brightness temperatures for land ($\epsilon = 1.0$) and ocean ($\epsilon = 0.7$) surfaces.

Brightness Temperature								
Atmospheric case	180.31 GHz		176.31 GHz		150.00 GHz		91.655 GHz	
	Land	Ocean	Land	Ocean	Land	Ocean	Land	Ocean
Clear tropical	264.71	264.71	277.58	277.36	291.19	265.12	295.95	237.72
Clear ML sum.	263.54	263.54	276.32	275.08	290.91	252.62	295.84	229.72
Clear ML winter	256.44	255.31	271.77	249.34	291.92	223.19	295.93	216.26
Cloud model 1	256.89	256.89	269.82	269.81	284.18	272.76	292.04	248.02
Cloud model 2	264.67	264.67	276.89	276.87	289.13	277.67	294.28	253.08
Cloud model 3	262.32	262.32	271.23	271.23	278.64	278.51	283.51	279.32
Cloud model 4	263.92	263.92	275.58	275.52	286.91	273.42	292.59	250.31
Cloud model 5	264.71	264.71	277.22	277.18	289.55	278.92	294.77	255.77

Table 4.3: Brightness temperatures for variable cloud thickness (Δz (km)) and LWC (gm^{-3}) for a fixed cloud base (1 km), emissivity (0.97), and a tropical atmosphere.

BRIGHTNESS TEMPERATURES (K)					
Cloud LWC	Δz (km)	FREQUENCY (GHz)			
		180.31	176.31	150.00	91.655
Cloud Model 1 LWC = 0.15	1	264.67	276.92	287.85	289.91
	2	264.08	276.00	286.20	288.91
	3	263.11	274.26	283.54	287.14
	4	261.99	271.69	280.13	284.67
	5	260.36	268.58	276.24	281.69
Cloud Model 2 LWC = 1.00	1	264.62	275.24	284.30	288.59
	2	263.42	272.68	280.90	285.34
	3	261.25	269.58	275.91	280.37
	4	258.78	265.44	269.86	274.15
	5	255.71	260.65	263.89	267.92
Cloud Model 3 LWC = 0.40	1	264.65	276.50	286.97	289.59
	2	263.90	275.16	284.43	287.69
	3	262.63	272.95	280.49	284.44
	4	261.17	269.61	275.41	279.97
	5	259.13	265.53	269.92	274.90

Table 4.4: Brightness temperatures for variable cloud base and LWC for a fixed emissivity ($\epsilon = 1.0$) and atmosphere (tropical).

BRIGHTNESS TEMPERATURE (K)						
Cloud Base (km)	LWC (gm^{-3})	FREQUENCY (GHz)				
		182.31	180.31	176.31	150.00	91.655
1	0.15	251.24	264.67	276.92	289.34	294.49
1.5	0.15	251.24	264.50	276.57	288.69	294.02
2	0.15	251.23	264.08	276.14	287.99	293.55
3	0.15	251.11	263.13	274.65	286.24	294.43
5	0.15	249.51	260.88	271.16	283.08	290.25
1	1.00	251.24	264.62	275.24	284.54	290.43
1.5	1.00	251.24	264.26	273.99	282.95	288.81
2	1.00	251.23	263.42	272.73	281.44	287.32
3	1.00	251.04	261.25	269.71	276.77	283.11
5	1.00	247.74	255.82	261.20	265.86	273.27

GHz channels brightness temperatures vary with liquid water content, cloud location, and cloud thickness.

Figures 4.15 and 4.16 are identical except for the emissivity (reflectivity). The latter figure shows the effects of the clouds by decreasing the 91.655 and 150 GHz brightness temperatures over a 300 K surface as the cloud liquid water content is increased. Contrast this to Figure 4.15 where the brightness temperature for a low emissivity surface (cold background at 210 K, as discussed above). In this case, the brightness temperatures of the window channels systematically increases as the liquid water path (LWP) is increased.

This yields the observation that clouds generally increase brightness temperatures over oceans and decrease brightness temperatures over land. These effects, however, appear only in the window channels and to a lesser extent in the 183 ± 7 GHz channel, depending on cloud altitude. This response to clouds can also be seen in Table 4.2. The near linear response of the window (especially) and line wing channel (as shown in Figure 4.13) to changes in LWC offers a simple way of retrieving this cloud property by using these channels. Several authors have considered this (including Isaac *et al.*, 1985).

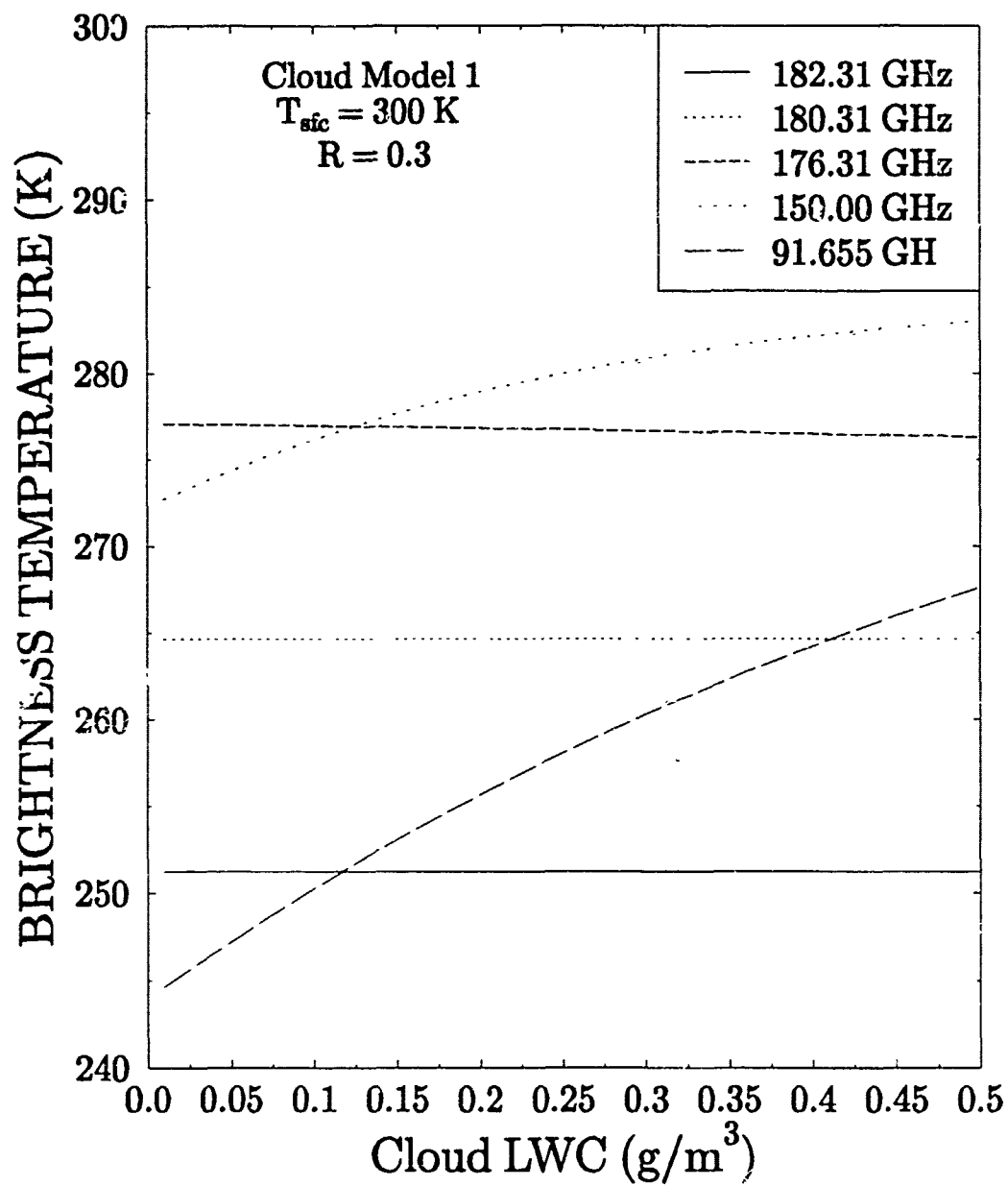


Figure 4.13: Brightness temperatures for Cloud Model 1 and a tropical atmosphere with LWC from 0.01 to 0.50 gm^{-3} .

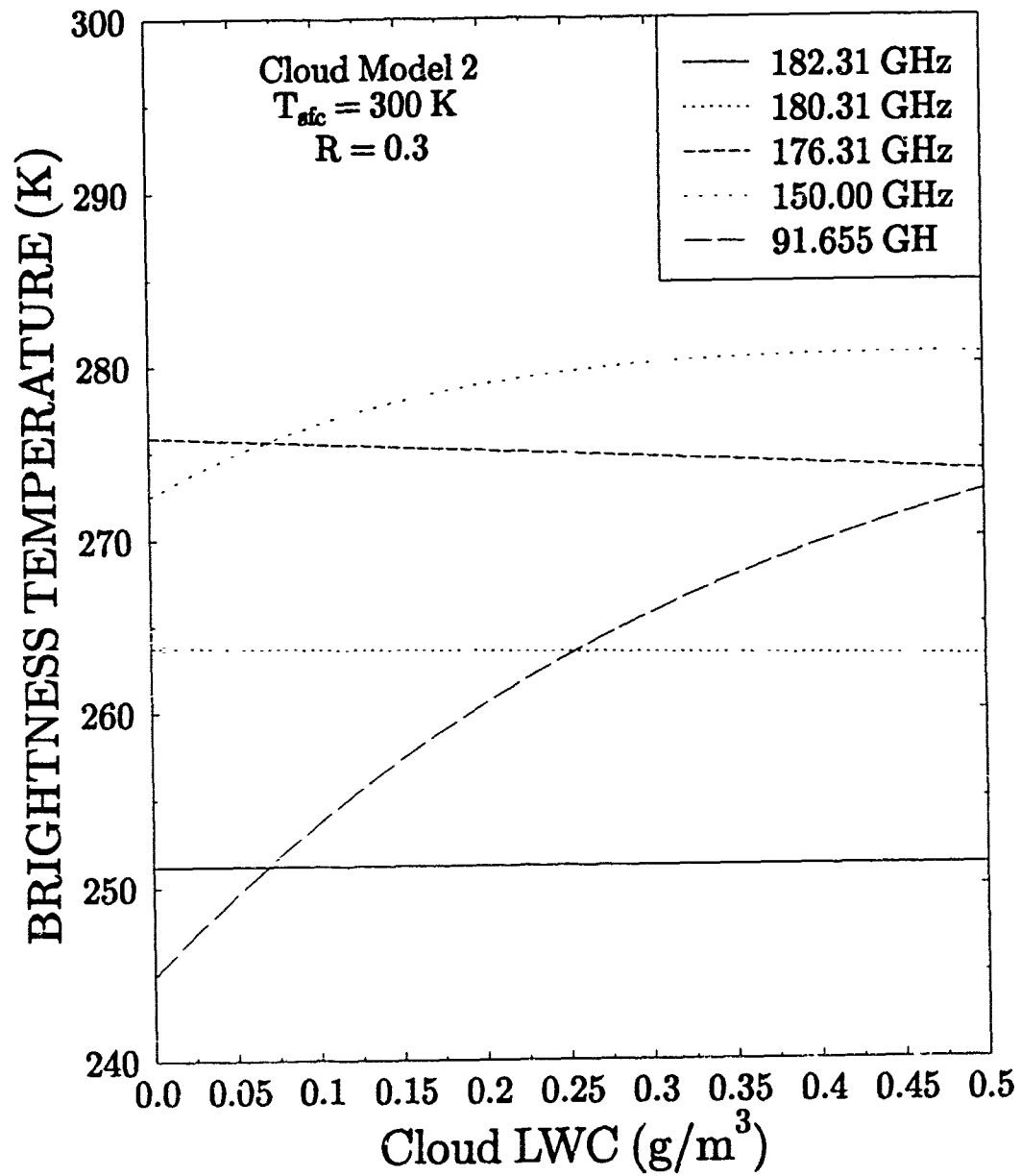


Figure 4.14: Brightness temperatures as in Figure 4.13 except for Cloud Model 2.

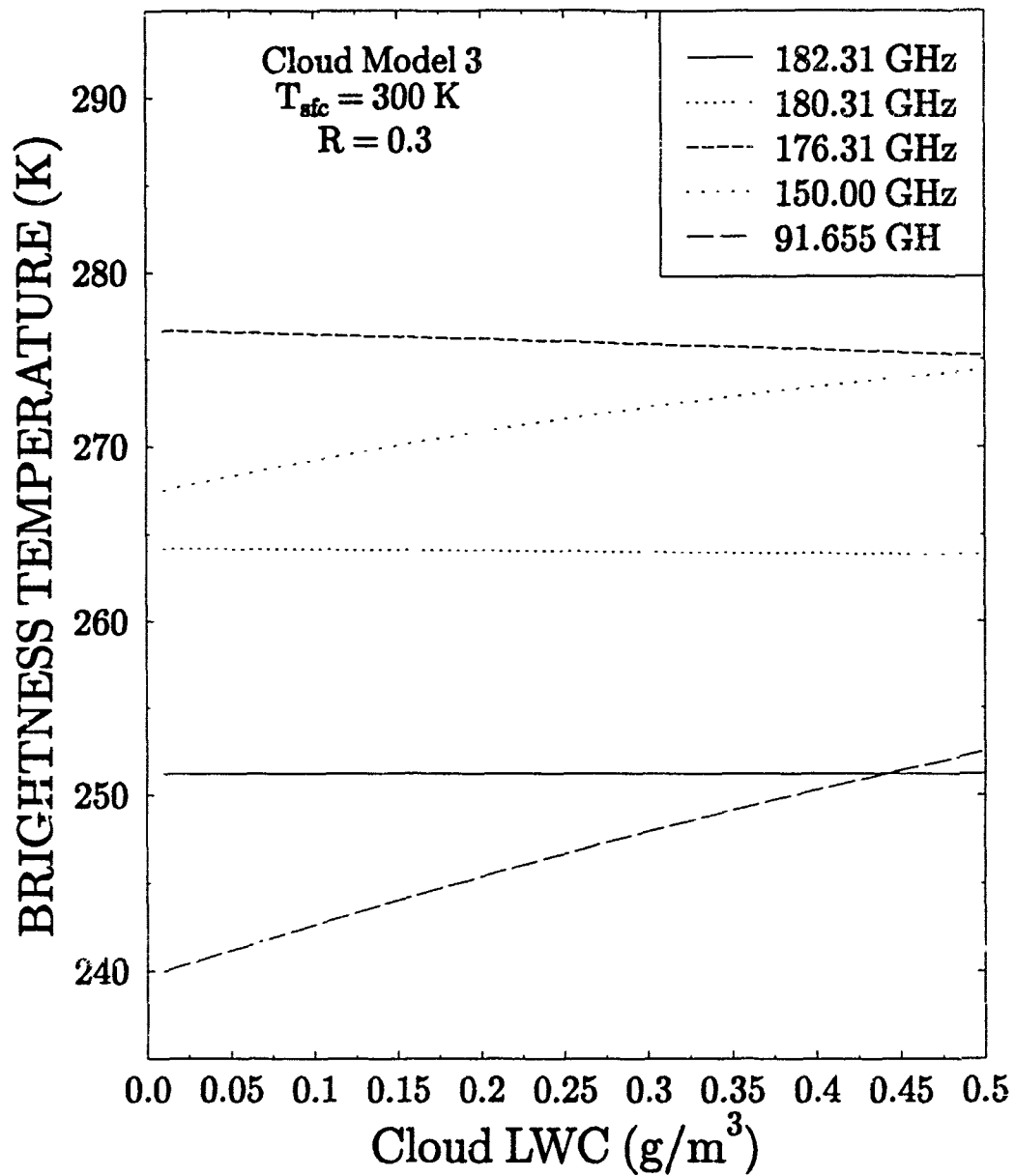


Figure 4.15: Brightness temperatures as in Figure 4.13 except for Cloud Model 3.

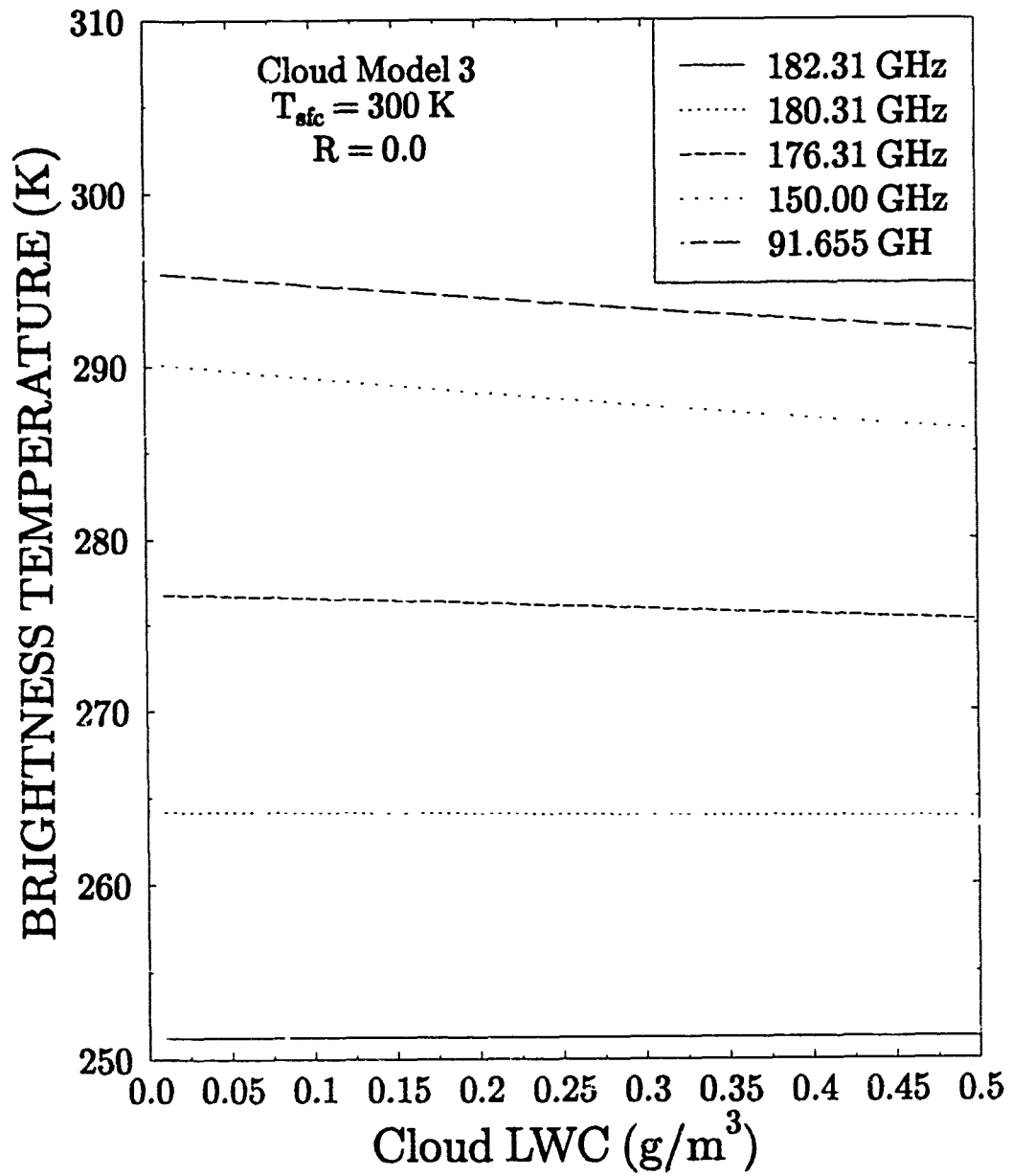


Figure 4.16: Brightness temperatures as in Figure 4.15 except for $R = 0.0$.

4.4 SCAN ANGLE EFFECTS

The effects of scan angle on brightness temperatures can be considered through the use of MPM92. Scan angle affects brightness temperatures since it changes the optical path. As shown in Figure 3.1, the scan angle (or scene station view angle as in Figure 3.1) on the SSM/T-2 varies between 1.5° and 40.5° as the sensor scans across a line. Unfortunately, there is no easy way to correct for this change in brightness temperature for the change in the atmospheric path which is viewed. Figures 4.17 and 4.18 show that the brightness temperature can both increase or decrease as the sensor moves away from nadir. There are competing effects here; limb darkening, occurs when the sensor moves away from nadir and the path length increases and the weighting functions move upwards vertically in the atmosphere. Limb brightening occurs for the wing and window channels which sense near the surface. The temperature of a cold surface is replaced by higher temperatures as the path is extended by viewing away from nadir. This complex problem would likely be handled operationally through the use of regression equations. For example, regression equations are used to solve the scan angle differences for the MSU (Grody, 1983).

4.5 INTERPRETATION OF RESULTS

The SSM/T-2 responds to a variety of atmospheric phenomenon in a manner much different than those instruments which preceded it in the remote sensing of the atmosphere. In this chapter it has been shown that:

1. Weighting functions and brightness temperatures are dependent on the moisture and temperature profile of the atmosphere.
2. The background and its emissivity have a significant effect on the brightness temperatures of the window channels.
3. Backgrounds with higher emissivities result in higher brightness temperatures.
4. Liquid water clouds that form low in the atmosphere have a profound influence on brightness temperatures in the window channels.

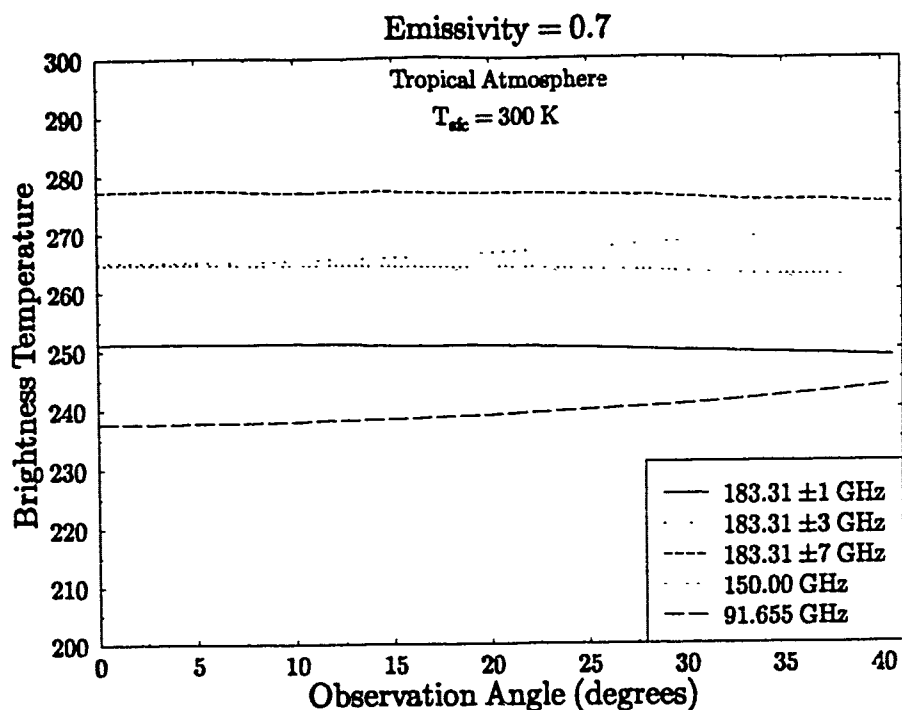


Figure 4.17: Brightness temperatures as a function of observation angle for a tropical atmosphere.

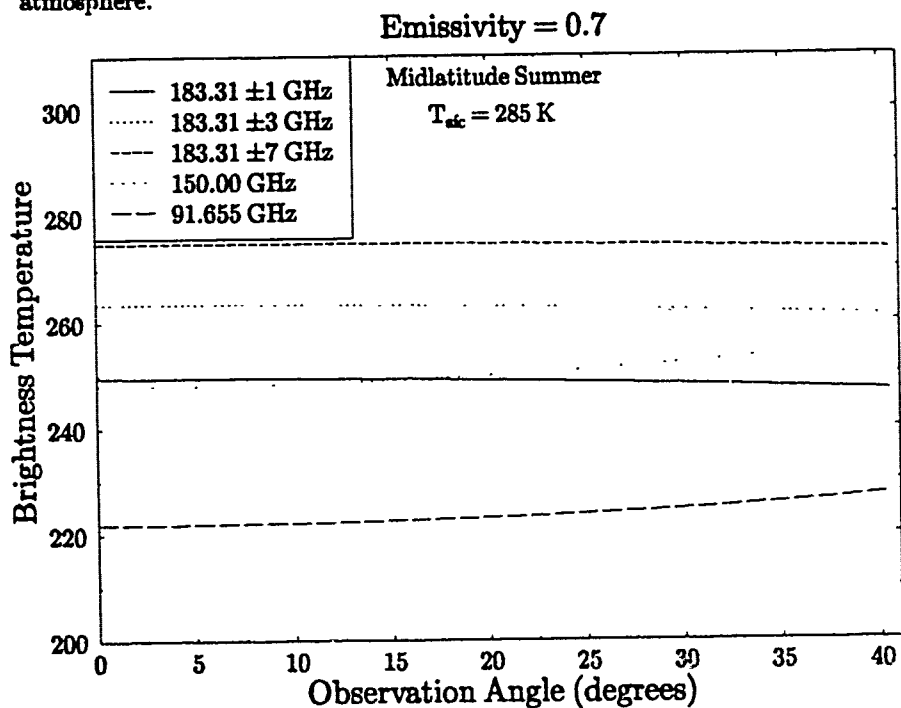


Figure 4.18: The same as Figure 4.17 except for a midlatitude summer atmosphere and $T_{at} = 285 \text{ K}$.

- (a) Increasing cloud LWC decreases brightness temperatures.
- (b) Higher clouds correspond to lower brightness temperatures.
- (c) Liquid water content affects the 91 and 150 GHZ channels brightness temperatures greatly.
- (d) Clouds generally increase brightness temperatures over ocean surfaces and decrease brightness temperatures over land.

Certainly water clouds affect brightness temperatures in a systematic manner. Clouds become more difficult to quantify when one considers the possibility of mixed phase clouds, ice clouds, and partial cloud cover.

Chapter 5

WATER VAPOR BURDEN

In this chapter a simple method is described for deriving the column vapor burden from brightness temperatures. It will be demonstrated how the measured brightness temperatures, especially those of 183 ± 1 GHz (Channel 2) and 183 ± 3 GHz (Channel 1), correspond to a level of constant water vapor overburden. This result together with temperature-pressure data are used to establish the burden at a constant pressure. The method is demonstrated using only Channel 2 brightness temperatures.

5.1 WATER VAPOR BURDEN AND THE SSM/T-2 FREQUENCIES

The approach followed is from the study of Rosenkranz *et al.* (1982) who describe the temperature weighting functions for both the oxygen band (e.g. SSM/T-1 frequencies) and for the water vapor absorption line at 183.31 GHz. They define the integrated column water vapor above a given level as the water vapor burden (U) which is proportional to τ , the optical depth. Rosenkranz *et al.* also noted that when weighting functions are expressed as functions of water vapor burden rather than as functions of pressure or temperature, these weighting functions are nearly symmetric in shape and their peaks are invariant with respect to changes in the water vapor profile. These functions are also displaced downward as the frequency varies away from the absorption line at 183 GHz.

Another way of stating this principle is that the water vapor burden may be expressed as:

$$U(h) = \int_h^{\infty} \rho(h') dh', \quad (5.1)$$

where $\rho(h)$ is the water vapor density as a function of height, h . This means that the satellite brightness temperature is a weighted average of the temperature profile. The

weighting is defined by the weighting function, which, when expressed in terms of U , is approximately invariant with respect to changes in $\rho(h)$. Therefore, for a temperature profile with (say) a linear lapse rate near the peak of the weighting function, the brightness temperature and thermometric temperature of the atmosphere will be equal at the peak of the weighting function (Wilheit and al Khalaf, 1993). This leads to the hypothesis that the water vapor burden at the level where the atmospheric temperature (T_t) equals the brightness temperature (T_b) will be constant for a given frequency independent of the water vapor profile.

To test this hypothesis, the 3 atmospheric profiles described in Chapter 3 were used for clear sky temperature/pressure profiles and various water vapor profiles (using the water vapor multiplicative factor) were employed to yield 47 cases. The water vapor burden was calculated using (5.1) where the height h is the altitude where $T_t = T_b$. Table 5.1 shows the results for these water vapor burdens for the brightness temperatures at 183.31 ± 1 GHz for these 47 different atmospheric cases.

Nine cases result in water vapor burdens of less than 0.35 kg/m^2 for the 47 cases in Table 5.1. Certainly, one can argue whether case 7 is a physically realistic atmosphere. The other cases with low water vapor burdens are for small water vapor multiplicative factors. Nonetheless, the hypothesis appears realistic for the 183.31 ± 1 GHz channel. For the cases considered in Table 5.1 a mean water vapor burden of 0.3735 kg/m^2 and a root mean square error (RMSE) value of 0.0256 kg/m^2 .

Water vapor burdens were also calculated for the same 47 cases for 183.31 ± 3 GHz. These results are listed in Table 5.2. Again the values of water vapor burden are reasonably constant with a mean and RMS values of 1.2739 kg/m^2 and 0.3709 kg/m^2 , respectively. The cases with very low water vapor burdens are characterized by optical depths of less than 4, meaning the surface emissivities are influencing the brightness temperatures. Computing these statistics for only the 40 highest cases yields a mean and RMSE of 1.4097 and 0.1486 kg/m^2 , respectively.

In Table 5.2, case 8 has a surface relative humidity of about 14% with the surface temperature near 20°C . Cases 16, 17, and 18 have relative humidities of 25–47% with a

Table 5.1: Water Vapor Overburdens (U) at 183 ± 1 GHz for $T_b = T_t$.

CASE	H ₂ O MULT. FACTOR	TEMPERATURE PROFILE	WATER VAPOR PROFILE	U (kg/m ²)	CWV (kg/m ²)
1	0.50	Tropical	Tropical	.4083	20.61
2	0.75	Tropical	Tropical	.3954	30.91
3	1.0	Tropical	Tropical	.3910	41.21
4	1.25	Tropical	Tropical	.3806	51.51
5	1.50	Tropical	Tropical	.3639	61.82
6	1.75	Tropical	Tropical	.3505	72.12
7	2.00	Tropical	Tropical	.3389	82.42
8	0.25	ML summer	ML summer	.3962	7.32
9	0.50	ML summer	ML summer	.3844	14.64
10	0.75	ML summer	ML summer	.3849	21.95
11	1.0	ML summer	ML summer	.3917	29.27
12	1.25	ML summer	ML summer	.3947	36.59
13	1.50	ML summer	ML summer	.3886	43.91
14	1.75	ML summer	ML summer	.4057	51.23
15	2.00	ML summer	ML summer	.3774	58.54
16	0.40	ML winter	ML winter	.3178	3.42
17	0.50	ML winter	ML winter	.3584	4.27
18	0.75	ML winter	ML winter	.3767	6.41
19	1.00	ML winter	ML winter	.3671	8.54
20	1.25	ML winter	ML winter	.3518	10.68
21	1.50	ML winter	ML winter	.3366	12.81
22	1.75	ML winter	ML winter	.3478	14.95
23	2.00	ML winter	ML winter	.3202	17.08
24	0.40	ML winter	ML summer	.3695	11.71
25	0.50	ML winter	ML summer	.3697	14.64
26	0.75	ML winter	ML summer	.3722	21.95
27	1.00	ML winter	ML summer	.3762	29.27
28	1.25	ML winter	ML summer	.3820	36.59
29	1.50	ML winter	ML summer	.3886	43.91
30	1.75	ML winter	ML summer	.3955	51.23
31	2.00	ML winter	ML summer	.4012	58.54
32	0.40	ML summer	ML winter	.3208	3.42
33	0.50	ML summer	ML winter	.3822	4.27
34	0.75	ML summer	ML winter	.4090	6.41
35	1.00	ML summer	ML winter	.3888	8.54
36	1.25	ML summer	ML winter	.3645	10.68
37	1.50	ML summer	ML winter	.3396	12.81
38	1.75	ML summer	ML winter	.3219	14.95
39	2.00	ML summer	ML winter	.3086	17.08
40	0.40	Tropical	ML summer	.3980	11.71
41	0.50	Tropical	ML summer	.4006	14.64
42	0.75	Tropical	ML summer	.4007	21.95
43	1.00	Tropical	ML summer	.4013	29.27
44	1.25	Tropical	ML summer	.3995	36.59
45	1.50	Tropical	ML summer	.3886	43.91
46	1.75	Tropical	ML summer	.3784	51.23
47	2.00	Tropical	ML summer	.3696	58.54

surface temperature of -1°C and cases 32–34 have relative humidities of 5–11%. Certainly, cases 32–34 would be extremely rare, a surface temperature of about 20°C and a relative humidity near 10% (although these surface conditions are occasionally observed in Colorado, but the surface pressure certainly isn't 1000 mb). The question of whether these atmospheres are realistic or not is debatable but if they happen, it will be very rarely.

There is also more scatter of the data for the ± 3 GHz channel compared to the ± 1 GHz channel. The results in Tables 5.1 and 5.2 correspond well with results of similar studies conducted by Wilheit and al Khalaf (1993).

Figures 5.1 and 5.2 are plots of the water vapor burden for the 47 cases for 183.31 ± 1 and 3 GHz, respectively (these are the data given in Tables 5.1 and 5.2). Figure 5.1 shows how the vapor burdens corresponding to the level at $T_b = T_t$ only slightly varies from atmosphere to atmosphere whereas Figure 5.2 shows that the water vapor burden is much more spread although the outliers are of a debatable, physically, as stated above.

Figures 5.3–5.6 show weighting functions plotted in terms of the burden U for the 183.31 ± 1 , 3, 7 GHz and 150.00 GHz channels, respectively. These figures graphically portray the essence of the hypothesis stated above. While the magnitudes of the weighting function change for each atmospheric profile, the peaks of these functions and their shape are remarkably similar for these different atmospheric profiles. This relative independence of the shape of $W(U)$ on both the temperature and moisture profiles provides a useful way of interpreting the SSM/T-2 brightness temperature distributions such as those shown in Figures 2.2–2.11.

5.2 CHANNEL 2 WATER VAPOR BURDEN MAP

Based on the discussion and results of the previous section, this section presents a retrieval of the water vapor burden for Channel 2 (183.31 ± 1 GHz) on a constant pressure surface. The data used in this retrieval consisted of the T-2 brightness temperatures described above and European Centre for Medium Range Weather Forecasts (ECMWF) monthly mean temperature and pressure analyses for March 1992 (used to simulate the temperature and pressure data which will normally be available from the SSM/T-1 Temperature Sounder). ECMWF monthly mean data were used because temperature data

Table 5.2: Water Vapor Overburden (U) at 183.31 ± 3 GHz for $T_b = T_t$.

CASE	H ₂ O MULT. FACTOR	TEMPERATURE PROFILE	WATER VAPOR PROFILE	U (kg/m ²)	CWV (kg/m ²)
1	0.50	Tropical	Tropical	1.4936	20.61
2	0.75	Tropical	Tropical	1.5346	30.91
3	1.0	Tropical	Tropical	1.5220	41.21
4	1.25	Tropical	Tropical	1.5389	51.51
5	1.50	Tropical	Tropical	1.5669	61.82
6	1.75	Tropical	Tropical	1.5923	72.12
7	2.00	Tropical	Tropical	1.6123	82.42
8	0.25	ML summer	ML summer	0.9340	7.32
9	0.50	ML summer	ML summer	1.1354	14.64
10	0.75	ML summer	ML summer	1.4097	21.95
11	1.0	ML summer	ML summer	1.4589	29.27
12	1.25	ML summer	ML summer	1.4913	36.59
13	1.50	ML summer	ML summer	1.5153	43.91
14	1.75	ML summer	ML summer	1.5346	51.23
15	2.00	ML summer	ML summer	0.2077	58.54
16	0.40	ML winter	ML winter	0.3847	3.42
17	0.50	ML winter	ML winter	0.6060	4.27
18	0.75	ML winter	ML winter	1.0605	6.41
19	1.00	ML winter	ML winter	1.1879	8.54
20	1.25	ML winter	ML winter	1.2347	10.68
21	1.50	ML winter	ML winter	1.2901	12.81
22	1.75	ML winter	ML winter	1.3126	14.95
23	2.00	ML winter	ML winter	1.3126	17.08
24	0.40	ML winter	ML summer	1.1331	11.71
25	0.50	ML winter	ML summer	1.2005	14.64
26	0.75	ML winter	ML summer	1.3006	21.95
27	1.00	ML winter	ML summer	1.3760	29.27
28	1.25	ML winter	ML summer	1.4165	36.59
29	1.50	ML winter	ML summer	1.4555	43.91
30	1.75	ML winter	ML summer	1.4848	51.23
31	2.00	ML winter	ML summer	1.5121	58.54
32	0.40	ML summer	ML winter	0.1346	3.42
33	0.50	ML summer	ML winter	0.2674	4.27
34	0.75	ML summer	ML winter	0.7516	6.41
35	1.00	ML summer	ML winter	1.1167	8.54
36	1.25	ML summer	ML winter	1.3064	10.68
37	1.50	ML summer	ML winter	1.3914	12.81
38	1.75	ML summer	ML winter	1.4259	14.95
39	2.00	ML summer	ML winter	1.4423	17.08
40	0.40	Tropical	ML summer	1.2619	11.71
41	0.50	Tropical	ML summer	1.3509	14.64
42	0.75	Tropical	ML summer	1.4658	21.95
43	1.00	Tropical	ML summer	1.4916	29.27
44	1.25	Tropical	ML summer	1.5028	36.59
45	1.50	Tropical	ML summer	1.5376	43.91
46	1.75	Tropical	ML summer	1.5730	51.23
47	2.00	Tropical	ML summer	1.6051	58.54

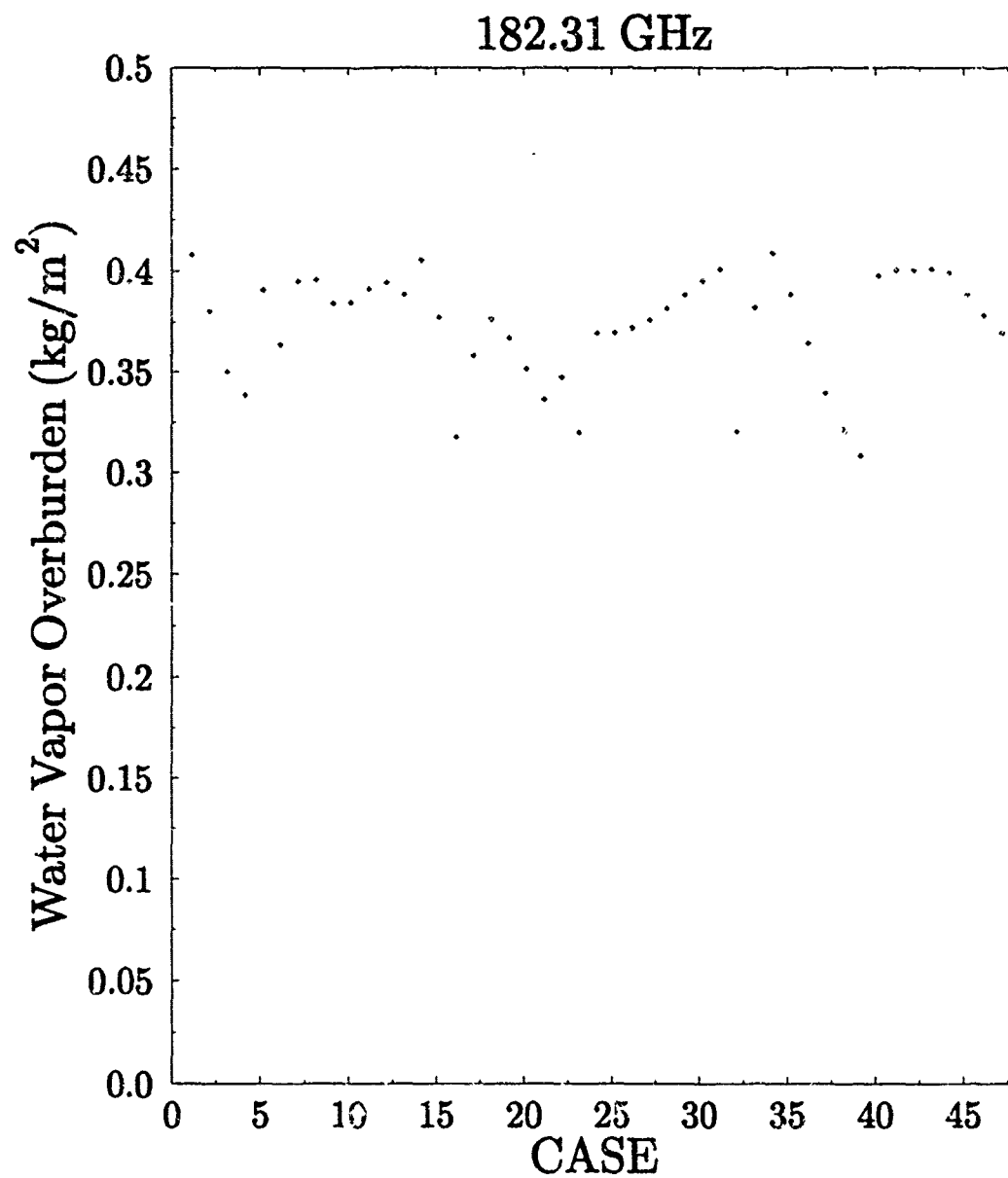


Figure 5.1: Water Vapor Overburdens at 183.31 ± 1 GHz for 47 Atmospheric Cases.

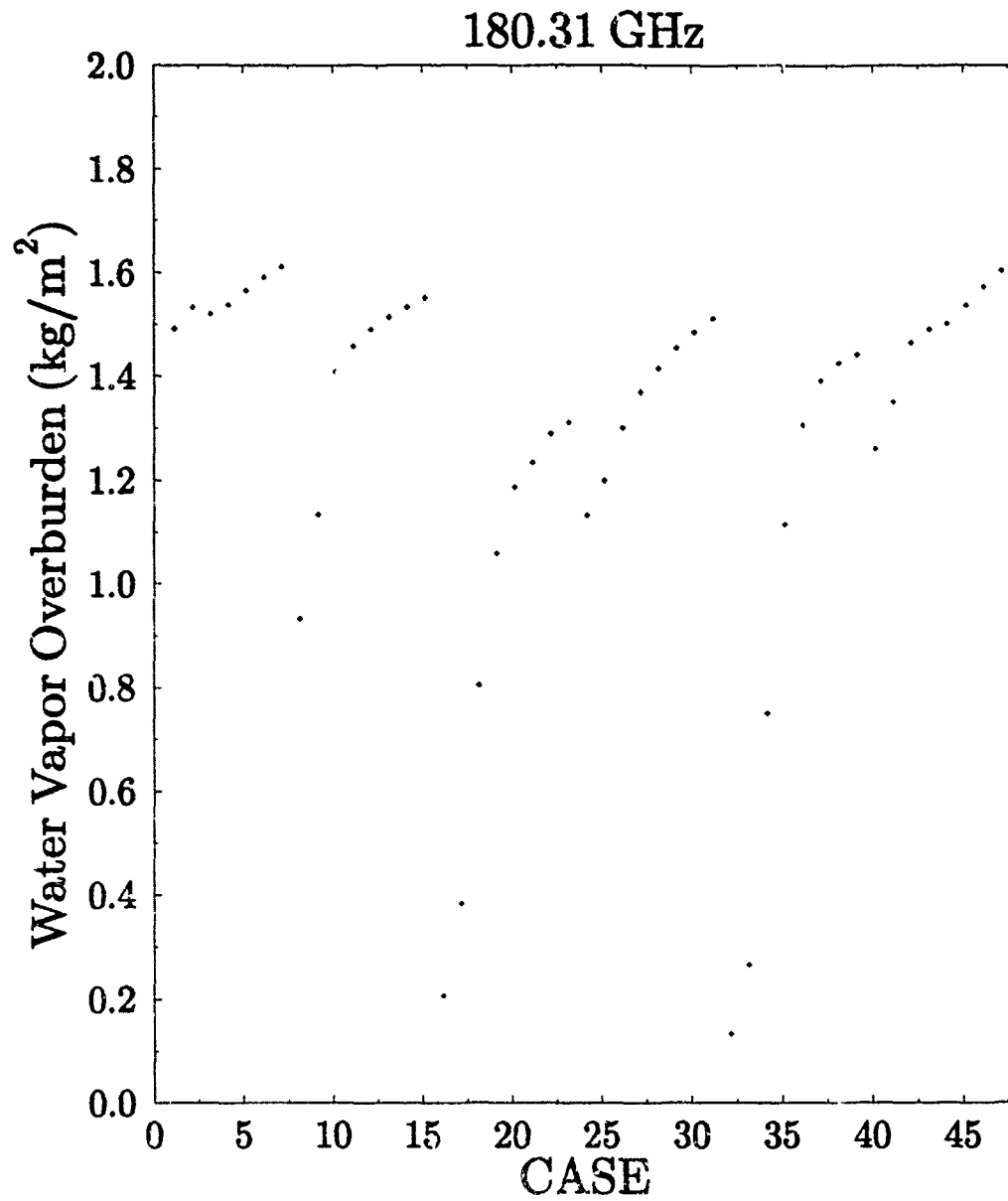


Figure 5.2: Water Vapor Overburden as in Figure 5.1 except at 180.31 GHz.

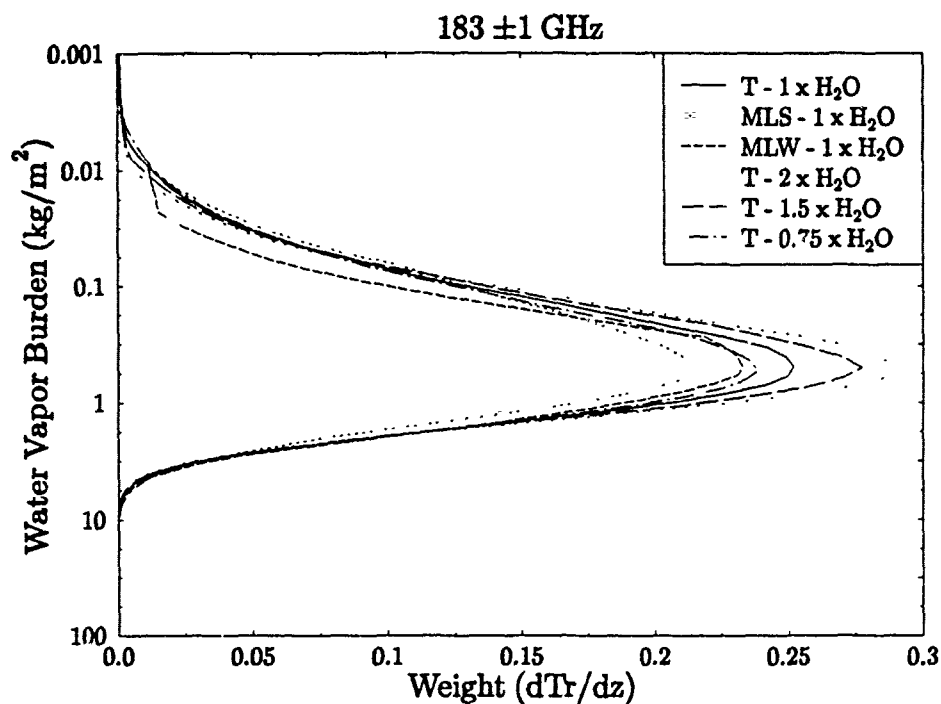


Figure 5.3: Water vapor burden for $183 \pm 1 \text{ GHz}$. Atmospheres are abbreviated as in text.

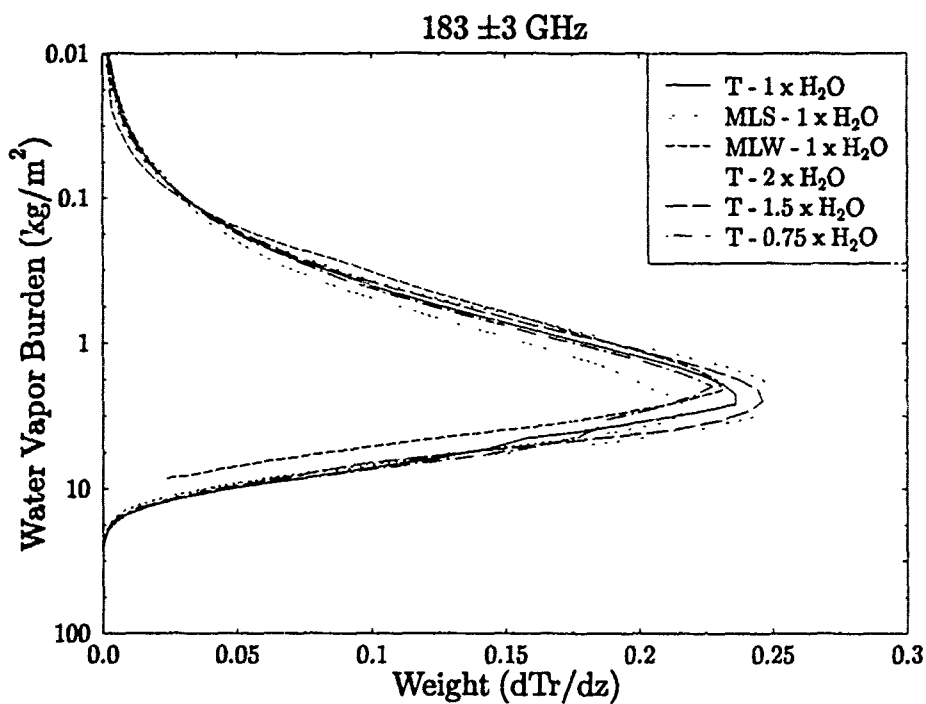


Figure 5.4: Same as in Figure 5.4 except for $183 \pm 3 \text{ GHz}$.

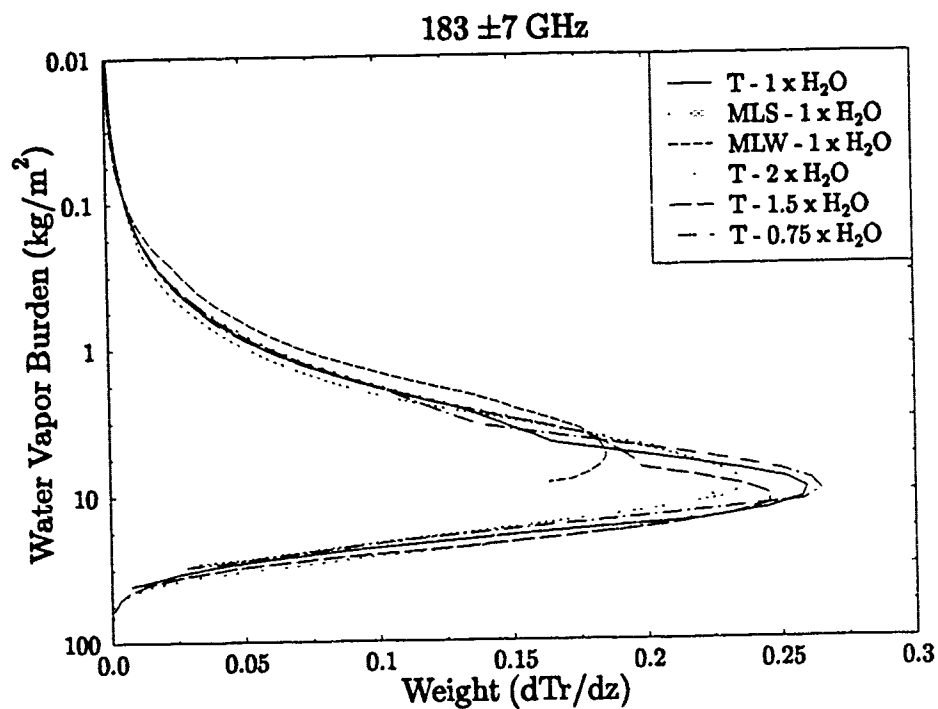


Figure 5.5: The same as Figure 5.3 except for $183.31 \pm 7 \text{ GHz}$.

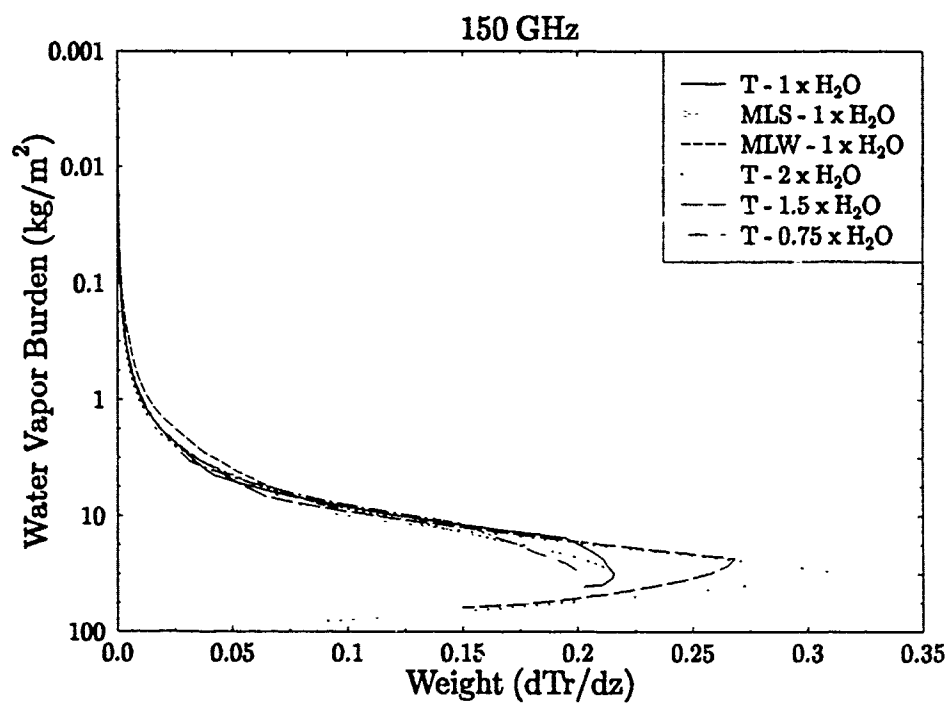


Figure 5.6: The same as Figure 5.3 except for 150 GHz.

coincident with the time of the SSM/T-2 observations was unavailable at the time of this research. The results presented here, especially in the tropics, where synoptic temperature variations are small, will not greatly alter the results presented.

The retrieval starts from the assumption that the brightness temperature and the thermometric temperature of the atmosphere are equal when the vapor burden is 0.3735 kg/m^2 (the mean value from Table 5.1). Using the temperature and pressure data of ECMWF from March 1992, the pressure p^* corresponding to the level where $T_t = T_b$ is derived by interpolation. Maps of p^* represent the contours of the constant U surface. High values of p^* correspond to dry conditions whereas low values of p^* correspond to a moist atmosphere.

A plot of the interpolated p^* derived in this way is presented in Figure 5.7. The pressure varies from high values in the mid-to-high latitudes (varying from 600-500 mb) to regions associated with deep convection in the equatorial regions that have $p^* < 300$ mb. These areas are found in North-central South America, the West Pacific and the South Pacific Convergence Zone (SPCZ), Indonesia extending west into the Indian Ocean, and portions of Central Africa. These regions may be considered to be the ascent region of the Hadley circulation which pumps water vapor from low in the atmosphere to near the tropopause. The subtropical high regions are not as distinct on this map as compared to the brightness temperature maps although some regions do show distinct maxima in p^* such as the Bay of Bengal, and in regions across the northern and southern Pacific. This also is not surprising since the upper level water vapor is carried from the equatorial region at upper levels towards the poles so this water vapor at upper levels would be expected to only drop off slowly. Pressures increase when moving away from the equator. This pressure difference between the tropics and the arctic regions is very large in the Southern Hemisphere whereas this difference is not nearly as great in the Northern Hemisphere.

After calculating this pressure at each grid point, the mean pressure, \bar{p}^* , is computed. A simple method for interpolating the water vapor information contained in Figure 5.7 to a constant pressure surface follows. This surface is selected as the mean pressure \bar{p}^* between 40° North and South latitude which for this case was 393 mb.

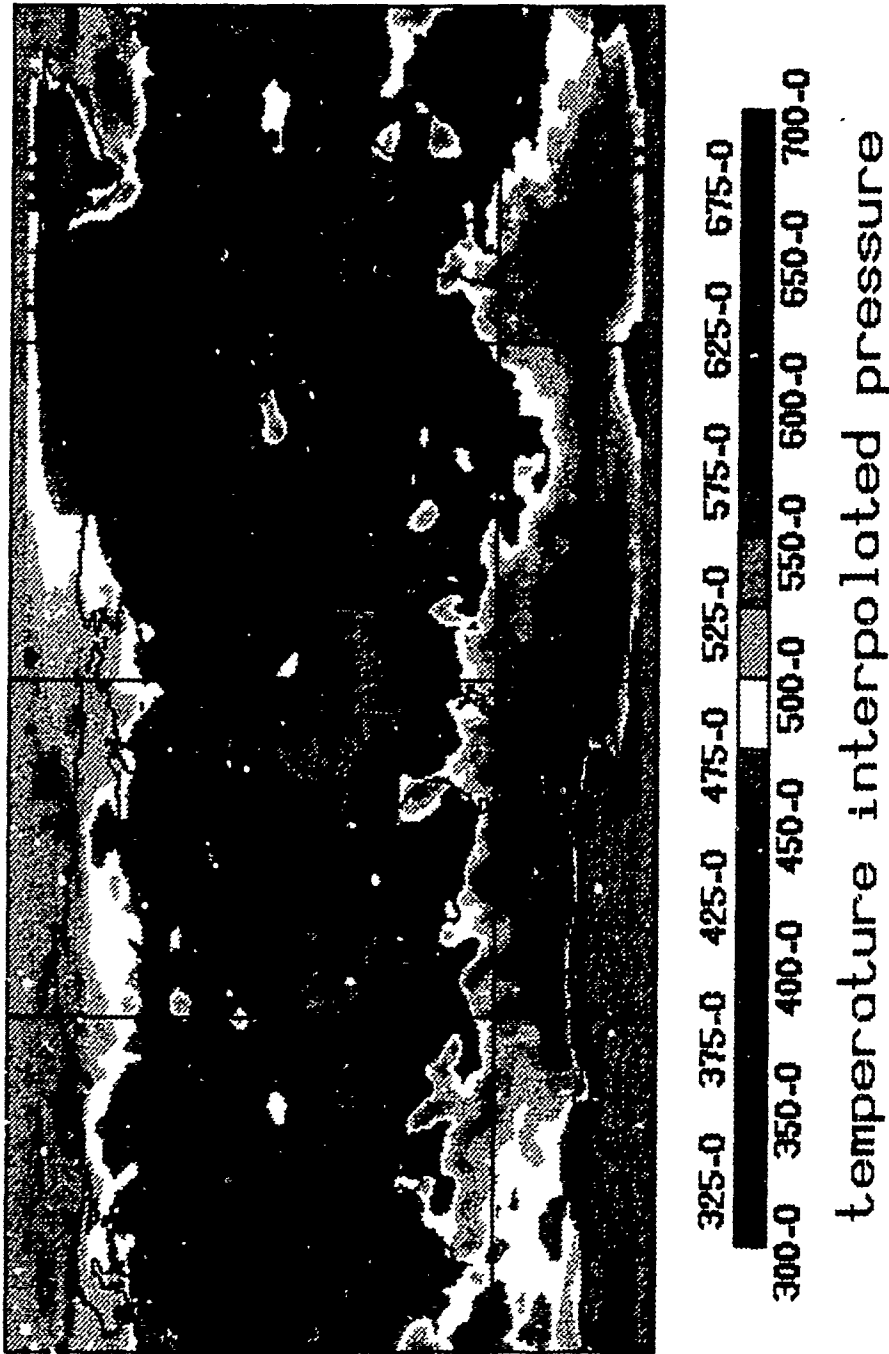


Figure 5.7: Map of pressure, p^* , where $T_t = T_b$.

The water vapor burden for Channel 2, U_2 has a value of 0.37 kg m^{-2} and may be expressed as the integral:

$$U_2 = \frac{1}{g} \int_{p^*}^0 r dp, \quad (5.2)$$

where g is the gravitational constant and r is the mixing ratio. Assuming the mixing ratio can be expressed by: $r = r_s \left(\frac{p}{p_0}\right)^\lambda$ and making the substitution $\tilde{p} = \frac{p}{p_0}$ where p_0 is the surface pressure and r_s the saturation mixing ratio, (5.2) can be rewritten as:

$$U_2 = \frac{r_s p_0}{g} \int_{\tilde{p}^*}^0 \tilde{p}^\lambda d\tilde{p}. \quad (5.3)$$

Finally, making the substitution $\tilde{p}^* = \frac{p^*}{p_0}$ and integrating results in an expression for U_2 :

$$U_2 = \frac{r_s p_0}{g(\lambda + 1)} (\tilde{p}^*)^{\lambda+1}. \quad (5.4)$$

The difference between $U(p^*)$ and $U(\tilde{p}^*)$ at each grid point is now determined and used to adjust the column overburden. This difference, ΔU can be written as (from (5.2)):

$$\Delta U = \frac{r_s p_0}{g} \int_{\tilde{p}^*}^{\tilde{p}} \tilde{p}^\lambda d\tilde{p}, \quad (5.5)$$

which, on integration, becomes:

$$\Delta U = \frac{r_s p_0}{g(\lambda + 1)} [(\tilde{p})^{\lambda+1} - (\tilde{p}^*)^{\lambda+1}] \quad (5.6)$$

On rearrangement using (5.4) for U_2 , (5.6) can be written:

$$\Delta U = \frac{U_2}{(\tilde{p}^*)^{\lambda+1}} [(\tilde{p})^{\lambda+1} - (\tilde{p}^*)^{\lambda+1}]. \quad (5.7)$$

Finally, recalling the definitions for \tilde{p} and \tilde{p}^* and rearranging results in an equation for ΔU which is added to the value of U_2 at each grid point:

$$\Delta U = U_2 \left[\left(\frac{\tilde{p}}{\tilde{p}^*} \right)^{\lambda+1} - 1 \right]. \quad (5.8)$$

Since \tilde{p}^* , the pressure onto which U is to be mapped, is given (393 mb), p^* is derived from the T-2 brightness temperature, and U_2 is known (0.37 kg/m^2), then ΔU can be readily determined and the burden $U(p^*) = U + \Delta U$ then follows. The water vapor overburden U at \tilde{p}^* were derived in this way and mapped (Figure 5.8). The water vapor

burden on the constant pressure surface is very high ($\sim 0.7\text{--}0.8 \text{ kg/m}^2$) in portions of the tropics and extremely low (below 0.2 kg/m^2) in most areas north of Antarctica. These results correlate well with the previous figure. The water vapor burden at $\sim 400 \text{ mb}$ would be expected to be larger at the tropics than towards the poles. Surprising is the magnitude of the differences between these regions.

This process is instructive when one considers that part of the operational output from the T-2 is layer water vapor, as stated in Chapter 2. Performing calculations which yield the water vapor burden on several levels means the layer water vapor mass can also be carried out in this way. Certainly the simplified approach shown above would not be used operationally but it does provide a framework to understand how, in a general sense, the layer vary in the atmosphere and may provide a valuable way of initializing more sophisticated retrieval approaches.



0.10 0.20 0.30 0.40 0.50 0.60 0.70 0.80
 0.05 0.15 0.25 0.35 0.45 0.55 0.65 0.75 0.85

SSM/T-2 Channel 2
 Water Vapor Overburden (kg/m^2)
 March 10-18, 1993

Figure 5.8: Water vapor burden on a constant pressure (393 mb) surface.

Chapter 6

CONCLUSIONS AND SUMMARY

6.1 SUMMARY

The opportunity to be among the first researchers to work with data from the SSM/T-2 Microwave Water Vapor Sounder presented a unique opportunity to examine some of the capabilities of this instrument. Since the SSM/T-2 is a new instrument, the characteristics of this instrument and the other instruments flown on the DMSP spacecraft F-11 were reviewed. The DMSP microwave suite, (SSM/I, SSM/T-1, and SSM/T-2 instruments), and the visible and infrared scanners result in a multi-spectral platform from which observations of the earth may be taken, including the first satellite platform with frequencies near the 183 GHz absorption line.

Remote sensing in the microwave regime has occurred since the 1960's. Techniques for remote sounding in the microwave region have been proposed since the 1970's but only since the launch of the SSM/T-2 has it become possible to profile the distribution of water vapor. Since this sounding approach is solved using weighting functions the properties of these functions for the SSM/T-2 frequencies are examined for a number of different circumstances.

Understanding the response of the measured SSM/T-2 brightness temperatures to a variety of factors (called sensitivity effects, herein) was achieved using a number of models, such as a model of the propagation of microwave radiation through the atmosphere, models of the meteorological state variables of the atmosphere, and simple models of the characteristics of clouds in the atmosphere. Examining how brightness temperatures respond to different atmospheric parameters provides conceptual framework necessary to understand the properties of the SSM/T-2 brightness temperatures and the weighting functions that characterize these temperatures

The T-2 data were analyzed by averaging these data in 1° latitude \times longitude bins over two time periods. Because of the small swath width, the result of discarding data from the 4 scan scenes furthest from nadir on each side, some regions are not sampled during the two time periods in March 1993 (10–14 and 16–18). The global maps of SSM/T-2 brightness temperatures derived for these two time periods were examined and related to the gross characteristics of the general circulation of the atmosphere. Additionally, some information about the surface characteristics of earth and the moisture profiles above the land surfaces are discernible from these brightness temperatures.

Comparisons of brightness temperatures from two regions of the tropical Pacific were presented. One of these regions was located within the TOGA COARE domain and is characterized by deep convection and moist conditions. The second region was over the Eastern Pacific under prevailing subsidence and thus represents conditions of drying.

The concept of the invariance of the weighting functions invariant with respect to water vapor overburden is tested. It is demonstrated that the level where Channel 2 and Channel 1 brightness temperatures match the thermodynamic temperature are levels of approximately equal overburden irrespective of the atmospheric profiles of temperature and moisture.

The pressure p^* , which corresponds to the level where the brightness temperature for Channel 2 equals the thermodynamic temperature, was derived by interpolation from temperature–pressure data. The water vapor burden, for Channel 2, U_2 , was then mapped on a constant pressure surface $\bar{p}^* = 393$ mb.

6.2 CONCLUSIONS

From the analyses of both model simulations and observations performed in this study, the following conclusions were made:

1. Weighting functions at T-2 frequencies (and therefore brightness temperatures) are strongly dependent on the profiles of water vapor. The dependence on temperature is weaker.

2. Background (surface) emissivities strongly affect brightness temperatures at 91 GHz, 150 GHz, and at 183 ± 7 GHz. Scenes characterized by backgrounds with high emissivities are scenes of high brightness temperatures.
3. Liquid water clouds profoundly affect brightness temperatures:
 - (a) Increased cloud liquid water content (LWC) decreases brightness temperatures over high emissivity backgrounds.
 - (b) Clouds generally increase brightness temperatures over low emissivity (i.e. ocean) surfaces and decrease brightness temperatures over high (i.e. land) emissivity surfaces.
4. An observational study of the T-2 brightness temperature maps results in the ability to see some characteristics of the known general circulation of the atmosphere. The subtropical regions with their associated subsidence and hence, high brightness temperatures, are striking features on the T-2 brightness temperature maps for all channels on the 183 GHz absorption line. The South Pacific Convergence Zone (SPCZ) and the Intertropical Convergence Zone (ITCZ) appear on the maps of Channels 1 and 2 which are indicative of high mid-to-upper tropospheric water vapor.
5. Surface characteristics can also be observed in the T-2 brightness temperature maps for the window channels (92 and 150 GHz). Arid land areas possess large emissivities and high brightness temperatures. All the land masses in the Southern Hemisphere appear warm in contrast to the relatively cold adjacent ocean regions.
6. Water vapor burdens are relatively constant for the two SSM/T-2 frequencies nearest the absorption line. The water vapor burden is 0.37 ± 0.02 kg/m² for Channel 2 and 1.4 ± 0.15 kg/m² for Channel 1. The pressure of the surface of constant vapor overburden, introduced here as p^* , varies from around 600 mb in high latitudes to pressures less than 300 mb in regions associated with moist convection.

7. Brightness temperatures and temperature-pressure profiles obtained from ECMWF analyses, combined with the above result, were then mapped onto a constant pressure surface. This provides a simple method for retrieving vapor overburden. The method was illustrated for a constant 393 mb pressure surface.

6.3 DISCUSSION OF FUTURE WORK

Obviously, since the SSM/T-2 represents a new microwave radiometer on a satellite there are a number of sensitivity issues which still need to be examined. The first issue that comes to mind is that both mixed phase and ice clouds are not discussed very much in the literature, except that the influence of ice clouds is negligible at the frequencies of the SSM/T-2. Mixed-phase clouds also represent a significant hurdle in the interpretation of brightness temperatures. Certainly, the ability to model this problem and quantify the effects of ice and mixed phase clouds would increase the ability to retrieve water vapor information.

A validation test of the retrieval scheme introduced here should also be undertaken. This could be accomplished using data from special intensive observation periods (e.g. TOGA COARE) where water vapor information derived from radiosonde observations could be compared with coincident T-2 data.

Improved models of the surface emissivity at the 183 GHz region are also needed. These models should address the emissivities ocean surfaces and sea ice and snow surfaces. The possibility of using the T-2 for snow cover mapping should also be investigated.

The 183 GHz region is under study by NASA in a high priority program to place a Microwave Imager and Sounder on a future geostationary satellite - the GEO-PLATFORM. A microwave sounder of this type would certainly improved the sampling capabilities for mesoscale forecasting.

I feel the immediate future (less than five years) will see an enormous amount of research along the lines of a synergistic approach/unified retrieval. The scanners and radiometers on DMSP spacecraft F-11 provide a data set which is as comprehensive as any. Certainly the SSM/I could be used for the ocean surface wind speeds and this

information could be used to help in the determination of the background emissivity over ocean surfaces for the 183 GHz channels. Additionally, the SSM/I and SSM/T-2 can be used together for column water vapor and cloud liquid water content. Here it may be possible to explore column water vapor over both land and ocean surfaces. Present SSM/I analysis of this column quantity is restricted to ocean areas only. The visible and infrared data from the OLS can be used for cloud type determination (and cloud cover) and the responses of the SSM/T-2 channels can be evaluated to improve the understanding of the effects of clouds in the 183 GHz region.

The SSM/T-2 will serve to only expand the research opportunities to those with a keen interest in water vapor and it will undoubtedly improve the ability of NWP models to forecast the state of the atmosphere. While a great deal of work remains to be done on the use of the 183 GHz absorption line for water vapor profiling, it has been an enlightening opportunity to use the T-2 data.

REFERENCES

- Barath, F.T., A.H. Barrett, J. Copeland, D.E. Jones, and A.E. Lilley, 1964: Mariner 2 microwave radiometer experiments and results. *Astron. J.*, **69**, 49-58.
- Bates, J.J. and G.L. Stephens, 1991: Global integrated water vapor from satellite data: preliminary results from a GVaP pilot study. Preprints *Fifth Conference on Climate Variations*, Denver, Amer. Meteor. Soc., 303-304.
- Bennett, W.H., 1987: Passive microwave sounders for air temperature and water vapor profiling. *NOAA NESDIS Tech. Rep. 35*, NOAA, Wash. D.C., 157-165.
- Boucher, D.J., B.H. Thomas, and A.M. Kishi, 1993: Performance of the DMSP SSM/T-2 microwave radiometer: a comparison between sensor derived, model analyzed, and radiosonde measured moisture variables. Preprints *8th Symp. on Meteorological Observations and Instrumentation*, Anaheim, CA, Amer. Meteor. Soc., J150-J152.
- Curtis, J.A., and B.W. Shipley, 1987: Air Force microwave programs: status and future plans. *NOAA NESDIS Tech. Rep. 35*, NOAA, Wash. D.C., 16-20.
- Eyre, J. and H. Woolf, 1988: Transmittance of atmospheric gases in the microwave region: a fast model. *Appl. Opt.*, **27**, 3244-3249.
- Falcone, V.J., L.W. Abreu, and E.P. Shettle, 1979: Atmospheric attenuation of millimeter and submillimeter waves: models and computer code. *Rep. AFGL-TR-79-0253*, 79pp., Air Force Geophysics Lab., Hanscom Air Force Base, Bedford MA.
- Falcone, V.J. and R.G. Isaacs, 1987: The DMSP Microwave Suite. *NOAA NESDIS Tech Rep. 35*, NOAA, Wash. D.C., 174-185.
- Fleming, H.E., N.C. Grody, and E.J. Kratz, 1991: The forward problem and corrections for the SSM/T satellite microwave temperature sounder. *IEEE Trans. Geosci. Remote Sensing*, **29**, 571-583.

Gaut, N.E., M.G. Fowler, R.G. Isaacs, D.T. Chang, and E.C. Reifstein, 1975: Studies of microwave remote sensing of atmospheric parameters. *Rep. AFCRL-TR-75-0007*, 75 pp., Air Force Cambridge Res. Lab., Bedford, MA.

Griffin, M.K., V.J. Falcone, J.F. Morrissey, R.G. Isaacs, J.D. Pickle, R. Kakar, J. Wang, and P. Racette, 1993: The Special Sensor Microwave Water Vapor Sounder (SSM/T-2): calibration study. Preprints *8th Symp. on Meteorological Observations and Instrumentation*, Anaheim CA, Amer. Meteor. Soc., J144-J149.

Grody, N.C., 1983: Severe storm observations using the Microwave Sounding Unit. *J. Climate Appl. Meteor.*, **22**, 609-625.

Hillger, D.W., and T.H. Vonder Haar, 1981: Retrieval and use of high resolution moisture and stability fields from NIMBUS 6 HIRS radiances in pre-convective situations. *Mon. Wea. Rev.*, **109**, 1788-1806.

Hoffman, R.N., C. Grassotti, R.G. Isaacs, J.F. Louis, T. Nehr Korn, and D.C. Norquist, 1990: Assessment of the impact of simulated satellite lidar wind and retrieved 183 GHz water vapor observations on a global data assimilation system. *Mon. Wea. Rev.*, **118**, 2513-2542.

Hollinger, J.P., J.L. Peirce, and G.A. Poe, 1990: SSM/I Instrument Evaluation. *IEEE Trans. Geosci. Remote Sensing*, **28**, B781-789.

Houghton, J.T., G.J. Jenkins, and J.J. Ephraums, eds., 1990: *Climate Change. The IPCC Scientific Assessment*. 365 pp., Cambridge University Press, Cambridge.

Isaacs, R.G., 1987: Review of 183 GHz moisture profiler retrieval studies. *Rep. AFGL-TR-87-0127*, 52 pp., Air Force Geophysics Lab., Hanscom Air Force Base, Bedford, MA.

Isaacs, R.G., and G. Deblonde, 1985: Water vapor profile retrievals at 183 GHz: land vs. ocean and clear vs. cloudy. *Rep. AFGL-TR-85-0095*, 88 pp., Air Force Geophysics Lab., Hanscom Air Force Base, Bedford, MA.

Isaacs, R.G., G. Deblonde, R.D. Worsham and M. Livshits, 1985: Millimeter wave moisture sounder feasibility study: the effect of cloud and precipitation on moisture retrievals. *Rep. AFGL-TR-85-0040*, 60 pp., Air Force Geophysics Lab., Hanscom Air Force Base, Bedford, MA.

Isaacs, R.G., and G. Deblonde, 1987: Millimeter wave moisture sounding: the effect of clouds. *Radio Sci.*, **22**, 367-377.

Jackson, D.L., 1992: On the role of SSM/I precipitable water over the globe and tropical pacific. M.S. Thesis, Colorado State University, Ft. Collins, 112 pp.

Kakar, R.K., 1983: Retrieval of clear sky moisture profiles using the 183 GHz water vapor line. *J. Climate Appl. Meteor.*, **22**, 1282-1289.

Kakar, R.K. and B.H. Lambrigtsen, 1984: A statistical method for the retrieval of atmospheric moisture profiles by microwave radiometry. *J. Climate Appl. Meteor.*, **23**, 1110-1114.

Liebe, H.J., 1989: MPM89 - an atmospheric mm-wave propagation model. *Int. J. IR & MM Waves*, **10**, 631-650.

Liebe, H.J., T. Manabe, and G.A. Hufford, 1989: Millimeter-wave attenuation and delay rates due to fog/cloud conditions. *IEEE Trans. Antennas Propagat.*, **AP-37**(12), 1617-1623.

Lindzen, R.S., 1990: Some coolness concerning global warming. *Bull. Amer. Meteor. Soc.*, **71**, 288-299.

Liou, K.N., P.T. Nipko, G.C. AufderHaar, and H.Y. Yeh, 1979: Development of the microwave radiative transfer program for cloudy atmospheres: application to DMSP SSM/T channels. *Rep. AFGL-TR-80-0051*, 120pp, Air Force Geophysics Lab., Hanscom Air Force Base, Bedford MA.

Lutz, R., T.T. Wilheit, J.R. Wang, and R.K. Kakar, 1991: Retrieval of atmospheric water vapor profiles using radiometric measurements at 183 and 90 GHz. *IEEE Trans. Geosci. Remote Sensing*, **GE-29**, 602-609.

McClatchey, R.A., R.W. Fenn, J.E.A. Selby, F.E. Volz, and J.S. Garing, 1972: Optical properties of the atmosphere. *Environ. Res. Pap.* 411, 108 pp., Air Force Cambridge Res. Lab., Bedford, MA.

Pandey, P.C., and R.K. Kakar, 1982: An empirical microwave emissivity model for a foam-covered sea. *IEEE J. Oceanic Eng.*, **OE-7**(3), 135-140.

Peixoto, J.P., and A.H. Oort, 1983: The atmospheric branch of the hydrological cycle and climate. in *Variations on the Global Water Budget*, D. Reidel, Norwell, Mass., 5-65.

Prabhakara, C. and G. Dalu, 1980: Passive remote sensing of the water vapor in the troposphere and its meteorological significance. In *Atmospheric Water Vapor*, edited by A. Deepak, T.D. Wilkenson, and L.H. Ruhnke, Academic Press, New York, 355-374.

Prabhakara, C., H.D. Chang, and A.T.C. Chang, 1982: Remote sensing of precipitable water over the oceans from Nimbus 7 microwave measurements. *J. Appl. Meteor.*, **21**, 59-68.

Ray, P.S., 1972: Broadband complex refractive indices of ice and water. *Appl. Opt.*, **11**, 1835-1844.

Racette, P.E., L.R. Dod, J.C. Shiue, R.F. Adler, D.M. Jackson, A.J. Gasiewski, and D.S. Zacharias, 1992: Millimeter-wave imaging radiometer for cloud, precipitation, and atmospheric water vapor studies. *IGARSS-92 Proceedings*, Houston TX.

Rosenkranz, P.W., M.J. Komichak, and D.H. Staelin, 1982: A method for estimation of atmospheric water vapor profiles by microwave radiometry. *J. Appl. Meteor.*, **21**, 1364-1370.

Schaerer, G. and T.T. Wilheit, 1979: A passive microwave technique for profiling of atmospheric water vapor. *Radio Sci.*, **14**, 371-375.

Schwartz, B.E. and C.A. Doswell III, 1991: North American radiosonde observations: problems, concerns, and a call to action. *Bull. Amer. Meteor. Soc.*, **72**, 1885-1896.

Smith, W.L., H.M. Woolf, C.M. Hayden, D.Q. Wark, and L.M. McMillan, 1979: The TIROS-N Operational Vertical Sounder. *Bull. Amer. Meteor. Soc.*, **60**, 1177-1187.

Smith, W.L., 1983: The retrieval of atmospheric profiles from VAS geostationary radiance observations. *J. Atmos. Sci.*, **40**, 2025-2035.

Spencer, R.W., J.R. Christy, and N.C. Grody, 1990: Global atmospheric temperature monitoring with satellite microwave measurements: method and results. *J. Clim.*, **3**, 111-128.

Staelin, D.H., K.F. Kunzi, R.L. Pettyjohn, R.K.L. Poon, R.W. Wilcox, and J.W. Walters, 1976: Remote sensing of atmospheric water vapor and liquid water with the Nimbus-5 microwave spectrometer. *J. Appl. Meteor.*, **15**, 1204-1214.

Stephens, G.L., and S. A. Tjemkes, 1992: Water vapour and its role in the earth's greenhouse. *Aust. J. Phys.*, submitted.

Stephens, G.L., 1993: *The Remote Sensing of the Lower Atmosphere: An Introduction*, Oxford, Oxford University Press, in press.

Twomey, S., 1977: *Introduction to the mathematics of inversion in remote sensing and indirect measurements*. 243 pp., Elsevier Scientific Publishing Company, Amsterdam.

Wang, J.R., and T.J. Schmugge, 1980: An empirical model for the complex dielectric permittivity of soils as a function of water content. *IEEE Trans. Geosci. Remote Sens.*, GE-18, 288-295.

Wang, J.R., J.L. King, T.T. Wilheit, G. Szejwach, L.H. Gessell, R.A. Nieman, D.S. Niver, B.M. Krupp, and J.A. Gagliano, 1983: Profiling atmospheric water vapor by microwave radiometry. *J. Climate Appl. Meteor.*, 24, 779-788.

Wang, J.R., W.C. Boncyk, L.R. Dod, and A.K. Sharma, 1992: Retrieval of total precipitable water over high latitude regions using radiometric measurements near 90 and 183 GHz. *J. Appl. Meteor.*, 31, 1368-1378.

Waters, J.W., 1976: Absorption and emission by atmospheric gases, in *Methods of Experimental Physics*, 12, Academic, New York, pp. 142-176.

Wilheit, T.T., 1979: A model for the microwave emissivity of the ocean's surface as a function of wind speed. *IEEE Trans. Geosci. Electron.*, GE-17, 244-249.

Wilheit, T.T., 1990: An algorithm for retrieving water vapor profiles in clear and cloudy atmospheres from 183 GHz radiometric measurements: simulation studies. *J. Appl. Meteor.*, 29, 508-515.

Wilheit, T.T., and A. al Khalaf, 1993: A simplified interpretation of the radiances from the SSM/T-2. *Meteorology and Atmospheric Physics*, submitted.

Wittmeyer, I.L., 1990: Satellite based estimates of global precipitable water and poleward latent heat transport. M.S. Thesis, Colorado State University, Ft. Collins, 76 pp.

Wittmeyer, I.L. and T.H. Vonder Haar, 1993: Analysis of the global ISCCO TOVS water vapor climatology. *J. Climate*, accepted.